Half-metal magnets Heusler compounds for spintronics

Charles Guillemard

Thèse de doctorat

présentée en vue de l'obtention du grade de
Docteur de l'Université de Lorraine
dans la spécialité
Physique

Half-metal magnets Heusler compounds for spintronics

---

soutenue publiquement le **17 octobre 2019** par

Charles Guillemard

devant le jury composé de :

Pr. Albert Fert Professeur à l'université Paris Sud - Thalès	Président du jury
Dr. Véronique Brouet Directrice de recherche CNRS - LPS	Rapportrice
Dr. Joo-Von Kim Chargé de recherche CNRS - C2N	Rapporteur
Pr. Virginie Serin Professeur à l'université de Toulouse - CEMES	Examinatrice
Dr. François Bertran Scientifique de ligne au synchrotron SOLEIL	Co-directeur de thèse
Pr. Stéphane Andrieu Professeur à l'Université de Lorraine - IJL	Directeur de thèse
Dr. Alexandre Bataille Chercheur CEA - LLB	Invité

Institut Jean Lamour - UMR CNRS 7198
Université de Lorraine - Faculté des Sciences et Technologies
Synchrotron SOLEIL

Résumé

L'électronique de spin

Le développement et l'amélioration des techniques d'évaporation de couches minces ont permis en 1988 de mettre en évidence l'effet de magnétorésistance géante [1] dans les vannes de spin par A. Fert et P. Grünberg (prix Nobel de physique en 2007). Une vanne de spin est une structure multi-couches composée de deux électrodes magnétiques séparées par un espaceur conducteur non magnétique. On observe alors une variation de la conductance du dispositif selon les directions respectives des aimantations des couches magnétiques. Cette découverte majeure est à l'origine d'une nouvelle branche de la physique de la matière condensée : l'électronique de spin ou "spintronique". Mélangeant magnétisme, nanotechnologie et électronique, l'importance de cette branche provient de sa grande richesse d'un point de vue fondamental et des nombreuses applications qui en découlent. En effet, depuis 1997, les têtes de lectures à effet GMR ont permis de mettre au point une nouvelle génération de disques durs et de mémoires magnétiques dont la capacité de stockage ne cesse d'augmenter. Quelques années plus tard, la découverte des jonctions tunnel magnétiques (JTM) où cette fois-ci, l'espaceur non magnétique est un isolant, a donné un nouveau souffle à la spintronique pour plusieurs raisons : courants consommés très inférieurs (puisque courant tunnel), meilleure "non-volatilité" des points mémoire, effet de mangéto-résistance plus grand, ce qui simplifie les systèmes de détection. Découvert initialement en 1975 par M. Jullière, l'effet de magnétorésistance tunnel a conduit à faire des JTM la nouvelle brique de base de la spintronique pour les mémoires magnétiques.

L'écriture de l'information revient donc à manipuler l'aimantation d'une des couches magnétiques de ce système à deux états : aimantations parallèles (grande conductance) ou antiparallèles (conductance faible)Cependant, l'utilisation d'un champ magnétique pour retourner l'aimantation par effet Zeeman est restrictive en terme de densité de dispositifs au sein d'une mémoire puisqu'il est difficile d'appliquer un champ magnétique suffisamment localisé, dans l'ère de la miniaturisation des édifices. La découverte de la rotation de l'aimantation par couple de transfert de spin en 1996 [2, 3] via un courant polarisé en spin fut le dernier verrou scientifique pour aboutir au produit appelé STT-MRAM (Spin Transfer Torque – Magnetic Random Access Memory). L'injection d'un courant polarisé en spin a pour effet de transférer du moment cinétique de spin aux électrons de la couche magnétique et, si ce transfert de moment est assez important, de retourner l'aimantation globale de la couche "libre" de la jonction. Cette méthode de renversement de l'aimantation des couches permet d'augmenter la densité de bits au sein d'une mémoire mais les courants nécessaires sont encore trop grands [4]. Il est possible de diminuer ce courant critique de retournement en jouant sur plusieurs facteurs. En particulier, injecter un courant d'électrons totalement polarisés en spin augmente l'efficacité du transfert de moment cinétique. De plus, le couple de transfert de spin fait précesser l'aimantation avant de la retourner. On voit donc que la diminution du coefficient d'amortissement magnétique (ou coefficient d'amortissement de Gilbert) permettra de diminuer

le courant nécessaire au retournement de l'aimantation. Enfin, obtenir une aimantation perpendiculaire au plan des couches permettrait également de diminuer le courant critique de retournement puisqu'on s'affranchirait de l'énergie de champ démagnétisant lors de la mise en précession de l'aimantation [5].

Les alliages d'Heusler

D'une manière générale, la spintronique est fondée sur la manipulation de courants (de charges ou de spins) afin de contrôler la configuration magnétique d'une structure, et réciproquement. Jusqu'à maintenant, les dispositifs utilisés dans ce domaine sont à base de couches minces de quelques nanomètres de matériaux ferromagnétiques standards tels que Fe, Co ou Ni et leurs alliages. Néanmoins, pour satisfaire les critères cités à la fin du paragraphe précédent, il est nécessaire de trouver des matériaux alternatifs qui possèdent des propriétés électroniques plus intéressantes. Comme nous allons le voir, les alliages d'Heusler sont d'excellents candidats pour la spintronique [6]. Ce sont des composés ternaires ferromagnétiques de formule chimique X_2YZ, où X et Y sont des métaux de transition et Z est généralement un élement *sp*. Les 3 éléments chimiques s'arrangent sur un réseau cubique à faces centrées qui comporte quatre sites différents. Ces alliages peuvent donc être sujets au désordre chimique, où les élements ne s'arrangent pas correctement sur leurs sites respectifs. Dans le cadre de cette thèse, l'étude se concentre sur les Heusler du type Co_2MnZ avec Z = Al, Si, Ga, Ge, Sn et Sb puisque ces composés sont théoriquement pourvus de propriétés exceptionnelles telles que la demi-métallicité magnétique et un très faible coefficient d'amortissement de Gilbert [7, 8].

Les demi-métaux magnétiques

Un matériau demi-métal magnétique (Half Metal Magnet - HMM) est un matériau magnétique qui ne possède pas de densité d'états au niveau de Fermi pour les électrons de spin minoritaires [9], on parle également de gap de spin. Autrement dit, les électrons de spin majoritaire (ceux qui définissent l'aimantation) ont un comportement métallique tandis que les électrons de spin minoritaire ont un comportement semi-conducteur. Une telle structure électronique permet de génerer des courants d'électrons complètement polarisés en spin. Des mesures de photoémission résolue en spin antérieures au début de cette thèse ont montré que l'alliage d'Heusler Co_2MnSi avait une polarisation de 100 % au niveau de Fermi [10]. De ce résultat très prometteur naquit l'intérêt de confirmer les prédictions théoriques sur la série d'alliages Co_2MnZ, dont plusieurs seraient HMM.

Conséquences sur l'amortissement magnétique

On a vu qu'un autre moyen pour réduire le courant critique de retournement de l'aimantation par couple de transfert de spin était d'avoir des matériaux avec un amortissement magnétique le plus faible possible. L'amortissement magnétique est une constante phénoménologique introduite par Gilbert pour décrire de manière simple le fait que l'aimantation d'un matériau magnétique ne précesse pas indéfiniment autour d'un champ magnétique appliqué mais finit par s'aligner avec ce dernier. En fait, la comparaison avec un pendule simple est très parlante : un pendule dans le vide oscille indéfiniment tandis que si on le plonge dans un fluide, il ne fera que quelques oscillations (en fonction de la viscosité du fluide) avant de

s'amortir le long de sa position d'équilibre, dictée par la gravité. Dans un solide, la position d'équilibre de l'aimantation est régie par un champ effectif regroupant plusieurs termes d'énergie (énergie d'échange, énergies d'anisotropies magnéto-cristallines, *etc*.). Plus le coefficient d'amortissement sera faible, plus il sera facile de faire précesser l'aimantation. De ce fait, le courant nécessaire au renversement par couple de transfert de spin sera plus faible. Cette constante est phénoménologique puisqu'il n'existe pas d'origine unique à cette dissipation d'énergie, ce qui en rend la description très difficile [11]. Des valeurs de coefficient d'amortissement records sont prédites pour les matériaux qui présentent le caractère HMM. En effet, une des origines de cet amortissement est la diffusion du moment cinétique de spin par les électrons de conduction. Dans les matériaux HMM, il n'y a aucune densité d'états au niveau de Fermi pour les électrons de spin minoritaires, il y a donc un canal de conduction en moins par rapport aux autres matériaux et une probabilité nulle de retourner le spin d'un électron après diffusion. On comprend alors pourquoi ils doivent avoir un coefficient d'amortissement le plus faible possible. Des calculs ont montré qu'il pouvait descendre dans la gamme des 10^{-5} [12], alors qu'il reste au-dessus de 10^{-3} dans les matériaux standards tels que les alliages Fe_xV_{1-x} [13].

Résultats principaux

Ce manuscrit est divisé en 5 chapitres dont 4 présentant des résultats expérimentaux. Dans le chapitre 2, nous montrons comment nous élaborons des couches minces de Co_2MnZ monocristallines en utilisant la technique d'épitaxie par jet moléculaire. Une attention particulière est portée à la vérification d'une excellente qualité structurale ainsi qu'un ordre chimique total. Pour ce faire, plusieurs études de diffraction (électrons, rayons X) sont menées et poussées jusqu'à leurs limites. En effet, vérifier que ces couches minces possèdent l'ordre chimique de type $L2_1$ (phase Heusler) a nécessité l'utilisation de la microscopie électronique en transmission ultra-haute résolution. Grâce à ces images de microscopie, l'ordre chimique est identifié et il s'avère qu'à l'exception de Co_2MnAl qui possède un désordre de type B2 (désordre Mn / Al), toutes les couches sont parfaitement ordonnées chimiquement (même si une phase inverse est observée pour Co_2MnSn). Les propriétés magnétiques statiques et notamment les moments atomiques par éléments sont obtenus à l'aide du dichroïsme magnétique circulaire effectué sur la ligne de lumière DEIMOS du synchrotron SOLEIL. Les résultats de diffraction, de microscopie et les valeurs de moments magnétiques confirment les calculs *ab initio*. Ils confirment également que ces couches soient des systèmes modèles, le plus proche possible des cristaux parfaits utilisés dans les calculs qui attribuent à ces alliages des propriétés extraordinaires.

Dans le chapitre 3, les calculs *ab initio* qui prédisent que toute la série Co_2MnZ possède un gap de spin minoritaire, ainsi que les modèles théoriques qui associent à ce gap un amortissement magnétique très faible sont expérimentalement vérifiés. En effet, la spectroscopie de photoémission résolue en spin effectuée sur la ligne de lumière CASSIOPEE du synchrotron SOLEIL a permis de mettre en évidence la demi métallicité magnétique des couches minces Co_2MnZ avec des caractéristiques dépendantes de l'élément Z (telles que la position du niveau de Fermi ou la largeur du gap). De plus, les mesures de résonance ferromagnétique montrent des coefficients dans la gamme des 10^{-4} pour quatre des six composés, avec une valeur minimale de 4.1×10^{-4} obtenues dans Co_2MnSi. Ces valeurs sont les plus basses reportées pour des couches minces conductrices. A la fin de ce chapitre, nous montrons que ces coefficients d'amortissement de Gilbert sont complètement corrélés à la structure électronique mesurée en photoémission. En particulier, la position du niveau de Fermi par rapport au gap est un paramètre primordial pour la réduction de l'amortissement.

Dans le chapitre 4, nous essayons de combiner les propriétés remarquables des composés Heusler Co_2MnZ avec l'aimantation perpendiculaire au plan des couches. Cette propriété est également requise pour réduire les courants de retournement par couple de transfert de spin. Pour ce faire, nous utilisons la forte anisotropie magnéto-cristalline du composé tétragonal Mn_3Ga, stabilisé sur une couche tampon de Pd. Ensuite, des super-réseaux Mn_3Ga / Co_2YZ sont élaborés et caractérisés par diffraction, microscopie, magnétométrie et dichroïsme magnétique circulaire. Tous les différents super-réseaux présentent l'anisotropie magnétique perpendiculaire au plan des couches, ce qui constitue un résultat très prometteur. Cependant, certaines propriétés magnétiques demeurent incontrôlées et incomprises (faibles rémanences à champs nuls et champs coercitifs trop élevés).

Finalement, dans le chapitre 5, nous utilisons les mesures de photoémission et de résonance ferromagnétiques sur la série d'alliages de substitution $Co_2MnSi_xAl_{1-x}$ obtenues dans le chapitre 3, où il a été montré que, suivant la composition x, la polarisation en spin au niveau de Fermi et l'amortissement de Gilbert pouvaient être graduellement contrôlés. Cette série d'alliages est donc parfaite pour vérifier expérimentalement les modèles théoriques, qui relient le temps de désaimantation ultrarapide induite par excitation laser au coefficient d'amortissement de Gilbert. Ces deux grandeurs, vivant sur deux échelles de temps différentes, apparaissent effectivement reliées en prenant en compte des processus de diffusion induisant le retournement des moments de spin.

Publications associated to this PhD thesis

(1) C. Guillemard, W. Zhang, G. Malinowski, C. De Melo-Sanchez, J. Gorchon, S. Petit-Watelot, J. Ghanbaja, S. Mangin, P. Le Fèvre, F. Bertran and S. Andrieu, "Unifying ultrafast demagnetization and intrinsic Gilbert damping in $Co_2MnAl_xSi_{1-x}$ Heusler compounds with tunable spin polarization", *in preparation*.

(2) C. Guillemard, S. Petit-Watelot, J.-C. Rojas-Sánchez, J. Hohlfeld, J. Ghanbaja, A. Bataille, P. Le Fèvre, F. Bertran and S. Andrieu, "Polycrystalline Co_2Mn-based Heusler thin films with high spin polarization and low magnetic damping", *Applied Physics Letters* **115**, 172401 (2019).

(3) C. Guillemard, S. Petit-Watelot, L. Pasquier, D. Pierre, J. Ghanbaja, J.-C. Rojas-Sánchez, A. Bataille, J. Rault, P. Le Fèvre, F. Bertran and S. Andrieu, "Ultralow Magnetic Damping in Co_2Mn-Based Heusler Compounds: Promising Materials for Spintronics", *Physical Review Applied* **11**, 064009 (2019).

(4) C. Guillemard, S. Petit-Watelot, S. Andrieu and J.-C. Rojas-Sánchez, "Charge-spin current conversion in high quality epitaxial Fe/Pt systems: Isotropic spin Hall angle along different in-plane crystalline directions", *Applied Physics Letters* **113**, 262404 (2018).

(5) T. L. Brown-Heft, J. A. Logan, A. P. McFadden, C. Guillemard, P. Le Fèvre, F. Bertran, S. Andrieu and C. J. Palmstrøm, "Epitaxial Heusler superlattice Co_2MnAl/Fe_2MnAl with perpendicular magnetic anisotropy and termination-dependent half-metallicity", *Physical Review Materials* **2**, 034402 (2018).

Contents

Introduction

As a result of many theoretical and experimental advances, spintronics, electronics that use both the charge and spin of the electron, is progressing. Predictions of many phenomena, such as high magneto-resistance in MgO-based magnetic tunnel junctions [14], magnetization reversal by spin-transfer torques (STTs) [2, 3], magnetization reversal by spin-orbit torques (SOTs) [15], and all optical switching (AOS) by direct laser excitation [16], offer possibilities to design magneto-resistive random-access memories, magnetic sensors, and novel logic devices. Most spintronic devices consist of thin-film heterostructures where interesting physics emerges at the interfaces [17]. For continued progress, magnetic materials with specific and dedicated properties are needed, such as a high Curie temperature and an appropriate magnetic anisotropy for thermal stability [18], a high spin polarization at the Fermi energy to obtain fully-spin-polarized currents, and a small magnetic damping to easily generate magnetization precession. All of these properties are desirable for STT-, SOT-, and AOS-based devices but also in spin waves-based devices, an emergent research field called "magnonics" [19].

However, it is increasingly challenging to achieve low magnetic damping in metallic magnetic materials. The magnetic damping reflects the ability of the magnetization to precess around an effective magnetic field. Dissipation occurs due to interactions with the environment, the precession amplitude decreases, and the oscillating magnetization aligns again with the effective field. This damping process is characterized by the phenomenological Gilbert damping coefficient α within the Landau-Lifshitz-Gilbert formalism [20]. For many emerging spintronic and magnonic applications, this is particularly important in low-power applications that exploit magnetic dynamics such as STT or SOT switching, where switching currents are directly proportional to α [21, 22].

While low damping parameters are often obtained in ferrimagnetic insulating oxides such as yttrium iron garnet, where $\alpha = 7.35 \times 10^{-5}$ can be observed in bulk [23], magnetic metals typically have much higher damping. For instance, Fe_xV_{1-x} and Fe_xCo_{1-x} alloys having a damping coefficient of around $\alpha = 2 \times 10^{-3}$ [13, 24] were considered state of the art for thin films. However, there is a broader class of materials called Half Metal Magnets (HMMs), where ultralow magnetic damping values emerge. The HMM behavior was discovered in 1983 when de Groot *et al.* [9] reported predictions of peculiar electronic properties of the NiMnSb half Heusler compound. Its electronic band structure was predicted to be in between that of a metal and an insulator. For the majority spin, responsible for the macroscopic magnetization, this material is a metal since electronic states are available around the Fermi energy (E_F). However, for minority spins, there is a gap around E_F. HMM are thus metallic for majority spins, whereas they are insulators for minority spins (at 0 K). Such a property leads to a full spin polarization at the Fermi energy, making those materials excellent candidates for spin current generation and filtering. Furthermore, additional theoretical studies performed on HMM materials highlighted another physical property

of major importance in spintronics: their magnetic damping coefficients were predicted to be extremely low compared with those of other conductive materials (a factor 100 below, in the range from 10^{-5} to 10^{-4}) [12, 25, 26].

In HMM materials, extremely low magnetic damping coefficients are predicted for the following reason. The electronic band structure imposes no density of states (DOS) for minority spins. This spin-channel exchange induced by spin flip scattering is thus forbidden and leads to a continuous magnetization precession [25, 27]. In practice, other dissipation processes are possible, leading to a nonzero damping coefficient, but even when they are taken into account, damping coefficients as low as 10^{-5} are predicted. The precession damping is thus much smaller in a HMM material than in a regular ferromagnetic material (with nonzero density of states at the Fermi energy for both spin channels). HMM materials are thus very promising materials for applications.

After the publication of the paper by de Groot *et al.* [9], HMM properties were theoretically predicted for many Heusler compounds and particularly for the Co_2MnZ series [7, 8, 28]. However, it took a significant effort for experimentalists to obtain direct verifications. Indeed, the experimental evidence of a spin gap in the minority spin channel was reported only recently in Co_2MnSi [10, 29]. On the other hand, as small magnetic damping coefficients were reported for several Heusler compounds, the measured values remained in the 10^{-3} range [30, 31], which is at least 10 times larger than predicted and comparable with standard metallic alloys cited above, which are not HMM materials. In 2016, a damping coefficient in the 10^{-4} range was measured for the first time [10] (7×10^{-4} in Co_2MnSi, which was confirmed by another group in 2018 [32]). However, the fact that the magnetic damping values reported in the literature dedicated to HMM materials are often higher than 10^{-3} is puzzling. Recent theoretical studies have reported that the magnetic damping can vary strongly according to the chemical disorder in the unit cell [12, 26, 33]. Thus, one big challenge when growing Co_2MnZ full Heusler thin films is to be as close as possible to the exact stoichiometry and achieve the chemically ordered $L2_1$ phase, as the outstanding properties of Heusler compounds are most often predicted for this specific phase.

In this work, we present a systematic study of Co_2MnZ Heusler thin films epitaxially grown by molecular beam epitaxy. The structural and chemical ordering inside the Heusler lattice was examined by diffraction and microscopy methods. Then, the spin-resolved density of states of those compounds was explored by spin-resolved photoemission spectroscopy performed at SOLEIL synchrotron facility and was shown to be tunable according to the Z element, as predicted by *ab initio* calculations. The magnetization dynamics was investigated afterward by ferromagnetic resonance and ultralow damping coefficients obtained on those compounds were shown to be linked to the underlying electronic structure.

In a second step, two exploratory studies were performed. First, Heusler superlattices using tetragonal Mn_3Ga and fcc Co_2YZ compounds were investigated in order to combine spin gaps and ultralow damping along with the perpendicular magnetic anisotropy necessary to reduce critical switching currents in STT or SOT-based devices. Second, the relation between the Gilbert damping and the ultrafast demagnetization time was analyzed in a quaternary Heusler series with tunable spin polarization and magnetic damping. Heusler compounds are excellent candidates to help shading light on the microscopic origins of the magnetization quenching at the (sub)picoseconds timescale induced by laser pulses and how to relate this quantity with the Gilbert damping that lives in a nanoseconds timescale. A general summary is proposed at the end of this manuscript, together with perspectives opened by the present work.

Chapter 1

Heusler compounds and spintronics

In this chapter, a brief overview of the spintronics applications, challenges and needs is presented. Then, Heusler compounds and particularly Co based full Heuslers are introduced as new promising materials for spintronics and magnon spintronics (magnonics). A short state of the art is given with both theoretical predictions and experimental realizations of their efficiency. Finally, the experimental procedure used in this thesis is presented.

1.1 Spintronics devices and needs

Spin electronics (spintronics) relies on the use of the electron spin as a supplementary degree of freedom to store and process information. Since the present work focuses on fundamental materials science more than devices, only a short introduction to spintronics is made in order to understand the basics and needs.

1.1.1 Magnetization reversal based systems

Spin valves and magnetic tunnel junctions

Developments in magnetism and thin films elaboration has led to the discovery of many effects relying on fundamental properties in condensed matter physics. Among them, the discovery of the Giant Magneto-Resistance (GMR) by A. Fert and P. Grünberg in spin valves [1] (Nobel prize in physics in 2007) signalled a new era in data storage, sensors and information processing. A spin valve is a thin film heterostructure made of two metallic ferromagnets spaced by a non magnetic metallic layer called the barrier. When the barrier is thinner than the spin diffusion length and when a current is flowing in the perpendicular direction, the relative orientation of the two magnetizations of the ferromagnets leads to a two states device: a low resistance state (R_p) when the two magnetizations are parallel and a high resistance state (R_{ap}) when they are anti-parallel[1]. Another promising phenomena is found in Magnetic Tunnel Junctions (MTJ), observed for the first time by Jullière [34]. This time, the barrier is an insulator and the current flows from one ferromagnetic electrode to the other by spin-dependent tunneling transport through the barrier [35], thus reducing the energy consumption of the device along with higher magneto-resistance ratios MR= $\frac{R_{ap}-R_p}{R_p}$.

[1] In some systems with peculiar electronic structures, the situation is reversed, but it is not our goal to go into these details here.

Spin transfer torque

MTJs and spin-valves have recently gained much interest with the theoretical prediction of magnetization reversal by STT by Slonczewski and Berger in 1996 [2, 3]. Reversal by STT consists in changing the state of a MTJ/spin valve between parallel and anti-parallel by injecting a spin polarized electron current. The first ferromagnet has its magnetization pinned and polarizes the current through the barrier. Therefore, spin momentum is transfered to the second ferromagnet, the free layer, in such an extent that the magnetization will precess until reversal occurs. For a MTJ with in plane magnetizations and the current flowing in the perpendicular direction, the switching critical current density is expressed by equation 1.1 [21]:

$$J_c^{\mathrm{STT}} = \left(\frac{\alpha}{\eta}\right)\frac{2e\tau M_S}{\hbar}\left(H + H_K^{\mathrm{eff}}\right), \tag{1.1}$$

with α the Gilbert damping coefficient, η the spin polarization of the current, e the electron charge, τ and M_S the free layer's thickness and magnetization. H is the applied magnetic field strength and H_K^{eff} the effective anisotropy field, containing magneto-crystalline and shape anisotropy constants (including the demagnetizing energy contribution).

MTJs have become one of the basic block for data storage since the experimental confirmation of magnetization reversal by STT [4]. This has motivated the development of a new type of non-volatile memory called STT - Magnetic Random Access Memory (STT-MRAM), sketched in figure 1.1, that could strongly increase the device density in magnetic memory as well as the data recording speed. The principle is that each MTJ behaves as a bit and is aligned along horizontal and vertical lines. The reading of information is easily made by a resistance measurement between the lines connecting a single MTJ. The writing is made thanks to STT by applying an electric current to switch the magnetization of the MTJ free layer.

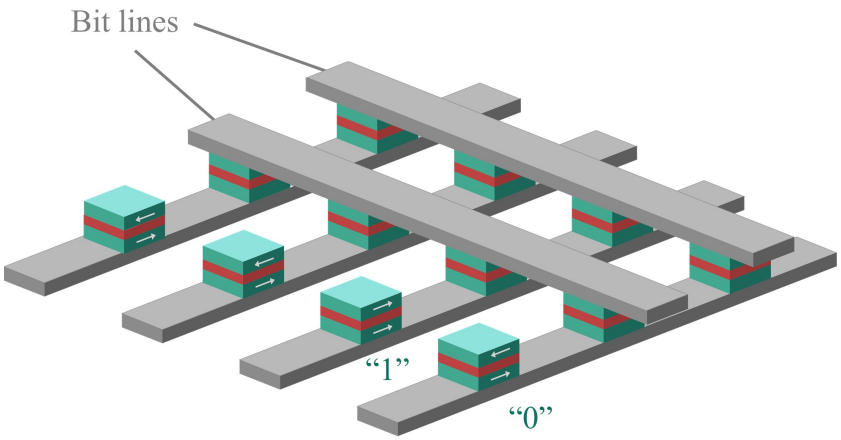

Figure 1.1: Sketch of a STT-MRAM.

Alternative ways to switch the magnetization

Recently, other ways to control the magnetic state of a layer have been experimentally evidenced. Indeed, magnetization reversal by Spin-Orbit Torque (SOT) [15] and All Optical Switching (AOS) [16] also offer a bright future for next generation spintronics devices.

In SOT based devices, a ferromagnetic layer is in direct contact with a non-magnetic metal with a high spin-orbit coupling (such as Ta, Pt or AuW alloys [36]). By applying a DC current through the metal, a transverse spin current is generated perpendicularly to the interface with the ferromagnetic layer, due to the Spin Hall Effect (SHE). This spin current generated by SHE in the non magnetic layer transfers spin momentum into the ferromagnetic layer. If the torque is strong enough, the magnetization of the ferromagnetic layer may switch [37], with a critical switching current density formula described by equation 1.2, proposed by Lee *et al.* for an in-plane magnetized layer [38]:

$$J_c^{\mathrm{SOT}} = \left(\frac{\alpha}{\theta_{\mathrm{SH}}^{\mathrm{eff}}}\right)\frac{2e\tau M_S}{\hbar}\left(H + H_K^{\mathrm{eff}}\right), \tag{1.2}$$

with $\theta_{\mathrm{SH}}^{\mathrm{eff}}$ the effective spin Hall angle that is intrinsic to the non magnetic metal and its interface with the magnetic layer. The fundamental difference with STT is that only a pure spin current is injected [2] in the ferromagnetic layer thus increasing the switching efficiency and the endurance of the device since there is no write voltage applied on a MTJ. SOT-MRAM using the same geometry than in figure 1.1 are also considered [39].

1.1.2 Systems without magnetization reversal

Spin torque nano-oscillators

Before reaching the switching critical current value by STT, the magnetization precesses around its equilibrium position. Manipulation of this precession regime has led to use MTJs as broadband Spin Torque Nano-Oscillators (STNO) [40]. One of the main advantages of such devices is the large tunability in the radio-frequency range with many applications, from microwave sources to neuromorphic computing [41].

Magnonics

Magnonics is a recent field that aims to manipulate spin waves (magnons) in magnetic materials to create data processing devices such as logic gates or magnon transistors [19, 42]. Spin waves can be generated either by using antennas and a radio-frequency signal, or by using a DC current that produces spin waves by STT (through an additional magnetic layer). There are many advantages of using magnons instead of electrons for logic operations. First of all, there is no Joule heat dissipation since no electron current is involved in the propagation. Moreover, through interferences, the phase of the spin wave provides a supplementary usable variable that could end the Boolean processing of information. Finally, the wavelength of operating magnon-based devices is largely tunable and spin waves can propagate over the millimeter scale[3] in low damping materials [43].

1.1.3 Common challenges in spintronics

Most spintronics devices consist of thin films heterostructures with interesting phenomena emerging at interfaces, surfaces and/or at ultra small thicknesses. Even though standard magnetic metals like Ni,

[2] no charge, thus the spin polarization η does not appear in equation 1.2

[3] Thus, way more larger than the spin diffusion length of electrons in a magnetic material

Fe, Co and their alloys or insulating ferromagnets like Yttrium Iron Garnet (YIG) offer promising results [44–46], novel materials with superior and dedicated properties are necessary to achieve significant breakthroughs in data storage and information processing technologies. In all applications cited above in this section, the desirable properties are:

(i) A high Curie temperature T_c and an appropriate magnetic anisotropy for thermal stability;

(ii) A small Gilbert damping α, the coefficient that characterizes how fast the magnetization precession is damped. For STT (equation 1.1) or SOT (equation 1.2), the smaller the damping, the easier the precession and thus the magnetization switching. For magnonics devices, a small damping coefficient means that spin waves can propagate over large distances without losing coherence. However, obtaining ultra small damping values in conductive layers is a big challenge in material science [13, 24];

(iii) A full spin polarization η at the Fermi energy. Indeed, as presented in equation 1.1 in the case of STT, the switching current will be strongly reduced if each electron transfers spin momentum in the free layer;

(iv) Heterostructures with the magnetization perpendicular to the film plane. It is theoretically and experimentally confirmed that the perpendicular anisotropy decreases the critical current in STT- and SOT-based devices [5]. This behavior is easily explained because there is no need to bring a supplementary amount of energy to overcome the demagnetizing field since it is already overcome by the total magnetic anisotropy in the device. Additionally, it makes the precession and therefore devices more symmetrical which is convenient for stability;

(v) A small magnetization to reduce the demagnetizing field and increase the stability of devices (toward antiferromagnetic spintronics [47]);

The strong improvement of the fundamental understanding in condensed matter physics and in thin film elaboration methods makes the tailoring of those desired properties reachable, but very challenging. In the present study, we focus on the use of a family of materials called Heusler compounds that could exhibit most, if not all, of those desired features.

1.2 Heusler compounds for spintronics

Like perovskites or pyrochlores, Heusler compounds belong to a large family of materials with a unit formula X_2YZ. Like in the first compound investigated by F. Heusler Cu_2MnSn [6], X and Y are transition metals and Z is usually an element from the main group of the periodic table (*sp* elements). They crystallize in a face centered cubic (fcc) structure made of four different crystallographic sites, represented in figure 1.2.

In all the present work, we were interested only in "full Heusler" compounds where X and X' atoms are the same[4] like in Cu_2MnSn. In full Heuslers, the two sites occupied by X and X' are chemically equivalent, they are just rotated by 45° with respect to each other. Y and Z atoms have 8 X atoms as first neighbors, resulting in a octahedral symmetry. X atoms have 4 Y and 4 Z atoms as first neighbors,

[4]Different from: (i) the LiMnPdSn structure where X, X' and Y are all different metals and (ii) "half-Heuslers" where X' site is not occupied, resulting in the NiMnSb structure.

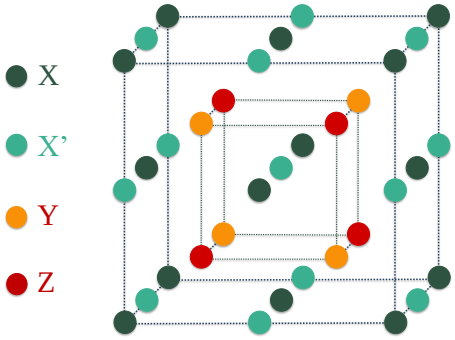

Figure 1.2: Unit cell of X_2YZ Heusler compounds.

resulting in a tetrahedral symmetry. The associated space group is $Fm\bar{3}m$ and the structure is referred as the $L2_1$ phase in the *Strukturbericht* notation that takes into account atomic ordering.

With three different chemical elements X, Y and Z, thousands of Heusler compounds can be elaborated. The high interest in this family is due to the high stability of the Heusler structure for many elements. Thereby, they provide an excellent playground to study and develop various topics such as thermoelectricity [48], superconductors [49], topological insulators [50], heavy fermions [51] and so on. In the scope of novel materials for spintronics applications, we are interested in half metal magnets which are going to be discussed in the following.

1.2.1 Half metal magnetism and Slater-Pauling behavior

Since its theoretical prediction in 1983 by de Groot *et al.* on the half-Heusler NiMnSb [9], Half Metal Magnetism (HMM) is very interesting for spintronics. This property reflects the capacity of a magnetic material to be conducting for majority spins and insulating for minority spins. In other words, there is a gap in the minority spin bands (which is, according to most calculations, an indirect gap [7, 8, 28] with the maximum of the occupied states at the Γ point and the minimum of empty states at the X point). As shown in figure 1.3 for Co_2CrSi Heusler compound [28], the spin gap is predicted in the whole Brillouin zone, resulting in fully spin polarized current within the material, in every direction. Obviously, such behaviors are extremely desirable for spintronics, where spin current generation and filtering are omnipresent.

Galanakis *et al.* have given an explanation on the origin of the half metal magnetism in full Heusler compounds [8, 52]. In particular, they explained the role of each element in the hybridization process that gives rise to a minority spin gap using group theory. According to their studies, the spin gap originates from the d bands hybridization between the X and Y transition metals. The Z element is not involved in such a process since its sp bands are located far below the Fermi energy. Nonetheless, the Z element is essential to stabilize the Heusler structure. In addition, they showed that full Heusler compounds must follow the Slater-Pauling behavior [53] to be HMM. This behavior explains many magnetic moment values for transition metals and alloys (but not all) by considering bands filling. With this point of view, the occupancy of spin down states is fixed and any extra electron fills only spin up bands. Therefore, the

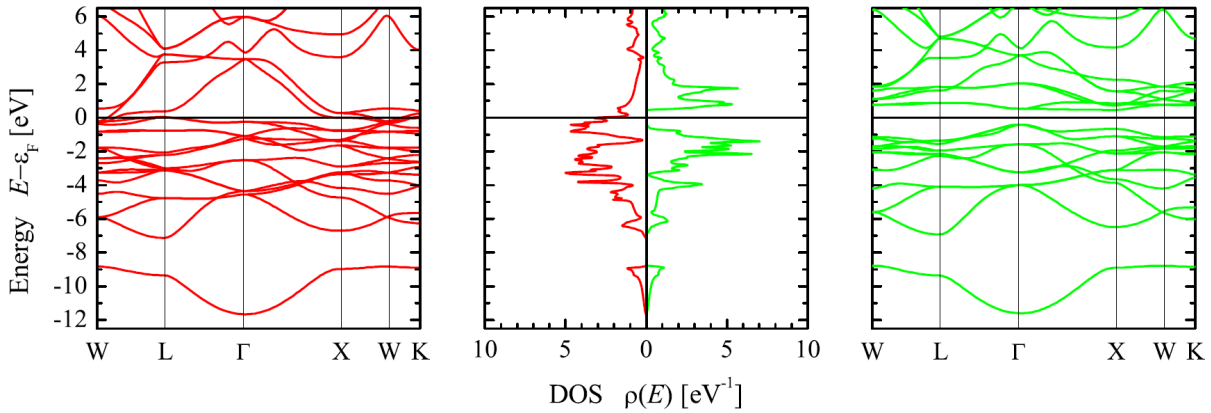

Figure 1.3: Total density of state calculated with up (red) and down (green) spin channels for Co_2CrSi Heusler alloys showing spin gap in the minority spin channel. From [28].

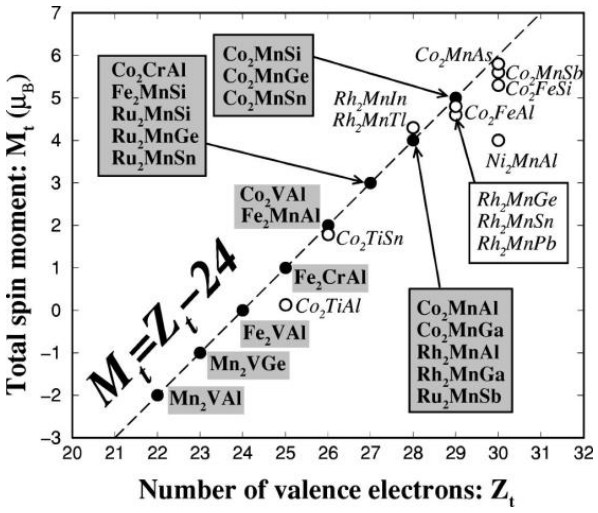

Figure 1.4: Calculated magnetic moment in X_2YZ Heusler compounds following the Slater-Pauling curve (dashed line). Open circles are for small deviations from the curve. From [8].

magnetic moment is given by $M_t = n_\uparrow - n_\downarrow$ where $n_{\uparrow,\downarrow}$ represent the number of electrons that fill valence bands with up and down spin. The total number of valence electrons is naturally given by $Z_t = n_\uparrow + n_\downarrow$. Then the magnetic moment can be expressed as $M_t = Z_t - 2n_\downarrow$. Galanakis *et al.* showed that in the case of full Heusler compounds, $n_\downarrow = 12$, with 4 *sp* bands from the Z element, $2\times e_g$, $3\times t_{2g}$ and $3\times t_{1u}$ bands coming from transition metals X and Y hybridization. It gives the $M_t = Z_t - 24$ μ_B per formula unit for X_2YZ full Heusler ferromagnets, as demonstrated in figure 1.4 taken from reference [8].

Following the Slater-Pauling curve as a mandatory condition to be HMM comes from the fact that everything is linked together. If the bands are not filled the right way and thus with a magnetic moment different from the Slater-Pauling curve, hybridization will be different and no gap will emerge. Magnetic moment values are thus an important parameter to control when growing HMM Heusler compounds.

1.2.2 Associated reduction of the Gilbert damping

The phenomenological Gilbert parameter α plays a key role in the magnetization precession and spin waves propagation. As it will be described in detail in chapter 3, the Gilbert damping is responsible for

the damping of the precession motion. Thus, it must be overcome to reverse the magnetization direction, either by STT or SOT (not clear yet for AOS). It acts like a fluid friction and originates in many mechanisms found in magnetic materials. Starting from the uniform magnetization precession (magnon with $k = 0$), the figure 1.5 sketches the main relaxation mechanisms that have to be taken into account in metals.

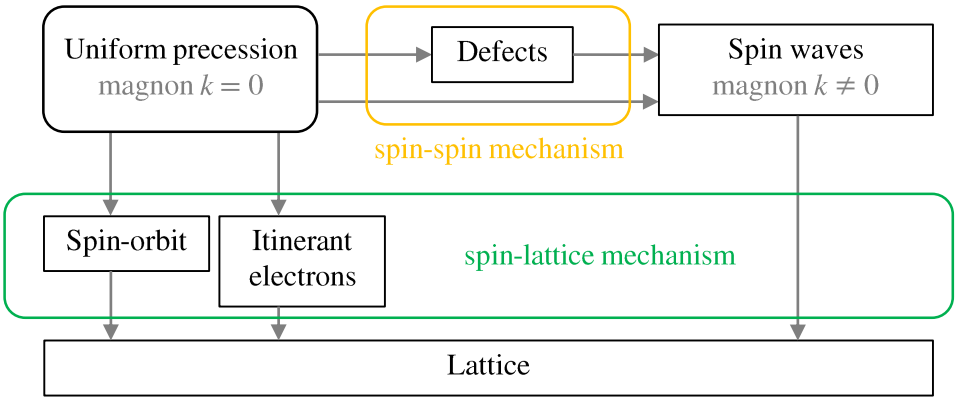

Figure 1.5: Main contributions of the relaxation of the uniform magnetization precession in ferromagnetic metals [54].

Even though there can be intermediate processes like spin to spin mechanisms (*e. g.* scattering by magnons), the energy dissipation of the uniform precession always ends up in spin to lattice relaxation mechanism, mediated by the spin-orbit interaction [55]. The predominant relaxation mechanism that occurs in metals[5] is the incoherent scattering of electron-hole pair excitations by phonons and magnons [27, 56]. Two processes in the relaxation of the magnetization precession induced by conduction electrons have to be distinguished:

(i) A spin-flip scattering that is explained in a three particles process [56], as shown in figure 1.6. In

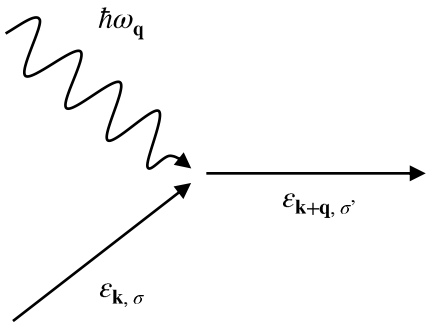

Figure 1.6: Three particle process involved in the spin flip process.

such a process, a magnon $\hbar\omega_{\mathbf{q}}$ with a wave vector $\mathbf{q}$ is annihilated with a conduction electron $\varepsilon_{\mathbf{k},\sigma}$ that has a momentum $\mathbf{k}$ and spin σ through the *sd* exchange interaction, resulting in an electron-hole pair excitation $\varepsilon_{\mathbf{k+q},\sigma'}$. Since the *sd* exchange interaction conserves the total angular momentum,

[5] contrary to insulating magnet like YIG

the spin σ' is flipped during the process. The electron-hole pair is then incoherently scattered by phonons and magnons resulting in a dissipation of the precession motion. This damping contribution is often referred as the "resistivity like" damping or "interband" damping with an expression proposed by Kamberský [27]:

$$\alpha_{sd} = \frac{\pi\gamma\hbar^2}{\mu_0 M_S} Z_F \frac{(g-2)^2}{\tau}, \tag{1.3}$$

where Z_F is the density of state at the Fermi energy (that can be considered as the number of relaxation channels [27]), g the Landé factor and τ the electron scattering time. α_{sd} is thus proportional to the resistivity.

(ii) The non spin-flip process comes from the spin-orbit interaction. Indeed, the uniform magnetization precession gives rise to a periodical change in the Fermi surface of a metal [27], due to anisotropic spin-orbit shifts of bands. In this model, the re-population of electrons in the "breathing Fermi surface" is a dissipative process. According to Kamberský [27], it mostly takes place within subbands of same spin index since it is the most probable scattering event. This term is often referred as the "intraband" damping or "conductivity like" damping:

$$\alpha_{\mathrm{SO}} = \frac{\pi\gamma}{\mu_0 M_S} Z_F \lambda_{\mathrm{SO}}^2 (g-2)^2 \tau, \tag{1.4}$$

where λ_{SO} is the spin-orbit interaction strength. Contrary to α_{sd}, α_{SO} is proportional to the conductivity.

The strong reduction of the Gilbert damping in HMM materials is thus easily explained. Indeed, conduction electrons cannot flip their spin since there are no electronic states available for minority spins (gap for minority spin bands). Thereby, the damping contribution α_{sd} vanishes. Nonetheless, other intrinsic (*e. g.* α_{SO}) and extrinsic (defects, inhomogeneities, 2-magnon scattering [57]) contributions to the damping still contribute to the dissipation.

1.2.3 Co_2MnZ compounds

In the present work, we were interested in the Co_2MnZ family of Heusler compounds because this family seems to satisfy most of the properties cited in section 1.1.3. Co_2MnZ compounds (and Heuslers in general) have been widely studied in the literature, theoretically [7, 8, 25, 28, 52, 58, 59] and experimentally [10, 29, 60–65] and an exhaustive state-of-the-art is thus almost impossible. However, important milestones and key points are going to be discussed. In the present work, we were interested in Co_2MnZ compounds with Z=Al, Si, Ga, Ge, Sn and Sb for their promising behavior and also for experimental reasons[6].

First of all, Curie temperatures in Co_2MnZ compounds were measured in the work of Webster [60] and are above 690 K, thus thermally stable for applications. They were reported to follow a linear trend with the magnetic moment (and thus with the number of valence electrons) and were calculated accurately by *ab initio* methods by Kübler *et al.* [59].

[6]For instance, we did not work on Co_2MnAs due to As gaseous state and toxicity. Nonetheless, theoretical studies on Co_2MnAs exist.

As presented in section 1.2.1, their magnetic moments follow a Slater-Pauling curve. Hence, they are experimentally and theoretically reported to be very close to 4 μ_B/f.u for Co_2MnZ with Z=Al and Ga [58], 5 μ_B/f.u for Z=Si, Ge, Sn [8, 60] and theoretically 6 μ_B/f.u for Z=Sb [66].

The two key parameters in Co_2MnZ Heusler compounds, namely the spin gap and ultra low damping, are discussed in the following.

Electronic structure calculations

In 1995, Ishida *et al.* [7] were among the firsts to calculate systematically band structures for the Co_2MnZ series of compounds. They showed very interesting results on $Co_2MnAl_{1-x}Si_x$, $Co_2MnGe_{1-x}As_x$ and $Co_2MnSn_{1-x}Sb_x$ series for $x \in [0, 1]$ (thus ternary and quaternary full Heusler compounds with $L2_1$ structure). First, they all exhibit a spin gap in their minority spin band structure with a width within $0.17 < \Delta_{gap} < 0.42$ eV, with the widest gap for Co_2MnSi. Secondly, they showed that the width of the gap and the position of the Fermi energy, in or outside the gap, is largely tunable depending on the x composition thus on the sp element electronic configuration. Later, several theoretical studies were carried out [28, 58, 66, 67] on the same compounds, with refined methods to calculate band structures and density of states. They all pointed out very consistent results with the study of Ishida *et al.* regarding the occurrence of spin gaps but with small differences. For instance, they showed that the gap widths were almost doubled (in eV). Additionally, Picozzi *et al.* [67] showed that the lattice constant plays an important role in the position of the Fermi energy with regards to the gap.

Electronic structure features for Co_2MnZ compounds will be discussed more accurately in chapter 3 but the global trend is the following: (i) large spin gaps for s^2p^2 elements Z=Si, Ge and Sn; (ii) Fermi energy E_F near the middle of the gap for Si, Ge; (iii) E_F near the minority spin valence band for Al, Ga, Sn; (iv) E_F near the minority spin conduction band for Sb. Nevertheless, they all have a strong spin polarization at E_F which is exciting for devices relying on spin current generation.

Gilbert damping calculations

The Gilbert damping coefficient encompasses many complex processes. Thus, the estimation of the α parameter remains difficult and is not available for all Co_2MnZ compounds. However, several theoretical studies have pointed out very low damping values for HMM compounds, sometimes comparable to YIG.

In particular, Liu *et al.* [25] have calculated the lowest achievable intrinsic damping constants using a combination of *ab initio* methods and an extended Hückel tight binding model. They found $\alpha = 6 \times 10^{-5}$ for Co_2MnSi and $\alpha = 1.9 \times 10^{-4}$ for Co_2MnGe, more than one order of magnitude smaller compared to values calculated for transition metals. In addition, Sakuma [26] and Pradines *et al.* [12] have shown that for Co_2MnSi and Co_2MnAl, the Gilbert constant were directly related to the minority DOS at the Fermi energy. By using first principle calculations, they found $\alpha = 1.1 \times 10^{-4}$ for Z=Si, with E_F in the middle of the spin gap, and $\alpha = 8.4 \times 10^{-4}$ for Z=Al, with E_F in the top of the minority spin valence band.

Even for compounds that are not pure HMM like Co_2MnAl (spin gap but E_F falls at the edge with the minority valence band), the Gilbert parameter is reduced compared to standard transition metals and alloys. For pure HMM compounds like Co_2MnSi and Co_2MnGe, the Gilbert damping is at least one or-

der of magnitude smaller which is very promising for magnetization reversal applications and magnonics.

According to calculations, Co_2MnZ compounds seem to be excellent candidates for spintronics. This family presents indeed almost every specifications required: a spin gap in the minority spin band structure, thermal stability and ultra small Gilbert damping coefficients. Moreover, several properties like the width of the gap or the magnetic moment appear to be tunable within the Co_2MnZ series, depending on the Z element.

1.2.4 Experimental demonstration of Co_2MnZ efficiency

As mentioned at the beginning of this section about Co_2MnZ compounds, many scientific papers are published everyday on Heusler compounds. It is therefore impossible to cite them all. Nevertheless, works that are related to the present study are going to be presented.

Co_2MnSi

The most studied compound in the series is Co_2MnSi. Its efficiency as a novel material for spintronics has been demonstrated first in 2009 by Ishikawa *et al.* [62], where they have reported a Tunnel Magneto-Resistance (TMR) ratio TMR=1135 % at 4.2 K in $Co_2Mn_\alpha Si_\gamma$/MgO/$Co_2Mn_\alpha Si_\gamma$ MTJs, the highest TMR ratio reported so far. In 2012, the same group published a paper [61] in which they reported a ratio TMR=1995 % at 4.2 K, thus almost two times higher than the previous one. They explained this increase by the reduction in the misfit dislocations density within the tunnel barrier by growing the bottom Co_2MnSi layer on top of a $Co_{50}Fe_{50}$ layer. Their results on Co_2MnSi based MTJs are shown in figure 1.7.

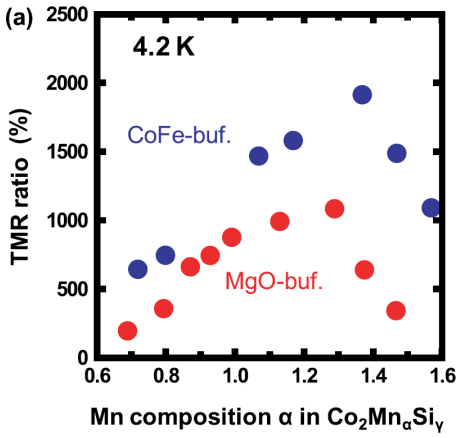

Figure 1.7: TMR ratios obtained on $Co_2Mn_\alpha Si_\gamma$ deposited on a $Co_{50}Fe_{50}$ buffer layer (blue points) and directly on MgO (red points) at T=4.2 K. From [61].

In 2014 and 2016, two groups have independently reported a direct experimental evidence of a spin gap in Co_2MnSi by using spin-resolved photoemission spectroscopy [10, 29] (as well as the occurrence of surface resonant states that will be discussed in chapter 3). Moreover, in the work of Andrieu *et al.* [10], they have reported an effective Gilbert coefficient $\alpha = 7\times10^{-4}$, the lowest value obtained on a conductive layer. In 2017, Stückler *et al.* [65] have successfully detected a propagation length up to 100 μm with

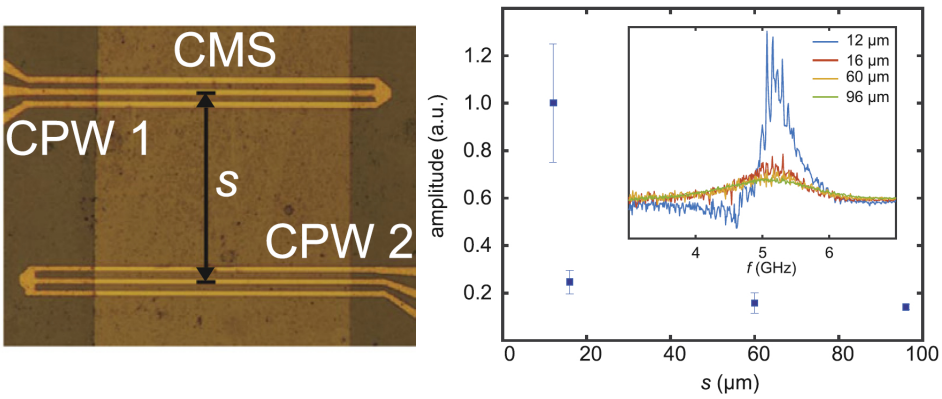

Figure 1.8: Design of the coplanar waveguides used to detect Damon-Eshbach spin waves over the distance s in Co_2MnSi [65].

Damon-Eshbach spin waves[7] in Co_2MnSi (figure 1.8), supporting the very small damping coefficients measured in this compound and high efficiency for magnonics.

Other Co_2MnZ compounds

Magnetic and structural properties of other Heusler compounds are also investigated. However, very few and/or disappointing results were obtained on epitaxial thin films regarding their spin polarization, Gilbert damping values and efficiency in MTJs. For instance, Sakuraba *et al.* have shown that Co_2MnAl/Al-O/CoFe/IrMn MTJs exhibit only TMR=65 % at room temperature and 83 % at 10 K [68]. This TMR ratio is not consistent with *ab initio* calculations that predict a high spin polarized material with the Fermi energy located at the edge between the minority spin valence band and the spin gap. Moreover, Oogane *et al.* [69] have reported a Gilbert damping value $\alpha = 6 \times 10^{-3}$ on the same compound, almost one order of magnitude higher than the theoretical predictions of Sakuma [26]. The spin polarization of epitaxial Co_2MnGa compound was investigated by spin resolved photoemission spectroscopy [70, 71] where a deceiving spin polarization value of 54 % was obtained.

Nonetheless, encouraging results have also been reported. Textured polycrystalline Co_2MnGe thin films were recently investigated by Shaw *et al.* [33] where an effective damping coefficient $\alpha = 1.4 \times 10^{-3}$ was reported, very promising for a polycrystalline material where defects and grain boundaries are significant mechanisms of the magnetization precession relaxation. Ludbrook *et al.* [63] have successfully reached perpendicularly magnetized epitaxial trilayers of MgO/Co_2MnGa/Pd by using interfacial magnetic anisotropy (up to 3.5 nm thick Co_2MnGa) which is very promising for perpendicular MTJs or spin valves.

1.2.5 Chemical disorder

With more than two different chemical elements in the unit cell, chemical disorder can manifest in many forms in ternary and quaternary Heusler compounds. Several theoretical studies point out that some type of chemical disorder must drastically change the physical properties such as the magnetic moment,

[7] Transverse to the magnetization.

the occurrence of the spin gap or the magnetic damping value. In the case of Co_2MnZ with Z=Al, Si and Ge, Sakura *et al.* [26], Pradines *et al.* [12] and Shaw *et al.* [33], have calculated that Mn ↔ Z swap (B2 disorder) does not affect much the physical properties whereas Co ↔ Mn ($D0_3$ disorder) or random swap (A2 disorder) completely destroy the spin gap (figure 1.9-left) or the low Gilbert damping coefficient (1.9-right).

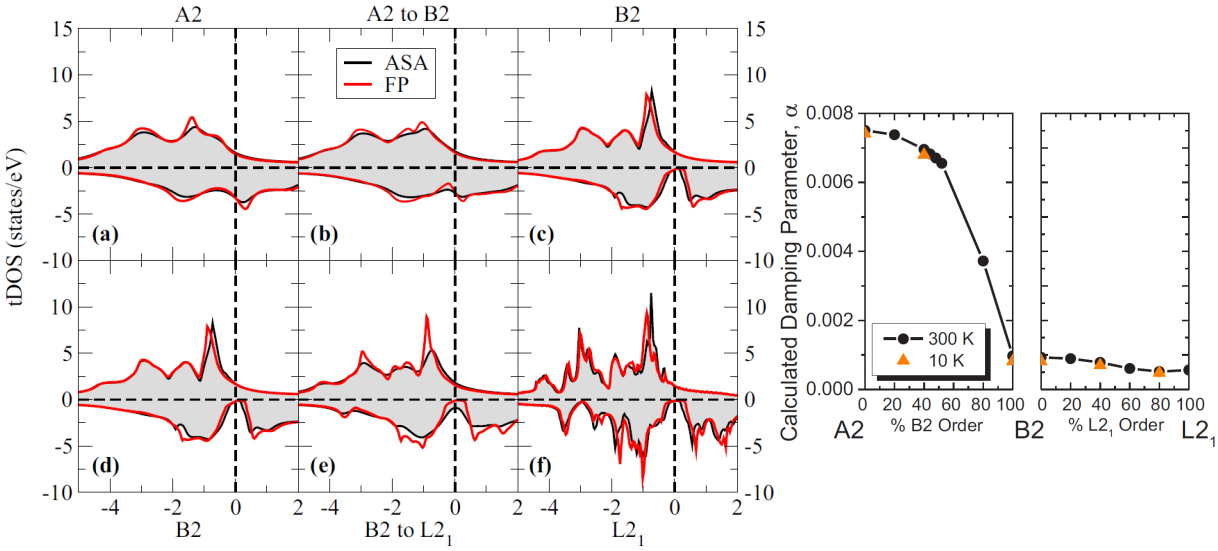

Figure 1.9: Co_2MnGe [33] spin-resolved total Density Of States tDOS calculated for (a) A2 phase (random disorder), (b) A2 to B2 phase, (c) and (d) B2 phase (Mn ↔ Z swap), (e) B2 to $L2_1$ phase and (f) $L2_1$ phase and associated Gilbert damping.

In the literature, there are few experimental studies about disorder, primarily because this parameter is very hard to control without adding defects, vacancies or simply affecting the structural quality. Nevertheless, Abdallah *et al.* [72] have studied Mn ↔ Si swap and Mn ↔ Co swap induced by He^+ ions irradiation in Co_2MnSi thin films. By using ferromagnetic resonance, they investigated on the change in dynamic magnetic properties. They confirmed that the B2 disorder barely affects the magnetic moment and damping, but that $D0_3$ disorder strongly increases the Gilbert damping coefficient, consistent with theoretical predictions. Chemical ordering is thus a key parameter to take into account when growing Heusler thin films in which outstanding properties are expected.

1.3 Experimental procedure

In the present work, our goal was to investigate Heusler compounds grown as thin films in order to: (i) compare their electronic structure with theoretical predictions and (ii) evaluate their potential to be used in spintronics.

In a first step, high quality epitaxial thin Co_2MnZ films with Z=Al, Si, Ga, Ge, Sn and Sb were grown. As limited information is available in the literature, the structure and the chemical ordering was systematically investigated with diffraction techniques (electrons, X-rays) and transmission electron microscopy. In addition, the static magnetic properties were explored using X-ray circular dichroism performed on a synchrotron source (a necessary step to be sure that we have systems as close as possible form the one on which calculations are performed).

Then, in order to confirm *ab initio* calculations that predict spin gaps with tunable characteristics within the Co_2MnZ series, spin-resolved photoemission spectroscopy was performed at the Cassiopée beamline at the SOLEIL synchrotron facility. Afterward, the dynamic magnetic properties were explored using perpendicular ferromagnetic resonance, the best way to measure accurately small Gilbert damping coefficients. Besides confirming that these compounds have ultra small Gilbert damping materials, the interplay between the obtained damping coefficients and the electronic structure near the Fermi energy was analyzed.

In a final step, two exploratory parts are presented. In the first one, the growth of Heusler superlattices was performed in order to combine perpendicular magnetic anisotropy with the outstanding properties of Heusler compounds at the same time, thus trying to answer to a big challenge in spintronics. In the second one, the tunable spin polarization in $Co_2MnSi_xAl_{1-x}$ series of compounds was used to shed light on the relation between the Gilbert damping α (nanosecond timescale) and the ultrafast demagnetization time τ_M ($\leq$ picosecond timescale) induced by laser pulses.

Chapter 2

Epitaxial Co_2MnZ thin films

In this chapter, we present the elaboration of Co_2MnZ epitaxial thin films using the molecular beam epitaxy technique. Then, structural and magnetic characterization results are presented, with a particular effort made to investigate the chemical order occurring in these epitaxial layers.

2.1 Epitaxial growth

2.1.1 Molecular beam epitaxy set-ups

All the epitaxial layers presented in this manuscript were grown using two different Molecular Beam Epitaxy (MBE) set-ups. The first one (figure 2.1a), specially designed for metallic alloys, offers the possibility to co-evaporate 9 chemical elements at the same time, thanks to the 3 electron guns (e-gun) with 6 pockets each and 6 Knudsen cells (K-cell). This makes a total of 24 elements in the chamber. Such a system is advantageous for growing numerous type of alloys like Heuslers and different buffer layers. Moreover, the MBE chamber is directly coupled to the 70 meters UHV TUBE facility at the Institut Jean Lamour which allows to perform characterization (such as Auger spectroscopy) of "as grown" layers without breaking the vacuum.

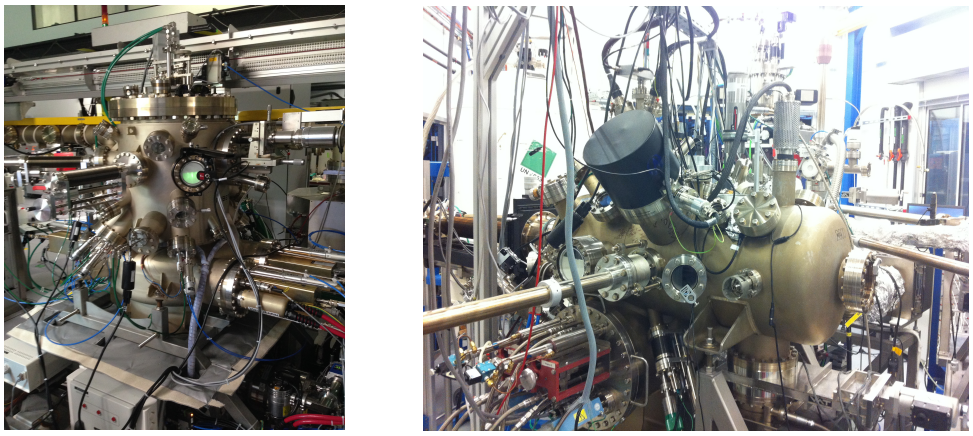

(a) Institut Jean Lamour (b) Cassiopée beamline

Figure 2.1: MBE chambers used to grow Co_2MnZ Heusler compounds

The second MBE chamber is located at the Cassiopée beamline at SOLEIL synchrotron source (figure 2.1b). The MBE is directly coupled to two photoemission spectroscopy chambers which will be depicted

in chapter 3. The chamber has 2 e-guns with 5 pockets each and 4 K-cells for a total of 14 elements. It has its own Auger electron spectroscope for chemical analysis. This MBE chamber is also efficient for multiple ternary alloys.

Both of growth chambers are equipped with a highly focused electron gun for Reflection High Energy Electron Diffraction (RHEED), used to control the growth process, as it is going to be discussed in next section.

2.1.2 Growth processing

Heusler compounds were evaporated directly on (001) oriented MgO single-crystals after an outgassing at 1200 K and a MgO buffer layer in order to smooth the surface and bury the possible contaminants like C below the surface. Typical RHEED patterns of the MgO substrate after preparation are shown in figure 2.2.

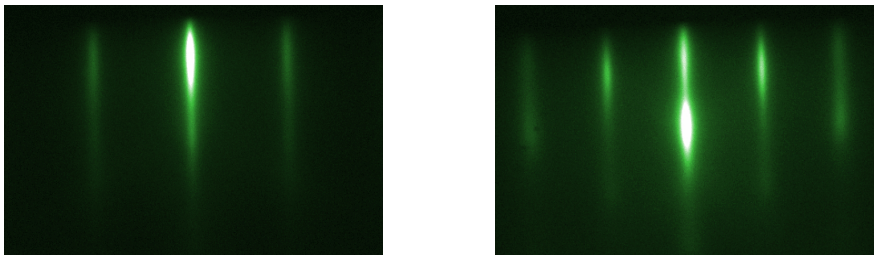

(a) [100] (b) [110]

Figure 2.2: Two typical RHEED patterns of MgO(001) substrate after the MgO buffer layer, aligning the beam along [100] and [110] MgO azimuths.

The homogeneous intensity of the streaks is a sign of a smooth surface with a good crystalline order because no additional streaks, points or rings are visible. MgO is an excellent substrate for Co_2MnZ Heuslers because they all have a cubic lattice and there are small misfits at the interface as shown in the table below. The epitaxial relationship between MgO and Co_2MnZ is the following : MgO[100](001) // Co_2MnZ[110](001) which explains why misfits are calculated with $\sqrt{2}a_{MgO} = 5.95$ Å (see figure 2.3). Cell parameters of Co_2MnZ alloys are taken from theoretical calculations of Faleev *et al.* [73].

	Co_2MnAl	Co_2MnSi	Co_2MnGa	Co_2MnGe	Co_2MnSn	Co_2MnSb
a (Å) [73]	5.73	5.63	5.73	5.74	5.98	6.01
Misfits with MgO	-4.3 %	-5.4 %	-3.8 %	-3.6 %	0.4 %	0.8 %

As often in a series, there is always one candidate which does not follow the same rules than others. Here and until the end of this work, Co_2MnSb is an exception since it does not grow on MgO substrate (see next section). Nevertheless, we managed to get Co_2MnSb(001) epitaxial films using a V buffer layer.

In order to grow Heusler compounds, the three (four in the case of quaternary Heuslers) elements are co-evaporated at the same time. Whatever the MBE chamber (IJL or Cassiopée), Co atoms are always evaporated by an e-gun since its vapor pressure is low. Hence, a high temperature is needed to achieve

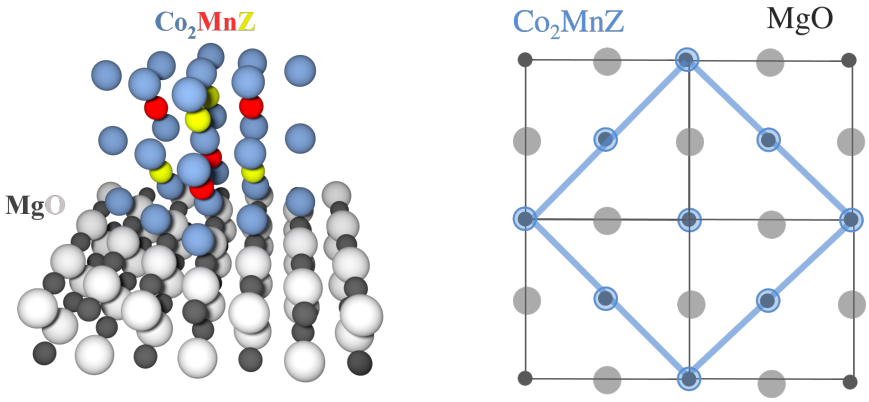

Figure 2.3: Epitaxial relationship between Co_2MnZ Heusler compounds and MgO substrate.

the pressure range of the evaporation mode (>1400 K for 10^{-4} mBar [74]). This is not the case for Mn atoms which are evaporated using a K-cell (~1100 K for 10^{-4} mBar [74]). Concerning the Z element, it depends on its chemical nature as follows: Al, Ga, Sn, Sb with a K-cell and Si, Ge with e-guns. Fluxes are calibrated using quartz micro-balances and the ratios between the different fluxes (in atoms.cm^{-2}.s^{-1}) always follow the equation 2.1 to maintain the 2:1:1 stoichiometry:

$$\begin{aligned} \phi_{\mathrm{Co}} &= \phi_{\mathrm{Mn}} + \phi_{\mathrm{Z}} \\ \phi_{\mathrm{Mn}} &= \phi_{\mathrm{Z}} \end{aligned} \tag{2.1}$$

For quaternary compounds presented further, the 2:1:1 stoichiometry is still maintained, but one element is partially substituted by another, like $Co_2MnSi_{0.25}Al_{0.75}$ for instance.

In this study, the typical order of magnitude for fluxes is $\phi_{Co} = 10^{14}$ at.cm^{-2}.s^{-1}. It leads to a growth rate of Co_2MnZ compounds around 0.3 Å.s^{-1} depending on the density and lattice parameter of the corresponding Heusler compound. The advantage of using e-guns over K-cells is the regulation of the flux during evaporation. Indeed, the power sent to the material is always regulated by a feedback loop, between the quartz micro-balance and the power supply, to keep the flux at the desired value. An example of e-gun regulation curves during a Co_2MnSi deposition is presented in figure 2.4. It has to be noted that the flux values at each point is an average over the 10 previous seconds. It is clearly visible that Co growth rate is very stable whereas Si is more noisy. Because the physical quantity measured by a quartz micro-balance is mass, this behavior is consistent with the Si atomic mass being lighter than Co atoms.

Generally, metals do not wet oxides because of the difference of surface energy density [75] which leads to a 3-dimensional growth of isolated islands (Volmer-Weber growth mode [76]). A compromise has to be made between thermodynamic laws that are ruling the epitaxial growth. By increasing the growth temperature, it will increase the surface diffusion length of adsorbed atoms and thus the distance between the isolated islands. If the temperature is set too high, it will form a discontinuous film with large 3-dimensional and well isolated islands. Nonetheless, the mobility of the adsorbed atoms has to be high enough to let the epitaxial process occurs and to let atoms self-organize at the surface, particularly in

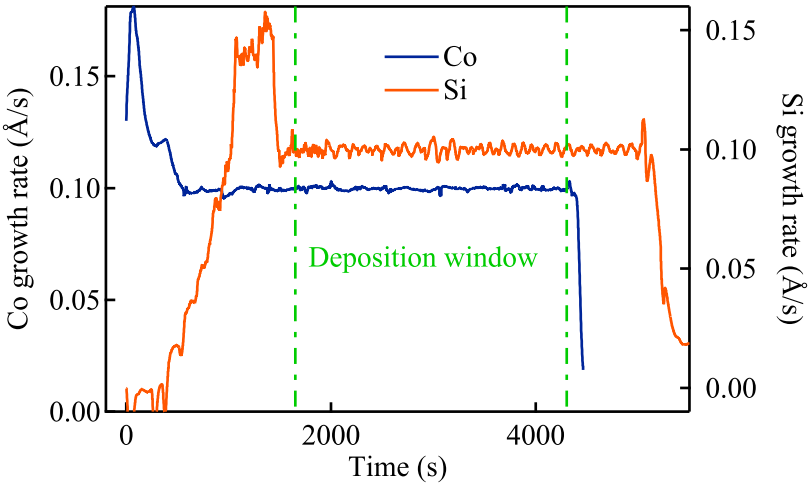

Figure 2.4: Growth rates of Co and Si during a deposition of Co_2MnSi Heusler compound. Deposition occurs when fluxes are stable (green dashed lines window).

the case of Heuslers where chemical ordering is needed. For Co_2MnZ compounds, we choose a growth temperature equal to 720 K. At this temperature, the epitaxial growth begins with a Volmer-Weber style but quickly, after few nanometers, islands coalesce together to form a continuous film and the growth mode switch to something close to Frank - Van der Merwe 2-dimensional mode [77]. The surface is easily smoothed afterward by annealing the layer at 1000 K as evidenced by RHEED and microscopy (next sections dedicated to the structure of Heusler layers).

2.1.3 *In situ* structural control by RHEED

A systematic control of the structure is allowed thanks to RHEED analysis during the deposition and during the annealing. All the following diffraction patterns are obtained with a 15 kV accelerated electron beam and with an incident angle smaller than 1°. According to the universal curve of the electron mean free path in matter ($\leq$ 10 nm at 15 keV) and due to the small incident angle, only the last atomic planes participate to the scattering of electrons ($10\sin(1) = 1.7$ Å), making RHEED a pure surface sensitive characterization method for flat surfaces.

As for X-rays, a quick structure factor calculation describes well the observed patterns[1]. Assuming that the sample is terminated by Co atoms at some place of the sample and MnZ atoms elsewhere (in the $L2_1$ structure), only MnZ planes will generate streaks of less intensity as shown in equation 2.2 and figure 2.5. In the following, these streaks will be referred as "half streaks". For any given h and k, the structure factor can be expressed as:

$$F_{hk} = \sum_{j=1}^{n} f_j e^{2i\pi \mathbf{q}.\mathbf{r}_j} = f_{\mathrm{Mn}} + f_{\mathrm{Z}}(-1)^{h+k} = \begin{cases} f_{\mathrm{Mn}} + f_{\mathrm{Z}} & \text{si} \quad h+k = 2n \\ f_{\mathrm{Mn}} - f_{\mathrm{Z}} & \text{si} \quad h+k = 2n+1 \end{cases} \tag{2.2}$$

where f_j is the atomic form factor of atom j on site $\mathbf{r}_j$ and $\mathbf{q}$ a reciprocal unit vector. Besides giving useful information on the quality of the surface as well as its symmetry, the [110] RHEED pattern appears as a first probing tool of the chemical order in Heusler layers (at least for the last atomic plane). As shown in

[1] With electron rather than X-rays, the scattering amplitude differs but a structure factor calculations is still available.

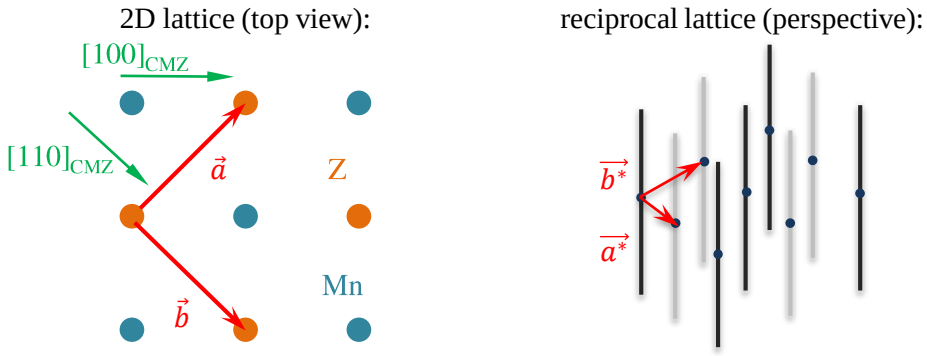

Figure 2.5: Surface lattice and 2D reciprocal lattice of Heuslers leading to two kind of streaks. The half streaks are visible when doing RHEED experiment in the $[110]_{Co_2MnZ}$ azimuth.

equation 2.2, if the Mn and Z atoms are randomly arranged on their sites, half streaks vanish.

Ternary compounds

Figure 2.6 shows all RHEED patterns obtained for Co_2MnZ with Z=Al, Si, Ga, Ge, Sn and Sb along the $[110]_{CMZ}$ azimuth in order to check half-streaks. The [100] RHEED pattern does not provide as much useful information as the [110] pattern, hence it is not shown in this study.

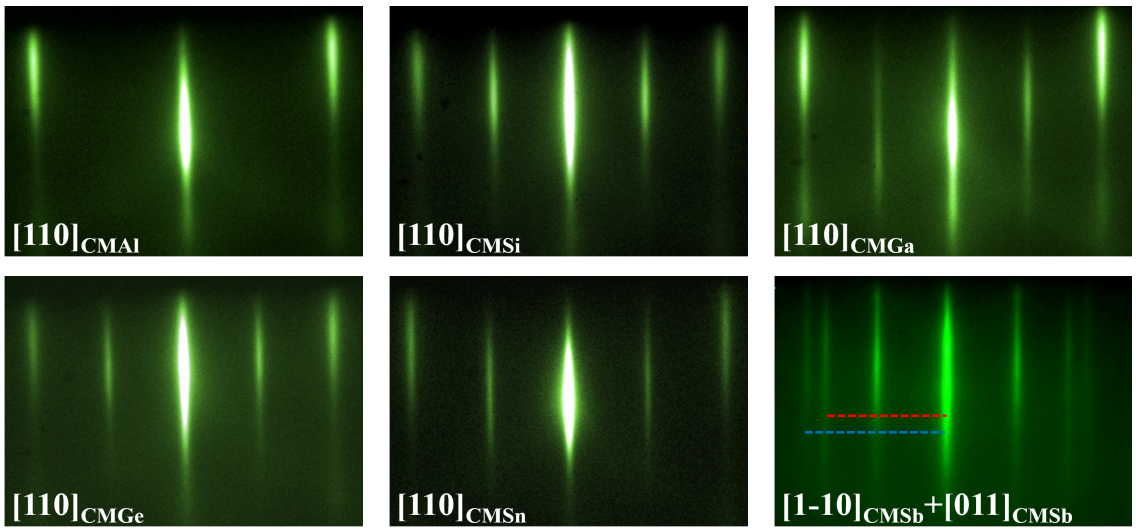

Figure 2.6: Co_2MnZ RHEED patterns on top of MgO. A growth along (001) is observed for every compound except Co_2MnSb where it is along (111).

First, Co_2MnAl compound does not have half streaks which is not compatible with the $L2_1$ structure but with B2 or A2 phases[2]. RHEED is not sufficient to conclude on the precise type of disorder occurring in Co_2MnAl thin layers but the presence of $L2_1$, B32a or $D0_3$ phases can be excluded. Still, the streaks are thin and smooth, showing a good crystalline quality of the Co_2MnAl layer. On the contrary, Co_2MnZ with Z = Si, Ga, Ge, Sn are presenting similar surface structures with a $L2_1$-compatible pattern and a proper crystalline quality as well.

[2]B2 phase well known in bulk samples as reported in by P. J. Webster [60], but also in thin films [78].

Finally, the peculiar case of Co_2MnSb grown directly on MgO(001) exhibits a growth along the (111) direction with two hexagonal domains turned by 30° (it leads to the same RHEED pattern every 30°). Two different set of streaks are observed on the pattern. The ratio between the red and blue length in figure 2.6 is exactly $\frac{\sqrt{3}}{2}$, confirming the growth along (111) axis with the epitaxial relationship : [100]MgO(001) // $[0\bar{1}\bar{1}]Co_2MnSb(111)$ + R30. Based on this, Co_2MnSb compound is always deposited on a V buffer layer because it stabilizes the growth along the (001) axis, as demonstrated by figures 2.7a and 2.7b. Moreover, RHEED patterns of $Co_2MnSb(001)$ are compatible with the $L2_1$ ordering. The growth of Co_2MnSb on V is performed at 500 K (instead of 720 K) and the annealing temperature has to be lower than 750 K otherwise V atoms diffuse in the Co_2MnSb layer, as checked by Auger spectroscopy on the TUBE.

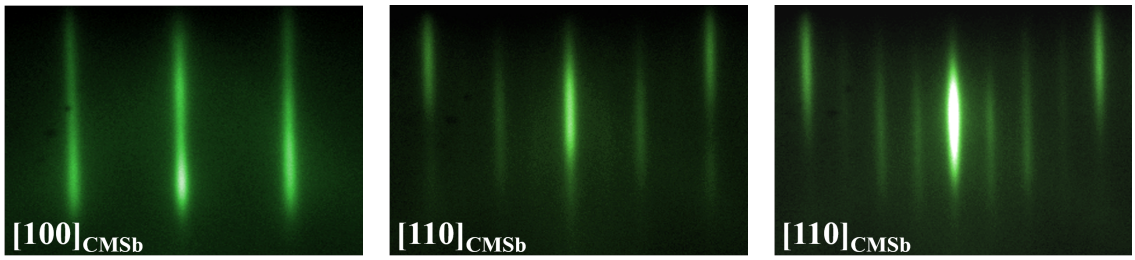

(a) (b) (c)

Figure 2.7: Growth of $Co_2MnSb(001)$ on top of a V buffer layer. (a) and (b) patterns were recorded just after annealing and (c) 10 minutes after annealing.

One more feature concerning the growth of Co_2MnSb has to be noted. Most of the time, when the sample cools down after annealing, the RHEED pattern along [110] azimuth changes a little, with the appearance of "quarter streaks" as shown in figure 2.7c. This type of 1x4 surface reconstruction is well known in half-Heusler alloys containing Sb (CoTiSb [79], NiMnSb [80]) and seems to occur also in full-Heusler compounds. It is necessary to keep that in mind for surface sensitive characterization techniques like photoemission spectroscopy that will be discussed later in this manuscript.

Quaternary compounds

Finally, quaternary Heusler compounds were grown in the same conditions than the previous ones: directly on MgO substrates with the same growth temperature. We were motivated by several reasons for growing such quaternary compounds, that will be described further in this manuscript. First, the $Co_2MnSi_xAl_{1-x}$ series is a good playground to study the chemical disorder transition. Additionally, the two series $Co_2MnSi_xAl_{1-x}$ and $Co_2MnGe_xGa_{1-x}$ are useful to study the change in electronic properties and magnetization dynamics.

The figure 2.8 shows the RHEED patterns obtained for the two series. Small differences in colors and contrast between some images originate in the two different RHEED set-ups corresponding to each MBE chambers. Figure 2.8a deals with the $Co_2MnSi_xAl_{1-x}$ series and a change in the pattern is clearly observable. Going from a $L2_1$-compatible pattern at $x = 1$ (Co_2MnSi) to a lower ordered phase for $x = 0$ (Co_2MnAl) with a continuous loss of half-streaks. For $x = 0.5$, half streaks are barely visible by tuning the contrast and intensity of the image. On the other hand, the $CMGe_xGa_{1-x}$ series on figure 2.8b does not present significant changes with the initial and final pattern compatible with the $L2_1$ structure.

The crystalline quality is still very good for all the quaternary compounds and chemical ordering can

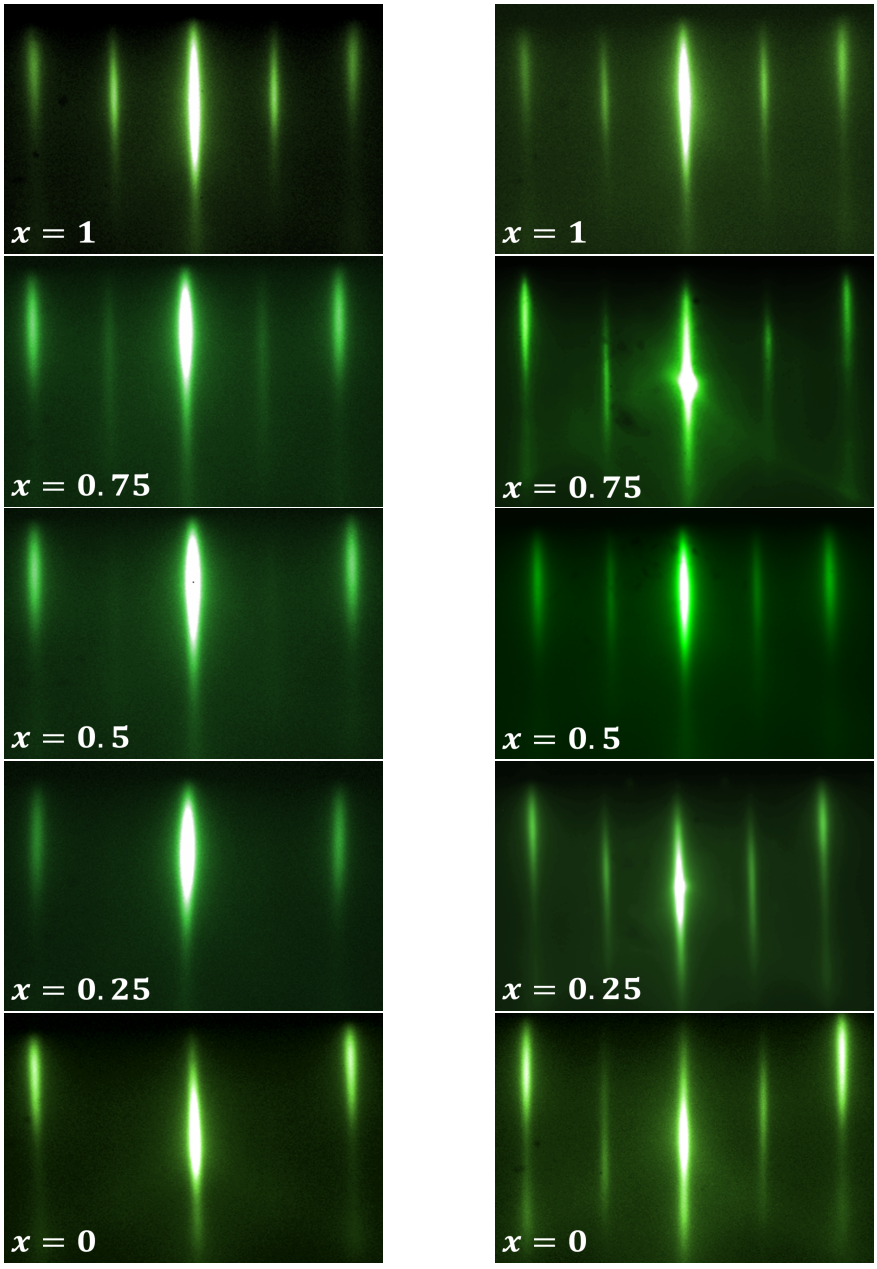

(a) $Co_2MnSi_xAl_{1-x}$ (b) $Co_2MnGe_xGa_{1-x}$

Figure 2.8: [110] RHEED patterns of quaternary Heusler alloys.

still take place with four elements. It is an additional demonstration of the stability of Co_2MnZ Heusler alloys.

Thickness control by RHEED intensity oscillations

Electron diffraction is also a powerful tool to check the reliability of the measured fluxes values by mean of RHEED intensity oscillations. This is not possible when growing Heuslers on MgO substrates because of the Volmer - Weber growth mode. But, Co_2MnZ Heuslers on a metallic buffer layer like V adopt a Frank - Van der Merwe growth mode at room temperature[3], where atomic layers are completed

[3] Also works with Cr and Pd

one after another (2D islands nucleation). With such a growth mode, the intensity along the 00l streaks oscillates [81] at the anti-Bragg condition $2d \sin\theta = (n+\frac{1}{2})\lambda$ because of the difference of path followed by electrons. This difference of path is induced by step edges. Each maximum corresponds to the completion of one atomic plane (minimal density of step edges) and each minimum corresponds to its half completion (maximal density of step edges). Thereby, if the flux values measured by the quartz micro-balance are correct, the period of the resulting oscillations should correspond to the calculated time to complete one atomic plane.

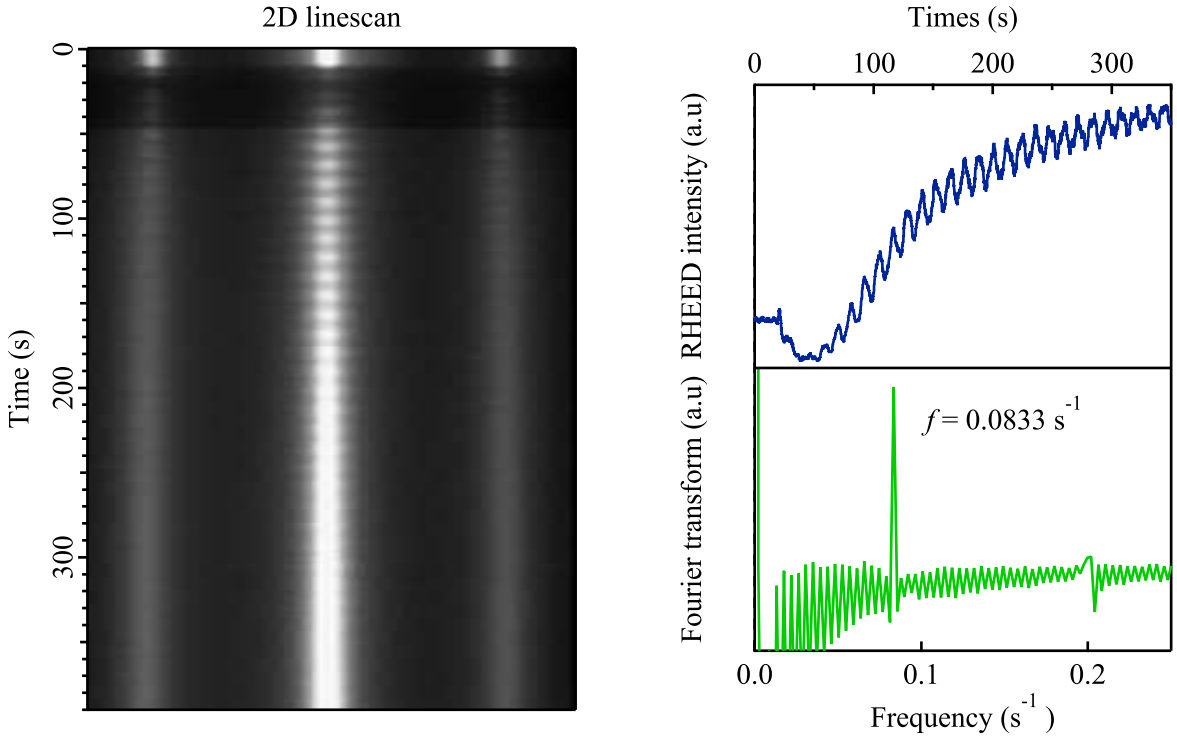

Figure 2.9: Left : 2D linescan of the [100] pattern of Co_2MnGa on top of a V buffer layer showing clear intensity oscillations. Right : vertical lineprofile on the 00l streak and the corresponding Fourier transform to extract the oscillation frequency.

For instance, in the case of Co_2MnGa, we chose to fix the Co flux to 10^{14} at.cm^{-2}.s^{-1} so that the calibrated fluxes with micro-balances were $\phi = \phi_{Co} + \phi_{Mn} + \phi_{Ga} = 2.10^{14}$ at.cm^{-2}.s^{-1}. As the atomic density of one plane of Co_2MnGa is $\frac{4}{a^2_{Co_2MnGa}} = 1.281\ 10^{15}$ at.cm^{-2}, the growth rate is expected to be 0.164 plane.s^{-1} (*i. e.* 6.1 s.plane^{-1}). We thus expect a 6.1 s RHEED oscillation period in a layer by layer growth mode. However, in the figure 2.9, the Fourier transform of the oscillations indicates a frequency of 0.0833 plane.s^{-1} (*i. e.* 12 s.plane^{-1}) which is doubled compared to the calculated value. Therefore it is possible to conclude than in the case of Co_2MnGa (also true for the whole Co_2MnZ series) on a V buffer layer, the growth in the Frank - Van der Merwe mode is bi-layer by bi-layer. Such a behavior is reported in the literature on semiconductors [82]. In the present case, it supports the idea that chemical order is favored in those compounds. Indeed, the system prefers to complete one basic cube with 8 Co atoms centered in the middle with Mn or Z. Moreover, this is a proof of a well controlled fluxes calibration and an indication of a good stoichiometry in alloys thereof. Additionally, the same experiment was done at higher temperatures (450 to 720 K) and it appears that the RHEED intensity oscillations vanish. It strongly suggests a “step flow” growth mode [83], where the adsorbed atoms do not nucleate as islands

but directly at the edge of steps. Thus, the density of step edges is never changing and no oscillations are observable by RHEED.

2.1.4 Auger spectroscopy for chemical analysis

All Co_2MnZ layers grown by MBE were analyzed by Auger Electron Spectroscopy (AES) which easily provides a qualitative chemical analysis without breaking the vacuum. The principle of AES relies on Auger transitions, unique to each element and energetically independent of the incoming radiation energy (most of the time, electrons). Typical Auger spectra for every compound are presented in figure 2.10. Since the quantitative analysis is very complex due to the high number of parameters that has to be taken into account[4], the following analysis is limited to the presence (or absence) of contaminants and a coarse Co-Mn ratio. This former ratio does not change much as expected by the constant 2:1 stoichiometry between Co and Mn. It is visible that all the surfaces are clean without any O (kinetic energy 510 eV) and

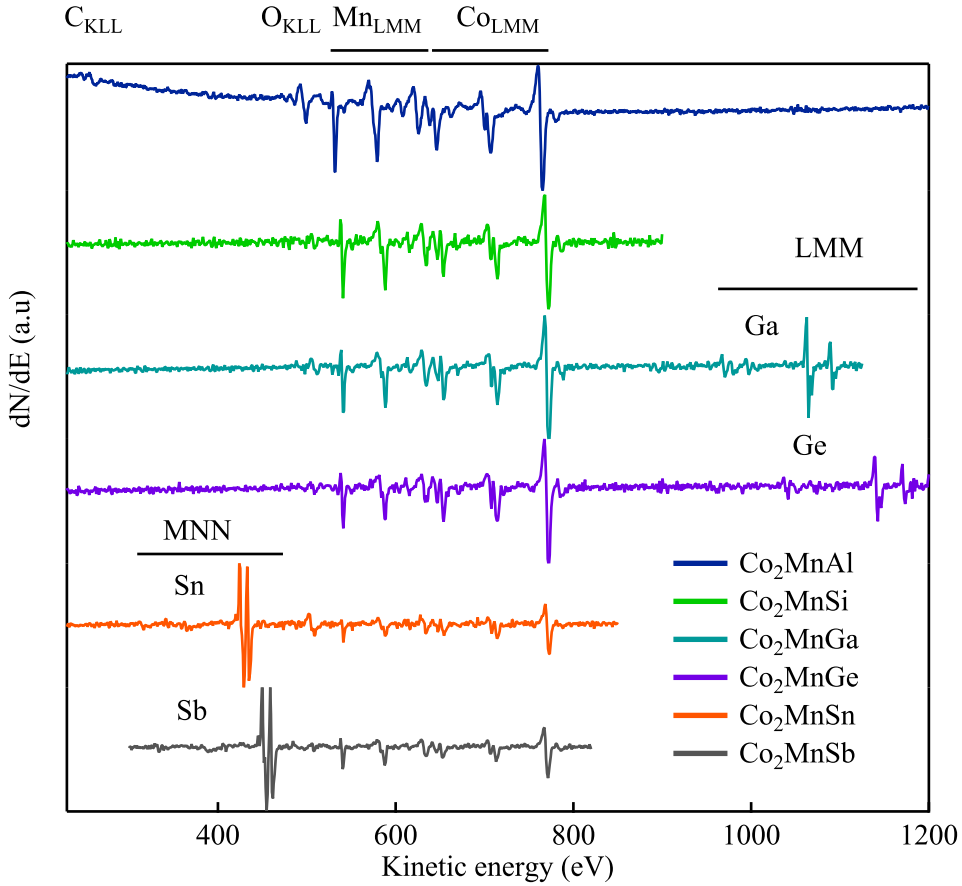

Figure 2.10: Auger spectroscopy of Co_2MnZ compounds with an incident electron energy of 3 keV.

C (271 eV) contamination detected in most cases (sometimes, observed but correlated with the quality of the vacuum inside the chamber after opening the system for instance). The KLL Auger transitions for Si and Al are too high in energy for the analyzers used here. Their LMM low energy transitions are also difficult to see. Therefore, only Ga, Ge, Sn and Sb transitions are visible with a large difference of cross sections between Ga, Ge on the one hand and Sn, Sb on the other.

[4]electron mean free path in the material, same set-up, transfer function of the analyzer at each energy, cross section of elements, plasmonic absorption, area of the surface illuminated *etc.*

2.2 X-ray diffraction

RHEED gives some information on the lattice and also on chemical ordering. However, this technique does not give any information on which kind of chemical ordering occurs (except B2 disorder). X-Ray Diffraction (XRD) is the primary technique to get such information so it was systematically used to characterize our samples. In this part, the theoretical aspects of XRD in the case of Heusler alloys are presented to understand what can be pointed out from "standard" XRD experiments (standard means not anomalous nor surface diffraction). Because the physical properties of an alloy could radically change depending on its chemical ordering, a structural investigation is necessary. Especially in the case of Heusler compounds where subtle properties like spin gap or small damping are predicted and are tried to be experimentally evidenced.

2.2.1 Heusler compounds structure

It is possible to differentiate the chemical disordered phases of Heusler compounds by XRD experiments. To do that, many Bragg reflections are necessary to resolve the crystalline and chemical structure but it cannot be achieved using a 4-circle Eulerian diffractometer used in this thesis. However, in the case of Heuslers, several chemical phases can be directly excluded just because a family of reflections is lacking in the diffraction pattern. The aim of this part is to introduce the different types of disorder in the typical Heusler phases and to obtain the associated structure factors using the occupation matrix method, elegantly proposed by Bacon *et al.* in 1971 [84].

Unit cell and "virtual" scattering amplitude

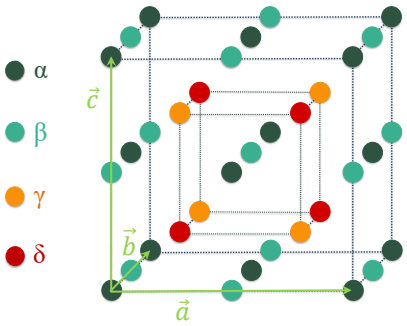

Figure 2.11: Heusler crystal unit cell with the four different crystalline sites : α, β, γ and δ.

As presented in chapter 1, Heusler alloys are cubic crystals made of 4 face centered cubic (fcc) sublattices represented in figure 2.11. Like every fcc, the primitive unit cell is rhombohedral. However, people always conveniently works with the fcc lattice. With four different sites in the cell, Heusler compounds have a canonical formula XX'YZ. In the case of the full-Heusler compounds, α and β sites are occupied by the same atoms (X=X') which results in the X_2YZ structure and $L2_1$ phase (the original "Cu_2MnSn" structure from the work of F. Heusler [6]).

The diffraction theory stipulates that the intensity of a Bragg's reflection is related to the structure factor $|F(\mathbf{q})|^2$, itself related to the scattering amplitude and the position of each atoms in the cell (equation 2.3). Like in [84], a way to calculate the structure factor for different chemical phases consists of

associating a virtual scattering amplitude to each site in the unit cell (α, β, γ and δ in figure 2.11). It is easier to deal with the crystallographic sites rather than the chemical element that is not the same from one phase to the other. It is a relevant method since the sites remain unchanged although the occupation rates change from one chemical ordering to the other. The scattering amplitude is given by:

$$F(\mathbf{q}) = \sum_u f_u e^{2i\pi \mathbf{q}.\mathbf{r}_u} \tag{2.3}$$

where $\mathbf{q}$ is a vector of the reciprocal lattice, f_u the scattering amplitude associated to the site u ($u = \alpha, \beta, \gamma, \delta$) and $\mathbf{r}_u$ the position of the site u in the cubic cell. Whatever the chemical phase, the position of all the sites in the cell can be described by only 4 positions, the rest of the atoms being placed in symmetry equivalent sites:

$$\begin{array}{lllllllll}
\text{site } \alpha & : & \mathbf{r}_\alpha = & \mathbf{0} & ; & \frac{1}{2}(\mathbf{a}+\mathbf{b}) & ; & \frac{1}{2}(\mathbf{a}+\mathbf{c}) & ; & \frac{1}{2}(\mathbf{b}+\mathbf{c}) \\
\text{site } \beta & : & \mathbf{r}_\beta = & \frac{1}{2}\mathbf{a} & ; & \frac{1}{2}\mathbf{b} & ; & \frac{1}{2}\mathbf{c} & ; & \frac{1}{2}(\mathbf{a}+\mathbf{b}+\mathbf{c}) \\
\text{site } \gamma & : & \mathbf{r}_\gamma = & \frac{3}{4}(\mathbf{a}+\mathbf{b}+\mathbf{c}) & ; & \frac{3}{4}\mathbf{b}+\frac{1}{4}(\mathbf{a}+\mathbf{c}) & ; & \frac{3}{4}\mathbf{c}+\frac{1}{4}(\mathbf{a}+\mathbf{b}) & ; & \frac{3}{4}\mathbf{a}+\frac{1}{4}(\mathbf{b}+\mathbf{c}) \\
\text{site } \delta & : & \mathbf{r}_\delta = & \frac{1}{4}(\mathbf{a}+\mathbf{b}+\mathbf{c}) & ; & \frac{1}{4}\mathbf{a}+\frac{3}{4}(\mathbf{b}+\mathbf{c}) & ; & \frac{1}{4}\mathbf{c}+\frac{3}{4}(\mathbf{a}+\mathbf{b}) & ; & \frac{1}{4}\mathbf{b}+\frac{3}{4}(\mathbf{c}+\mathbf{a})
\end{array}$$

Starting from these positions and expression 2.3, the structure factor can be expressed as:

$$\begin{aligned}
F_{hkl} =& f_\alpha[1+(-1)^{h+k}+(-1)^{k+l}+(-1)^{h+l}] \\
&+f_\beta[(-1)^h+(-1)^k+(-1)^l+(-1)^{h+k+l}] \\
&+f_\gamma.e^{i\frac{\pi}{2}(h+k+l)}[(-1)^{h+k+l}+(-1)^h+(-1)^k+(-1)^l] \\
&+f_\delta.e^{i\frac{\pi}{2}(h+k+l)}[1+(-1)^{k+l}+(-1)^{h+k}+(-1)^{h+l}].
\end{aligned} \tag{2.4}$$

First, there are extinctions because of the Bravais lattice (fcc) which implies that h, k and l must be of the same parity, otherwise $F_{hkl} = 0$. Besides, the structure factor has a 4-order cyclicality on $h+k+l$ due to the term $e^{i\frac{\pi}{2}(h+k+l)}$. Depending on the h, k and l indexes, the different values taken by F_{hkl} are summarized in the table 2.1.

(h,k,l) conditions	$F(h,k,l)$
h, k and l evens, $h+k+l = 4n$	$F = 4(f_\alpha + f_\beta + f_\gamma + f_\delta)$
h, k and l odds, $h+k+l = 4n+1$	$F = 4[f_\alpha - f_\beta - e^{i\frac{\pi}{2}}(f_\gamma - f_\delta)]$
h, k and l evens, $h+k+l = 4n+2$	$F = 4(f_\alpha + f_\beta - f_\gamma - f_\delta)$
h, k and l odds, $h+k+l = 4n+3$	$F = 4[f_\alpha - f_\beta - e^{-i\frac{\pi}{2}}(f_\gamma - f_\delta)]$

Table 2.1: Structure factor associated to a Heusler type structure crystallographic sites

Now, the structure factor for each upcoming phase can be easily deduced using an occupation matrix that associates the virtual scattering amplitude of the sites f_u with $u = \alpha, \beta, \gamma, \delta$ to the real scattering amplitude of atoms in the cell f_i with $i = X, X', Y, Z$.

Chemical disorder and occupation matrices

Sometimes, to minimize its energy, the system crystallizes in a different way by changing its occupation rate on each site. Even if the stoichiometry remains unchanged in the crystal, this mixing gives rise to other chemical phases that are represented in the figure 2.12 in the case of full-Heusler compounds. It is important to note that sometimes, this disorder leads to different space groups.

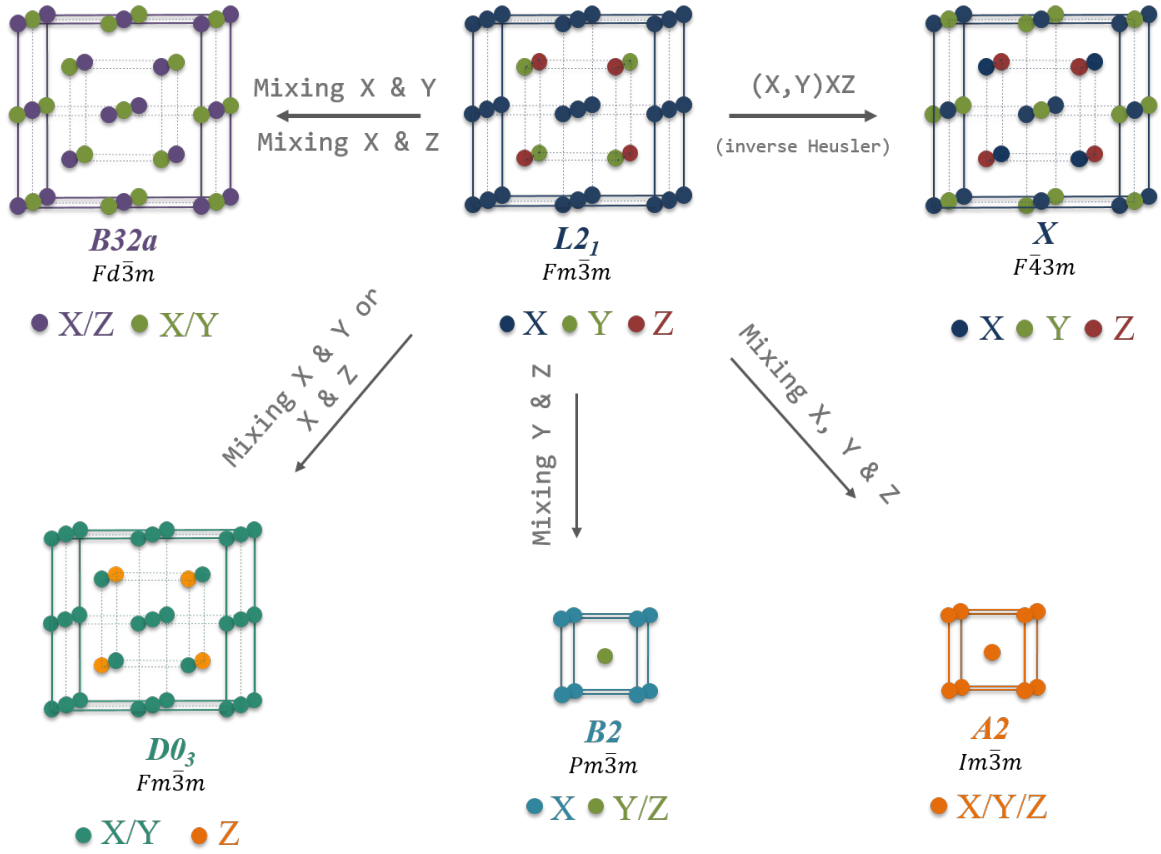

Figure 2.12: Six chemical phases in X_2YZ Heusler compounds. Starting from the fully ordered $L2_1$ to the disordered B32a, $D0_3$, A2 and B2. The X phase is the "inverse" Heusler compound. (Image inspired from [85]).

Let us define the occupation matrix Γ which represents the occupation rates of each atoms on each crystalline sites. Thus, this matrix allows us to deal from the f_u to the f_i as shown in equation 2.5.

$$\mathbf{f}_u = \Gamma \mathbf{f}_i$$

$$\begin{pmatrix} f_\alpha \\ f_\beta \\ f_\gamma \\ f_\delta \end{pmatrix} = \begin{pmatrix} \Gamma_{\alpha X} & \Gamma_{\alpha X'} & \Gamma_{\alpha Y} & \Gamma_{\alpha Z} \\ \Gamma_{\beta X} & \Gamma_{\beta X'} & \Gamma_{\beta Y} & \Gamma_{\beta Z} \\ \Gamma_{\gamma X} & \Gamma_{\gamma X'} & \Gamma_{\gamma Y} & \Gamma_{\gamma Z} \\ \Gamma_{\delta X} & \Gamma_{\delta X'} & \Gamma_{\delta Y} & \Gamma_{\delta Z} \end{pmatrix} \begin{pmatrix} f_X \\ f_{X'} \\ f_Y \\ f_Z \end{pmatrix} \tag{2.5}$$

Each Γ_{ui} is the occupation rate of atom i on the site u. Obviously, if the stoichiometry is kept constant, the Γ_{ui} coefficients undergo mathematical constraints. The sum of the coefficients on each row and column should be equal to 1 because there is no more than 1 Mn per formula unit for instance. With 4 sites u and

4 atoms i, it leads to 8 equations with a simplification in this case where X and X' atoms are the same. Furthermore, in the following matrices, the X and X' atoms are chosen distinguishable which means that the first family of Co atoms are strictly on site α and the second on site β. It allows to write the $L2_1$ matrix as the unitary matrix and does not change the final results. The different occupation matrices Γ corresponding to phases shown in figure 2.12 are given in equations 2.6. Γ_X is a special case here. Strictly speaking, the X phase is also a perfectly ordered phase ("inverse" Heusler structure [52, 73]).

$$\Gamma_{L2_1} = \begin{pmatrix} 1 & 0 & 0 & 0 \\ 0 & 1 & 0 & 0 \\ 0 & 0 & 1 & 0 \\ 0 & 0 & 0 & 1 \end{pmatrix} = \mathbb{1} \qquad \Gamma_{B32a} = \begin{pmatrix} \frac{1}{2} & 0 & 0 & \frac{1}{2} \\ 0 & \frac{1}{2} & \frac{1}{2} & 0 \\ 0 & \frac{1}{2} & \frac{1}{2} & 0 \\ \frac{1}{2} & 0 & 0 & \frac{1}{2} \end{pmatrix}$$

$$\Gamma_{D0_3} = \begin{pmatrix} \frac{2}{3} & 0 & \frac{1}{3} & 0 \\ 0 & \frac{2}{3} & \frac{1}{3} & 0 \\ \frac{1}{3} & \frac{1}{3} & \frac{1}{3} & 0 \\ 0 & 0 & 0 & 1 \end{pmatrix} \qquad \Gamma_{B2} = \begin{pmatrix} 1 & 0 & 0 & 0 \\ 0 & 1 & 0 & 0 \\ 0 & 0 & \frac{1}{2} & \frac{1}{2} \\ 0 & 0 & \frac{1}{2} & \frac{1}{2} \end{pmatrix} \tag{2.6}$$

$$\Gamma_{A2} = \begin{pmatrix} \frac{1}{4} & \frac{1}{4} & \frac{1}{4} & \frac{1}{4} \\ \frac{1}{4} & \frac{1}{4} & \frac{1}{4} & \frac{1}{4} \\ \frac{1}{4} & \frac{1}{4} & \frac{1}{4} & \frac{1}{4} \\ \frac{1}{4} & \frac{1}{4} & \frac{1}{4} & \frac{1}{4} \end{pmatrix} \qquad \Gamma_X = \begin{pmatrix} 1 & 0 & 0 & 0 \\ 0 & 0 & 1 & 0 \\ 0 & 1 & 0 & 0 \\ 0 & 0 & 0 & 1 \end{pmatrix}$$

Structure factors

All the structure factors corresponding to figure 2.12 phases are calculated in the following table 2.2. In this present chapter, X and Y will always stand for Co and Mn, respectively. It is convenient to see that at least 3 phases can be quickly distinguished by XRD. Indeed, F_{B32a}, F_{B2} and F_{A2} are presenting extinctions for some families of peaks. It is a more complicated situation for F_{L2_1}, F_{D0_3} and F_X phases which do not present any particular extinction other than fcc systematic extinctions. Indeed, they all present a very similar structure factor because f_{Co} and f_{Mn} are very close due to the proximity of electron number (27 and 25 respectively).

Phase	(h,k,l) conditions	Structure factor
$L2_1$	$h+k+l = 4n$	$F = 4(2f_X + f_Y + f_Z)$
	$h+k+l = 4n+1$	$F = 4(f_Z - f_Y)e^{i\frac{\pi}{2}}$
	$h+k+l = 4n+2$	$F = 4(2f_X - f_Y - f_Z)$
	$h+k+l = 4n+3$	$F = 4(f_Z - f_Y)e^{-i\frac{\pi}{2}}$

X	$h+k+l=4n$	$F=4(2f_X+f_Y+f_Z)$
	$h+k+l=4n+1$	$F=4(f_Z-f_Y)e^{i\frac{\pi}{2}}$
	$h+k+l=4n+2$	$F=4(f_Y-f_Z)$
	$h+k+l=4n+3$	$F=4(f_Z-f_Y)e^{-i\frac{\pi}{2}}$
DO_3	$h+k+l=4n$	$F=4(2f_X+f_Y+f_Z)$
	$h+k+l=4n+1$	$F=4(f_Z-\frac{2}{3}f_X-\frac{1}{3}f_Y)e^{i\frac{\pi}{2}}$
	$h+k+l=4n+2$	$F=4(\frac{2}{3}f_X+\frac{1}{3}f_Y-f_Z)$
	$h+k+l=4n+3$	$F=4(f_Z-\frac{2}{3}f_X-\frac{1}{3}f_Y)e^{-i\frac{\pi}{2}}$
B32a	$h+k+l=4n$	$F=4(2f_X+f_Y+f_Z)$
	$h+k+l=4n+1$	$F=2(f_Z-f_Y)(1+e^{i\frac{\pi}{2}})$
	$h+k+l=4n+2$	$F=0$
	$h+k+l=4n+3$	$F=2(f_Z-f_Y)(1+e^{-i\frac{\pi}{2}})$
B2	$h+k+l=4n$	$F=4(2f_X+f_Y+f_Z)$
	$h+k+l=4n+1$	$F=0$
	$h+k+l=4n+2$	$F=4(2f_X-f_Y-f_Z)$
	$h+k+l=4n+3$	$F=0$
A2	$h+k+l=4n$	$F=4(2f_X+f_Y+f_Z)$
	$h+k+l=4n+1$	$F=0$
	$h+k+l=4n+2$	$F=0$
	$h+k+l=4n+3$	$F=0$

Table 2.2: Structure factors calculation for every chemical phase of a X_2YZ Heusler type structure

2.2.2 Experimental results

XRD measurements were performed using two different diffractometers that both use the Cu K_α radiation with $\lambda = 1.54056$ Å. The first one, used for symmetrical configuration only, is a Bruker D8 Advance with a Ge(111) monochromator and a 1D detector for fast data acquisitions. The second set-up, mostly used for non-symmetrical configurations, is a PanAnalytical X'Pert Pro MRD diffractometer equipped with a high resolution 4-circles goniometer that allows to orient the samples precisely in many directions. The latter is used for large angles and small angles (X-ray reflectometry) measurements. It has a filter to discriminate the K_β radiation from Cu and a PIXCel point detector.

Layers thickness determination

X-ray Reflectometry (XRR) is a useful technique relying on reflection and interferences undergone by X-rays passing through thin layers at very small angles. The path difference δ followed by X-rays is due to the specific refractive index of each layer as well as their thickness (and of course the incident angle of X-rays). This difference of path generates an interference pattern whith an angle dependence. The

principle of the measurement relies on a $\theta - 2\theta$ scan and is shown on figure 2.13. It allows the precise determination of layers thicknesses along with their density and roughness.

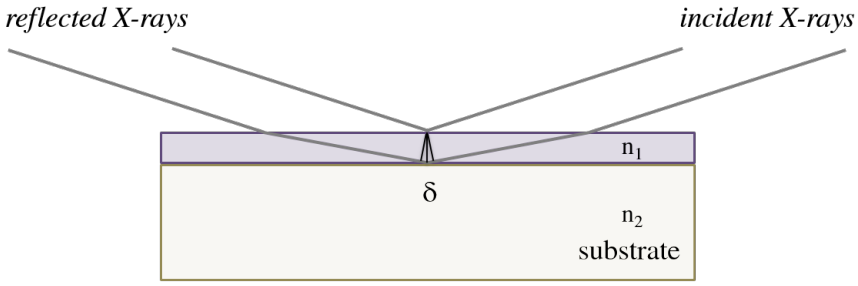

Figure 2.13: XRR principle.

XRR curves for each compound and the corresponding fits made with the PanAnalytical software *X'Pert Reflectivity* are presented in figure 2.14. The fitting parameters, *i. e.* density and thickness, are presented in the table 2.3 as well as the theoretical density and the thickness predicted by quartz micro-balances calibration. In a first step, the same number of Co atoms were deposited for every sample. Because the density of each Heusler compound is different, the resulting thicknesses are also different from one compound to the other. Now that the densities in those thin films are confirmed to be close to the theoretical ones, a precise control of the thickness can be achieved with quartz micro-balances.

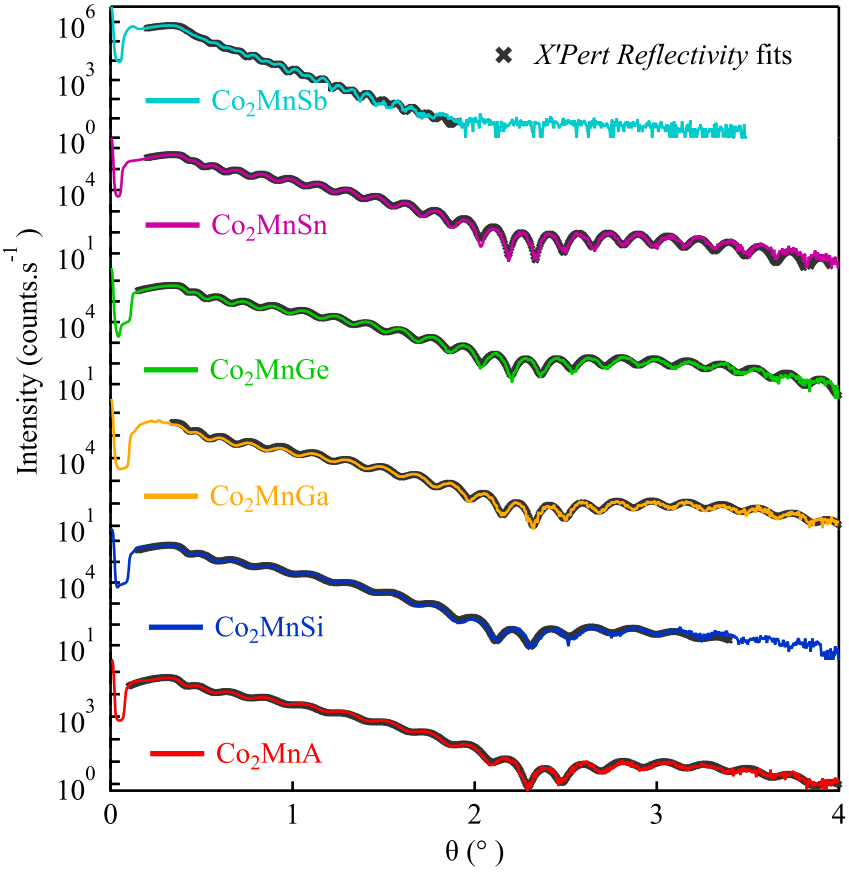

Figure 2.14: XRR curves for Co_2MnZ compounds.

	τ_{quartz} (nm)	d_{theory} (g.cm^{-3})	τ_{XRR} (nm)	d_{XRR} (g.cm^{-3})
Co_2MnAl	17.2	6.94	17.73	6.7
Co_2MnSi	17	7.4	17.26	7.34
Co_2MnGa	20.6	8.43	21.22	8.42
Co_2MnGe	21	8.57	22.52	8.38
Co_2MnSn	24.9	8.96	24.85	8.71
Co_2MnSb	24.8	9.38	32.61	8.99

Table 2.3: Expected thicknesses from quartz micro-balances calibration, theoretical density and finally thicknesses and density from XRR experiments.

XRR curves are all well fitted and present very similar shape except for Co_2MnSb grown on a V buffer layer. For Z=Al, Si, Ga, Ge and Sn, the fits are excellent. The evaluated thicknesses of the Co_2MnZ and Au capping are very similar to the expected ones. The case of Co_2MnSb is quite different: the thickness extracted from the fit is higher than the expected one. The oscillations are much less clear than with the other Heuslers, due to a larger roughness. This will be confirmed in the TEM section.

Symmetrical configuration

Even if the growth direction and orientation with the substrate is already known thanks to RHEED, it is important to perform a scan in a symmetrical configuration, where the scattering vector **q** is perpendicular to the sample surface in a $\theta - 2\theta$ configuration. It means that it will put any planes parallel to the surface in diffraction condition. The figure 2.15 shows the measurements for Co_2MnZ layers. In the following, we discuss first the XRD results obtained on Co_2MnZ with Z=Al, Si, Ga, Ge and Sn. A second part is dedicated to Co_2MnSb.

The growth is indeed along (001) for every compounds, as shown previously by RHEED characterization. The systematic extinction in fcc lattice implies that (001) and (003) (h, k, l different parity) reflections must vanish as observed in figure 2.15. This is also true for the MgO substrate which is fcc as well. Moreover, the shifts of the peaks are visible indicating a variation of lattice parameters from one compound to the other. On the (002) Co_2MnZ peaks (and sometimes (004)), Kiessig fringes are visible and are a proof of an excellent crystalline quality with well define interfaces. The period of the fringes are inversely proportional to the thickness of the layer. The extracted thicknesses are in complete agreement with those obtained by XRR. One last feature must be clarified : the huge bump around the (002) peak of the MgO substrate, on its left for Z = Si and Ge, on its right for Z = Al, Ga, Sn and Sb. It is due to the Au capping layer, grown on top of the samples in order to protect the films. The small thickness (2 nm) of the capping layer is responsible for the large width of the peak (width is inversely proportional to the number of atoms that scatter the incoming X-ray radiation). Furthermore, it has been observed with RHEED that for Z = Si and Ge, the Au layer has grown along (111) direction whereas it was along (001) for every other compound. It explains the location of the bump compared to the (002) MgO reflection. Indeed, Au also has a fcc lattice with a cell parameter $a = 4.08$ Å so the (002) reflection should be located at $q = 3.08$ Å^{-1} and the (111) at $q = 2.67$ Å^{-1}. But, on figure 2.15, the (111) reflection of Au is

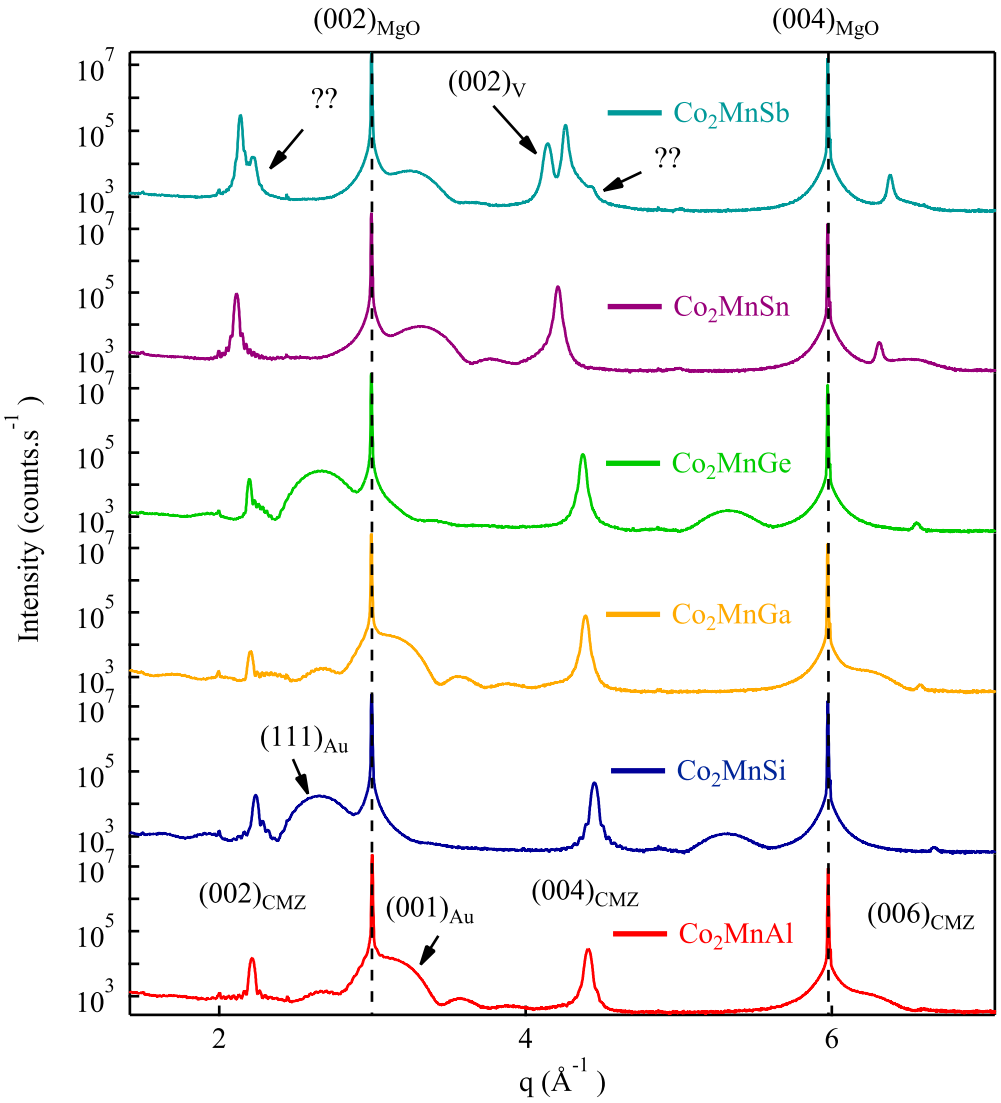

Figure 2.15: XRD measurements in symmetrical configuration of the Co_2MnZ series.

located around $q = 2.645$ Å^{-1} because of a small expansion of the lattice parameter on top of Co_2MnSi and Co_2MnGe. The situation is reversed for (002) because it is located between $q = 3.18$ and 3.34 Å^{-1} so the Au lattice is well contracted for Z = Al, Ga and Sn. These different Au growth directions will be confirmed by electron microscopy.

The case of Co_2MnSb is puzzling. The growth along (001) is confirmed and so is the growth of Au along (001) but there are several additional peaks. First, in $q = 4.142$ Å^{-1}, there is the (002) reflection of body centered cubic (bcc) V with a cell parameter of 3.03 Å. There are two peaks beside the (002) and (004) reflections of Co_2MnSb with a corresponding $q = 2.22$ and $q = 4.44$ Å^{-1}. They surely belong to the same family but no matching phase involving Co, Mn, Sb and alloy thereof has been found in any database. Moreover, it is the only compound for which the (002) reflection is more intense than the (004). This behavior is not compatible with the structure factors calculated for the Heusler structure in table 2.2. Indeed, whatever the chemical phase occurring in a Heusler type structure, $|F_{002}|^2$ is always smaller than $|F_{004}|^2$. As the present Co_2MnSb structure cannot be described in our structural framework, we will not

discuss it further in this XRD section but later in the section dedicated to electron microscopy.

Non-symmetrical configuration

In order to get more information about the Heusler compounds structure, it is necessary to find other peaks that are not along the film normal. Thanks to the 4-circles goniometer, it is possible to move the sample in space using 3 other angles, allowing us to measure peaks like (111) and (311). In a first step, the intensity of each peak is not analyzed. Only a qualitative analysis is provided because in the table 2.2, those peaks of different order ($4n+1$, $4n+3$ *etc.*) are able to discriminate phases among others just because they are observed.

Ternary alloys. The figure 2.16 shows the (111) and (311) reflections of Co_2MnZ with Z = Al, Si, Ga, Ge, Sn. Those peaks where measured by rotating the sample with different angles. Once again, the shift in 2θ is visible and is consistent with the corresponding cell parameter of each alloy. Additionally, there are no such peaks for Co_2MnAl. As expected by *in situ* RHEED during the growth, diffraction patterns of Co_2MnAl are not compatible with a $L2_1$ phase but clearly indicate a B2 disorder (F_{4n} and $F_{4n+2} \neq 0$ but F_{4n+1} and $F_{4n+3} = 0$, see table 2.2). Consequently, it is important to keep in mind that the unit cell of Co_2MnAl is no more fcc considering the B2 phase. The corresponding space group becomes $Pm\bar{3}m$ (primitive unit cell). As shown by figure 2.12, its real cell parameter is two times smaller thus, on the diffraction pattern of figure 2.15, the (00l) peaks of Co_2MnAl are not (002), (004) *etc.* but (001), (002) and so on.

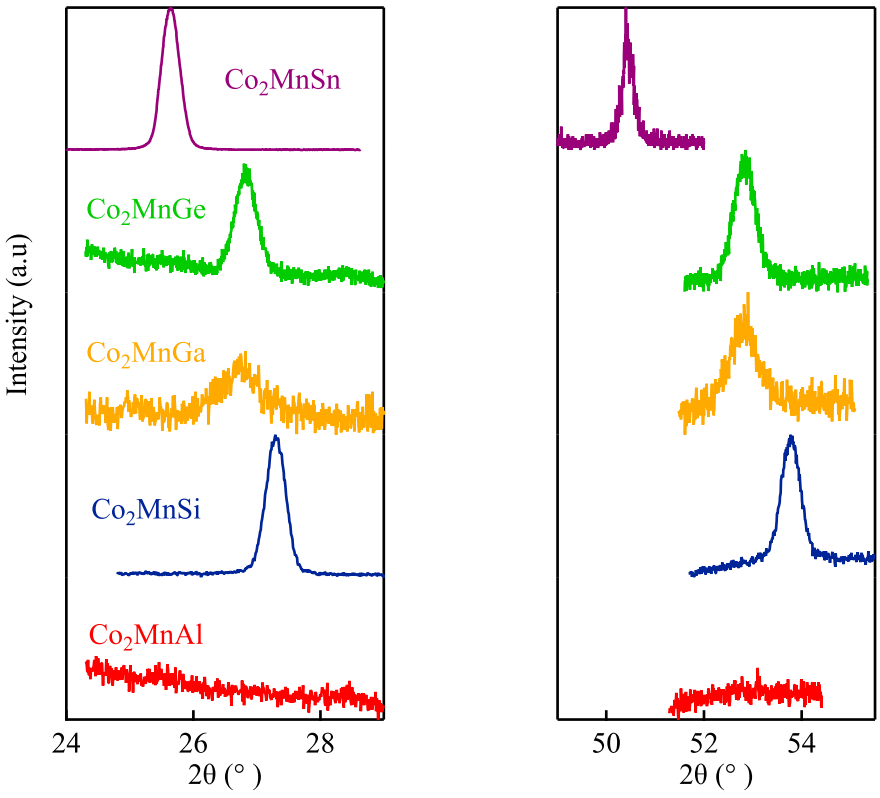

(a) (111) (b) (311)

Figure 2.16: Examples of non-symmetrical reflections for Co_2MnZ alloys.

Nevertheless and for simplicity, we keep the Heusler fcc denomination in order to compare its chemical ordering with the other compounds. Concerning the rest of the series, it is not possible to conclude on the chemical phase but it is for sure one between $L2_1$, $D0_3$ and X (inverse) phase. In order to answer this question, a pseudo-quantitative analysis will be led in the end of this section.

Quaternary alloys. Quaternary series of Heusler have been measured by XRD in non-symmetrical configuration to investigate on the change in chemical and structural order during the substitution of one element by another. The figure 2.17 shows the (111) and (220) reflections of the two series.

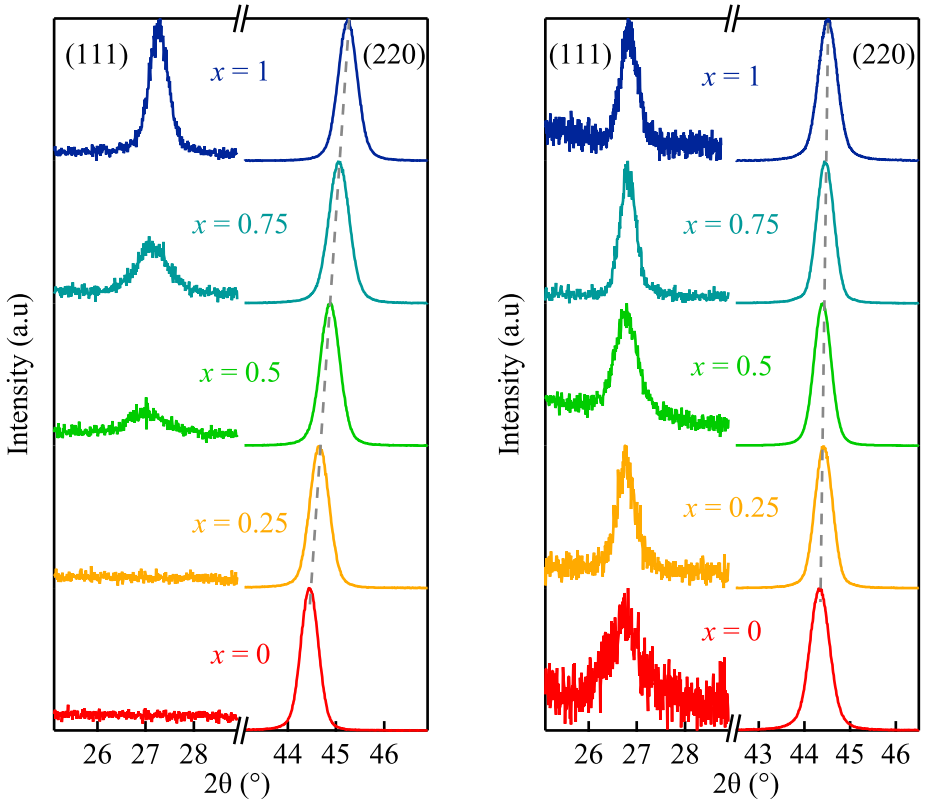

(a) $Co_2MnSi_xAl_{1-x}$ (b) $Co_2MnGe_xGa_{1-x}$

Figure 2.17: (111) and (220) reflections of quaternary Heusler compounds with different substitution rate x. Dashed lines are guide to the eyes to show the lattice constant evolution with x.

As shown already in figure 2.8 with RHEED, the $Co_2MnSi_xAl_{1-x}$ series (figure 2.17a) undergoes a continuous chemical transition, which can be deduced by the loss of the (111) reflection. By decreasing x, the chemical ordering varies from a $L2_1$-compatible structure to a B2 structure that arranges randomly Mn and Z atoms. In the case of quaternary compounds like $Co_2MnSi_{25}Al_{75}$, a B2 disorder means that Mn, Si and Al are mixed altogether on sites γ and δ of the figure 2.11. Nonetheless, it is not possible to conclude on the existence of ordered fractions in these quaternary compounds with no (111) reflections. Indeed, when X-rays are scattered by a crystal, the crystal's interference function distributes the intensity in different directions of space (diffraction). The higher the number of scattering atoms, the stricter the scattering in space. It means that a lot of intensity is distributed in small directions in space (Dirac deltas for infinite crystals). If there are small $L2_1$ clusters in a predominantly B2 matrix, the resulting (111)

peak could be too small to emerge from the background. To conclude on this series, the shift in 2θ is large and indicates a continuous change of the lattice parameter from $x = 0$ to $x = 1$, as a solid solution. The gray dashed line on the (220) reflection is a guide to the eye to see that the shift appears linear with x. This result is another proof of the good control of the stoichiometry in our MBE systems.

The XRD spectra obtained on the $Co_2MnGe_xGa_{1-x}$ series are shown in figure 2.17b. Contrary to $Co_2MnSi_xAl_{1-x}$, the spectra are compatible with the $L2_1$ structure whatever x since the (111) reflection is present for the entire substitution range. Its intensity should decrease from $x = 1$ to $x = 0$, due to the structure factor F_{4n+3} that is always smaller for Co_2MnGa than Co_2MnGe (whatever the chemical phase between $L2_1$, $D0_3$ or X see table 2.2). This is indeed the trend observed on the figure 2.17b but a quantitative analysis is difficult since Ge atoms have only one more electron than Ga. Thereby, slight changes in intensity could be explained by some change in the measurement conditions. Finally, for this series, the (220) and (111) peaks do not move with x. This is not surprising because the lattice constants of Co_2MnGa and Co_2MnGe are very close.

In conclusion, both series of quaternary alloys are still high-quality single-crystals that appears to behave as solid solutions. The lattice parameters change linearly with the substitution rate. In the case of $Co_2MnSi_xAl_{1-x}$, a continuous chemical transition is observed as suspected by previous RHEED experiments. However, small domains chemically ordered could exist in a disordered matrix. For $Co_2MnGe_xGa_{1-x}$, the structure is compatible with the $L2_1$ phase whatever the substitution rate x, as expected by RHEED.

Lattice constants

Lattice parameters of the whole set of Co_2MnZ alloys are extracted from different peaks involving all the Miller indices. They are very close to theoretical values and experimental bulk ones. They are plotted in figure 2.18 versus the covalent radius of each Z element. Lattice constants of the $Co_2MnGe_xGa_{1-x}$ are not indicated for clarity reasons and because there is not enough sensitivity to measure differences below 0.01 Å. Horizontal error bars traduce the estimated error on the stoichiometry.

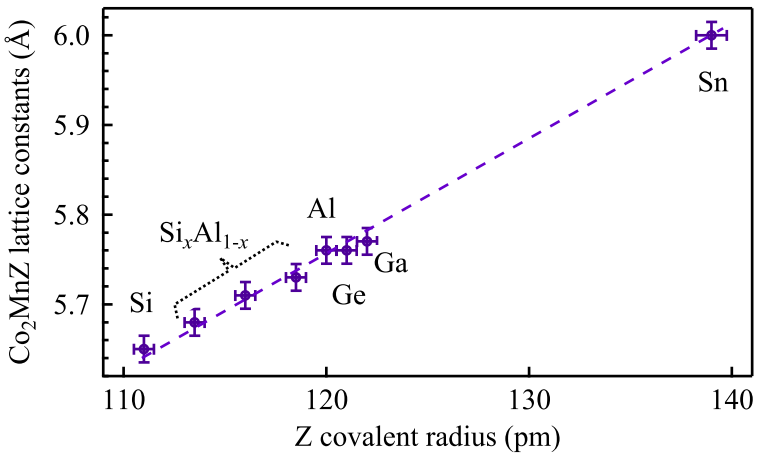

Figure 2.18: Ternary and quaternary Co_2MnZ lattice constants determined by XRD versus Z covalent radius. The dashed line is the trend expected in covalent solids.

The relationship between the cell parameter and the covalent radius of Z is linear, supporting the fact that Co_2MnZ crystals do not bind as full metals but are hybrid materials, in between metals and covalent solids, as predicted by theory.

Relative quantitative analysis attempt on ternary compounds

XRD intensity analysis is very tricky. A lot of corrections and extremely well controlled parameters are necessary to perform a quantitative analysis. The equation 2.7 represents the intensity of a diffracted peak, that is found in many books and lectures [86],

$$I_{\mathrm{CMZ}}(hkl) = \frac{\lambda^3 r_0^2 V}{\bar{\omega} V_c} LPA_{\mathrm{f}}TE|F_{\mathrm{CMZ}}(hkl)|^2, \tag{2.7}$$

where $I_{\mathrm{CMZ}}(hkl)$ is the peak intensity, λ the wavelength of the radiation, r_0 the classical electron radius, V the crystal volume, $\bar{\omega}$ the angular scanning velocity and $LPA_{\mathrm{f}}TE$ the different correction factors : Lorentz factor L, polarization factor P, absorption factor A_{f}, thermal diffuse scattering factor T and extinction and multiple diffraction factor E. The different correction factors are either known or neglected (*i. e.* equal to 1):

(i) L the Lorentz correction factor directly related to the time during which the reciprocal lattice point pass through the Ewald sphere (time-of-reflection opportunity);

(ii) P the polarization factor. There is a vector cross product between the polarization of the incoming X-ray radiation and the direction of the scattered beam;

(iii) A_{f} the absorption factor : the intensity of a radiation passing through matter follows a simple $I = I_0 e^{-\mu t}$ rule with μ the absorption coefficient and t the film thickness. Every compounds has its own μ related to mass absorption coefficients;

(iv) T the correction for thermal diffuse scattering (or inelastic phonon scattering). This correction factor is known by calculations that rely on elastic constants [87]. We neglect this correction factor, supported by the lecture of G. J. McIntyre at HERCULES school [88] *"For most structural studies though thermal diffuse scattering is ignored to a very good approximation since omitting the correction affects only the thermal displacement parameters"*;

(v) E the correction for extinction and multiple diffraction when several reciprocal lattice points are very close to the Ewald sphere.

Here, the principle of the relative quantitative analysis is to compare the same (hkl) peak for each compound. By doing the measurement in the exact same conditions (wavelength, scanning velocity), all the correction factors $LPA_{\mathrm{f}}TE$ are the same in each XRD diagram. Indeed, for one given reflection, the Lorentz factor is almost the same for every Heuslers because they have a close lattice constant. The polarization factor is linked to (i) the X-ray source which is the same for every measurement and (ii) to the angle of the scattered beam which is considered constant due to similar lattice constants of Co_2MnZ compounds. The absorption factor is negligible for $\simeq 20$ nm layers. Finally, the correction for extinction and multiple diffraction has to be taken into account only in molecular crystals. Now, the intensity only depends on the crystal volume V, the unit cell volume V_c and the structure factor $|F_{\mathrm{CMZ}}(hkl)|^2$. The

equation 2.7 can thus be expressed with the thickness τ of the layers and the lattice constant a by considering that the surface shined by X-rays is always the same for a fixed geometry (since we compare the same peak between all compounds):

$$\begin{aligned} I_{\mathrm{CMZ}}(hkl) &\propto \frac{\tau}{a^6}|F_{\mathrm{CMZ}}(hkl)|^2 \\ \mathrm{A} = \sqrt{I_{\mathrm{CMZ}}(hkl)\frac{a^6}{\tau}} &\propto \pm F_{\mathrm{CMZ}}(hkl) \end{aligned} \tag{2.8}$$

In this context, the parameter A should be linear with $F_{\mathrm{CMZ}}(hkl)$ for one given peak. Interestingly, $F_{\mathrm{CMZ}}(hkl)$ is different between the $L2_1$, $D0_3$ and inverse X chemical phase. Therefore, by plotting the measured A for every compounds and for one given peak, it might be possible to differentiate the chemical phase in presence. For each alloy, the corresponding structure factor was calculated using scattering amplitudes from the DABAX Data Base, by taking into account the θ angle dependence.

The figure 2.19 shows the extracted A parameter from equation 2.8 using the (111) peak. It is plotted versus the structure factor for the $L2_1$ phases (same as X for $h+k+l = 4n+3$) and the $D0_3$ phase. The

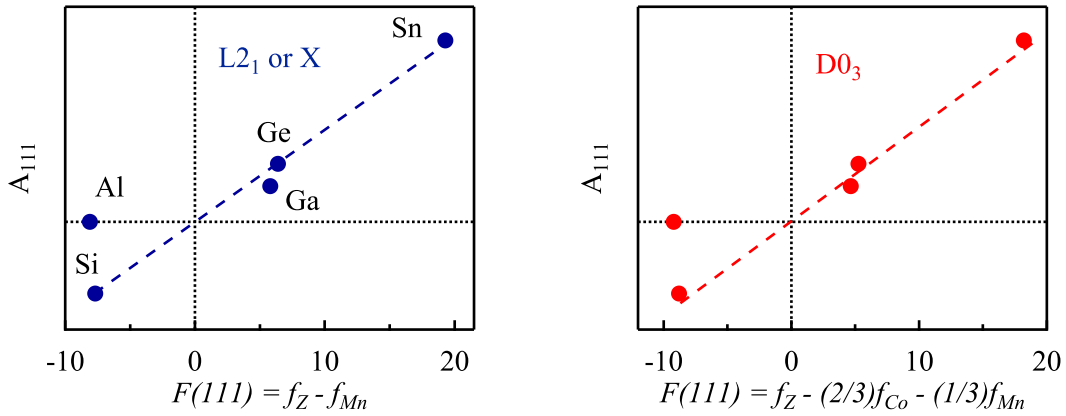

Figure 2.19: Area of (111) peak versus structure factor for the $L2_1$ (same as X) and $D0_3$ chemical phases

law is indeed linear as predicted by the intensity calculation. It means that all the previous approximations are not irrelevant. It is clearly visible that Co_2MnAl does not belong to those phases. Moreover, the fact that the line crosses the origin is mandatory because the intensity should be zero if $F(hkl) = 0$. Actually, the difference of structure factor between the disordered phases is very small due to the proximity of Co and Mn in number of electrons. The fact that the line fits well the data points for the two phases indicates that the sensitivity of the experiments is apparently not enough to distinguish between $D0_3$ and $L2_1$.

In the same way, the A_{222} parameters are plotted on figure 2.20 considering the structural factors of $L2_1$, $D0_3$ and X chemical phase. The data points are linear for the 3 phases but if it passes through zero for $D0_3$ and X phases, this is not the case for $L2_1$. According to all the approximations, this anomaly is however not sufficient to exclude this phase in our films.

Finally, it is hard to conclude on the chemical phase occurring in Co_2MnZ films with this method. Because the $L2_1$, $D0_3$ and X phases are close in term of structure factor, the measurements require a higher level of accuracy. However, the fact that the equation 2.8 is verified indicates that the series crys-

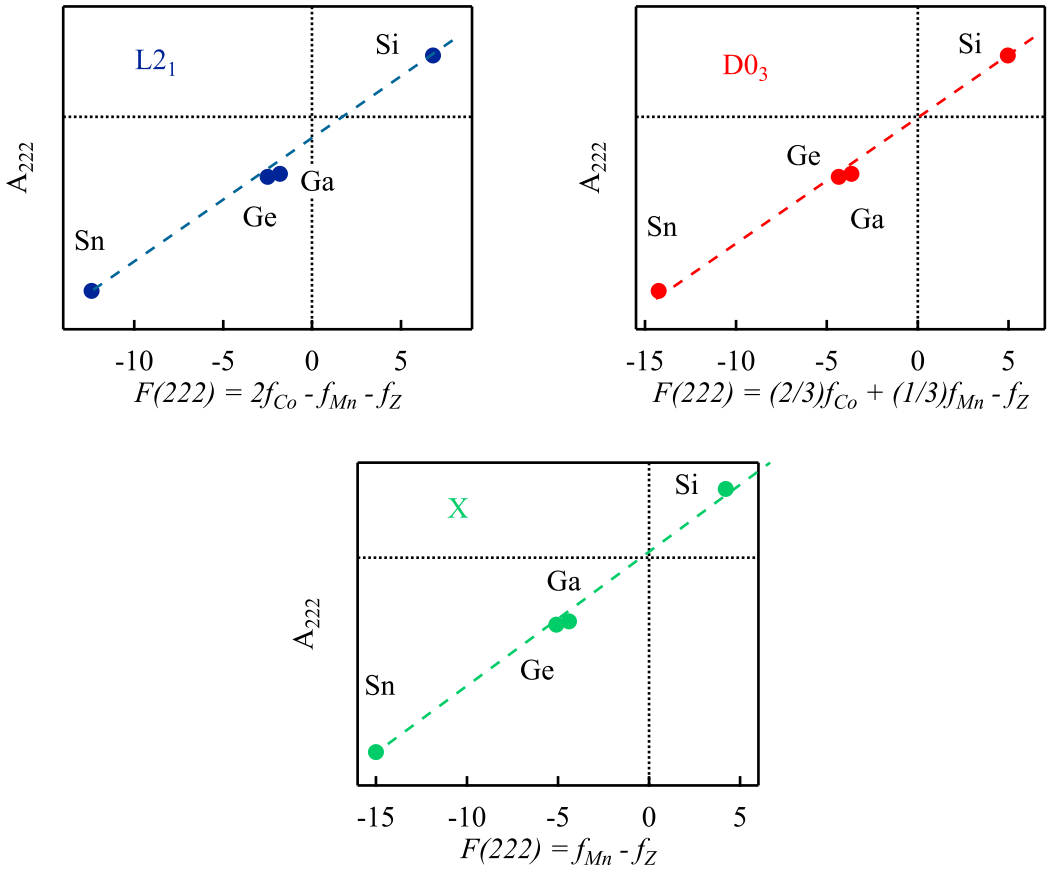

Figure 2.20: Comparison of (222) peak area versus structure factor for the $L2_1$, $D0_3$ and X chemical phases

tallizes indeed in the Heusler type structure and that the present method could work for a slightly higher difference between X and Y elements in number of electrons (for instance in Co_2TiZ alloys). This study is finally essential in the context of Heusler films grown for spintronics. Indeed, in many papers, people claimed the $L2_1$ phase existence in their films by showing the occurrence of (111) and (311) peaks. Here, we clearly demonstrate that this is absolutely not enough to conclude on the chemical phase.

The remaining doubt on the chemical phase in Co_2MnZ alloys was the primary motivation to perform transmission electron microscopy on our films, which is the subject of the next section.

2.3 Scanning transmission electron microscopy

The Co_2MnZ series was analyzed by Scanning Transmission Electron Microscopy (STEM). The goal was to identify which chemical phase is taking place in each Co_2MnZ compound since our XRD study did not answer to this question. In particular, images obtained by High Angle Annular Dark Field (STEM-HAADF) detection are going to be discussed because a contrast between atoms with a close electron number is achievable. HAADF is a method where electrons that are scattered at high angle are collected in an annular detector around the incident beam. Since heavy elements scatter electrons much more than lighter ones, brightness indicates heavy elements and darkness light elements. This investigation was

carried out by the microscopy team at the IJL using a JEM - ARM 200F Cold FEG TEM/STEM, always operating at 200 kV and equipped with a spherical aberration (C_s) probe and image correctors. It has a point resolution of 1.2 Å in TEM mode and 0.78 Å in STEM mode.

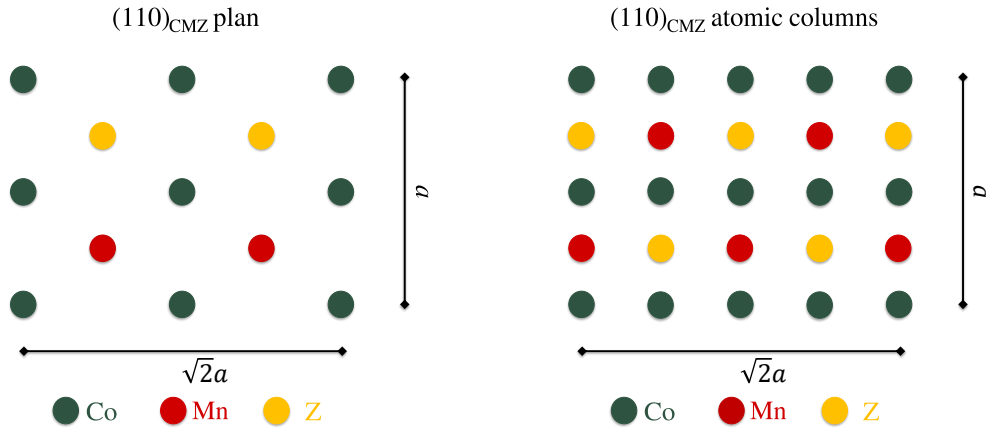

Figure 2.21: (110) plane of the Co_2MnZ cell and all atomic columns along the [110] zone axis, with a $L2_1$ type structure.

50-60 nm thick cross sections were prepared by a focused ion beam etching with Ga ions. With such a thickness, the 200 kV accelerated electrons get trough all the section. Hence, all the atomic columns are visible. By chance, the epitaxial relationship between the substrate and Co_2MnZ layers allows us to do a cut along the $[110]_{CMZ}$ crystallographic axis without high difficulty ([110] zone axis). Thus, as demonstrated in figure 2.21, columns with only Mn, Co and Z atoms should be visible, in the case of a $L2_1$ structure of course.

With such a difference of number of electron in the Z elements (Al = 13 e^- → Sb = 51 e^-), very specific contrasts are expected to be observed from a compound to another. Due to the proximity of Co and Mn in number of electrons, a systematic process is performed to differentiate each element. Starting from raw images, the process consists in doing a Fast Fourier Transform (FFT) to get a reciprocal lattice pattern. Then the FFT is filtered to remove noise and to select only spots of interest. Afterward, an inverse FFT is executed. The resulting image allows us to discriminate elements by doing line profiles of the intensity, thanks to the appreciable signal over noise ratio. In the following, compounds within the series will be separated according to the Z element weight (linked to the number of electrons) as light (Z=Al, Si and $Si_{0.5}Al_{0.5}$), middle (Z=Ga, Ge) and heavy (Z=Sn and Sb).

2.3.1 Co_2MnAl, Co_2MnSi and $Co_2MnSi_{0.5}Al_{0.5}$ (light Z)

In this section, Al and Si are lighter than Co and Mn. It should result in dark columns for Al and Si with regard to Mn and Co. STEM is a direct imaging of the sample and allows us to analyze on the direct lattice. The figure 2.22 shows raw images performed in STEM-HAADF mode for Co_2MnAl on the left and Co_2MnSi on the right as well as their FFT.

First, raw images indicate the growth of the Au capping layer in the (001) direction for Co_2MnAl and (111) direction for Co_2MnSi, confirming the XRD experiment. Indeed, the Au inter-atomic distance cannot be resolved in the latter case. The distance between 2 Au columns in this configuration is 1.44 Å whereas it is 2.04 Å when the growth is along (001) direction. Nonetheless, the epitaxy of Au on top

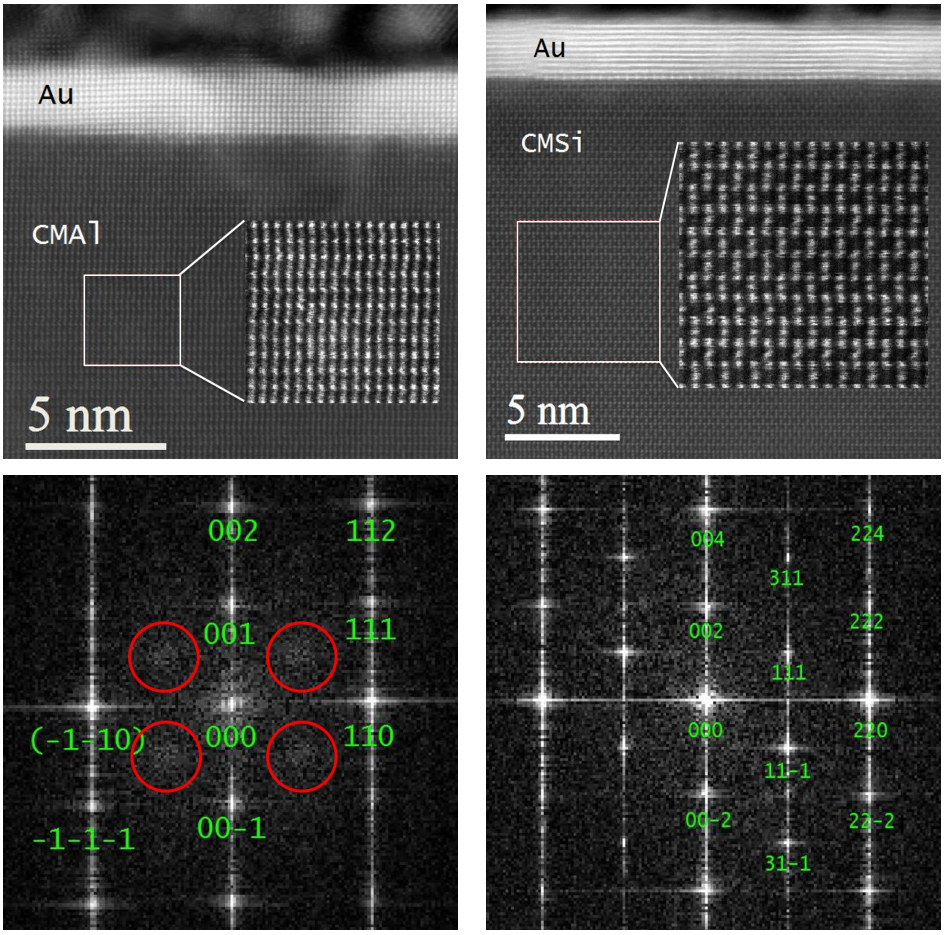

Figure 2.22: STEM-HAADF raw images along the [110] zone axis of Co_2MnAl (left) and Co_2MnSi (right) together with Au capping layers. Little inserts are a magnification of the white frames. The corresponding FFT are shown below.

of both layers is really good. Interfaces are very flat and sharp and atomic planes of Au are completely parallel[5].

Concerning the Heusler layers, there is obviously a difference between Co_2MnAl and Co_2MnSi. Co_2MnAl is surely in a B2 disordered phase where Mn and Al atoms (columns in the present case) are randomly mixed up, leading to the loss of specific reflections in diffraction experiments (see previous section). It is visible in the insert of figure 2.22 left that there are one line of Co columns alternated with one line of Mn / Al mixed columns. The B2 phase is also confirmed with the FFT (left one on figure 2.22), where the indexed reflections are not compatible with the $L2_1$ phase. However, broad spots with very small intensity are visible at the location of the missing peaks (indicated by red circles) and suggest that there should be a tiny fraction of Mn / Al ordering distributed in the B2 layer. Images obtained on Co_2MnSi are different. The structure is now compatible with the structure on figure 2.21 even if it is not possible to differentiate Co and Mn columns with the eye. Si atoms are difficult to see because they are very dark in HAADF mode. The corresponding FFT on the right shows a $L2_1$ compatibility of Co_2MnSi with the presence of the expected reflections. The figure 2.23 shows inverse FFT images of the inserts of figure 2.22 and the corresponding intensity line profiles. The B2 ordering is clearly visible for Co_2MnAl, as reported in the literature [30, 78] whereas the presence of $L2_1$ order is confirmed for Co_2MnSi. By

[5]promising for spin valves applications

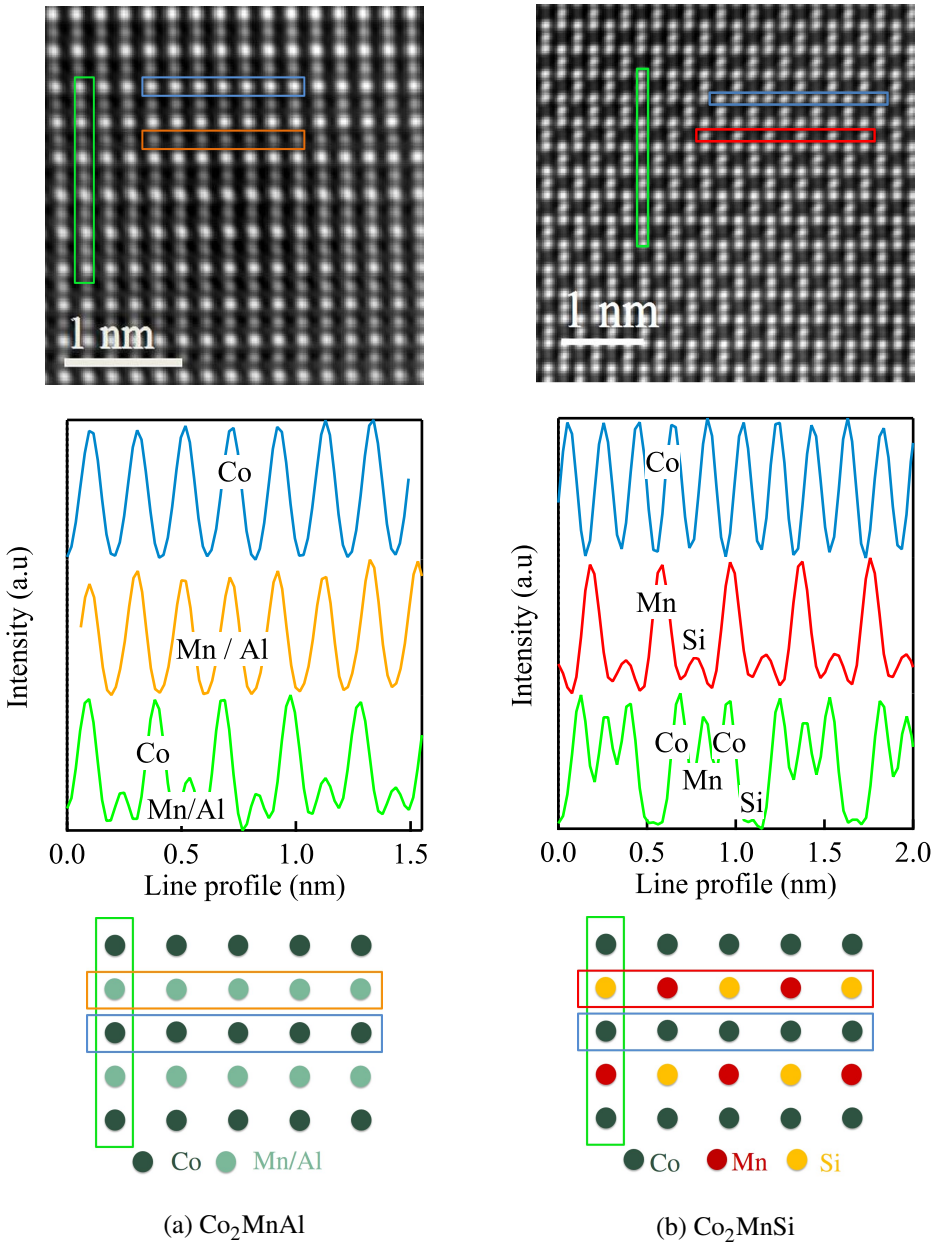

(a) Co_2MnAl (b) Co_2MnSi

Figure 2.23: Inverse FFT of figure 2.22 along with line profiles and the corresponding (110) atomic columns for (a) Co_2MnAl (B2) and (b) Co_2MnSi ($L2_1$).

analyzing line profiles, it is possible to discriminate Mn from Co columns and the resulting profiles are in agreement with the figure 2.21 for Co_2MnSi. It has to be carefully noted that it is not possible to ensure that there are no fractions of disorder in the layer even if $L2_1$ type prevails. B2 or $L2_1$, the crystalline quality of both layers is very good with not much crystallographic defects. The orientation and epitaxial relationship is once again confirmed here.

Finally, it is interesting to see what happens in a quaternary $Co_2MnSi_xAl_{1-x}$ alloy where the (111) peak corresponding to the $L2_1$ order decreases and vanishes when increasing the substitution rate x (see figure 2.17a). As Co_2MnSi is $L2_1$ ordered and Co_2MnAl is B2, the best candidate to investigate on how is arranged the disorder in the layer is naturally $Co_2MnSi_{0.5}Al_{0.5}$. Two raw HAADF images obtained on two different locations on the cross section are shown in figure 2.24. The presence of two types of

patterns is visible. They are roughly outlined in red and blue. The blue area is the exact same pattern than Co_2MnAl with a B2 ordering where there are alternated lines of Co and Mn / Z columns. The red one corresponds to the $L2_1$ pattern obtained on Co_2MnSi. Both types of ordering are more visible on the right image with a higher magnification. Consequently, $Co_2MnSi_{0.5}Al_{0.5}$ is made of $L2_1$ and B2 domains.

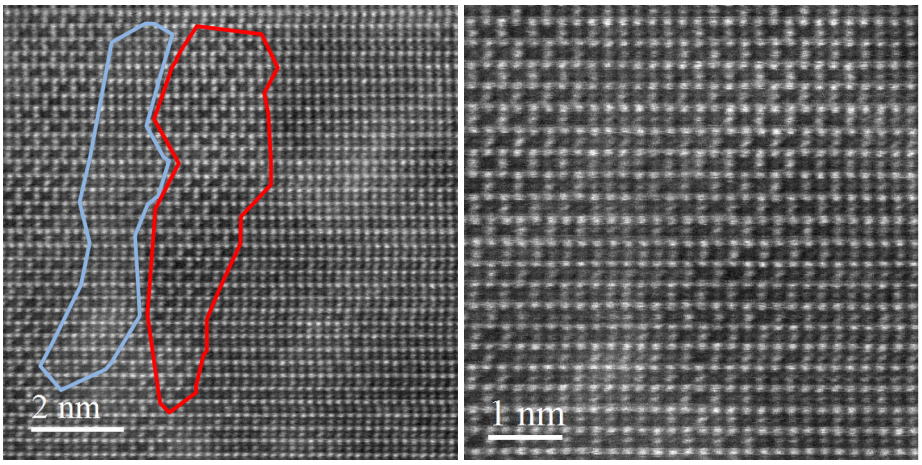

Figure 2.24: HAADF raw images of $Co_2MnSi_{0.5}Al_{0.5}$ with different magnification at different location on the cross section. Both $L2_1$ (red) and B2 (blue) domains are visible on both images, at the nanometer scale.

From several locations observed in the present sample, it seems that the B2 type slightly prevails but it is hard to quantify. Anyway, the chemical transition observed in $Co_2MnSi_xAl_{1-x}$ alloys is made of B2 and $L2_1$ domains, for which the predominance of one type over the other must depend on the substitution rate x. For the present rate $x = 0.5$, domains have a typical length scale of around 10 nm.

Nonetheless, it is impossible to conclude on the chemical nature of the two types of clusters. Are the $L2_1$ domains preferentially made of Co_2MnSi and B2 domains of Co_2MnAl ? To answer this question, one must carry out Energy Dispersive X-ray fluorescence (EDX) where a chemical analysis is done precisely by mapping the fluorescence of elements, excited by the 200 kV electron beam. Unfortunately, due to the stoichiometry, the number of Al and Si atoms is much lower than Co and Mn atoms[6]. In addition to that, the fluorescence of those two light elements is measured at K edges, which exhibits a very small cross section. For these two reasons, the efficiency of the experiment was too low to perform a chemical mapping with an atomic resolution (or at least, domain resolution).

2.3.2 Co_2MnGa and Co_2MnGe (middle Z)

Here, the 4 elements have similar contrasts since they all have a close number of electrons (Mn: 25 e^-, Co: 27 e^-, Ga: 31 e^-, Ge: 32 e^-). Naturally, the contrast between each columns, even without disorder, is barely visible with the eye. It makes the analysis more tricky but still possible with HAADF mode.

Figure 2.25 represents STEM-HAADF raw images of a Co_2MnGa layer on the left and Co_2MnGe on the right, both including the Au capping layer. Like in the previous section, Au capping has grown along (001) for Co_2MnGa whereas it is along (111) direction for Co_2MnGe. The quality of Au layers and

[6]One out of eight atoms is Si and so are Al atoms

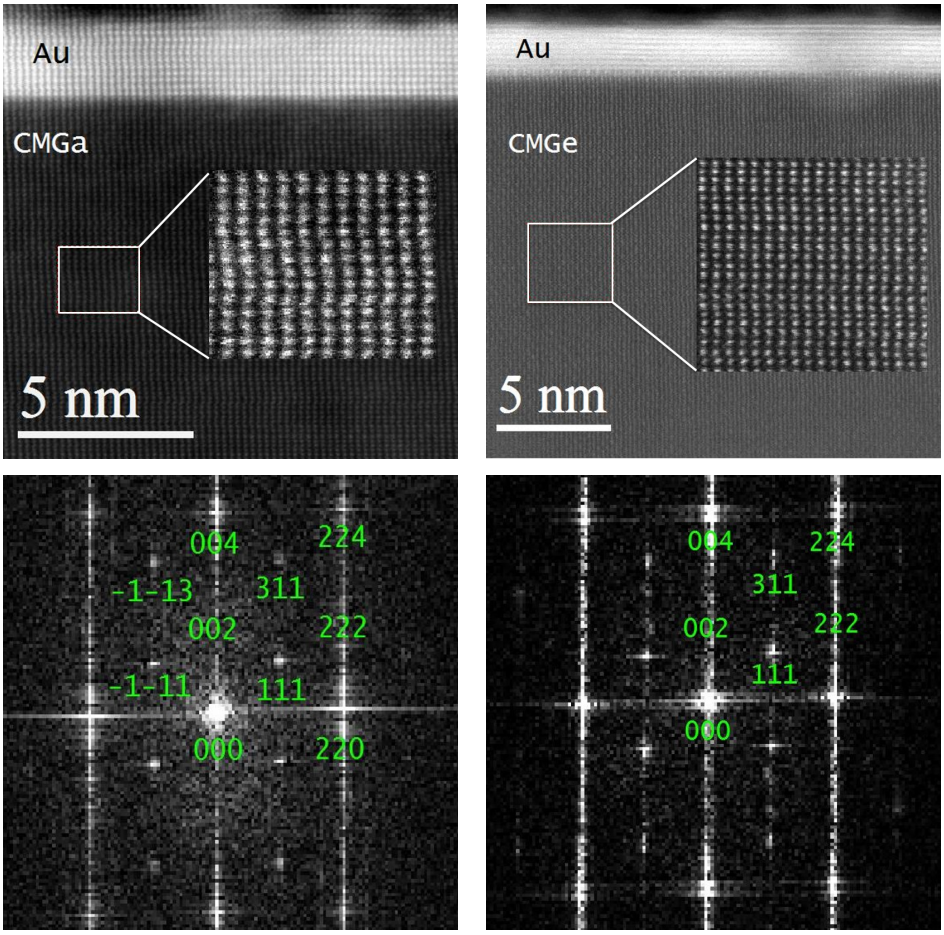

Figure 2.25: STEM-HAADF raw images along the [110] zone axis of Co_2MnGa (left) and Co_2MnGe (right) together with Au capping layers. Little inserts are a magnification of the white frames. The corresponding FFT are visible below.

interfaces with Co_2MnGa and Ge are also very good, like for the two previous materials.

As predicted, the contrast between each column in the two Heusler layers is almost the same, making the interpretation of raw images extremely difficult. For both layers, the FFT shows (111), (311) *etc.* reflections compatible with $L2_1$ order. However, one might be surprised by the extremely low intensity of $h+k+l=4n+2$ type of reflection. But, according to the table 2.2, this is a normal behavior because it is the smaller structure factor value for those compounds. The crystalline quality of the Co_2MnGa layer appears to be a little lower than Co_2MnGe. It is especially visible on the FFT where spots are not as clear as Co_2MnSi for instance. Still, the layer is visibly single crystalline. The corresponding inverse FFT after filtering are shown in figure 2.26. It is still difficult to distinguish with the eye any contrast of intensity, except maybe for the brightest Ge columns on the right of the figure 2.26. Here, line profiles are necessary to discriminate every columns and to get the chemical ordering in both layers. The pattern is the same than Co_2MnSi, and the figure 2.21 (but with a different contrast) which indicates a main $L2_1$ order. If there are different fractions of disorder in the layers, it must not concern mixing between Mn and Z columns because the difference of intensity on the red line profiles could not be visible otherwise.

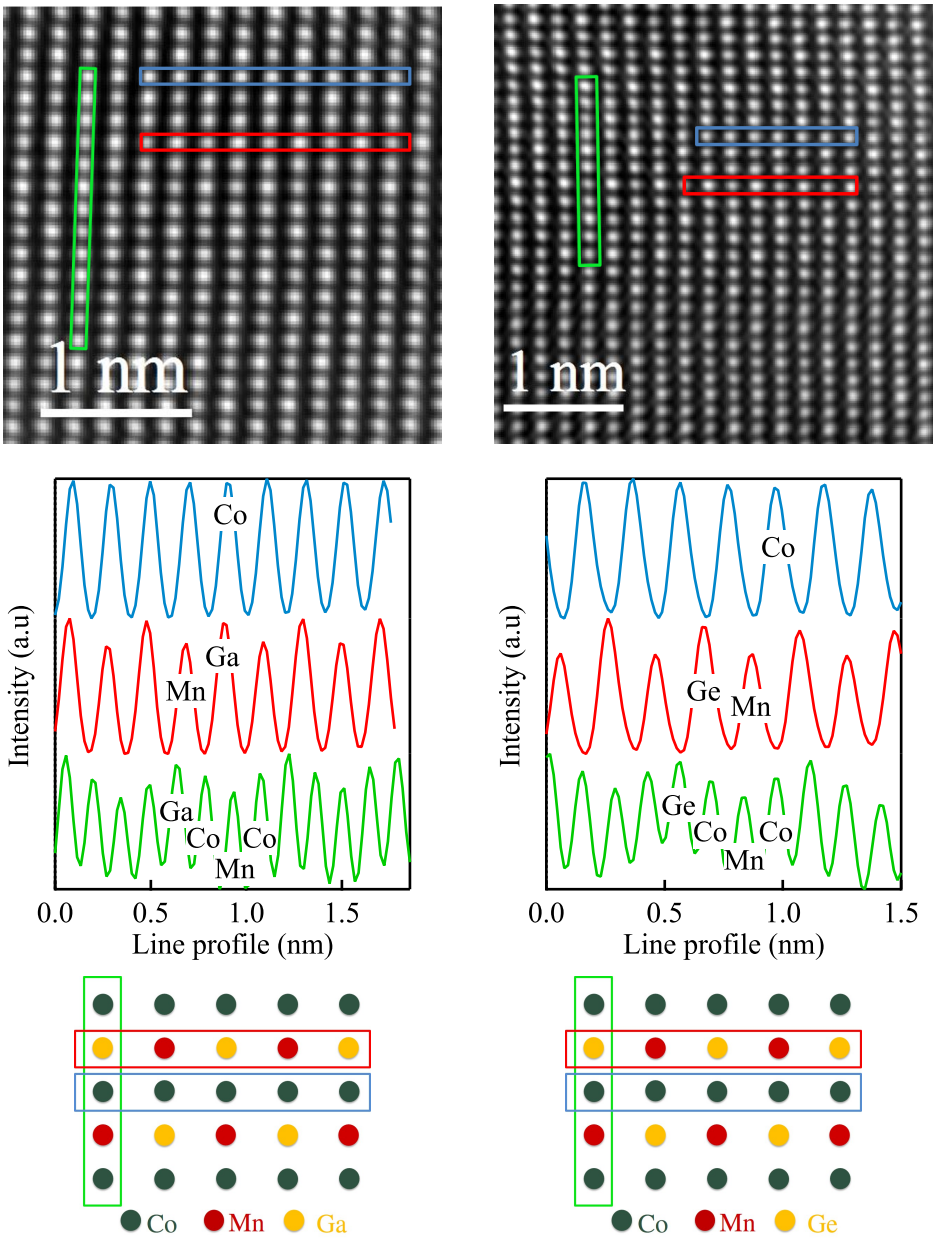

(a) Co_2MnGa (b) Co_2MnGe

Figure 2.26: Inverse FFT of figure 2.25 along with line profiles and the corresponding $L2_1$ (110) atomic columns for (a) Co_2MnGa and (b) Co_2MnGe.

2.3.3 Co_2MnSn and Co_2MnSb (heavy Z)

For these two compounds, columns made of the heavy Z element should be the brightest columns. Thus, the whole image contrast is reversed compared to Co_2MnSi. Since the case of Co_2MnSb remains puzzling, the following discussion and analysis will be split up in two subsections.

Co_2MnSn

Sn has nearly two times more electrons than Mn and Co. It should automatically be the brightest in TEM and this is exactly what is observed in HAADF image on figure 2.27. For this compounds, the

Au capping layer has grown along the (001) direction with also a very good epitaxial quality. The raw HAADF image shows a very good crystal quality of the Heusler layer as well and a chemical ordering is already visible, at least for Sn columns. The FFT shows the right pattern, with all the reflections expected for the $L2_1$ structure.

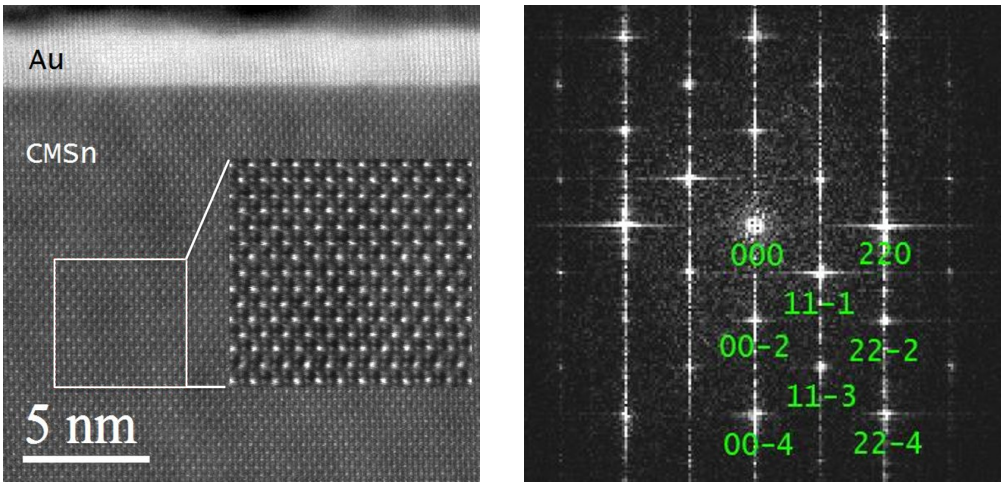

Figure 2.27: Left: STEM-HAADF raw image along the [110] zone axis of Co_2MnSn and Au capping layer. The insert is a magnification of the white frame. Right: fast Fourier transform of the white frame with indexation of reflections.

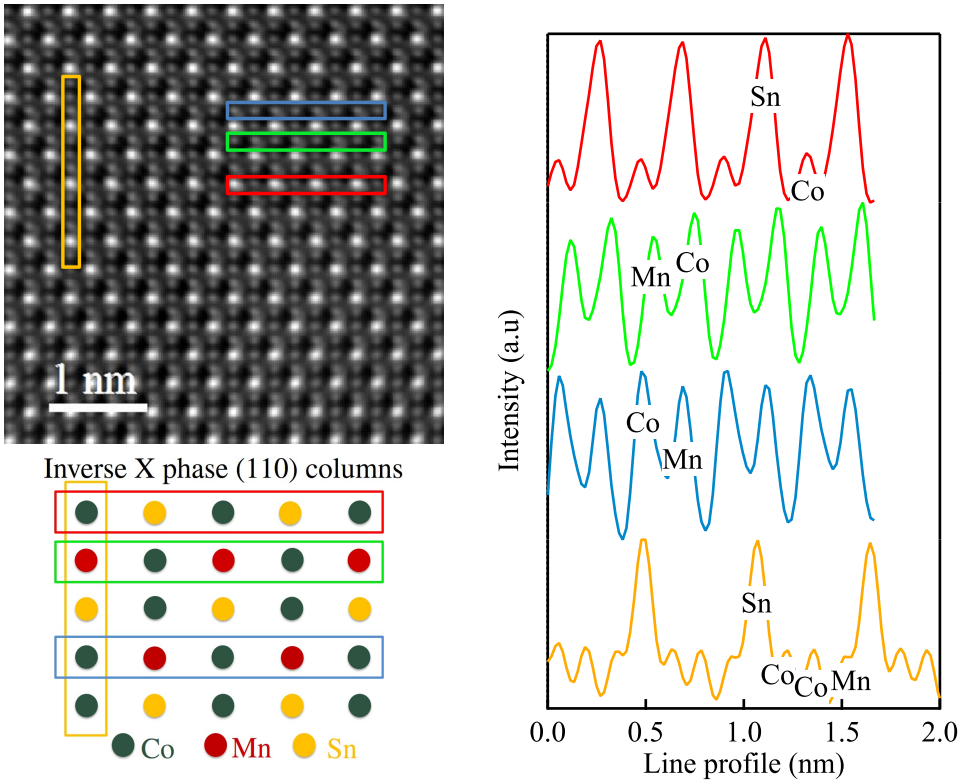

Figure 2.28: Inverse FFT of figure 2.27 and the corresponding line profiles showing a dominance of the X phase.

The figure 2.28 shows the inverse FFT and the corresponding intensity line profiles. According to those profiles, it appears that the $L2_1$ order is not the main phase in the layer. Indeed, they are indicating the X phase (inverse Heusler phase) as dominant. The (110) atomic columns for this phase is also sketched on the figure 2.28 where Co atoms of site β and Mn atoms of site γ (see figures 2.11 and 2.12) are swapped.

Co_2MnSb

In the case of a Heusler type structure, HAADF images of Co_2MnSb should be the same than Co_2MnSn. But, with previous diffraction results where the $4n + 2$ peak is more intense than the $4n$, Co_2MnSb surely has different crystalline sites than those depicted on sketch 2.11 (and hence a different fcc cell). Moreover, XRD reveals at least one additional structural phase (see figure 2.15), where unidentified reflections are visible. A raw HR-TEM image is shown on figure 2.29-left where the poor quality of the interface with Au is visible along with defects in the Co_2MnSb layer. Nonetheless, the interface

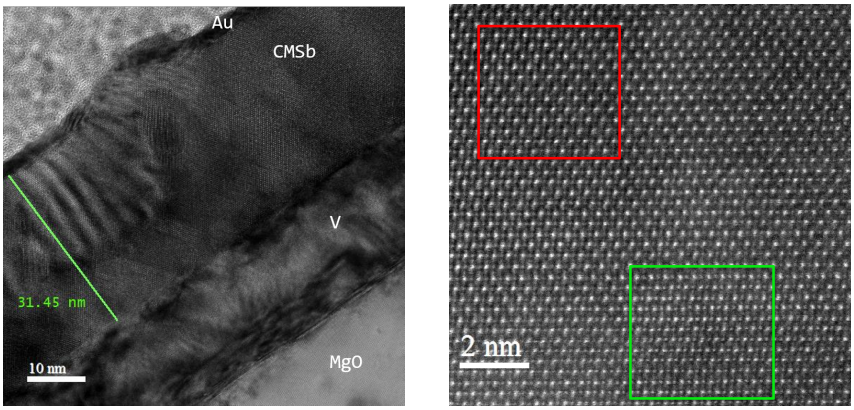

Figure 2.29: Left: HR-TEM raw image of Co_2MnSb, V buffer and Au capping layers. Right: raw HAADF image showing at least two different chemical phases.

with the V buffer layer appears to be correct. The right part of the figure 2.29 is a raw HAADF image showing at least two chemical phases in the Co_2MnSb layer. In the red square, it is tempting to associate a $L2_1$ structure to the present HAADF image but the quality is not high enough to clearly see what is between the Sb columns. In the green square, it is not possible to say if it is a disordered version of the red square phase, or if it is another structural one. In any case, this Co_2MnSb layer surely presents several structural/chemical orders.

Moreover, EDX was performed on the Co_2MnSb layer to check the global stoichiometry and if segregation was taking place somewhere in the sample. The result is shown on figure 2.30. An inhomogeneity is found in the middle with a higher content of Co, but it is difficult to say more. Additionally, it is very interesting to see that there are only Co atoms at the interface with the V buffer layer. The Mn and Sb atoms start few atomic layers after.

At this point, Co_2MnSb already presents complications during the growth (reproducibility from one layer to another), surface reconstruction problems and a peculiar behavior in XRD (compared to the rest of the series). Thus the resolution of its structure is not a primary concern in the scope of this thesis since it is already a poor candidate for possible spintronic applications.

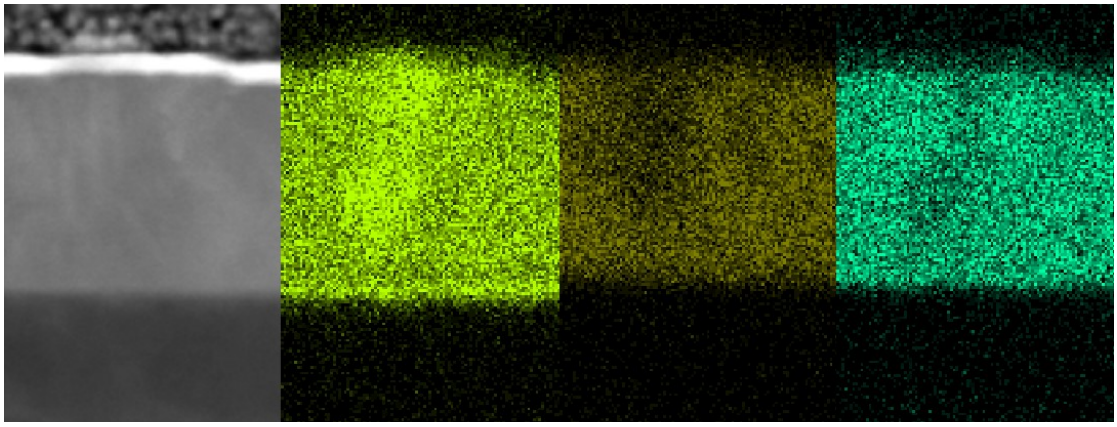

Figure 2.30: EDX map at the Co (bright yellow), Mn (brown) and Sb (cyan) edges. An inhomogeneous area can be seen in the middle.

2.3.4 TEM thickness determination

Electronic microscopy is a good technique to determine the thickness of a layer. With this, table 2.3 can be completed and values from each technique are now summarized in table 2.4. Experimental values determined by XRR and TEM are very close to values determined by quartz micro-balances except for Co_2MnSb. Small differences can be explained by (i) experimental uncertainties from each set-up (mostly quartz micro-balances, around 5%) and (ii) TEM is a local probe whereas XRR is global. For every compound, a very good control of the thickness during the growth process can be confirmed, justifying a sticking coefficient of 1 considered for the quartz micro-balance.

	τ_{quartz} (nm)	τ_{XRR} (nm)	τ_{TEM} (nm)	Main phase
Co_2MnAl	17.2	17.73	17.5	B2
Co_2MnSi	17	17.26	17.05	$L2_1$
Co_2MnGa	20.6	21.22	21.08	$L2_1$
Co_2MnGe	21	22.52	22.12	$L2_1$
Co_2MnSn	24.9	24.85	24.41	X
Co_2MnSb	24.8	32.61	31.45	-

Table 2.4: Thicknesses from quartz micro-balance calibration, XRR and TEM.

For Co_2MnSb, such a difference in thickness indicates indeed that it does not crystallize the same way than the rest of the series and explains the difference of behavior in XRD and TEM. In this peculiar compound, the sticking coefficient value of 1 used on the quartz micro-balance may be wrong. Indeed, Sb atoms are evaporated as Sb_2 and Sb_4 molecules. They may not be dissociated in atomic Sb at the surface of the quartz and hence will not be adsorbed on its surface. Thus, the flux measured by the quartz is smaller than the real Sb flux. On the contrary, Sb_n molecules can dissociate in the presence of Mn and Co atoms at the surface of the substrate and will adsorb in this case. This scenario could explain the difference in thickness and also in structure occurring in our films due to the wrong stoichiometry.

2.4 Magnetic properties

We have seen in chapter 1 that the values of magnetic moment in Heusler compounds were important. In particular, it must follow the Slater-Pauling curve to be HMM. The static magnetic properties of the Co_2MnZ series were analyzed using two different methods. In a first step, the macroscopic magnetic properties of each layer were measured. Then, atomic magnetic moments values and magnetic coupling between elements were determined by X-ray magnetic circular dichroism.

2.4.1 Macroscopic measurements and in-plane anisotropy

The magnetic moments of the Heusler layers were measured using a Physical Properties Measurement System - Vibrating Sample Magnetometer (PPMS-VSM) provided by Quantum Design. It has a sensitivity $< 10^{-9}$ A.m^2 (10^{-6} emu) when operating in vibrating measurement mode. PPMS-VSM measurements are not the best to extract the value of the magnetization for each alloy, at least in this configuration for different reasons. First of all, MgO substrates are diamagnetic which implies that the curves must be corrected by a slope equal to the diamagnetic susceptibility $\chi_{dia} = 2.10^{-5}$ [89]. Then, it is well known

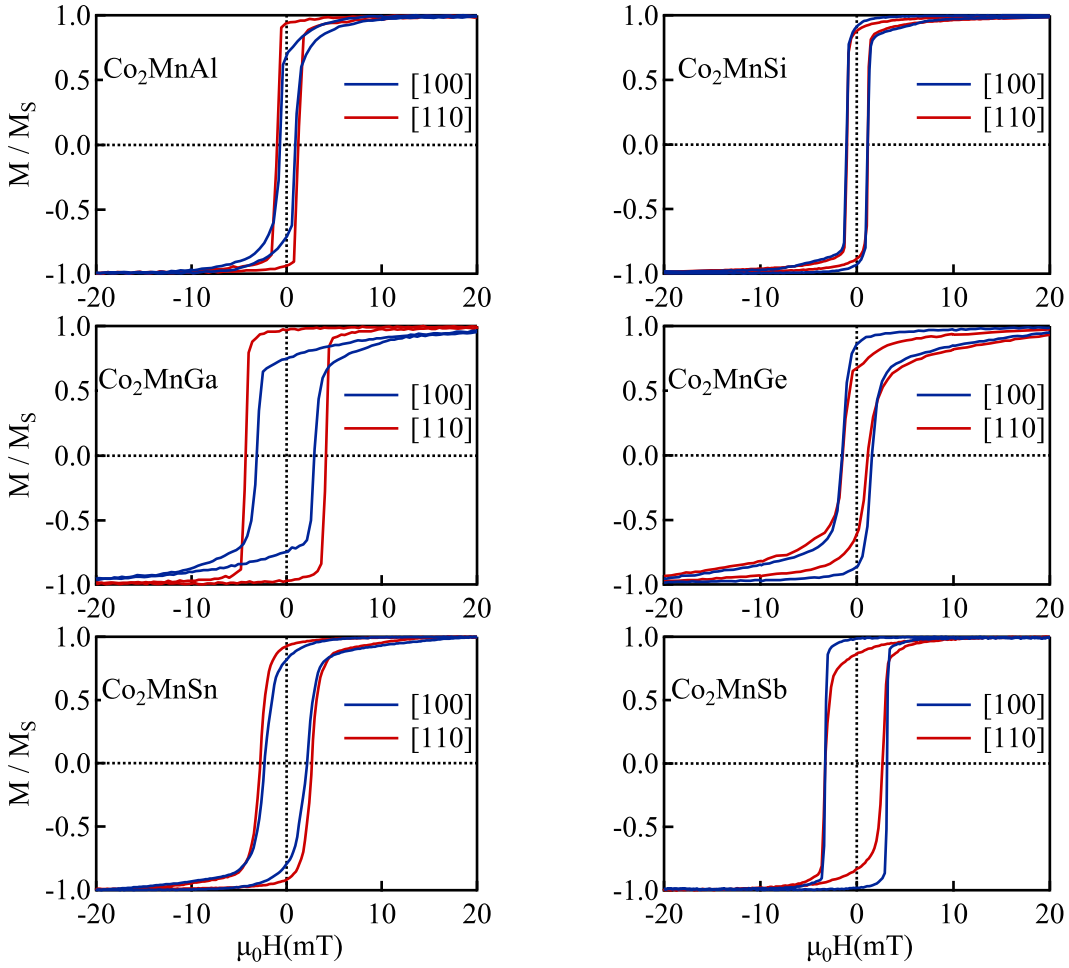

Figure 2.31: PPMS measurements of CMZ alloys.

that MgO substrates present a weak ferromagnetic signal due to impurities from the fabrication process [89]. Moreover, the sample must be cut into pieces to fit in the magnetometer. The magnetic moment

measured is divided by the magnetic volume to obtain the magnetization. The thicknesses, as shown in the previous section, are well controlled but this is not the case of the area of each piece and a small deviation strongly impacts on the resulting magnetization value. Since all the moments are directly measured by X-ray magnetic circular dichroism as described in the next section, and by ferromagnetic resonance as described in the next chapter, we defer the discussion of this point.

Figure 2.31 shows hysteresis loops for each Co_2MnZ alloy with a measurement along the 2 main crystalline axis in plane: [100] and [110]. The magnetic moments plotted on figure 2.31 are normalized by the saturation magnetic moment for a more suitable comparison between every graph. As reported by previous work on different epitaxial Co_2MnZ Heusler alloys [90–92], they all have a cubic type magneto-crystalline anisotropy with a four-fold symmetry (nonetheless, a two-fold anisotropy can be induced by strain [90] which is not the case here). The in-plane magneto-crystalline anisotropy was found to be very small except for Co_2MnGa (so small that for one given compound, the measurements along the two different axis exhibit almost the same curve). An easy axis along [100] is found for Co_2MnZ with Z=Si, Ge, Sb and along [110] for Z=Al, Ga, Sn.

Co_2MnGa is a special case. Its in-plane anisotropy is qualitatively larger than the rest of the series, as reported by Pechan *et al.* [90]. It appears that the presence of Ga increases the coupling to the lattice field, with the emergence of a larger magneto-crystalline anisotropy compared to the other Co_2MnZ compounds. This peculiar behavior will be indeed verified (and shall be positive for applications) later in this work, in the part dedicated to the perpendicular magnetic anisotropy in Mn_3Ga-based super-lattices.

2.4.2 X-ray magnetic circular dichroism

X-ray Magnetic Circular Dichroism (XMCD) is a powerful tool to obtain element-resolved magnetic moments (*i. e.* the magnetic moment carried by each atom in the cell). A dichroism experiment consists in measuring an absorption edge, for left and right circular polarization of light. For transition metals, electronic transitions of interest are the $L_{2,3}$, respectively from $2p^{\frac{1}{2}}$ and $2p^{\frac{3}{2}}$ localized states to the valence d band. The difference of both absorption spectra is called the dichroic signal. Its origin involves two important aspects of the light-matter interaction. The first one is the selection rules of the dipolar electric Hamiltonian that can be tuned according to the direction of the circular polarization of light (right or left). The other is inherent to non-localized magnetism, where the difference between spin up and down density of empty states in a magnetic material gives different weights to the transition probability (since the spin is conserved with the dipolar electric Hamiltonian). Because the full description of this technique can be found in different papers and books [93–95] and is not central for this work, only the important relations and key points for the case of transition metals are given here.

DEIMOS beamline and experimental features

The following experiments were performed on the DEIMOS beamline at SOLEIL synchrotron source. DEIMOS is dedicated to absorption experiments, and particularly magnetic dichroism. Measurements were done in the "CroMag" chamber under UHV conditions. The magnetic field is produced by a superconducting coil that can go to $\pm$ 7 T, in the direction of incoming X-rays. The X-ray beam is provided by an APPLE II HU52 undulator (helicoidal undulator) that allows an easy change of the light polarization direction and an energy range going from 350 to 2500 eV. A plane grating monochromator ensures the

selection in energy of the beam and is dynamically coupled to the undulator with a fast energy scanning ability. An accurate description of the beamline can be found in [96, 97].

All the layers measured by XMCD presented in this section were grown at the Institut Jean Lamour. They were 20 nm thick and capped with 2 nm of Ag (instead of usual Au due to the vicinity of some Au transitions with other elements). The absorption signal was measured in total electron yield by measuring the current going from the ground to the sample to neutralize all the electrons leaving the layer, due to the photoelectric effect. Moreover, all the following measurements were performed at 4.2 K for experimental simplicity[7]. Magnetic moments should not change much between 4.2 K and room temperature, because of high Curie temperatures in the Co_2MnZ series [60] (> 690 K).

Experimental results

In the following, $\sigma^-(B)$ stands for the absorption signal with a right circular polarization of light and a positive magnetic field value. By time reversal symmetry, this is equivalent to $\sigma^-(B) = \sigma^+(-B) = \sigma_N$ and so does $\sigma^+(B) = \sigma^-(-B) = \sigma_P$. This leads to four different types of measurement with a redundancy to eliminate any possible asymmetry in the detection. The resulting dichroic signal is written as $\sigma_N - \sigma_P$ after normalization at the absorption value before the L_3 edge. The dichroic signal is integrated over the energy range and its value after the L_3 (L_2) edge is noted p (q respectively). The total absorption signal, without magnetic asymmetry is taken as $\sigma_0 = \frac{\sigma_N+\sigma_P}{2}$ (previously corrected from an arctangent background weighted by the branching ratio of $L_{2,3}$ edges: 2 times more electron on $2p^{\frac{3}{2}}$ than $2p^{\frac{1}{2}}$). Its integration is directly proportional to the number of absorbing atoms and is noted r.

Figure 2.32 shows how the p, q and r values are extracted from XMCD experimental data. Those values can be directly linked to the atomic spin and orbital moments, and thus to the magnetic moments of each elements, by applying the sum rules that leads to equations 2.9 [75]. In the following equation, the intra-atomic magnetic dipole operator $\langle T_z \rangle$ is assumed to be small enough to be negligible in crystals with a cubic symmetry [98, 99],

$$\begin{aligned} \langle L_z \rangle &= -\frac{n_h}{P\cos(\theta)}\frac{2q}{3r}, \qquad \langle S_z \rangle = -\frac{n_h}{P\cos(\theta)}\frac{3p-2q}{2r}, \\ \langle M \rangle &= \langle L_z \rangle + 2\langle S_z \rangle, \end{aligned} \tag{2.9}$$

where n_h is the number of holes in d bands, P the polarization rate of the incoming X-ray beam, θ the angle between the magnetization and the X-ray beam. On the DEIMOS beamline, P is higher than 99.6 % and the magnetization was saturated along the X-ray beam (out of the plane of the film) thanks to a 4 T magnetic field so that $P\cos(\theta) \simeq 1$, even at 4 K. For transition metals like Fe, Co and Ni, values given by XMCD experiments using equations 2.9 are reliable and in good agreement with other characterization methods [100]. For Mn and Cr though, the spin moment values have to be corrected by a coefficient due to the too small spin-orbit coupling which leads to an overlap of the $L_{2,3}$ edges and makes the determination of p difficult. From the work of Dürr *et al.* [101], this correction factor is calculated to be $f = 1.5$ on the spin magnetic moment of Mn atoms. Concerning the number of holes for Mn and Co, we take values

[7] in the UHV chamber CroMag, the manipulator is cooled down along with the superconducting coil using liquid He. Therefore, it is simpler to let the manipulator and thus the sample at this temperature instead of heating it up.

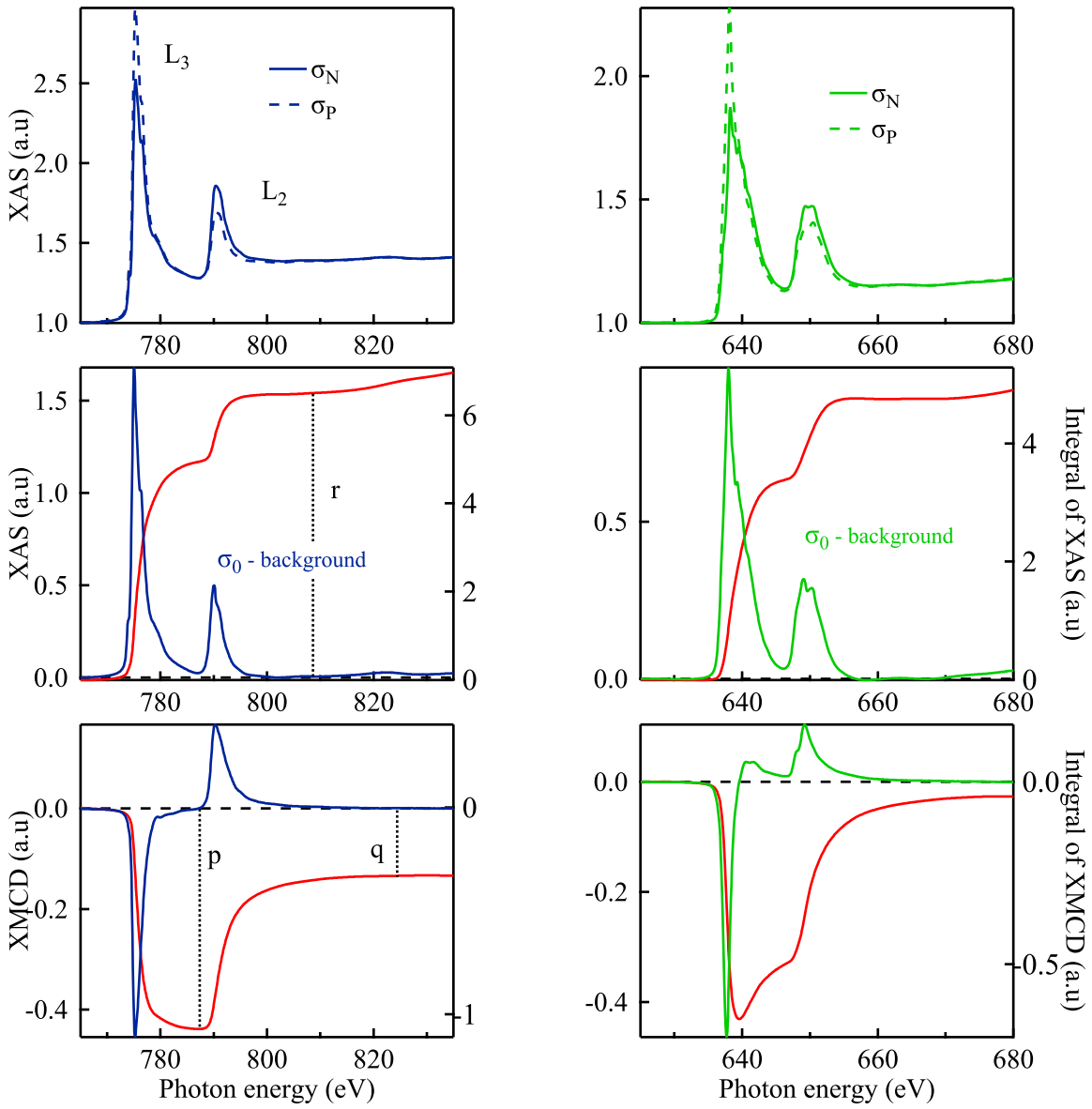

Figure 2.32: Absorption and dichroism signal of Co_2MnGa Heusler compound at the L_2 and L_3 edges of Co on the left (blue) and Mn the right (green).

from calculations because no experimental values are available. Hence a value of $n_h = 5$ is taken for Mn and $n_h = 2.54$ for Co [91].

An example of data treatment process is shown in figure 2.32 for Co_2MnGa. On top, the X-ray Absorption Spectroscopy (XAS) signal with the two polarization of incoming photons. In the middle of the same figure, the background-corrected σ_0 XAS signal is plotted along with the corresponding integration that allows to extract the r value. Finally, at the bottom, the dichroic signal and its integration are also plotted. The blue curves (left part) represent absorption and dichroic spectra of Co and the green curves (right part) are for Mn. One can see from the XMCD curves that they are ferromagnetically coupled to each other (same dichroic signal variation: negative at L_3 and positive at L_2), as expected from calculations and previous experiments on Co_2MnZ alloys. Moreover, a multiplets structure is observed for Mn, as reported in the literature [98]. It reflects the strong hybridization of Mn atoms in its environment. Also

for Mn spectra, it is visible here that L_2 and L_3 edges are overlapping a little that makes the determination of p difficult.

Concerning Z elements, *ab initio* calculations predict a very small moments antiferromagnetically coupled with Co and Mn [12, 91]. Nonetheless, due to the energy range available on the beamline, only $L_{2,3}$ edges of Z=Ga and Ge were reachable (Al and Si L edges < 100 eV, Sn L edges > 3.9 keV and M edges are too small in cross section). No analysis could be performed on those measurements because of complex absorption spectra, as shown in figure 2.33 for Ga. But, in figure 2.33, the dichroic signal of Ga is reversed compared to the one of Mn and Co of figure 2.32, confirming the antiferromagnetic coupling of Ga with Co and Mn. Because Co_2MnSi and Co_2MnGe have been studied by XMCD extensively [91, 98, 102, 103], and because measurements on all Co_2MnZ layers are similar, only data from Co_2MnGa compound are presented.

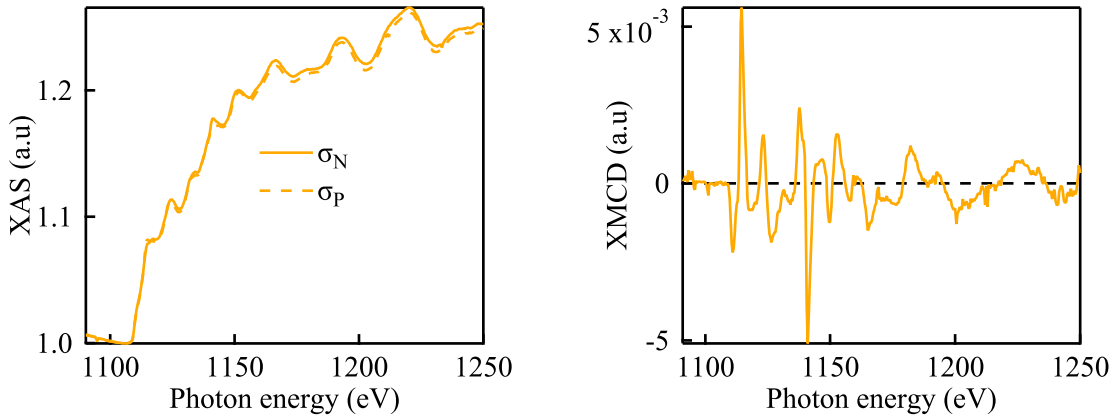

Figure 2.33: Absorption and dichroism signal at the L_2 and L_3 edges of Ga. The XMCD signal is really small and reversed compared to Co and Mn, in qualitative agreement with theory.

Similar XMCD measurements and data treatment were performed for the Co_2MnZ series. The obtained magnetic moments are reported in table 2.5.

	Co (μ_B)		Mn (μ_B)		$\langle M_t \rangle$
	m_{orb}	m_{spin}	m_{orb}	m_{spin}	(μ_B / f.u)
Co_2MnAl	0.09	0.92	0.03	1.78	3.83
Co_2MnSi	0.09	1.0	0.04	2.87	5.09
Co_2MnGa	0.09	0.98	0.03	2.94	5.11
Co_2MnGe	0.07	0.89	0.01	2.55	4.48
Co_2MnSn	0.08	0.88	0.01	2.52	4.45

Table 2.5: Element resolved spin and orbital magnetic moments for the Co_2MnZ series obtained by XMCD at 4.2 K. The last column is the total magnetic moment per formula unit (/f.u).

Out of plane hysteresis loops

By setting the beamline energy at the maximum of XMCD signal for any magnetic element, it is possible to obtain hysteresis loops by sweeping the static magnetic field. Indeed, for a given photon polarization, the dichroism signal changes of sign when the magnetization is reversed. For experimental reason, only out of plane hysteresis loops were measured at the L_3 edge of Co since it is the main chemical element in the Heusler structure. One has to note that similar loops were obtained at the Mn edge (but with more noise) indicating a unique ferromagnetic behavior of the whole film.

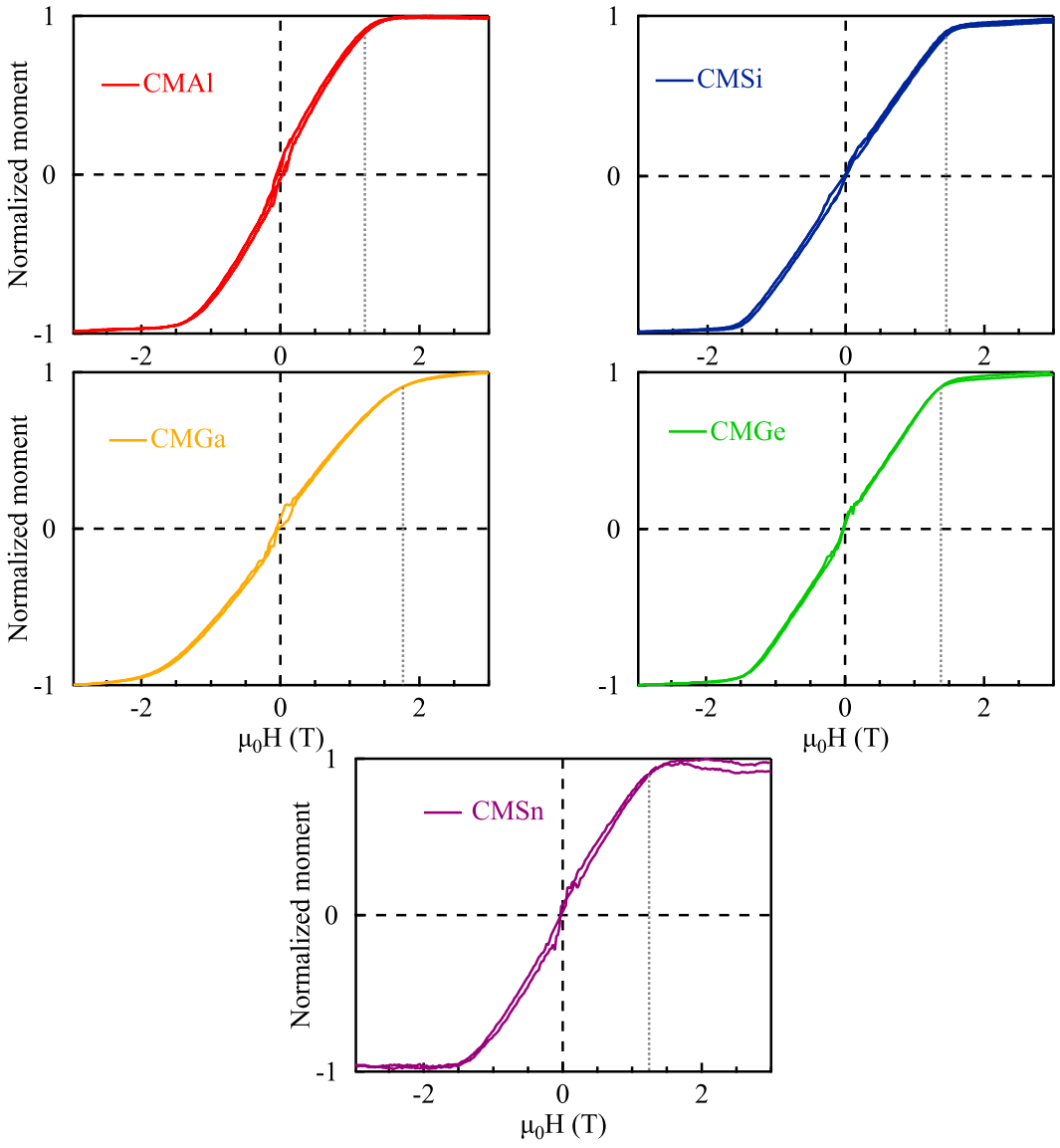

Figure 2.34: Out of plane hysteresis loops of Co_2MnZ series.

The hysteresis loops measured on the Co_2MnZ series are shown in figure 2.34. Unsurprisingly, the out of plane direction is clearly a hard axis for every Co_2MnZ compound. The field for which the magnetization reaches 0.9 of the saturation is represented by the gray dashed lines. The saturation field is between 1.4 and 1.6 T for every compound except for Co_2MnGa where the magnetization needs almost 2 T of external field to be saturated. It can be explained by magnetic anisotropy that makes the [110]

direction an easy axis (and equivalent ones by cubic symmetry) as shown in figure 2.31. Thus, the out of plane direction is not one of those easy axis (growth along [001]). The magnetization has to overcome the magneto-crystalline anisotropy in addition to the demagnetizing field to be out of the plane. This is of course the case for all compounds with a [110] easy axis (like Co_2MnAl for instance) but it has been shown that the magneto-crystalline anisotropy was particularly strong in Co_2MnGa compound. The larger anisotropy field in Co_2MnGa compared to the other compounds is confirmed once again.

2.5 Summary and discussion

Extensive experimental investigations were carried out for Co_2MnZ Heusler compounds. In addition to summarize this chapter, a comparison with different works is presented. In particular, the comparison with *ab initio* calculations is interesting to see if the basic properties like lattice constants and chemical ordering match with predictions. This is a prerequisite for the forthcoming work regarding the electronic and magnetization dynamics properties.

All the lattice constants obtained in the present work are summarized in table 2.6 and compared with other experimental works on thin films, bulk samples and theoretical calculations. Small differences with

	Present work	Thin films	Bulk [60]	Calculations [73]
Co_2MnAl	5.76	5.78 [104]	5.76	5.7
Co_2MnSi	5.65	5.65 [10]	5.65	5.63
Co_2MnGa	5.77	5.79 [105]	5.77	5.73
Co_2MnGe	5.76	5.77 [106]	5.74	5.74
Co_2MnSn	6.00	6.00 [107]	6.00	5.98
Co_2MnSb	5.93	-	5.93	6.01

Table 2.6: Lattice constants from the present work and other experimental and theoretical values.

other thin films can be explained by the thickness dependence due to strains, or by differences in stoichiometry. In the present work, all layers are about 20 nm thick and grown on top of MgO substrates which is not always the case in the cited references (sometimes grown on GaAs substrates). The agreement with bulk values is extremely good. Theoretical values tend to be underestimated but are also in good agreement. The largest difference between experiments and theory is obtained for Co_2MnSb. This can be explained since the calculations assume a $L2_1$ structure whereas we are sure that this is not the structure in our films.

The possibility to have some chemical disorder in Heusler compounds has been known for a long time. However, very few experimental and/or theoretical studies address this point. In the present work, chemical phases for the Co_2MnZ compounds are found to be:

(i) $L2_1$ for Co_2MnSi, Co_2MnGa, Co_2MnGe;

(ii) B2 for Co_2MnAl;

(iii) Inverse X for Co_2MnSn;

(iv) Unknown for Co_2MnSb but surely different from the $L2_1$ Heusler type structure.

In the work of P. J. Webster [60], neutron diffraction on bulk samples was used to resolve the chemical ordering in the same series of alloys. They obtained the same order than in the present work, with a perfectly ordered phase for every compounds, except Co_2MnAl for which a B2 phase takes place. The reason for which Mn and Al atoms are mixed together is unknown. Nonetheless, it seems that it is proper to Heusler alloys containing Al because Co_2MnAl and Co_2FeAl are B2 whereas Co_2MnSi and Co_2FeSi are $L2_1$. It gives a hint on the chemical nature of B2 domains in figure 2.24, which might be made of Co_2MnAl more than Co_2MnSi. Moreover, they did not detect an inverse phase in Co_2MnSn compound like in the present study. Consequently, Co_2MnSn is $L2_1$ in bulk but the inverse structure is stabilized in our thin films. We have no explanation on this difference of behavior between thin films and bulk samples. For Co_2MnSb, we have seen that large errors are made on the thickness. Additionally, several chemical and structural phases were observed by TEM and XRD. All of this can be explained by a wrong sticking coefficient value on the quartz during the fluxes calibration. The real sticking coefficient value could be determined and then it would be very interesting to perform the growth of Co_2MnSb with the right stoichiometry, to see if it crystallizes in the Heusler type structure. It was not done in this study due to a lack of time.

Only one theoretical study was found about the ground state energy depending on the chemical ordering in a Heusler structure [12]. It was done for Co_2MnSi and they showed that $L2_1$ was the more stable phase. Additionally, we have seen in chapter 1 that the interesting properties should be conserved between $L2_1$ and B2 phases (*e. g.* spin gap is conserved) [12, 26, 33]. We thus hope that the B2 disorder in Co_2MnAl will not strongly affect its behavior.

As discussed in the introduction chapter, according to the work of I. Galanakis *et al.* [8], Heusler compounds must follow the Slater-Pauling curve concerning their magnetic moment, in order to be HMM. For Co_2MnZ alloys, the Slater-Pauling curve corresponds to a moment of $M_t = Z_t - 24\ \mu_B$ per formula unit, with Z_t standing for the number of valence electrons: 5 μ_B/f.u for Z=Si, Ge and Sn and 4 μ_B/f.u for Z=Al and Ga. Magnetic moments obtained by XMCD are summarized in the following table 2.7 along with moments obtained in different works on bulk samples and calculations.

	Present work (4.2 K)	Bulk (4.2 K) [60]	Calculations (0 K)[8]
Co_2MnAl	3.83	4.01	3.97
Co_2MnSi	5.09	5.07	4.94
Co_2MnGa	5.11	4.05	4.06
Co_2MnGe	4.48	5.11	4.94
Co_2MnSn	4.45	5.08	4.98

Table 2.7: Magnetic moments extracted by XMCD in this study with other values from bulk samples and calculations.

Magnetic moments of the present work are within 10 % of error with the theoretical calculations (Slater-Pauling curve) and bulk samples values. Except for Co_2MnGa, where there is 1 supplementary

μ_B in the structure. It is surprising to find such a high moment for Co_2MnGa because the usual trend in thin films is the opposite, with fewer μ_B [63, 90]. However, thanks to the structural study of the present work, the high epitaxial quality and chemical order of the present Co_2MGa layers are confirmed. The accordance of magnetic moments with theory in the series are an additional proof that those compounds are ordered with the good stoichiometry. Indeed, Mn atoms carry a high magnetic moment ($\sim 3\ \mu_B$) only if they are located on the good crystallographic sites [72].

Finally, out-of-plane and in-plane hysteresis loops reveal small magneto-crystalline anisotropies for the Co_2MnZ compounds. The [100] and [110] directions of some compounds are even almost isotropic. Nevertheless, one candidate does not follow this trend: Co_2MnGa. The anisotropy field is found larger in this compound compared to the rest of the Co_2MnZ series. This confirms theoretical calculations on highly anisotropic Heusler compound containing Ga [108]. In addition, the fact that Co_2MnGa compound has a higher magneto-crystalline anisotropy than other Co_2MnZ compounds and does not match the Slater-Pauling curve might not be a coincidence.

To summarize this chapter, Co_2MnZ with Z=Al, Si, Ga, Ge, Sn, Sb Heusler alloys have been grown with the MBE technique. The high crystalline quality of all compounds has been demonstrated by several methods of diffraction and microscopy. Besides, the value of magnetic moments obtained by XMCD are in good agreement with theory and support chemically ordered films. However, it has rapidly been observed that there are a number of issues with Co_2MnSb. The growth is not well controlled, likely due to a wrong sticking coefficient value when calibrating the fluxes. Hysteresis loops have been measured from magnetometry and XMCD and show a weak anisotropy field in the Co_2MnZ series except for Co_2MnGa.

This complete set of characterizations was necessary before going further: Heusler alloys provide an excellent playground to explore the interplay between the spin polarization and the magnetic damping, which is the subject of the next chapter.

Chapter 3

Interplay between the electronic structure and the magnetic damping

A number of theoretical calculations have been performed on Co_2MnZ (Z=Al, Si, Ga, Ge, Sn and Sb) Heusler compounds [7, 28, 58, 66, 67]. In all of these compounds, a spin gap in the minority spin density of state is predicted[1]. According to *ab initio* calculations, the width of the spin gap and the location of the Fermi energy E_F in the band structure are tuned depending on the Z element. Nonetheless, few experimental studies aim to investigate on the electronic structure of those compounds. Indeed, Co_2MnSi and Co_2MnAl have been studied in those references [10, 78], on the same set-up than the present study. A spin gap was observed on Co_2MnSi and a spin polarization of 0.6 was observed for Co_2MnAl. Co_2MnGa single crystal was studied by photo-emission spectroscopy by Hahn *et al.* [70], using spin dependent diffraction on a W(001) crystal as a spin detector. It was done using a He lamp, with $\hbar\omega = 21.2$ eV and no possibility to tune the photon energy. Furthermore, the quality of the epitaxial layer appears to be slightly lower than in the present work since they obtained $L2_1$ order only after annealing and not on the as-deposited layer. They also had oxidation problem on their layer, which is not the case in this work (see figure 2.10). They obtained a spin polarization of 0.34 at E_F for this compound. Finally, no experimental studies of the density of state were found for Co_2MnGe, Co_2MnSn and Co_2MnSb.

In this chapter, we provide an experimental investigation of the electronic structure by using spin resolved photo-emission spectroscopy on all the Co_2MnZ epitaxial layers characterized in the previous chapter. We also study the two quaternary $Co_2MnZ_x^{IV}Z_{1-x}^{III}$ series for two reasons. The first is that they behave as solid solutions which means that a continuous change in the electronic structure should be observed. The second is that a chemical transition is observed for one of the two series and, it is therefore interesting to see how it affects the electronic structure. Finally, polycrystals are elaborated and measured because they are very interesting for industrial applications and also because in this case, the whole Brillouin zone is probed by photo-emission spectroscopy without ambiguity.

As this series provide a various playground in terms of electronic structure, we are interested in magnetic damping measurements on the same layers which are presented in the second part of this chapter. Finally, we demonstrate that the magnetic damping measured by ferromagnetic resonance is indeed linked to the underlying electronic structure, particularly in the case of HMM compounds.

[1] Except Co_2MnGa and Co_2MnAl. There is a small amount of density of state in the minority spin channel that gives a zone of strong spin polarization called a "pseudo gap".

3.1 Spin Resolved photo-emission Spectroscopy

In this part, electronic properties and more precisely the spin polarization of the Co_2MnZ series is investigated. In the literature, the spin polarization is extracted using the point contact Andreev reflection method [109–111] which consists of measuring the electrical transport at the interface between a normal and a superconducting material [112]. In such studies, the Spin Polarization (SP) can be extracted from conductance curves obtained at temperatures below the superconducting critical temperature. This is consequently not a direct measurement of the SP. On the contrary, Spin Resolved-photo-emission Spectroscopy (SR-PES) is a direct method where the polarization is measured without any approximations except the limitation due to the sensitivity of the instrumental set-up. The evidence of a minority spin gap in Co_2MnSi in previous works [10, 29] by photo-emission spectroscopy has highly motivated the use of SR-PES as the best way to measure spin polarizations[2].

In a first step, general considerations about photo-emission spectroscopy and spin resolution will be approached. Then, the Cassiopée beamline and experimental details are presented and eventually, spin polarization results on Co_2MnZ Heusler alloys will be discussed.

3.1.1 The three-step model

The photo-emission process is one of the most important consequences of the interaction between light and matter. Its explanation has taken a lot of effort and its understanding is still far from being complete, mainly due to the many-body problem. It begins with the following relation 3.1 published by Einstein, ensuring the energy conservation between an electron, in a solid, absorbing a photon:

$$E_{kin} - E_B + \Phi = \hbar\omega, \tag{3.1}$$

where E_{kin} is the kinetic energy of the photo-electron, E_B the binding energy of the electron in the solid, $\hbar\omega$ the photon energy and Φ the work function of the solid. Equation 3.1 represents the energy conservation of the entire process, from absorption of the photon to the electron expelled from the material. This process is easily understood with the well known "three-step model" which decomposes the complex photo-emission process into three steps [115]. The steps are: (i) an optical excitation from an initial Bloch state $|\psi_k^i\rangle$ to a final Bloch state $|\psi_k^f\rangle$ above the Fermi energy; (ii) the transport of the photo-electron to the surface; (iii) the escape of the photo-electron in the vacuum, described by a plane wave. The momentum transferred by a photon is considered to be very small compared to the width of the Brillouin zone, so optical transitions are characterized by $k_f = k_i$ (vertical transitions) in a reduced Brillouin zone[3]. A more complex and realistic description of the process is given by the one-step model where electronic states are a superposition of the initial Bloch wave, the final plane wave and a damped wave in the material traducing the finite mean free path of the electron within the material.

Optical excitation

As represented in figure 3.1, the relation 3.1 can be re-written in a more suitable form to work with in terms of electronic transitions in a solid. With $E_B = E_i$ and $E_f = \Phi + E_{kin}$, and by considering vertical transitions, the equation of energy conservation can be expressed as:

[2]Polarized positron-annihilation can also be used to measure the spin polarization [113, 114] but seems to require complex experimental and theoretical skills

[3]Rigorously, they are defined as $k_f = k_i + G$ in an extended Brillouin zone scheme, with G a reciprocal lattice vector.

$$E_f(\mathbf{k}) - E_i(\mathbf{k}) = \hbar\omega, \tag{3.2}$$

with $E_f(\mathbf{k})$ and $E_i(\mathbf{k})$ respectively representing the energy of the final and initial Bloch states of the electron, respectively. This equation describes the resonant nature of electronic transitions.

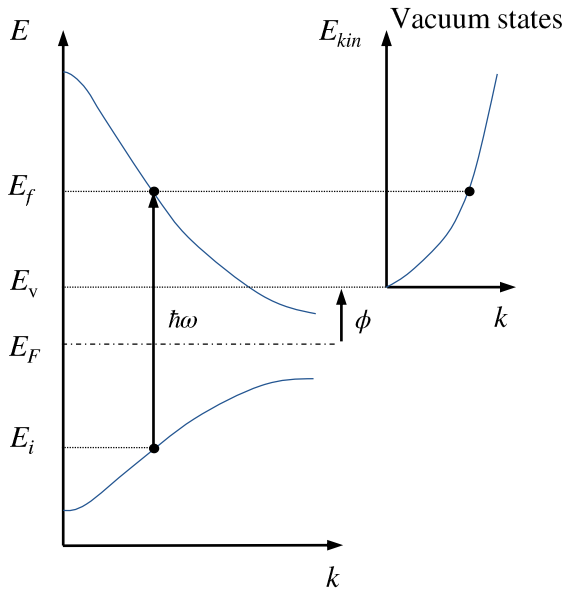

Figure 3.1: Sketch of the photo-emission process, with E_v and E_F representing the vacuum energy level and the Fermi energy. From [116].

In the photo-emission process, the first step is the electronic transition when a photon is absorbed. It is described in quantum mechanics by the following Hamiltonian:

$$H = \frac{[\mathbf{p} - q\mathbf{A}(\mathbf{r},t)]^2}{2m} + q\varphi(\mathbf{r},t) + V = H_0 + H_{int}, \tag{3.3}$$

where $\mathbf{A}(\mathbf{r},t)$ and $\varphi(\mathbf{r},t)$ are the potentials associated to electromagnetic field of the radiation, with the minimal coupling between the electromagnetic field and $\mathbf{p}$, the momentum of the electron. V is the potential seen by the electron in the solid where electron-electron interactions are averaged. By using the commutation relation between $\mathbf{A}(\mathbf{r},t)$ and $\mathbf{p}$, and by using the Coulomb gauge ($\nabla.\mathbf{A}(\mathbf{r},t) = 0$ and $\varphi(\mathbf{r},t) = 0$), the interaction Hamiltonian can be expressed as:

$$H_{int} = \frac{1}{2m}\big[-2q\mathbf{A}(\mathbf{r},t).\mathbf{p} + q^2|\mathbf{A}(\mathbf{r},t)|^2\big] \simeq -\frac{q}{m}\mathbf{A}(\mathbf{r},t).\mathbf{p} \tag{3.4}$$

It should be noted that the term in $|\mathbf{A}(\mathbf{r},t)|^2$ is negligible with conventional sources [117], even with synchrotrons. From this point, the dipolar electric approximation is considered: the spatial variation of the electric field (thus $\mathbf{A}(\mathbf{r},t)$) to be negligible compared to the characteristic length of an electronic state. This assumption is completely justified with wavelengths used for valence band photo-emission and it leads to $\mathbf{A}(\mathbf{r},t) = \mathbf{A}_0(t)e^{i\mathbf{k}.\mathbf{r}} = \mathbf{A}_0(t)(1 + i\mathbf{k}.\mathbf{r} + ...) = \mathbf{A}(t)$. Matrix elements, which couple the initial and final Bloch states, and the Fermi's golden rule on the transition rate can be written more easily with such

an approximation:

$$\begin{aligned} \left|\langle \psi_k^f | H_{int} | \psi_k^i \rangle\right|^2 &= \frac{q^2}{m^2} \left|\langle \psi_k^f | \mathbf{p}.\mathbf{A} | \psi_k^i \rangle\right|^2 \\ \omega_{fi} &= \frac{2\pi q^2}{\hbar m^2} \left|\langle \psi_k^f | \mathbf{p}.\mathbf{A} | \psi_k^i \rangle\right|^2 \delta(E_f(\mathbf{k}) - E_i(\mathbf{k}) - \hbar\omega) \end{aligned} \tag{3.5}$$

At this point, it is important to note that $E_f(\mathbf{k})$ as well as the final state $|\psi_k^f\rangle$ depend on the photon energy used for the excitation. Does such a final state with this special $\mathbf{k}$ exist to satisfy the $\delta(E_f(\mathbf{k}) - E_i(\mathbf{k}) - \hbar\omega)$ condition ? In the present work, a photon energy of several tens of eV is used. At those energies, it is assumed that an excited electron will always find a $E_f(\mathbf{k})$-matching final Bloch state. Therefore, photo-emission experiments allow to probe the occupied band structure of a material.

In the case of an electron in a central potential (Hydrogen atom) the dipolar electric Hamiltonian gives rise to specific selection rule regarding the initial and final eigenstates states $|l, m\rangle$: $\Delta l = \pm 1$, $\Delta m = 0, \pm 1$ and $\Delta s = 0$. It is no longer the case in a periodic potential (*i. e.* crystals) where the symmetry of the lattice and spin-orbit coupling are changing the quantum indices that characterize the new eigenstates. Hopefully, the selection rule concerning the spin is unchanged and allows to do SR-PES (the dipolar interaction does not affect the spin number). But, an additional contribution based on symmetry arguments makes the transition even more selective: the polarization of the incoming radiation. This part will be discussed later.

Transport to the surface

In the 3-step model, after the optical excitation to an empty Bloch state, the electron has to move to the surface of the solid. On its way, the photo-electron can be scattered by inelastic processes and will thus loose its initial energy and momentum. They are called secondary electrons. If those scattered electrons have still enough energy to go out of the solid, this process adds a continuous background to a photo-emission spectrum. Additionally this finite lifetime of the photo-electron in the solid is partially responsible for the broadening of electronic states which are not Dirac deltas in a real experiment.

The finite lifetime of photo-electrons in solids gives rise to another important mechanism: the uncertainty on the perpendicular component of $\mathbf{k}$. Indeed, the inelastic mean free path of photo-electrons limits the depth probed by a photo-emission experiments. In other words, photo-electrons collected in an analyzer all come from a distance to the surface nearly equivalent or smaller to the mean free path. It also means that the electronic transitions that sent an electron from $|\psi_k^i\rangle$ to $|\psi_k^f\rangle$ are made within this depth, therefore the crystal can not be considered infinite in the z direction. The Bloch states are strongly perturbed by the symmetry breaking near the surface and $k_\perp$, which is conserved during electronic transitions, is subject to an uncertainty $\Delta k_\perp$ as large as the mean free path λ is small:

$$\begin{aligned} \Delta p \Delta z &\geq \frac{\hbar}{2} \\ \Delta k_\perp &\sim \frac{1}{\lambda} \end{aligned} \tag{3.6}$$

The consequences of this are shown schematically in figure 3.2. For a photon energy of 30 eV (typical values in the present work), $\lambda \sim 3$ to 4 monolayers according to the universal curve of the inelastic mean

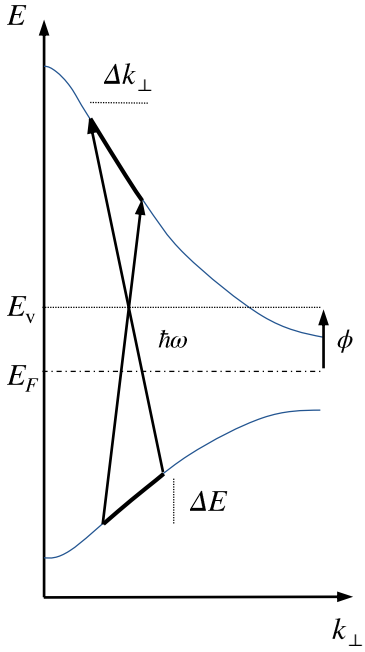

Figure 3.2: Representation of the uncertainty on $k_\perp$ and therefore on E. From [118].

free path of electrons in matter. For Co_2MnZ Heusler compounds, it results in an uncertainty $\Delta k_\perp \sim 0.17$ $Å^{-1}$.

Escape from the solid

The last step is the electron escaping the solid or more precisely, the transmission of the photo-electron from the solid to the vacuum through the surface. As depicted in the end of the previous paragraph, the surface breaks the symmetry of translation and thus the perpendicular component of the wave vector is not conserved between the solid and the vacuum, leading to $k_{int\perp} \neq k_{ext\perp}$. The translational invariance in the plane of the surface is conserved and so is the parallel component of the wave vector: $\mathbf{k}_{int\parallel} = \mathbf{k}_{ext\parallel}$. Figure 3.3 represents the transformation of the wave vector when it goes through the surface. The different relations that link the wave vector outside and inside the crystal can be determined. From figure 3.3, it is easily deduced that $\mathbf{k}_{int\parallel} = \mathbf{k}_{ext\parallel} = \mathbf{k}_{ext}\sin(\theta)$. Furthermore, in the vacuum, the dispersion relation of a free electron is given by:

$$E_{kin} = \frac{\hbar^2 k_{ext}^2}{2m}, \tag{3.7}$$

which leads to :

$$\mathbf{k}_{int\parallel} = \mathbf{k}_{ext\parallel} = \sqrt{\frac{2m}{\hbar^2}E_{kin}}\sin(\theta) \tag{3.8}$$

The relation 3.8 is the main expression allowing the band structure to be measured in Angle Resolved Photo-Emission Spectroscopy (ARPES) technique because it allows the dispersion relation of electronic states in the crystal to be determined. In the present work, no ARPES measurements were carried out but the relation is still important in SR-PES[4], as it will be explained further. Concerning the perpendicular component of the wave vector, a relation can be found by considering that the band of final states is

[4]In SR-PES, the analyzed electrons are integrated over a $\Delta k_\parallel$

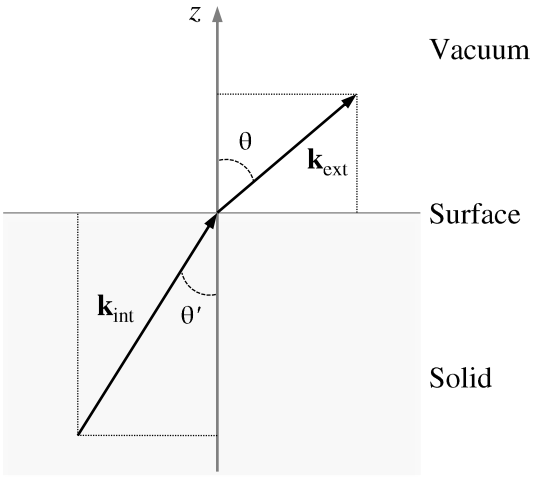

Figure 3.3: Geometrical relation between $\mathbf{k}_{int}$ and $\mathbf{k}_{ext}$.

parabolic like a quasi-free electron with the following dispersion relation:

$$E_f = \frac{\hbar^2 k_{int}^2}{2m} - U_0 + \phi, \tag{3.9}$$

U_0 is known as the inner potential. By replacing k_{int}^2 by $(k_{int\parallel}^2 + k_{int\perp}^2)$, and by writting $E_f = E_{kin} + \phi$, the following relation is obtained:

$$k_{int\perp} = \sqrt{\frac{2m}{\hbar^2} E_{kin} \cos^2(\theta) + U_0} \tag{3.10}$$

In summary, $\mathbf{k}_{int\parallel}$ can be precisely extracted from photo-emission spectroscopy. This is not the case for $\mathbf{k}_{int\perp}$ since the inner potential U_0 is undetermined. Nonetheless, U_0 can be estimated by calculations (around 12 eV for $3d$ metals [119]).

Surface states

The breaking in the translational symmetry in the perpendicular direction makes the surface a singular place to hold electronic states. Surface states are localized in the last atomic plane of the crystal and thus live exclusively at the surface. It means that the associated wave function is rapidly damped outside the surface, in the vacuum but also in the bulk of the crystal. Most of photo-emission studies on surface states deal with Tamm or Shockley states [116, 120, 121]. These states can arise from different considerations in the potential felt by Bloch waves near the surface and lies in the gap of the bulk band structure.

Surface states coupled with bulk states also exists and are known as interfacial resonant states. These states, located very close to the Fermi energy, appear to be a general characteristic of bcc (001) transition metals, observed in W, Ta, Fe and Cr and present an exchange splitting in the case of ferromagnetic metals [122].

Whatever the nature of the surface state, the fact that it is completely confined in one atomic plane implies that the indetermination on $k_\perp$ is quasi-infinite. In other words, a transition between an initial

surface state and a final Bloch state is always permitted, whatever the $k_\perp$ (*i. e.* whatever the excitation energy $\hbar\omega$). Therefore, in photo-emission spectra, such an electronic state should not scatter in $k_\perp$ because the initial surface state involved in the transition is flat due to the uncertainty on $k_\perp$[5]. It is generally a way to determine if a transition comes from surface states in a photo-emission experiment. Obviously, surface states vanish when a monolayer of another chemical element is adsorbed at the surface. It is also a way to determine if the transition involves a surface state.

3.1.2 Mott scattering for spin resolution

As demonstrated above with the three-step model, a photo-emission experiment allows one to extract the band structure of a material or the integrated density of state of the valence band. In order to resolve the density of state in spin, one has to discriminate electrons according to their spins (additionally with their energy and even $k_\parallel$). It is mainly achieved with two techniques: the spin-dependent diffraction of low energy electrons [124, 125], and by using Mott detection where electrons are scattered by a target due to the spin-orbit interaction [126, 127], generally Au or Th. The basic concepts of the Mott detection, used on the Cassiopée beamline at SOLEIL synchrotron source, will be introduced.

Spin-orbit interaction

In 1929, N. F. Mott calculated the fully relativistic case of an electron scattered by an atomic nucleus [128], using the Dirac equation. A relativistic electron in a central Coulomb potential feels an energy contribution due to the interaction between its own spin and the electric field generated by the nucleus[6]. This term U_{SO} is developed in equation 3.11. Consequently, the scattering of a relativistic electron by a nucleus is spin dependent and is the fundamental principle of the Mott detection. An accurate description of the relativistic scattering of an electron by a nuclei can be found in [128–130].

$$U_{SO} = -\frac{e}{2m^2c^2}\mathbf{s}\cdot(\mathbf{E}\times\mathbf{p}) = -\frac{e}{2m^2c^2}\mathbf{s}\cdot\left(-\frac{1}{e}\frac{dV}{dr}\frac{\mathbf{r}}{r}\times\mathbf{p}\right) = \frac{1}{2m^2c^2}\frac{1}{r}\frac{dV}{dr}(\mathbf{s}\cdot\mathbf{l}) \tag{3.11}$$

Spin and angular momentum scattering dependence

A schematic illustration of the spin-orbit dependence of the scattering by a nucleus is given in figure 3.4-left. The sign of the energy contribution depends on the relative orientation of the spin and angular momentum of the scattered electron.

By its relativistic nature and as demonstrated by relation 3.11, the U_{SO} term will be larger for high velocity electrons which explains why they have to be highly accelerated before being scattered by the target in a conventional experimental set-up[7]. Moreover, the interaction will gain in intensity as the electric potential generated by the nucleus is high, and translates the need of heavy atoms as efficient targets (like Au or Th) [131].

For a given scattering angle, the cross section of the interaction will also be spin dependent and the asymmetry (maximum in the difference between spin up and down cross sections) is maximal for an angle $\gamma = 120°$. Unfortunately, this is also the value for which the cross sections values are minimal [131]. The

[5] However, surface states scatter in $k_\parallel$. One can see the Shockley states of (111) oriented surface of noble metals in [123].
[6] In the frame of the electron, this time varying electric field gives rise to a magnetic field.
[7] 28 keV on the Cassiopée set-up which makes $\beta = \frac{v}{c} = 0.33$.

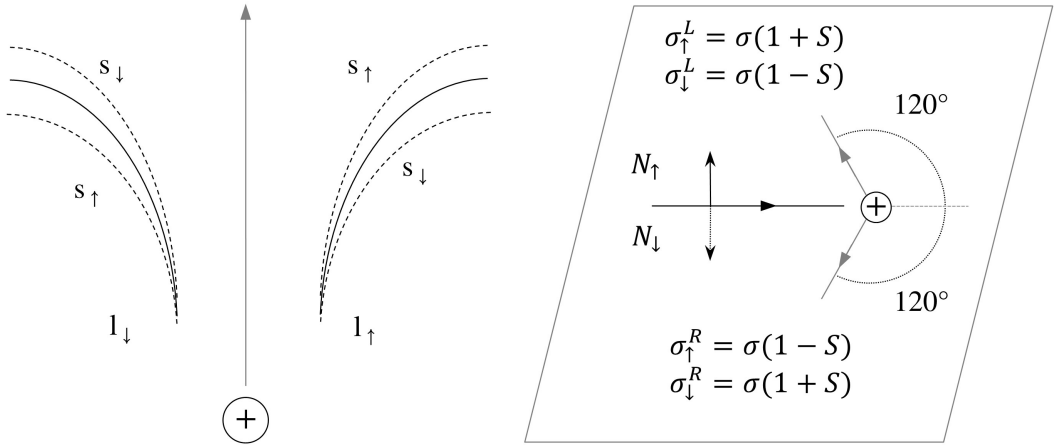

Figure 3.4: Left: effect of the spin-orbit interaction U_{SO} on a scattered electron (dash lines). Right: spin and angular momentum dependence in cross sections at the maximum of asymmetry $\gamma = 120°$.

cross section between spin up and spin down for a given orbital momentum can be written as follows:

$$\begin{aligned} \sigma_\uparrow &= \sigma(1+S) \\ \sigma_\downarrow &= \sigma(1-S) \end{aligned} \tag{3.12}$$

The situation is reversed for the other value of l as shown in the right panel of figure 3.4. S is the Sherman function that describes the asymmetry in the scattering cross section between up and down spins. The figure 3.4-right represents how each electron is scattered according to their spin and orbital momentum at the maximal asymmetry angles $\gamma = \pm 120°$, in the scattering plane. In order to measure the spin polarization in the scattered electrons, a Mott detector is thus made of two detectors placed at 120° from the incident beam. The spin polarization P of the incoming electron beam is naturally expressed as:

$$P = \frac{N_\uparrow - N_\downarrow}{N_\uparrow + N_\downarrow} = \frac{N_\uparrow - N_\downarrow}{N} \tag{3.13}$$

It is possible to write the number of electrons arriving at the left and right detectors $N_{L,R}$:

$$\begin{aligned} N_L &= N_\uparrow \sigma_\uparrow + N_\downarrow \sigma_\downarrow = \sigma(1+PS)\frac{N}{2} \\ N_R &= N_\uparrow \sigma_\downarrow + N_\downarrow \sigma_\uparrow = \sigma(1-PS)\frac{N}{2} \end{aligned} \tag{3.14}$$

And hence, the asymmetry is now given by:

$$A = \frac{N_L - N_R}{N_L + N_R} = PS \tag{3.15}$$

A SR-PES experiment based on Mott detection consists in measuring this asymmetry A to extract the polarization of the photo-electron beam.

Instrumental asymmetry

Finally, another source of asymmetry that has nothing to do with the spin polarization has to be taken into account. It comes from the instrumental asymmetry of the two detectors that can have different sensitivities or misalignments. In this case, it is possible to eliminate this instrumental asymmetry by reversing the role of each detector, by mean of magnetization reversal of the measured sample. The correction procedure is well described in reference [118] and consists of doing the geometric average of the signal delivered by each detector, for each magnetization direction. Therefore, to obtain the spin polarization of a sample, two measurements are necessary: one in each direction of magnetization along the quantification axis.

3.1.3 Experimental details

As the basic concepts of SR-PES are now introduced, few details regarding the experimental part are presented. First, a description of the Cassiopée beamline is given. Then, a small discussion to show what is probed in Co_2MnZ Heusler compounds in this experimental configuration is proposed

The Cassiopée beamline

The Cassiopée beamline is fully dedicated to photo-emission spectroscopies. It comprises three UHV chambers that are all connected. A sketch of the three chambers is presented in figure 3.5a. One of the chambers is an MBE (see figure 2.1-right) and the two others are photo-emission chambers, one for ARPES and the second one for SR-PES. Epitaxial layers are grown in the MBE, as described at the beginning of the previous chapter. They are then directly transferred after the growth to the photo-emission chamber.

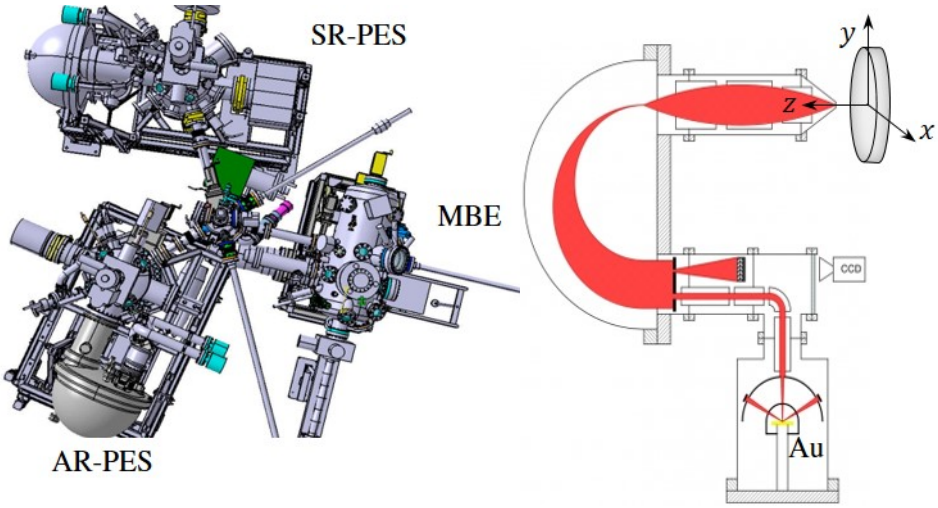

(a) The three chambers

(b) Modified Scienta SES 2002

Figure 3.5: View of the Cassiopée end stations and the hemispherical + Mott analyzer of the SR-PES chamber.

The low energy photons needed to explore the valence band are produced using an electromagnetic HU256 undulator[8]. This insertion device offers the possibility to choose the light polarization (linear ver-

[8] A period of 256 mm between each dipole

tical/horizontal, circular right/left). It produces photons in a range 8-155 eV. The beam energy is selected by using a plane grating monochromator with an energy resolution $\frac{E}{\Delta E} > 2 \times 10^4$ and can be sent to the desired end station.

The SR-PES chamber is equipped with a Scienta SES 2002 analyzer, slightly modified to be coupled with a Mott detector (figure 3.5b). Therefore, photo-electrons are first selected in energy in the hemispherical analyzer. They are then accelerated toward the Au target that scatters them according to their spin. At the Cassiopée beamline, the Mott detector is operating at 28 keV of scattering energy with an inelastic window equal to 800 eV. This gives a Sherman function $S = 0.12$ [10, 132]. Moreover, the Mott detector is actually made of two pairs of detectors, able to measure the spin components in two directions (in-plane and out-of-plane). The figure of merit is around FoM $= 2 \times 10^{-5}$ which means that approximatively one thousand incident electrons are needed to detect only one in the Mott channeltron. That is why the energy resolution is not as good as in ARPES measurements to keep a maximum of electrons (slits of the analyzer wide open). Here, the resolution is fixed at $\Delta E \sim 120$ meV.

For the following spectra, a photon energy in the range of 24-45 eV is used to make a compromise between the photo-emission cross section (drops quickly after $\hbar\omega \sim 50$ eV [133]) and the depth for which photo-electrons are able to escape from the solid. In other words, a good compromise is to keep a maximum of photo-electron signal while still being able to probe the bulk density of state.

A slit allows electrons at the entrance of the analyzer to be detected with an angular aperture of $\pm\ 8°$, in the direction of the scattering plane. By using the relation 3.8, this aperture corresponds, for a photon energy of 37 eV (and a work function $\phi = 4$ eV), to $\Delta k \sim \pm\ 0.41$ Å^{-1}.

Features of Co_2MnZ alloys

In theory, the spin gap in a HMM material is present in the whole Brillouin Zone (BZ). Consequently, to verify that Co_2MnZ alloys are indeed HMM, one has to probe the maximum of the BZ in order to be as close as possible from the total Density Of State (DOS). In view of the typical lattice parameter in the Co_2MnZ series (see figure 2.18), the BZ will be too large to be easily probed in its completeness. In figure 3.5b, the z direction corresponds to the [001] direction of Co_2MnZ and x to the [110] direction which is also the direction of the entrance slit. It means that the measured DOS is integrated over a $\Delta k \sim \pm 0.41$ Å^{-1} in the ΓK direction (Σ direction) of the BZ. Along Σ, the BZ width from Co_2MnSi to Co_2MnSn, is in the range 1.38-1.47 Å^{-1}. During SR-PES, the DOS is hence integrated over 56 to 59 % along Σ. The height of the entrance slit is so small that only the electrons from the interaction plane (xOz on the figure 3.5b) are accepted. The integration over the direction k_y is then neglected.

In addition, the photon energy allows probing along the ΓX direction (Δ direction). For photon energies of 30, 37 and 45 eV, and by using the relation 3.10 (inner potential $U_0 = 12$ eV, typical value), it gives positions in $k_z = 3.16$, 3.43 and 3.73 Å^{-1}, corresponding to locations in the third BZ for Co_2MnZ compounds. Reduced in the first BZ, these points are located very close to X on the Δ direction. By taking into account the uncertainty on $\Delta k_z \sim 0.17$ Å^{-1} estimated few paragraphs before, it is almost as if the DOS were integrated along a continuous line in the Δ direction. A sketch of the BZ of fcc crystals is represented on figure 3.6. The integrated DOS in the BZ in the present experiment is drawn in orange.

By taking into account all the cubic symmetries, the probed DOS is far from being negligible although it is not the total DOS.

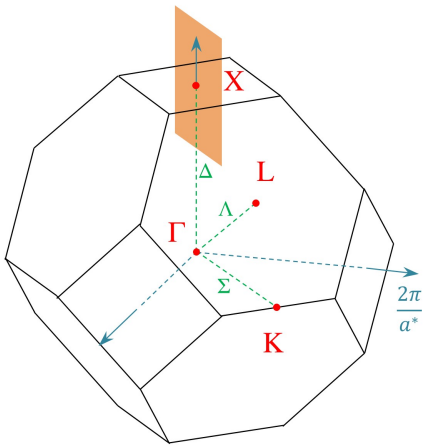

Figure 3.6: Brillouin zone of a fcc crystal. High symmetry points (red) and directions (green) are indicated. The orange plane represents the probed zone in the present SR-PES experimental set-up.

Finally, only photo-electrons with a wave vector **k** directed toward the analyzer are detected. Due to the orientation of $Co_2MnZ(001)$ crystals and that of the interaction plane, each emitted photo-electron comes from a transition that involves Bloch states of Δ symmetry. In this direction, the wave vector **k** belongs to the C_{4v} ($4mm$) symmetry group with five irreducible representations: Δ_1, Δ_1', Δ_2, Δ_2' and Δ_5. The final state of the photo-electron detected by the analyzer has to be even with regard to the plane of interaction (defined by the incident photon and the emitted photo-electron : plane xOz in figure 3.5b). Otherwise, the associated wave function will automatically present a node in this plane and cannot be detected. Only the representation Δ_1 has an even parity with this symmetry plane and can thus be a final state of a transition. So, in order to have a non zero matrix element (equation 3.5), the initial state involved in the transition must have the same parity as the dipolar electric Hamiltonian (hence the photon polarization), regarding the plane of interaction. It means that the direction of the linear polarization on the radiation allows a selection, in symmetry, of the excited states. This phenomenon is described elegantly with group theory in several works [134–136]. Thus, if the polarization of the radiation is out of the plane of interaction (direction y in the figure 3.5b, polarization "s"), the initial state must be odd with respect to the plane of interaction. And if the polarization is in the plane of interaction (a component along x and z, polarization "p"), the initial state must be even. The Δ_1 is even, the Δ_5 (doubly degenerated) has both an even and odd part. The possible transitions are summarized in the table 3.1:

Polarization	Transitions allowed
in plane (p)	$\Delta_{1,5} \rightarrow \Delta_1$
out of plane (s)	$\Delta_5 \rightarrow \Delta_1$

Table 3.1: Allowed transitions in the Δ direction in a photo-emission experiment, when the plane of interaction is perpendicular to the (001) face of the crystal.

This way, it is possible to resolve some states in symmetry by changing the polarization of the radiation.

In the following, results on the different Co_2MnZ alloys are going to be presented and discussed. The semi-conductor terminology: Z^{III} =Al, Ga (third column), Z^{IV} =Si, Ge, Sn (fourth column) and Z^{V} =Sb (fifth column) is largely used here since electronic properties depend on the number of valence electrons in the structure. Moreover, the spin polarization of a magnetic material cannot be higher than the value of its magnetization remanence. Spin polarizations are thus corrected afterward by the remanence measured by magnetometry (of the exact same sample).

3.1.4 Ternary Co_2MnZ compounds

Co_2MnZ^{IV} compounds

Co_2MnSi. Co_2MnSi has been widely studied in reference [10] and the following results are taken from the same work. However, the main experimental results are recalled here for a better understanding of the trend in Co_2MnZ^{IV} compounds (Z^{IV} =Si, Ge, Sn).

SR-PES spectra obtained on Co_2MnSi are summarized in figure 3.7, using the *p* polarization of light (Δ_1 and Δ_5 initial states excited). Blue curves correspond to the majority spin channel and the red ones to the minority spin channel. The Spin Polarization (SP) is plotted in green. The curves are all plotted versus the binding energy where the Fermi level is naturally the zero on this scale and is determined by looking at the inflection point in the PES spectrum. The figure 3.7 holds a lot of information that are going to be discussed.

First of all, there is a transition localized around -1 eV below E_F, denoted D in the figure 3.7, weakly split by exchange coupling between the majority and minority DOS. This transition barely disperses in k_z (flat band) since its position in binding energy remains almost unchanged with all the different photon energies. This transition might be associated to initial states of *d* nature.

Secondly, there is a surface state denoted by $S_\uparrow$ in the majority spin channel with a position, in binding energy, indicated by the blue line. Unfortunately, it comes with its counterpart $S_\downarrow$ in the minority spin channel. The rule on the k_z dispersion usually used to recognize surface states can not be applied here due to the strong resonant nature of this transition. It was indeed observed for photon energies between 30 and 45 eV, with a maximum of intensity at 37 eV. Nonetheless, it has been shown in reference [10] that it surely comes from the surface since it vanishes entirely when a layer of MgO or Mn is deposited on top of the Co_2MnSi surface. This surface state completely disappears above 50 eV. Such a resonant behavior cannot be associated to a Tamm or Shockley type surface state.

Using a 37 eV photon energy, a spin gap in the minority DOS is visible at the exact position of $S_\uparrow$, -0.325 eV below E_F. For each photon energy, it corresponds exactly to the position of the maximum of SP represented by the green line. The SP drops to lower values at E_F when the surface transition is excited due to $S_\downarrow$, located at -0.075 eV, too close to E_F. On the other hand, for photon energies higher than 40 eV, when the surface transition is not excited but the photo-emission cross section is very small, the minority DOS near E_F is almost zero and could go in favor of a minority spin gap even though the spin polarization is not indicating a spin gap.

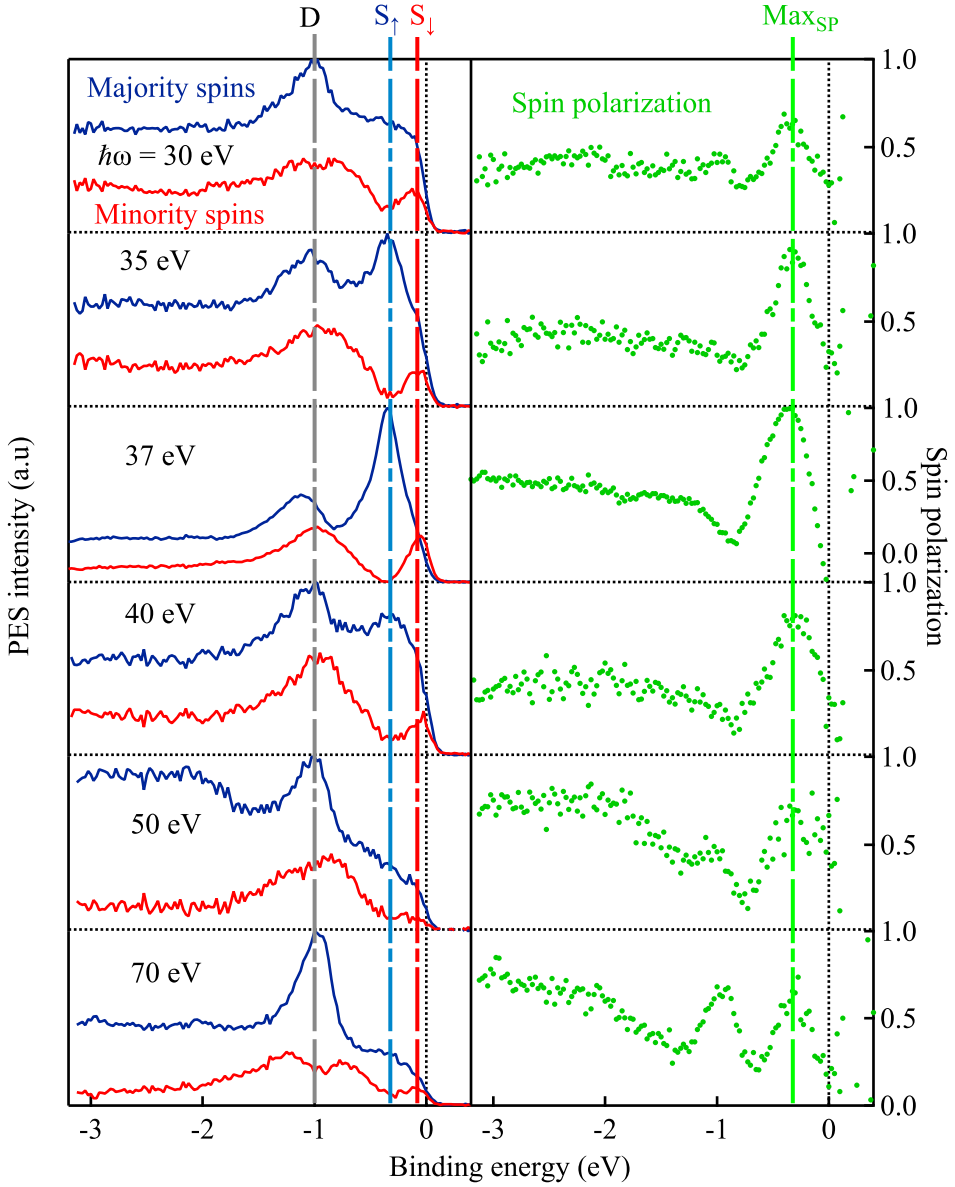

Figure 3.7: SR-PES spectra of Co_2MnSi compound for different photon energies with *p* polarization. The position of the resonant surface states $S_\uparrow$ ($S_\downarrow$) for the majority (minority) spin channel is represented by the blue (red) line. The maximum of SP is represented with the green line.

Co_2MnGe. SR-PES spectra obtained on Co_2MnGe using *p* polarization of light with photon energies of 30, 37 and 45 eV are shown in figure 3.8. Both majority and minority PES spectra have the same global shape than those of Co_2MnSi. The transition denoted D is almost at the same location in binding energy, approximatively -1.09 eV below E_F, and is still scarcely dispersing in k_z.

The resonant surface transition is also present in this compound but is excited with a different photon energy range, a little lower than Co_2MnSi. The maximum of intensity of the surface state is obtained, in this case, for a photon energy between 30 and 37 eV. Additionally, the exchange splitting between $S_\uparrow$ and $S_\downarrow$ seems a little smaller. The position of $S_\uparrow$, -0.28 eV, still corresponds to the minimum of the minority DOS and hence to the maximum of SP. Exactly as for Co_2MnSi, the SP is largely suppressed at E_F due

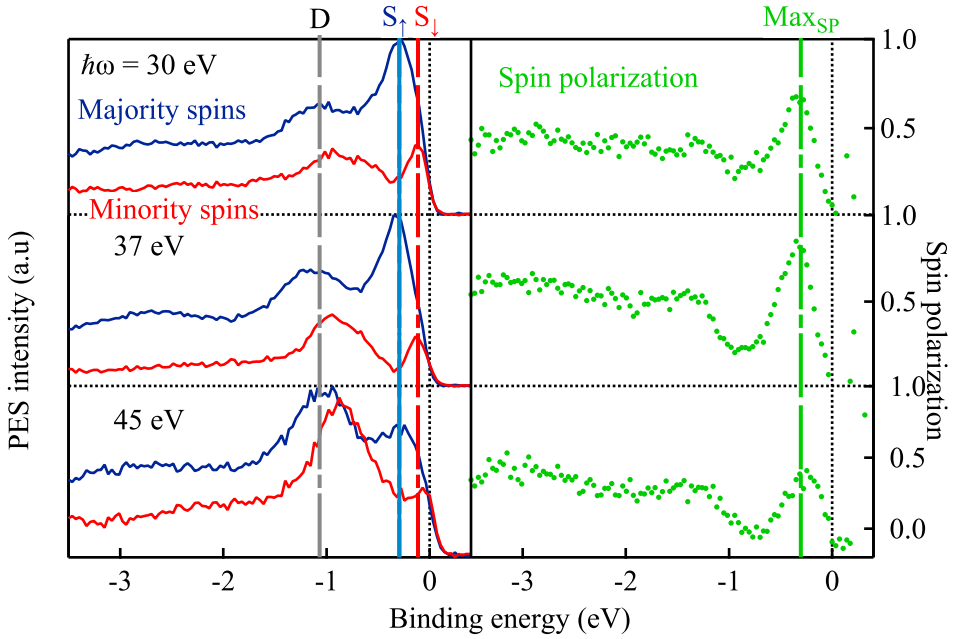

Figure 3.8: SR-PES spectra of Co_2MnGe compound for different photon energies with *p* polarization. The position of the resonant surface states $S_\uparrow$ ($S_\downarrow$) for the majority (minority) spin channel is represented by the blue (red) line. The maximum of SP is represented with the green line.

to the emergence of $S_\downarrow$ in the minority DOS, located at -0.105 eV in binding energy. The fact that both states $S_\uparrow$ and $S_\downarrow$ are closer to each other does not allow to see a spin gap.

Co_2MnSn. Sn being also an element from the fourth columns, a similar PES spectra should be observed. Spectra obtained on Co_2MnSn compound using the *p* polarization of light with 24, 27, 30 and 33 eV photon energies are shown in figure 3.9. The PES spectra is indeed similar to the two previous Co_2MnZ^{IV} compounds, presenting only small differences.

Once again, the D transition in the majority spin PES spectra is located around -0.95 eV. Moreover, D is still not dispersing with various excitation energies. For this compound, the surface transition is also observed but at smaller values of photon energies. It resonates at its maximum for $\hbar\omega = 27$ eV. The splitting of $S_\uparrow$ and $S_\downarrow$ is the smallest of the three compounds and $S_\uparrow$ is located only at -0.21 eV below the Fermi energy. Nonetheless, the location of $S_\uparrow$ still corresponds to the maximum of SP (or the minimum of minority DOS). As in Co_2MnGe, the emergence of $S_\downarrow$ too close to the minimum of the minority PES spectra does not allow to observe a spin gap and the SP is one more time very small at E_F.

The different parameters of the Co_2MnZ^{IV} compounds like the location, in binding energy, of D, $S_\uparrow$, $S_\downarrow$, $\Delta S = S_\uparrow - S_\downarrow$ and the maximum of SP observed for the maximum of resonance $\hbar\omega_{res}$ of the surface state are summarized in table 3.2. D transitions are located at similar binding energies for every compounds, with a little decrease from Si to Sn. Moreover, it has been shown in figure 3.7, 3.8 and 3.9 that they do not scatter in k_z. Therefore, they must involve flat bulk bands for which positions in binding energy may depend on the number of valence electrons in a rigid band model (which is constant in Co_2MnZ^{IV} compounds). The surface state exists in the three compounds, with different range in activa-

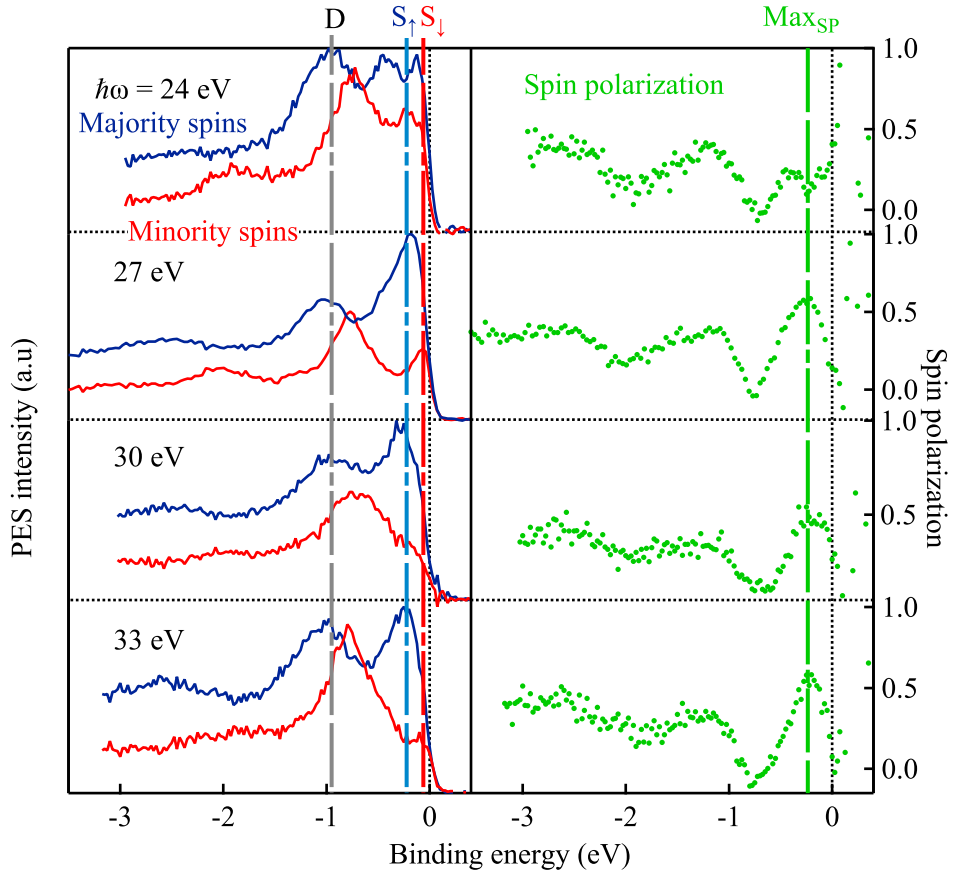

Figure 3.9: SR-PES spectra of Co_2MnSn compound for different photon energies with *p* polarization. The position of the resonant surface states $S_\uparrow$ ($S_\downarrow$) for the majority (minority) spin channel is represented by the blue (red) line. The maximum of SP is represented with the green half-dash line.

Co_2MnZ^{IV}	D (eV)	$S_\uparrow$ (eV)	$S_\downarrow$ (eV)	ΔS (eV)	$\hbar\omega_{res}$ (eV)	Max SP
Co_2MnSi	-1.1	-0.325	-0.075	0.25	37	1
Co_2MnGe	-1.09	-0.28	-0.105	0.175	30-35	0.8
Co_2MnSn	-0.98	-0.21	-0.07	0.14	27	0.6

Table 3.2: Parameters extracted from SR-PES spectra of the Co_2MnZ^{IV} compounds.

tion energy but it is hard to go further in the understanding of the photon energy dependency. Regardless of this resonance, $S_\uparrow$ and $S_\downarrow$ progressively approach E_F as the Z^{IV} element gets heavier. The exchange splitting between them, ΔS, also decreases from Si to Sn. This behavior might explain the reduction of SP from 1 with Co_2MnSi to 0.6 with Co_2MnSn. Indeed, starting from the assumption that the gap exists in the three compounds (it exists in Co_2MnSi though), it can be seen in Co_2MnSi because the splitting is large enough. As it gets smaller, the place where states should not exist in the minority PES spectra is filled by $S_\downarrow$ and the SP drops to small values.

In these compounds, these surface states are barriers to probe spin gaps. However, in the previous work on Co_2MnSi [10], it has been shown that it is possible to not excite the surface transition by changing

the polarization of the light from *p* to *s*. Thereby, the measured PES spectra in *s* polarization reflects better the bulk DOS. According to table 3.1, it means that the surface state on Co_2MnSi has a Δ_1 symmetry. When the surface transition does not appear in the SR-PES spectra, the SP is recovered near E_F and the spin gap can be observed.

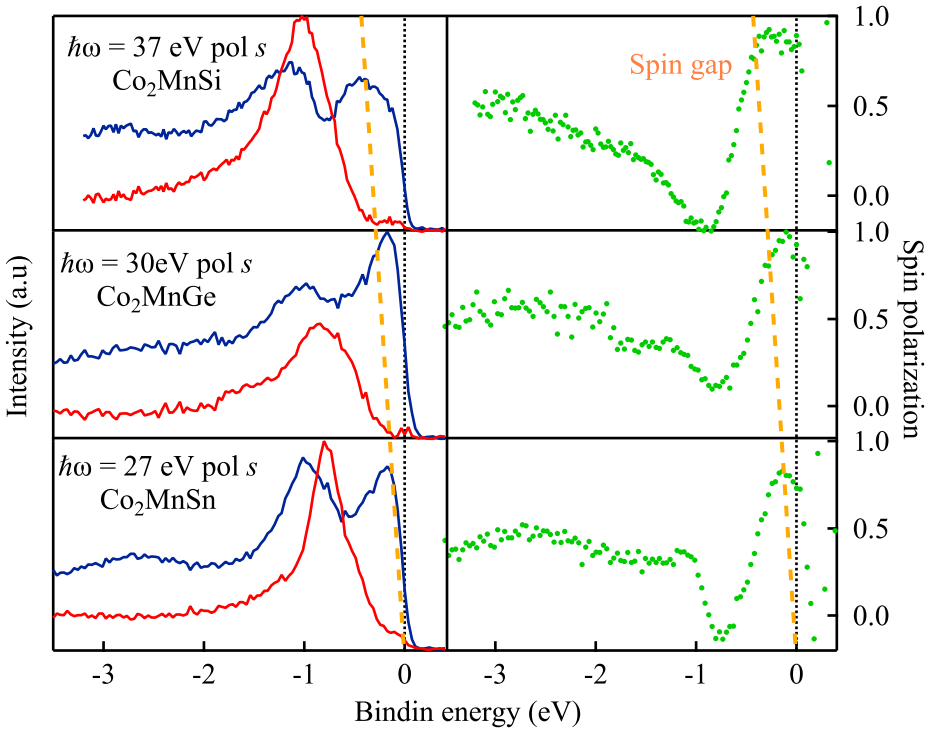

Figure 3.10: SR-PES spectra of Co_2MnZ^{IV} compounds with *s* polarization of light. Spin gaps are indicated by the orange dashed lines.

SR-PES spectra of Co_2MnZ^{IV} compounds using *s* polarization of the incoming radiation are shown in figure 3.10. D transitions are still present with the same shape than with *p* polarization. The spectral weight is reduced though, with any doubts because flat bands involved must be of Δ_1 and Δ_5 symmetries and a part of the transitions are now forbidden. The global shape remains unchanged in the DOS except near the Fermi energy. For the three compounds, the surface state is no longer excited and spin gaps become visible. This means that $S_\uparrow$ and $S_\downarrow$ are of Δ_1 symmetry, like in Co_2MnSi. Near the Fermi level, the minority PES spectra clearly drops to near-zero values for the three compounds. There is no more $S_\downarrow$ states suppressing the SP. The beginning of the spin gap approaches E_F from Z=Si to Z=Sn, as it was foreseen by table 3.2. In a reversed point of view, E_F is getting closer to the top of the minority valence band when Z^{IV} becomes heavier.

It appears that Co_2MnZ^{IV} are all HMM, at least for specific photon energies. However, the measured SP is not 1 for higher photon energies with some DOS present in the minority spin channel when probing in k_z (by changing photon energies). This could be due to surface defects (steps, vacancies), impurities or quite simply because those compounds are no pure HMM in the whole BZ. In addition, the low photoemission cross section at higher energies coupled with the small FoM of the Mott detection may lead to too low efficiency in the spin resolution. Thereby the measured SP could lose of its meaningfulness. Nevertheless, Co_2MnZ^{IV} are all highly polarized magnetic materials.

Co_2MnZ^{III} compounds

Co_2MnZ_{III} compounds have one less valence electron in their structure. Thus, electronic properties should be different and the way this lack of electron changes the SR-PES spectra is addressed in the following.

Co_2MnAl. The spectra obtained in Co_2MnAl are represented in the figure 3.11 for three different photon energies. The shape of the DOS for both minority and majority spin channels does not change much from 30 to 45 eV. The D transition at -0.685 eV, assuredly of the same nature than for Co_2MnZ^{IV} compounds, is closer to E_F and supports the fact that the rigid band model is suitable for Co_2MnZ alloys. The k_z dispersion of D remains negligible. Additionally, there are no surface states observed for this compound. $S_\uparrow$ and $S_\downarrow$ must be above the Fermi energy in the empty states and can not be measured with SR-PES. Another possibility is that perhaps the resonant surface state is proper to a $L2_1$ ordering and

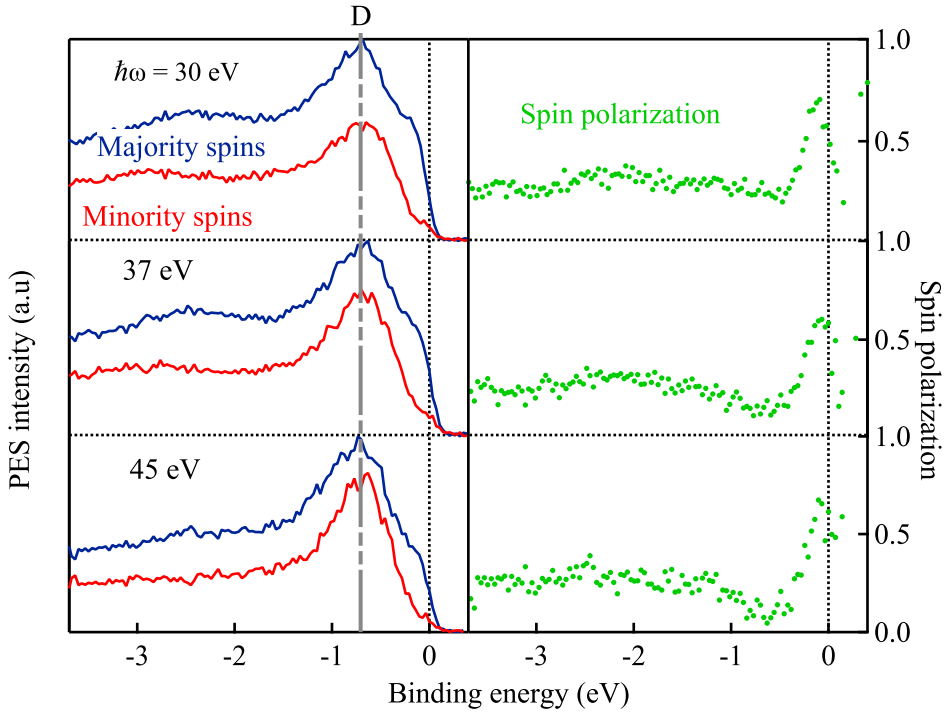

Figure 3.11: SR-PES spectra of Co_2MnAl compound for different photon energies with *p* polarization. The gray line represents the position of D transitions.

consequently cannot exist in Co_2MnAl with a B2 disorder (Mn/Al random mixing). The maximum of SP is now located directly at E_F and reaches 0.75 at $\hbar\omega = 30$ eV. For each photon energy though, the minority PES spectra strongly decreases in the neighborhood of E_F as if the beginning of the spin gap was very close to E_F. Co_2MnAl may not be HMM, but the shape of the minority PES spectra suggests that a spin gap[9] could exist in the band structure. Comparing with Co_2MnZ^{IV} compounds, it is not surprising that the Fermi energy is lowered in the band structure for Z^{III} elements and thus falls in between the minority valence band and the gap.

[9] or at least a zone of strong polarization, called a pseudo-gap in the literature

Co_2MnGa. Spectra obtained in Co_2MnGa layer for the same photon energies than Co_2MnAl with *p* polarization are shown in figure 3.12. The D transition is a little bit lower in binding energy, located at -0.8 eV. The global shape for the three spectra is the same, with an increasing majority PES spectra at E_F, and a vanishing minority spectra, resulting in SP=1 at the E_F. For this compound, a spin gap is well defined and clearly observed, even with *p* polarization. The very beginning of the surface state in the

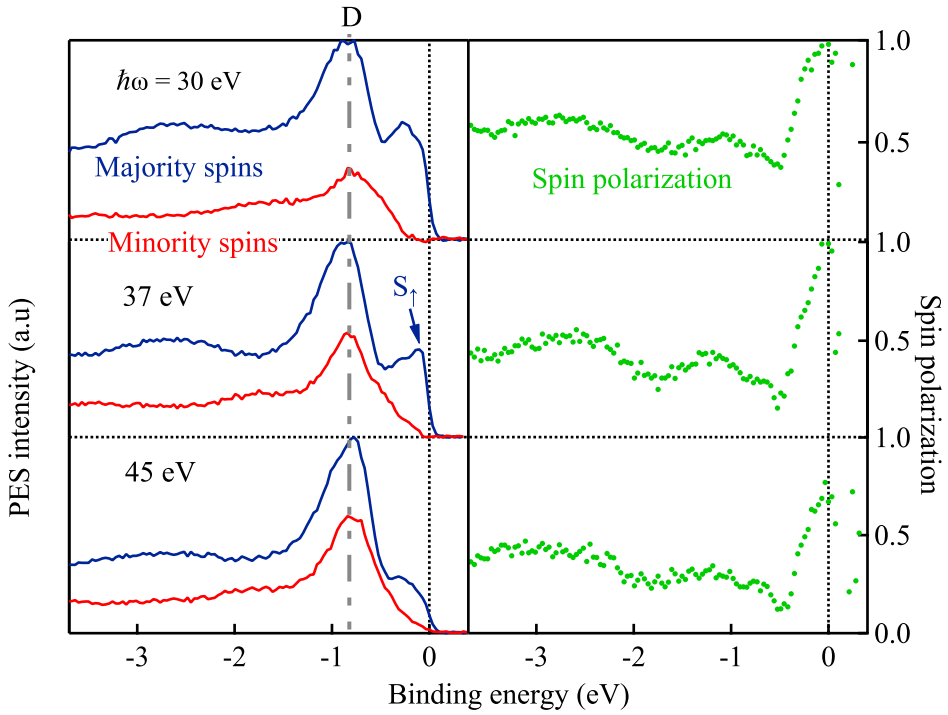

Figure 3.12: SR-PES spectra of Co_2MnGa compound for different photon energies with *p* polarization. The gray line represents the position of D transitions.

majority spin DOS, $S_\uparrow$, is observed at 37 eV close to E_F. This state vanishes at other photon energies and with *s* polarization of light, as demonstrated in figure 3.13. The surface state has also a Δ_1 symmetry, like in Co_2MnZ^{IV} alloys.

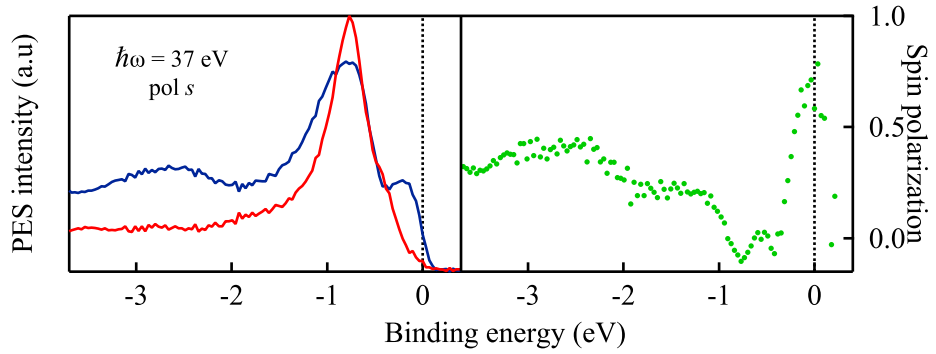

Figure 3.13: SR-PES spectra of Co_2MnGa compound for 37 eV of photon energy with *s* polarization.

Finally, Co_2MnGa Heusler compound seems to be HMM as well. The Fermi level falls in the gap for this compound unlike in Co_2MnAl where it appears to be at the top end of the valence band. In any case, in Co_2MnZ_{III} alloys, the minority valence band is clearly closer to the Fermy energy, resulting in

a smaller measured gap in SR-PES experiments. This feature is easily understood by considering the difference in valence electron number between the two families of compounds.

Co_2MnZ^V compound

To see what happens with a V type element was the initial motivation to elaborate Co_2MnSb epitaxial layers. SR-PES spectra of Co_2MnSb compound for 30, 37 and 45 eV of photon energies are shown in figure 3.14. The state that looks like the D transition should be smaller in binding energy compared to $Co_2MnZ^{III,IV}$ compounds because here, there are more valence electrons. In the rigid band model vision,

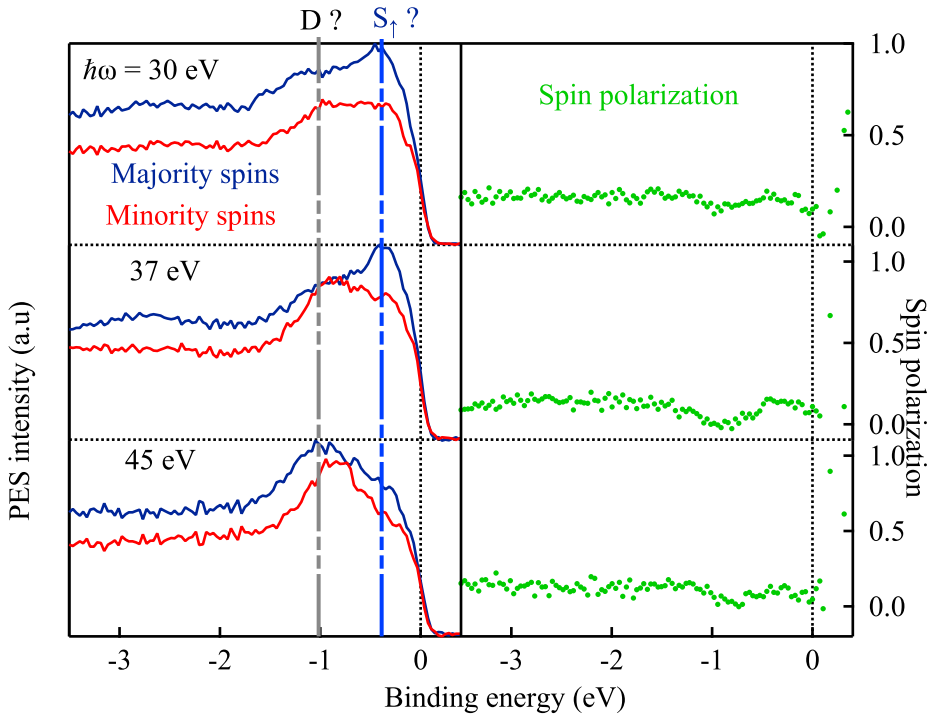

Figure 3.14: SR-PES spectra of Co_2MnSb compound for 30 and 37 eV of photon energies with *p* polarization.

the Fermi level should be higher in the band structure. There is also a small peak in the majority DOS that could be assimilated to the surface state $S_\uparrow$, resonant for 30 and 37 eV but not at 45 eV. Nonetheless, it is not as clear as for others Co_2MnZ alloys.

Finally, beside being flat on the whole range of binding energy, the SP does not reach more than 0.18 and was not the same from one Co_2MnSb layer to the other. Additionally, we have seen in the previous chapter that the stoichiometry was certainly not respected for this compound. Because SR-PES is a surface sensitive technique, the flatness and low SP could be caused by the Sb reconstruction at the surface (see figure 2.7) with a vanishing magnetic moment. Or, as suggested by the figure 2.15 and by TEM, due to several structural and chemical phases taking place in Co_2MnSb layers. SR-PES experiments highlight one more time the singular behavior of this compound, compared to the rest of the series.

3.1.5 Quaternary $Co_2MnZ^{IV}_xZ^{III}_{1-x}$ compounds

This series of compounds are used to investigate what happens when a Z^{IV} is progressively substituted by a Z^{III} with one less valence electron. In both series, the initial compound at $x = 1$ has a spin gap, hidden by a surface state of Δ_1 symmetry (see previous sections). For the final compound at $x = 0$, on the other hand, the surface state is above the Fermi energy that seems to fall at the edge between the minority spin valence band and the gap.

The PES spectra obtained on the $Co_2MnSi_xAl_{1-x}$ set of alloys are shown in figure 3.15 (at 37 eV of photon energy with *p* and *s* photon electric polarizations). The dashed lines represent the position of the

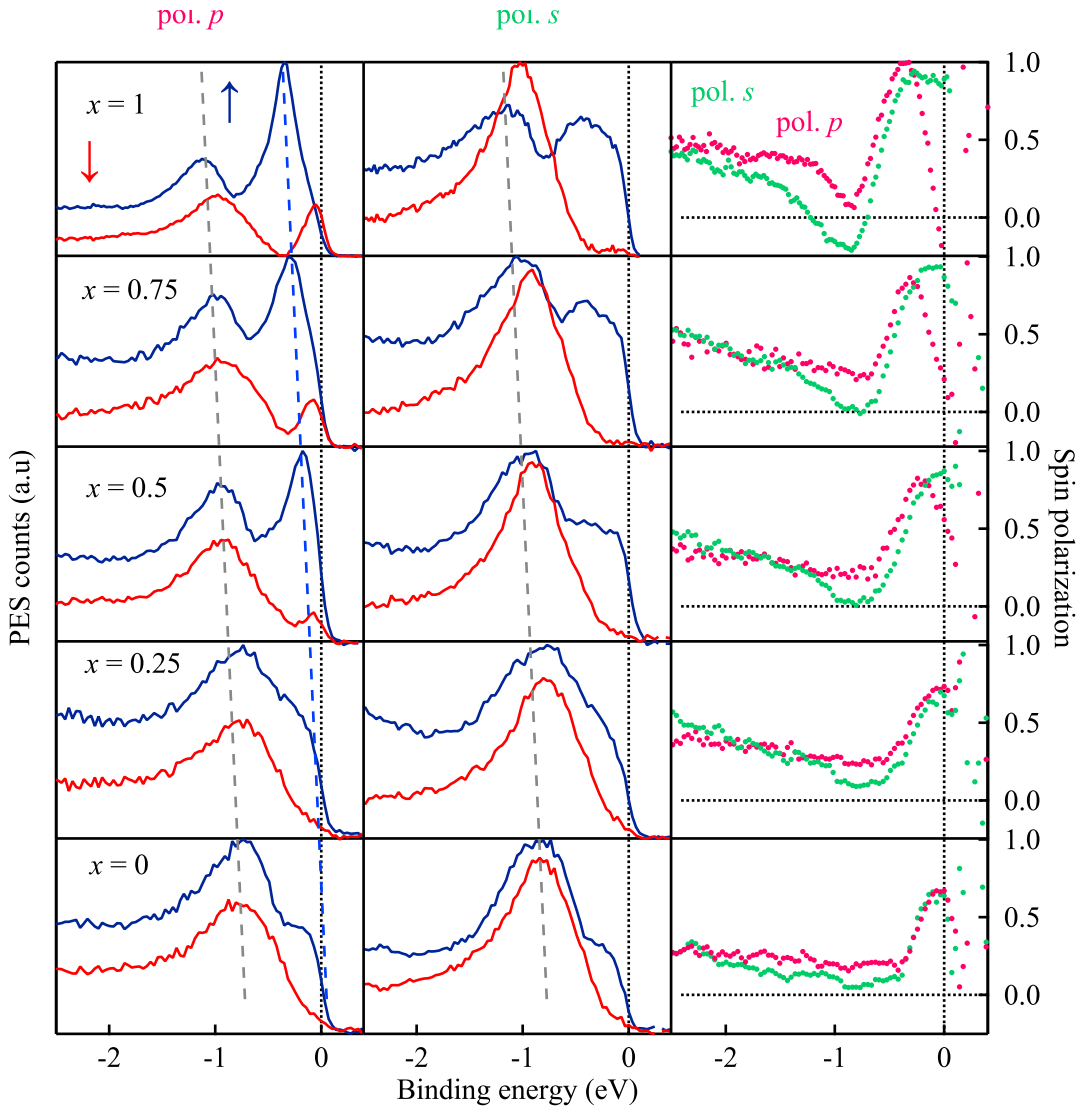

Figure 3.15: $Co_2MnSi_xAl_{1-x}$ SR-PES spectra at 37 eV of photon energy. The left column are spectra measures with *p* photon polarization, the middle column are spectra obtained with *s* photon polarization and the right column represents the corresponding spin polarizations. The shift of D and $S_\uparrow$ states is indicated with gray and blue lines.

main transitions previously observed: D and the majority spin surface state $S_\uparrow$. First of all, the rigid band model, where the Fermi energy moves downward in the band structure by removing one electron, seems

to be completely relevant. The shift of the D transition, as well as $S_{\uparrow}$, is quite linear with the substitution rate x. The surface state evolves in binding energy and is indeed sent in empty states at $x \leq 0.25$ (as observed in Co_2MnAl). The same shift is also visible on the spin polarization, where the maximum of SP shifts toward E_F by decreasing x. Using the s photon polarization (middle column in figure 3.15), we are able to measure the spin gap. We see that the gap width is decreasing and that some small minority spin DOS appears at E_F by decreasing x. $Co_2MnSi_xAl_{1-x}$ compounds thus provide a series of materials with a continuously tunable electronic structure.

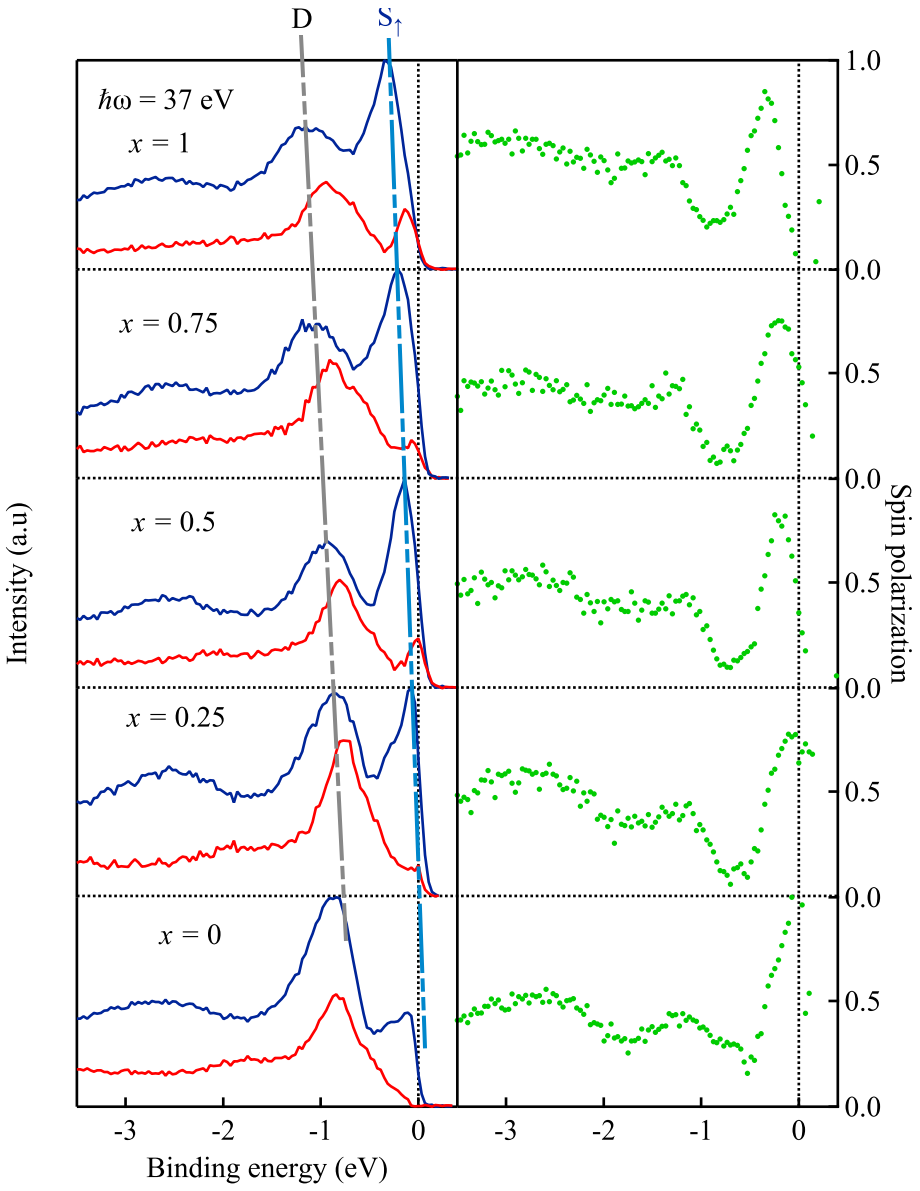

Figure 3.16: $Co_2MnGe_xGa_{1-x}$ SR-PES spectra at 37 eV of photon energy with p polarization. The shift of D and $S_{\uparrow}$ states is indicated with gray and blue lines.

The same global behavior is obtained for $Co_2MnGe_xGa_{1-x}$ alloys as shown in figure 3.16, where the same photon energy but only the p photon polarization was used. The shift of D in binding energy is also linear. The majority surface state $S_{\uparrow}$ linearly ends up in empty states when $x = 0$. This time, the SP does not decrease by decreasing x and E_F falls just above the valence band for $x = 0$, giving SP=1 as previously observed in figure 3.12 for Co_2MnGa. By changing the light polarization from p to s, one

would have observed a spin gap for the entire range of substitution rate x, with once again the width of the gap getting smaller by decreasing x.

For both series of alloys, the Fermi energy varies with x accordingly with the variation of the number of electrons in the valence band. This behavior is well represented in figure 3.17 where the distance between the D transition and the Fermi energy is plotted versus the number of valence electron in the structure (equivalent to the substitution rate x). The fact that the rigid band model fits well the observed spectra is in agreement with a solid solution behavior, already observed in XRD in the previous chapter. Nonetheless, the existence of two different slopes for the linear fits is puzzling. This is due to the B2 disorder in Co_2MnAl which generates a small shift in the band structure, or Co_2MnGa having specific hybridizations that could explain its strong magneto-crystalline anisotropy and surprising high magnetic moment[10], or both cases at the same time.

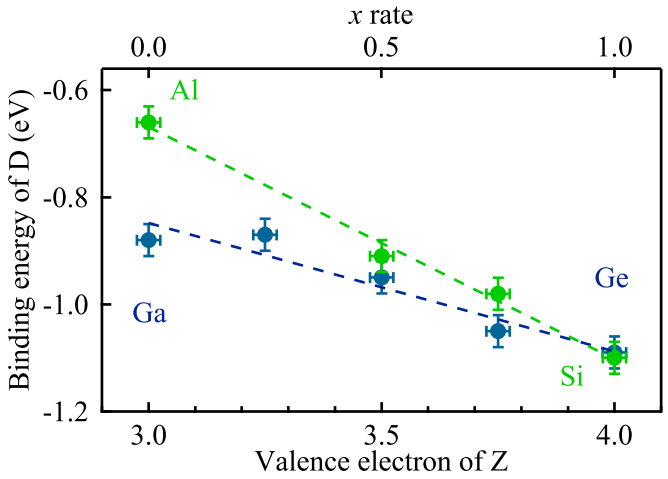

Figure 3.17: The position in binding energy of the transition D versus the number of valence electron of Z in the $Co_2MnZ^{IV}_xZ^{III}_{1-x}$ series of alloys. Dashed lines are fits assuming a solid solution behavior.

3.1.6 Polycrystals

Photo-emission measurements on polycrystals are the best way to explore the BZ in its completeness. Indeed, in a polycrystal, grains are oriented in every possible directions of space and thus, there are no more limitations in the probed BZ, whatever the angular aperture.

Co_2MnZ polycrystals with Z=Si, Ga, Ge were elaborated on the MBE chamber at the Cassiopée beamline in the same conditions than epitaxial films. MgO substrates were replaced by amorphous glass substrates, beforehand cleaned with acetone and alcohol. They were outgassed under vacuum at the same temperature than MgO substrates and the growth of Co_2MnZ alloys was also performed at 720 K. The polycrystalline nature and high roughness of the samples were ensured by the exclusive presence of rings on RHEED patterns (see appendix A). There likely is a slight fiber-like texture though, due to vanishing arcs on some rings [137].

[10] And also the forthcoming value of the magnetic damping

Co_2MnSi. SR-PES spectra on Co_2MnSi polycrystal are shown in figure 3.18 for different photon energy and polarization of light. The D transition is still observed at -1 eV, like in the epitaxial case and an additional transition, denoted A, is observed at -0.56 eV, but only for the majority spin channel.

For a (001) oriented crystal, changing the photon energy is equivalent to probing the band structure along k_z. For a polycrystal though, the perpendicular direction can not be associated with a peculiar direction of **k**. Additionally, every **k** directions are already integrated thanks to the multiple grain orientations. It explains why almost no differences are observed between 45 and 37 eV of photon energies with the same polarization of light in figure 3.18.

Moreover, the selection in symmetry of the excited states by changing the polarization of light was correct for a (001) oriented fcc crystal. Now that there are grains in every direction, there is no symmetry argument available for the **k** vectors of photo-electrons. It is therefore impossible to conclude on the symmetry of the excited states. Nevertheless, at 37 eV for Co_2MnSi, there are two states that can be associated to $S_\uparrow$ and $S_\downarrow$. They are indeed at the exact same position than in table 3.2. They are attenuated at 45 eV (resonant nature of the state) and vanish with *s* polarization (Δ_1 symmetry of the state) as demonstrated by the figure 3.18. This surface state is specific to (001) oriented grains in the polycrystalline film.

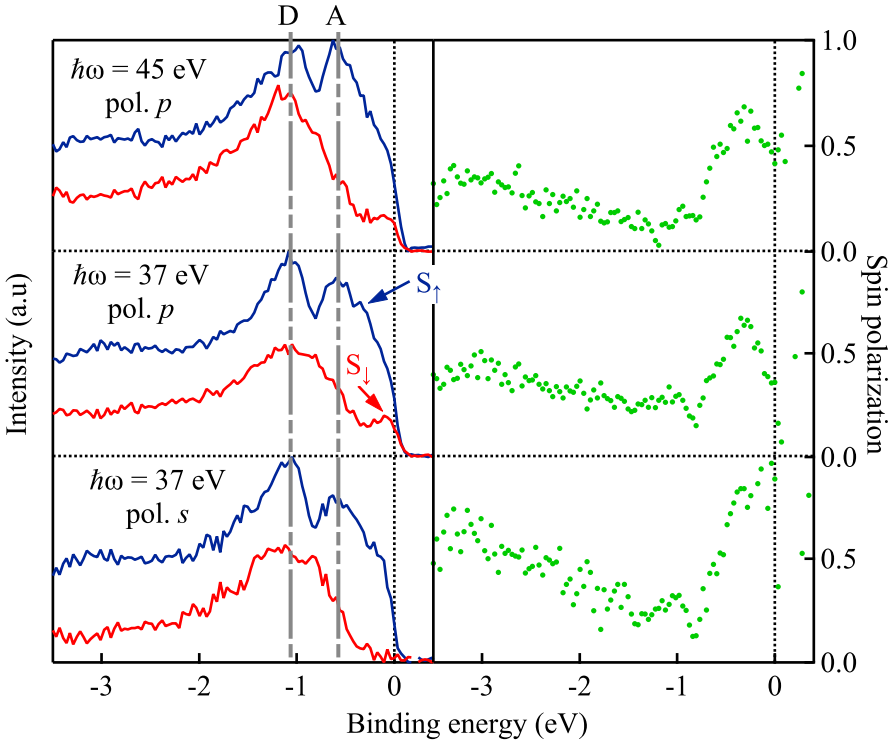

Figure 3.18: SR-PES spectra on Co_2MnSi polycrystal, with a photon energy of 45 and 37 eV in *p* polarization and 37 eV with *s* polarization.

If all the minority DOS that suppresses the SP in *p* polarization comes from the surface state $S_\downarrow$, Co_2MnSi polycrystals appear to have a spin gap of the same width than in (001) epitaxial films, but in the whole BZ (bottom of figure 3.18). However, it is uncertain if no minority DOS near E_F coming from a bulk band is killed by the *s* polarization of light. In any case, Co_2MnSi polycrystal is a highly spin polarized material.

Co_2MnGe. As already demonstrated in epitaxial films, the shape of the SR-PES spectra of Co_2MnGe is very similar to Co_2MnSi. In figure 3.19, SR-PES spectra on Co_2MnGe show the exact same transitions, D and A, observed at the same binding energies: -1 and -0.56 eV, respectively. The minority DOS drops near E_F to almost 0 in *p* polarization but a small remaining DOS reduces the SP. This small DOS corresponds perfectly, in binding energy, to the location of $S_\downarrow$ from table 3.2. Like in Co_2MnSi polycrystal, this minority DOS near E_F is associated to the surface state transition of (001) oriented grains, vanishing in *s* polarization of light as shown by the bottom of figure 3.19.

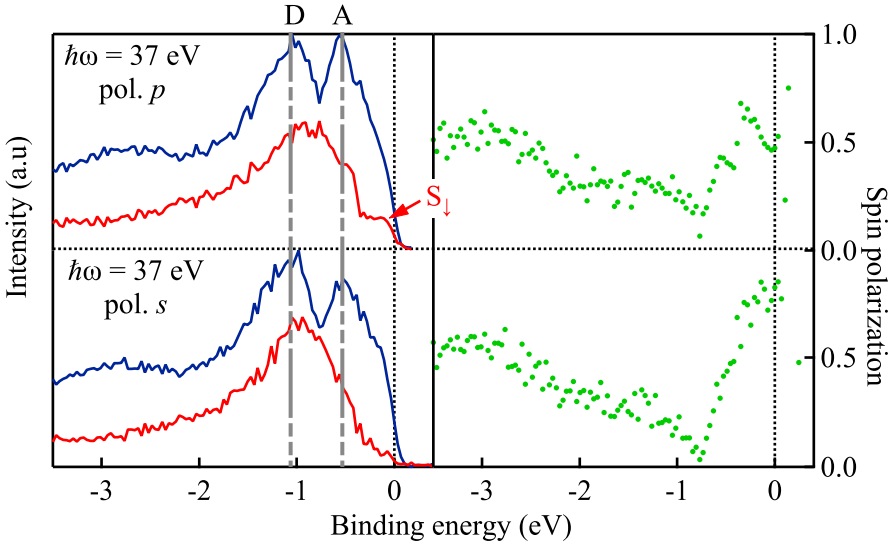

Figure 3.19: SR-PES spectra on Co_2MnGe polycrystal, with a photon energy of 37 eV in *p* and *s* polarization.

In *s* polarization, the SP is recovered. The minority DOS clearly vanishes near the Fermi energy which is compatible with a spin gap, even if the SP is not completely 1. The gap seems a little narrower than in Co_2MnSi, confirming previous observations on the single-crystalline cases.

Co_2MnGa. Finally, the figure 3.20 shows SR-PES measurements obtained for Co_2MnGa polycrystal for 37 eV of photon energy in *p* and *s* polarization. The global shape is the same than for Co_2MnZ^{IV} polycrystals. Both D and A transitions are present but are higher in binding energies: -0.7 for D and -0.2 for A. The D transition is slightly shifted compared to (001) single-crystal where it was at -0.85 eV, but it is easily explained by considering the reduced part of the BZ probed in the single-crystalline case that might disregard bands.

The rigid band model is one more time verified, with a Fermi energy closer to D and A. Like in (001) single-crystals, the maximum of SP is located at E_F. Besides, there are no differences with the two polarizations of light for this compound, like in the single-crystal. It is consistent with the behavior observed in the epitaxial film, where surface states $S_\uparrow$ and $S_\downarrow$ from (001) oriented grains are above E_F, in empty states and are thus never excited, whatever the polarization of the radiation.

Furthermore, like in epitaxial films, E_F moves downward in the band structure for Co_2MnZ^{III} compounds. Consequently, it falls in the minority valence band but not far from a possible spin gap which explains the increasing, but not full, SP around E_F.

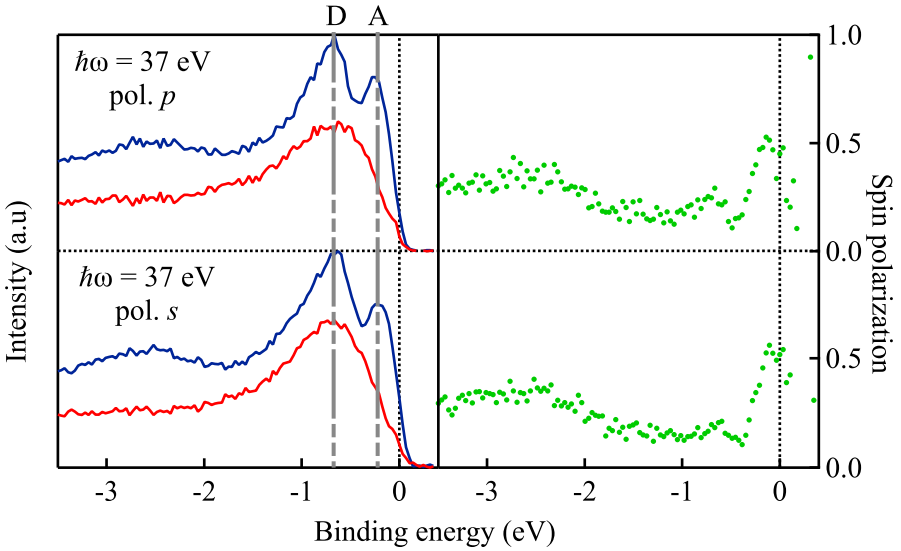

Figure 3.20: SR-PES spectra on Co_2MnGa polycrystal, with a photon energy of 37 eV in *p* and *s* polarization.

To conclude on polycrystals, the important point is that the complete BZ is explored. The numerous structures in the DOS are a sign of good quality polycrystals. The shape of the minority DOS for Co_2MnZ^{IV} compounds is compatible with a full spin gap near the Fermi energy. On the other hand, for Co_2MnGa with one less valence electron, the Fermi level is located at the end of the minority valence band, just before the spin gap, confirming the suitability of the rigid band model.

Measurements on (001) single-crystals appear to be well representative of the total DOS. By probing the whole BZ in polycrystals, there is only one supplementary transition, A, but it concerns the majority spin channel hence it does not affect the spin gap, at least for Co_2MnZ^{IV} alloys. For Co_2MnZ^{III} alloy Co_2MnGa, the SP has changed a little in the polycrystal. There is an additional small minority DOS located just at the Fermi energy that does not allow to get 1 in SP compared to figure 3.12. Still, the global shape is the same between single and polycrystals with a high SP at the Fermi energy.

3.1.7 Comparison with calculated band structures

Since a lot of band structure calculations are available in the literature, our measurements provide good tests for the theoretical predictions. Conversely, band structure calculations are also a good support to understand the PES measurements.

The D transition, observed in every compound, corresponds to *d* band initial states of 3*d* transition metals, Co and Mn[11]. D might be associated to the bands located around -1 eV for Co_2MnZ^{IV} compounds, shown in figure 3.21. This position in binding energy corresponds to the measured values in SR-PES. Additionally, it has been observed, by varying the photon energy (probing at different locations along ΓX direction), that the D transition does not disperse. If one looks closely at those bands in the ΓX direction indicated by the red arrow on figure 3.21, they are indeed almost flat. Other associations between

[11] that are hybridized into e_g, t_{2g}, e_u, t_{1u}, the irreducible representations of simple cubic O_h symmetry group.

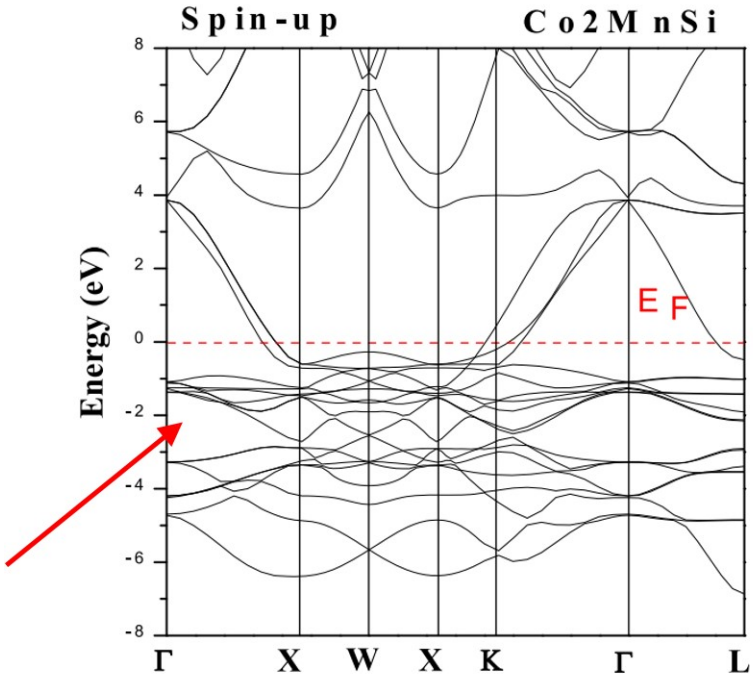

Figure 3.21: Calculated band structure of Co_2MnSi majority spins from [138].

calculated bands and observed transitions (like the transition A in polycrystals) are hardly comparable due to matrix elements effects[12], instrumental resolution and defects on the surface.

The key point for HMM Heusler compounds lies in the minority spin gap features: its width as well as the position of E_F within the gap. For clarity reasons, the comparison will begin with Co_2MnZ^{IV} alloys, then Co_2MnZ^{III} and finally Co_2MnZ^{V} compounds, to follow the previous progression. It should be noted however that a complete comparison with calculations can not be made because only occupied states are probed by a photo-emission experiment.

Co_2MnZ^{IV} compounds

The calculated band gap width and position of the Fermi energy are summarized in the table 3.3 from different calculations, as well as the measured values from figure 3.10.

Despite some dispersion in values from the different references, the general trend is the same. The minority spin gap width Δ_{gap} is larger for Co_2MnSi and gets narrower with the increase in number of electrons of the Z^{IV} element. In addition to this behavior, the position of the Fermi energy also decreases with regards to the spin gap. It starts approximatively at the middle of the gap for Co_2MnSi and ends up at the top of the minority valence band for Co_2MnSn. The qualitative trend is sketched in the figure 3.22. S. Picozzi *et al.* [67] explain this behavior by taking into account two effects : the *p* state of the Z element (which is similar for Si, Ge and Sn) and the lattice constant *a*. They show that both the minority spin valence and conduction bands are shifted upward compared to E_F when increasing *a*[13]. Additionally, they have calculated that the valence and conduction bands are not evolving with the same

[12] In a PES experiment, we are not probing directly the band structure of the solid. We are probing transitions between two Bloch states as shown in equation 3.5. It means that the measured intensity strongly depends on the availability of final states, as well as the light-matter interaction term, here described by the scalar product **p**.**A**.

[13] $a_{CMSi} = 5.65$, $a_{CMGe} = 5.75$ and $a_{CMSn} = 6.00$ Å.

	S. Ishida *et al.* [7]		S. Picozzi *et al.* [67]		H. Kandpal *et al.* [28]		Present work
	Δ_{gap}	$E_F - E_{VB}$	Δ_{gap}	$E_F - E_{VB}$	Δ_{gap}	$E_F - E_{VB}$	$E_F - E_{VB}$
Co_2MnSi	0.42	0.36	0.81	0.33	0.80	0.29	0.35
Co_2MnGe	0.21	0.09	0.54	0.03	0.58	0.05	0.2
Co_2MnSn	0.17	-0.06	-	< 0	0.41	-0.18	≤ 0

Table 3.3: Width of the minority spin gap Δ_{gap} and position of the Fermi energy compared to the minority valence band from three different theoretical works. $E_F - E_{VB} < 0$ means that the Fermi energy is located below the gap. All values are in eV.

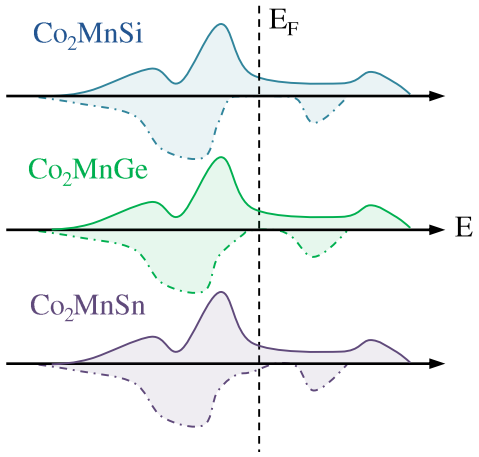

Figure 3.22: The qualitative trend followed by Co_2MnZ^{IV} alloys according to calculations [7, 28, 67] that matches the present experimental study.

slope by increasing *a*, therefore the width of the gap decreases as well.

In SR-PES experiments, only the part of the gap below E_F can be probed. The position of the Fermi energy compared to the gap is thus meaningless to speak of. However, the distance between the top of the minority valence band and the Fermi energy can be measured and this is what is compared to calculations in the table 3.3. Experimental data are in good agreement with the trend sketched in figure 3.22 even though it is impossible to know if E_F is in the middle of the gap or close to the minority conduction band.

Co_2MnZ^{III} compounds

Calculations all agree on the fact that Co_2MnZ^{III} are not pure HMM. The spin gap is actually a zone of very small minority DOS called a "pseudo gap" [28, 58]. One should not be able to differentiate a gap from a pseudo gap with SR-PES due to the too high sensitivity required.

Additionally, they show that the Fermi level falls in the minority valence band. The following table 3.4 shows the width of the pseudo gap Δ_{gap} and the distance between the Fermi level and the top of the minority valence band. All values are in eV.

Experimental values of the present studies are just indications because one is not able to probe above the Fermi level with SR-PES experiments. Thus, the top of the valence band can not be measured if E_F is below. Nonetheless, the trend follows the calculations for Co_2MnAl with a minority DOS not completely

	S. Ishida *et al.* [7]		K. Özdoğan *et al.* [58]		H. Kandpal *et al.* [28]		Present work
	Δ_{gap}	$E_F - E_{VB}$	Δ_{gap}	$E_F - E_{VB}$	Δ_{gap}	$E_F - E_{VB}$	$E_F - E_{VB}$
Co_2MnAl	0.31	-0.1	-	< 0	0.66	-0.17	< 0
Co_2MnGa	-	-	-	< 0	0.30	-0.36	≥ 0

Table 3.4: Width of the minority spin gap Δ_{gap} and position of the Fermi energy compared to the minority valence band from three different theoretical works. $E_F - E_{VB} < 0$ means that the Fermi energy is located below the gap. Experimental values from the present study are taken from figures 3.11 and 3.12. All values are in eV.

vanishing when approaching the Fermi energy. The case of Co_2MnGa is more puzzling. According to calculations, its SP should be lower than Co_2MnAl due to the location of E_F, well embedded in the minority valence band. However, a spin gap is experimentally observed in figure 3.12. The shape of the minority DOS on the same figure indicates that E_F falls indeed very close to the valence band but, apparently, slightly above it. Globally, for Co_2MnZ^{III} compounds, the situation is similar to the case of Co_2MnSn on the sketch 3.22.

Co_2MnZ^{V} compound

Theoretical works also exist for the Co_2MnSb alloy. In reference [66], they found the barely dispersing bands associated to the D transition at almost -2 eV in binding energy (suiting the rigid band model), which is not compatible at all with the observation of figure 3.14. Calculated gap features are shown in table 3.5 and once again show the same trend. For this compound, E_F is located very close to the minority conduction band.

	S. Ishida *et al.* [7]		H. Huang *et al.* [66]		Present work
	Δ_{gap}	$E_F - E_{CB}$	Δ_{gap}	$E_F - E_{CB}$	
Co_2MnSb	0.33	0.06	0.65	-0.09	no gap

Table 3.5: Width of the minority spin gap Δ_{gap} and position of the Fermi energy compared to the minority conduction band from two different theoretical works. $E_F - E_{CB} > 0$ means that E_F is located above the gap. All values are in eV.

No spin gap was experimentally observed in the present study for Co_2MnSb. This is not completely surprising given the structural / chemical defects in the crystal and the Sb reconstruction at the surface.

Quaternary $Co_2MnZ^{IV}_xZ^{III}_{1-x}$

Calculations were performed on the $Co_2MnSi_xAl_{1-x}$ series by S. Ishida *et al.* [7]. They found that E_F was indeed moving downward in the band structure by decreasing x and crosses the top of the minority spin valence band around $x = 0.4$. This is qualitatively consistent with the PES spectra observed in figure 3.15. On the other hand, no calculations were found for the second series $Co_2MnGe_xGa_{1-x}$.

Those $Co_2MnZ^{IV}_xZ^{III}_{1-x}$ series of alloys were extremely important to observe well the tuning of the Fermi energy in the band structure by removing one electron. As it will be demonstrated further in this chapter, the position of the Fermi level and its surroundings in term of minority DOS, in each alloy, will be of the greatest importance to explain the magnetic damping results.

3.2 Magnetic damping measurements

The aim of this section is to present magnetization dynamics measurements obtained on the same compounds characterized before, to access in particular the magnetic damping. An overview of magnetization dynamics without spin transfer torque and the fundamental principle of a FerroMagnetic Resonance (FMR) experiment are introduced first.

3.2.1 Magnetization dynamics

Accurate descriptions of the magnetization dynamics are done in several works [54, 139]. The objective in this section is to give direct key points to understand FMR results obtained on our different materials.

The Landau Lifshitz Gilbert equation

In this work, the magnetization dynamics $\mathbf{M}(\mathbf{r},t)$ is described by the phenomenological equation 3.16 called the Landau Lifshitz Gilbert (LLG) equation [140, 141].

$$\frac{d\mathbf{M}(\mathbf{r},t)}{dt} = -\gamma_0\mathbf{M}(\mathbf{r},t)\times\mathbf{H_{eff}}(\mathbf{r},t) + \frac{\alpha}{\mathrm{M_S}}\mathbf{M}(\mathbf{r},t)\times\frac{d\mathbf{M}(\mathbf{r},t)}{dt}, \tag{3.16}$$

where $\gamma_0 = \gamma\mu_0$ with $\frac{\gamma_0}{2\pi} = 28$ GHz.T^{-1} the gyromagnetic ratio of the free electron multiplied by the magnetic vacuum permeability. $\mathbf{H}_{\mathrm{eff}}(\mathbf{r},t)$ represents the effective field felt locally by the magnetization, which will be described later, $|\mathbf{M}| = \mathrm{M_S}$ the saturation magnetization and α, the Gilbert damping. The first term $-\gamma_0\mathbf{M}(\mathbf{r},t)\times\mathbf{H_{eff}}(\mathbf{r},t)$ is obtained in a similar way than the Ehrenfest theorem applied on the dynamics of the spin moment in quantum mechanics[14]. The effect of this term is to put the magnetization into a precession motion around the direction of $\mathbf{H_{eff}}$, exactly like in nuclear magnetic resonance for the nuclear magnetic moment. By considering only this term, the magnetization would never stop precessing around the effective field. It means that the magnetization would never be aligned along the effective field. The addition of the second term $\frac{\alpha}{\mathrm{M_S}}\mathbf{M}(\mathbf{r},t)\times\frac{d\mathbf{M}(\mathbf{r},t)}{dt}$ in equation 3.16 ensures that the magnetization precession is damped toward the effective field in a finite time, according to experimental observations. The magnetic damping α is a phenomenological dimensionless constant introduced by Gilbert and acts like a fluid friction. Even though the magnetization is damped along the direction of $\mathbf{H_{eff}}$, its magnitude is conserved under the LLG equation, allowing us to write $\mathbf{M}(\mathbf{r},t) = M_S\mathbf{m}(\mathbf{r},t)$, with $\mathbf{m}$ a unit vector.

In the following, derivations are made under the macrospin approximation. It means that all the electronic magnetic moments act coherently together without any spatial variation ($\mathbf{m}(\mathbf{r},t) = \mathbf{m}(t)$), leading

[14] By doing the assumption that only the spin momentum participates in the magnetization due to the quench of the orbital moment in transition metals.

to a direct correspondence between the magnetization and a microscopic magnetic moment. This assumption is justified when the magnetic material is well saturated with a static external magnetic field and for a non propagative $k = 0$ spin wave (*i. e.* FMR mode) like in the present study.

The effective field $\mathbf{H_{eff}}$

In nuclear magnetic resonance, the energy landscape is mainly made of the Zeeman interaction between the external static magnetic field and the nuclear moments. In a magnetic solid however, electronic spin and orbital moments and thus magnetic moments undergo different energy terms. The energy density terms taken into account in the present work are summarized in the equation 3.17 containing the exchange coupling term $\varepsilon_{\text{Exchange}}$, the magnetocrystalline anisotropy term $\varepsilon_{\text{Anisotropy}}$, the Zeeman energy due to the external applied field $\varepsilon_{\text{Zeeman}}$ and the demagnetizing field energy $\varepsilon_{\text{Demag}}$.

$$\varepsilon_{\text{Total}} = \varepsilon_{\text{Exchange}} + \varepsilon_{\text{Anisotropy}} + \varepsilon_{\text{Zeeman}} + \varepsilon_{\text{Demag}} \tag{3.17}$$

The different terms can be developed as follows:

(i) The exchange interaction term, $\varepsilon_{\text{Exchange}}$ results of the competition between the Coulomb interaction and the Pauli exclusion principle, supporting the alignment of adjacent spins in a very short range. At a mesoscopic scale, the exchange energy density can be written as:

$$\varepsilon_{\text{Exchange}} = A(\nabla \mathbf{m})^2, \tag{3.18}$$

with A the exchange stiffness in J.m^{-1} and $\mathbf{m} = \frac{\mathbf{M}}{M_S}$ the normalized magnetization. In ferromagnetic materials, the exchange interaction tends to align adjacent spins to minimize the system energy. With the macrospin approximation, the magnetization direction is the same everywhere in the sample, making this term equal to zero.

(ii) In the case of Co_2MnZ compounds, the anisotropy term $\varepsilon_{\text{Anisotropy}}$ is given by the cubic anisotropy expression, expressed as:

$$\varepsilon_{\text{Anisotropy}} = -K_1(m_x^2 m_y^2 + m_x^2 m_z^2 + m_z^2 m_y^2) + K_2 m_x^2 m_y^2 m_z^2, \tag{3.19}$$

where K_1 is the first order anisotropy constant in J.m^{-3} and $m_{x,y,z}$ are the projections of the normalized magnetization along the x, y, z directions coinciding with the cubic crystal lattice. The anisotropy constant K_1 is taken positive (negative) when the easy (hard) axis of the material coincide with the x, y, z directions of the lattice. The higher order term K_2 is easily neglected since the anisotropy is already very small in those compounds, as demonstrated in the previous chapter.

(iii) The Zeeman term is a simple consequence of the interaction between the external static magnetic field $\mathbf{H_0}$ with the spin magnetic moments in the materials (hence with the magnetization). With the macrospin approximation, the Zeeman energy density term is simply written as:

$$\varepsilon_{\text{Zeeman}} = -\mu_0 M_S \mathbf{m}(t) \cdot \mathbf{H_0}(t) \tag{3.20}$$

(iv) The demagnetizing energy term, $\varepsilon_{\text{Demag}}$, is due to the stray field generated by all the moment in the volume, on the local magnetization that produces a demagnetizing field $\mathbf{H}_{\text{Demag}}$. Starting from

Maxwell's equations and by making this demagnetizing field interact with the magnetization in a dipolar way, the demagnetizing energy density term in thin films (with x the out of plane direction) can be approximated by [142]:

$$\varepsilon_{\text{Demag}} = \frac{1}{2}\mu_0 M_S^2 m_x^2 \tag{3.21}$$

This term is always opposed to put the magnetization in the out of plane direction in thin films.

By considering the geometry in figure 3.23, where the static magnetic field is applied in the perpendicular direction of the thin film, the equation 3.17 can be expanded to read:

$$\varepsilon_{\text{Total}} = K_1(m_x^2 m_y^2 + m_x^2 m_z^2 + m_z^2 m_y^2) - \mu_0 M_S H_0 m_x + \frac{1}{2}\mu_0 M_S^2 m_x^2 \tag{3.22}$$

The effective field $\mathbf{H_{eff}}$, can be derived from the total magnetic energy,

$$\mathbf{H_{eff}} = -\frac{1}{\mu_0 M_S}\nabla_{\mathbf{m}}(\varepsilon_{\text{Total}}). \tag{3.23}$$

In our FMR experiments, the static magnetic field (applied out of the plane of the film) is strong enough to saturate the magnetization along a direction that corresponds to a minimum of the cubic magneto-crystalline energy (along x in the present work, see figure 3.23). Therefore, by keeping only first order terms in the magnetosryctalline anisotropy energy, the resulting effective field has the following expression:

$$\mathbf{H_{eff}} = \begin{pmatrix} H_0 - m_x(M_S - H_k) \\ 0 \\ 0 \end{pmatrix} = \begin{pmatrix} H_0 - m_x M_{\text{eff}} \\ 0 \\ 0 \end{pmatrix}, \tag{3.24}$$

with $H_k = \frac{2K_1}{\mu_0 M_S}$ being the anisotropy field and $M_{\text{eff}} = M_S - H_k$ the effective magnetization. This expression for $\mathbf{H_{eff}}$ allows us to derive the LLG equation and to obtain an expression for the magnetization motion.

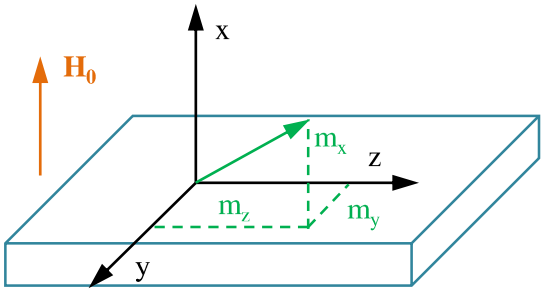

Figure 3.23: Cartesian frame used in the present section.

Linearization and resolution of the LLG equation

By using equations 3.16 and 3.24, a system of three non linear equations is obtained. In a FMR experiment, the excitation field is small enough in amplitude to consider the small oscillations regime that allows us to linearize such a system of equations. For a static magnetic field $\mathbf{H_0}$ strong enough to saturate

the magnetization out of the plane, the direction x on figure 3.23 becomes the equilibrium position. The small oscillation regime is equivalent to considering that $m_{y,z} \ll 1$ and that $m_x = \sqrt{1 - m_y^2 - m_z^2} \simeq 1 - \frac{1}{2}(m_z^2 + m_y^2) \simeq 1$, to first order in m_x. By using this conservation of m_x, the system of interest is now reduced to the transverse components of the magnetization $m_{y,z}$. After a few lines of derivation, the LLG equation reads:

$$\frac{d\mathbf{m}(t)}{dt} = \frac{\gamma_0 \widetilde{H}}{1+\alpha^2} \begin{pmatrix} -\alpha & -1 \\ 1 & -\alpha \end{pmatrix} \mathbf{m}(t) \tag{3.25}$$

With $\widetilde{H} = H_0 - M_{\text{eff}}$. To decouple those two equations, the matrix must be diagonalized in the complex space $\mathbb{C}$. The two eigenvalues, denoted λ and its conjugate λ^* are simply:

$$\lambda = -\frac{\gamma_0 \widetilde{H}}{1+\alpha^2}(\alpha + i) \qquad \lambda^* = \frac{\gamma_0 \widetilde{H}}{1+\alpha^2}(i - \alpha) \tag{3.26}$$

The diagonalization leads to new eigenstates in which the transverse components of the magnetization take a different form from $m_{y,z}$. Derivations of new eigenstates to find the new components of $\mathbf{m}$ in this diagonal basis are not necessary. It can be shown [139] that the expression of $m_{y,z}$ can still be expressed in the following form:

$$\begin{cases} m_y(t) = [Ae^{i\omega_r t} + Be^{-i\omega_r t}]e^{-\frac{t}{\tau}} \\ m_z(t) = [Ce^{i\omega_r t} + De^{-i\omega_r t}]e^{-\frac{t}{\tau}} \end{cases} \tag{3.27}$$

Which is an harmonic form (complex exponential) multiplied by a damping term (real exponential). The motion of the magnetization is indeed a damped precession around its equilibrium position, fixed by $\mathbf{H_0}$ in our experimental configuration. The two important parameters of the motion, the pulsation ω_r and the relaxation time τ are:

$$\omega_r = \frac{\gamma_0 \widetilde{H}}{1+\alpha^2} \qquad \tau = \frac{1+\alpha^2}{\alpha \gamma_0 \widetilde{H}} \tag{3.28}$$

The magnetization precession describes a circular spiral (figure 3.24) because the two transverse components of the magnetization are equivalent in amplitude in the perpendicular geometry. There are two

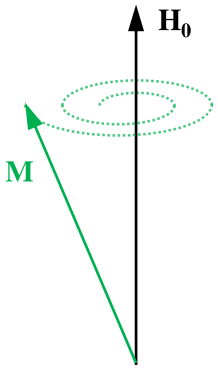

Figure 3.24: Sketch of the precession motion of the magnetization $\mathbf{M}$ when $\mathbf{H_0}$ is applied in the perpendicular direction of the film.

important features to note in equations 3.28. First, when $\alpha < 1$, the relaxation time increases by decreasing α. In this case ($\alpha < 1$), the higher the damping, the shorter the precession motion. Second, for small dampings like in the present work ($\alpha < 5 \times 10^{-3}$), the frequency is equivalent to the Larmor frequency.

An FMR experiment aims to measure those two parameters.

3.2.2 Ferromagnetic resonance

FMR relies on the study of the magnetic response of the magnetization to a small monochromatic radio-frequency (RF) oscillating magnetic field. It is measured thanks to the dynamic magnetic susceptibility of the sample through the linear response of the magnetization to the exciting field. The experimental set-up and geometry used in this study are discussed in the following.

Linear response and dynamic susceptibility

The basic principle of a FMR experiment is to measure the system's response to an harmonic excitation. A linear response regime is obtained when the exciting field is very small in amplitude compared to the effective field field $\mathbf{H_{eff}}$. It means that the energy landscape is not altered by the excitation. The response of the magnetization follows the frequency of the harmonic excitation field with a proportionality coefficient called the dynamic magnetic susceptibility. It is a (2x2) tensor which depends on the frequency of the harmonic excitation. Let us define the harmonic field $\mathbf{h}(\omega)$ and the response of the transverse components of the magnetization $m_{y,z}(\omega)$:

$$\mathbf{h}(\omega) = \mathrm{Re}(\mathbf{h}e^{-i\omega t}) \qquad \mathbf{m}(\omega) = \mathrm{Re}(\mathbf{m}e^{-i\omega t}) \tag{3.29}$$

Application of this harmonic field leads to a new effective field:

$$\mathbf{H_{eff}} = \begin{pmatrix} H_0 - m_x M_{\mathrm{eff}} + h_x \\ h_y \\ h_z \end{pmatrix} \tag{3.30}$$

By replacing this new effective field in the LLG equation 3.16, and after linearization, we obtain:

$$\mathbf{m}(\omega) = \gamma_0 M_S \begin{pmatrix} -i\omega\alpha + \gamma_0 \widetilde{H} & +i\omega \\ -i\omega & -i\omega\alpha + \gamma_0 \widetilde{H} \end{pmatrix}^{-1} \mathbf{h}(\omega) \tag{3.31}$$

The definition of the dynamic susceptibility allows us to write the dynamic susceptibility tensor $\chi(\omega)$ as:

$$\begin{pmatrix} m_y(\omega) \\ m_z(\omega) \end{pmatrix} = \begin{pmatrix} \chi_{yy} & \chi_{yz} \\ \chi_{zy} & \chi_{zz} \end{pmatrix} \begin{pmatrix} h_y(\omega) \\ h_z(\omega) \end{pmatrix} \tag{3.32}$$

With $\chi(\omega) = \chi^{'}(\omega) + i\chi^{''}(\omega)$. Nonetheless, in our present set-up described in the following, the RF field is applied along the y direction. It means that $h_z = 0$ and thus that only χ_{yy} and χ_{yz} have to be considered. Moreover, χ_{zy} is the coefficient that relate the m_z response to the h_y excitation. The dynamics of M_z does not play a role in the variation of inductance measured by the Vector Network Analyzer (VNA) where z is the propagation direction of the wave that produces the harmonic field. Thereby, only $\chi_{yy}(\omega)$ is probed in our geometry and is expressed in equation 3.33 by neglecting all the terms $\alpha^2 + 1 \simeq 1$, completely justified in this study where typical values of α are 10^{-3}.

$$\chi'_{yy}(\omega) \simeq \gamma_0 M_S \frac{\omega_r(\omega_r^2 - \omega^2)}{(\omega_r^2 - \omega^2)^2 + \Delta^2\omega^2}$$
$$\chi''_{yy}(\omega) \simeq \gamma_0 M_S \frac{(\alpha\omega_r^2 + \omega^2)\omega}{(\omega_r^2 - \omega^2)^2 + \Delta^2\omega^2} \tag{3.33}$$

with $\omega_r = \gamma_0 \widetilde{H}$ the resonance frequency of the equation 3.28 (still neglecting α^2 compared to the unity) and $\Delta = 2\omega_r\alpha$. The dynamic susceptibility has thus a typical shape of a resonance phenomenon, similar to a Lorentzian and the derivative of a Lorentzian functions as real and imaginary parts. The two parts of the susceptibility are naturally centered at $\omega = \omega_r$ and the Full Width at Half Maximum (FWHM) is equal to $\Delta = 2\alpha\omega_r$. An example of susceptibility terms versus the frequency of the harmonic field is plotted in the figure 3.25 using equation 3.33. The next step is to measure the dynamic susceptibility, or at least one coefficient of the tensor by using a VNA. This way, we can obtain intrinsic magnetic parameters like the Gilbert damping α, the gyromagnetic ratio γ_0 and the effective magnetization M_{eff}.

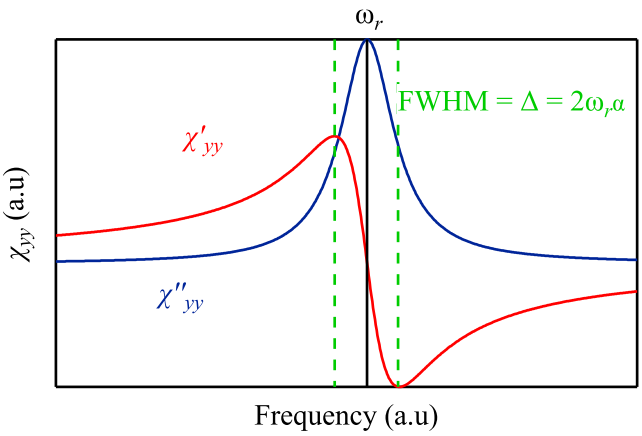

Figure 3.25: Example of imaginary and real parts of a dynamic susceptibility in the present study. The magnetic damping is proportional to the width of the resonance peak.

Broadband VNA-FMR and experimental features

FMR is a common method to extract intrinsic parameters of the magnetization dynamics in thin films. It is always made by mean of dynamic susceptibility measurements. Two methods have to be distinguished. The first one is achieved by putting the sample in a RF cavity which allows an harmonic field of small amplitude to be generated. Then, a static magnetic field is swept and there is an absorption of the RF power when the value of $\mathbf{H_0}$ matches with the resonance frequency of the system (see previous section on the susceptibility). The second one, which is used in the present study, uses a VNA to produce and analyze an RF signal that flows in a ground-signal-ground (GSG) coplanar waveguide as shown in figure 3.26. In that case, the frequency is swept and the static field is fixed. Using this method, the energy landscape felt by the magnetization does not change since the static field is fixed.

It can be shown that the scattering matrix S, which is the physical quantity measured by the VNA,

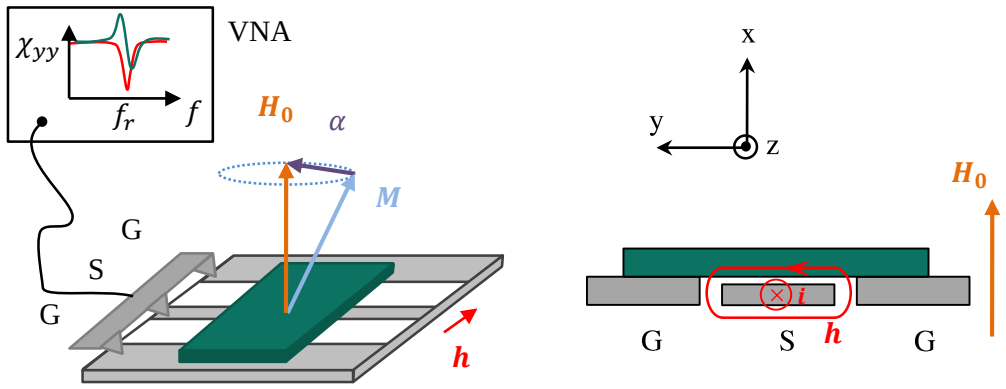

Figure 3.26: Sketch of the broadband VNA-FMR set-up and the GSG coplanar waveguide.

can be linked to the dynamic susceptibility [54, 143]. In the present work, measurements are made in reflection which means that only the S_{11} parameter of the scattering matrix is measured and is related to the χ_{yy} coefficient of the dynamic susceptibility. The two parts of $\chi_{yy}(\omega)$ are measured and correspond to the phase and amplitude of the reflected RF signal. Therefore, according to equation 3.33 and figure 3.25, the magnetic damping can be extracted by looking at the width of the resonance peak, proportional to α. However, there is often an inhomogeneous linewidth at zero frequency. It finds its origin in defects and inhomogeneity in the magnetic phase probed by the RF field (intrinsic inhomogeneity) and in the experimental broadening like spatial and/or amplitude inhomogeneity in the static and RF magnetic fields (extrinsic). Due to this inhomogeneous linewidth, the magnetic damping is extracted by looking at the linear variation of the linewidth with the static magnetic field, as represented in equations 3.34 concerning the Half Width at Half Maximum (HWHM) Δf. The inhomogeneous linewidth Δf_0 thus corresponds to the HWHM when the static field matches with M_{eff}.

$$\begin{aligned} f_r &= \gamma_0(H_0 - M_{\text{eff}}) \\ \Delta f &= \alpha f_r + \Delta f_0 = \text{HWHM} \end{aligned} \tag{3.34}$$

with $M_{\text{eff}} = M_S - H_k$. Thanks to these two equations, the magnetization as well as the magnetic damping can be extracted, by using linear fits of the resonance frequency and HWHM of the resonance peaks for different values of static magnetic field H_0.

Two-magnon scattering avoiding. The static magnetic field $\mathbf{H_0}$ has been chosen out of the plane of the film to avoid the broadening of the resonance peak due to two-magnon scattering [144]. FMR refers to the uniform non-propagative spin wave excitation with a momentum $k = 0$. Nonetheless, many spin wave modes with $k \neq 0$ exist and are not directly excited by the microwave field. The uniform FMR spin wave can be coupled to these non-uniform modes due to inhomogeneities in the microwave field, thereby decreasing the relaxation time of the precession motion (increasing the linewidth of the resonance peak [57]). This mechanism occurs only when the dispersion relation of non-uniform magnons crosses the FMR frequency (degeneracy). When the magnetization is in plane, there is a large density of $k \neq 0$ magnons states that allows scattering of the FMR mode. Those $k \neq 0$ states are no more available, at the FMR frequency, when the magnetization is out of the plane of the thin film [57, 144–146]. Then, the out

of plane geometry allows to get a better estimation of the intrinsic damping.

Susceptibility fitting. In order to plot the curves described by equations 3.34, one has to be able to fit correctly the real and imaginary parts of the susceptibility measured by the VNA. The first step is to remove the background of the χ_{yy} coefficient [54]. It is done by correcting the trace of interest recorded by the VNA by a reference signal that does not contain magnetic effects from the layer. Then, a Wolfram Mathematica program has been developed. It fits simultaneously the two parts of χ_{yy} using the same parameters (linewidth, resonance frequency) for better accuracy. In the program, there is also a "mixing angle" parameter that mixes the real and imaginary parts as follows:

$$\begin{aligned} \chi_{\mathrm{Re}} &= \cos(\theta)\chi_{yy}^{'} + \sin(\theta)\chi_{yy}^{''} \\ \chi_{\mathrm{Im}} &= -\sin(\theta)\chi_{yy}^{'} + \cos(\theta)\chi_{yy}^{''} \end{aligned} \tag{3.35}$$

This mixing angle θ does not change the resonance frequency and linewidth of the peak. θ is often very close to zero but takes higher values when the resonance does not have a well-defined Lorentzian shape. It traduces the coupling between the sample and the waveguide and therefore the presence of eddy currents, which contribute to extrinsically increase the damping (see next paragraph).

As it will be shown further, due to the well Lorentzian shaped resonances in most of Heusler compounds, high quality fits are obtained with this process (with most of the time, $\theta = 0$).

Effective α_{eff} values. The effective damping contains extrinsic contributions known as the radiative damping, the eddy currents damping and the spin-pumping contributions (equation 3.36).

$$\alpha_{\mathrm{eff}} = \alpha_{\mathrm{int}} + \alpha_{\mathrm{eddy}} + \alpha_{\mathrm{rad}} + \alpha_{\mathrm{sp}} \tag{3.36}$$

α_{eddy} and α_{rad} both originate from eddy currents that are induced by the time-varying flux of the precessing magnetic moments (Faraday's law). The generated alternative currents re-induce small out of phase magnetic fields that broaden the FMR peak. α_{eddy} is the damping contribution from eddy currents induced within the sample. It is linked to the magnetization, the resistivity and the thickness of the thin film [147]. In the other hand, α_{rad} is the contribution from eddy currents induced in the waveguide and depends on other parameters like the sample and waveguide dimensions [147]. Those two α_{eddy} and α_{rad} contributions are linked to the mixing angle described in the previous paragraph. Care was taken to consider only measurements with almost 0 mixing angle, meaning that eddy currents coupling is small. The spin pumping contribution α_{sp} comes from the transverse spin current generated toward the capping layer which is also a relaxation contribution to the uniform precession. It is nonetheless assumed to be small in Au layers [148] (the capping layer mostly used in this study).

The measurement of these contributions is very involved and often requires a series of samples to be grown and relies on theoretical models [24, 33, 147]. Additionally, this correction process requires a precise control of geometrical parameters of the experiment that can induce errors. Therefore we did not try to subtract these contributions. All forthcoming magnetic damping values presented in this section are raw effective values, corresponding to α_{eff} in equation 3.36. **So we always measure an upper limit of the magnetic damping, meaning that the intrinsic damping must be smaller**.

3.2.3 Ternary Co_2MnZ compounds

To compare with the photo-emission section, the division between $Co_2MnZ^{IV, III, V}$ alloys is still being used, with the same order.

Co_2MnZ^{IV}

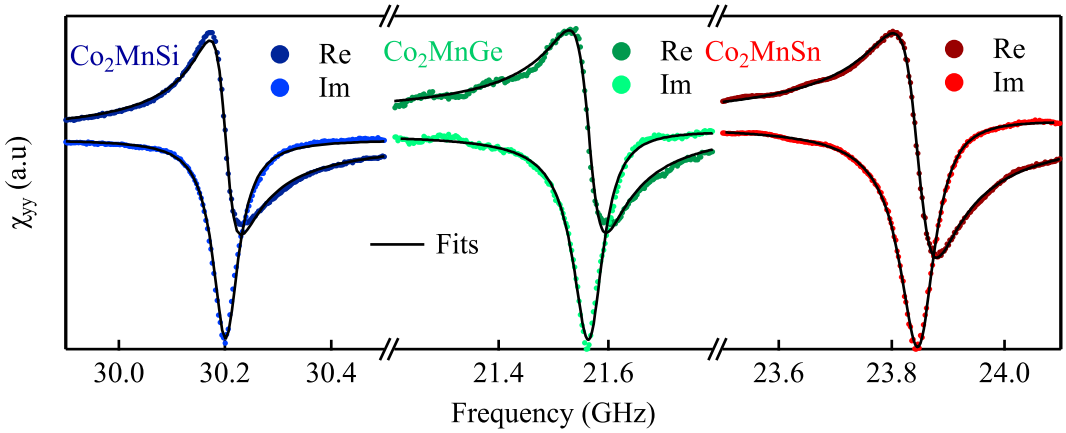

Figure 3.27: Examples of χ_{yy} measurements for Co_2MnSi (blue curves), Co_2MnGe (green curves) and Co_2MnSn (red curves) at room temperature. Measurements are taken at different values of static magnetic field: respectively 2.38 T, 1.9 T and 2.05 T. Black lines are fits using the Mathematica program.

The figure 3.27 shows the measured χ_{yy} parameters for Co_2MnSi (blue curves), Co_2MnGe (green curves) and Co_2MnSn (red curves), each for different static magnetic field values and after subtraction of the background. All the curves have a good signal to noise ratio, with a very well defined resonance peak. On the same figure are added the fits (black curves) made with the Mathematica program. Important parameters like the resonance frequency and the HWHM are extracted from those fits and are plotted in figure 3.28 that are experimental illustrations of the two equations 3.34.

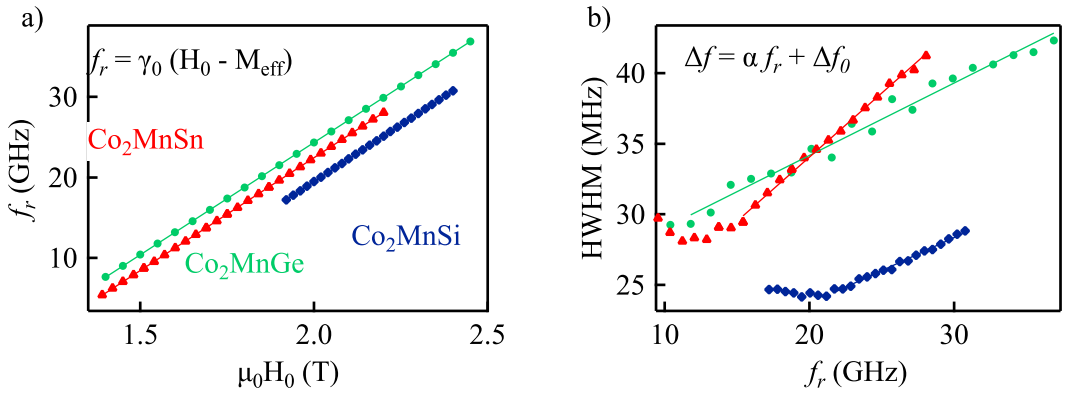

Figure 3.28: FMR measurements for Co_2MnSi (blue curves), Co_2MnGe (green curves) and Co_2MnSn (red curves) at room temperature. a) the variation of the resonance frequency with field that gives access to the magnetization and the Landé g factor through γ_0. b) increase of the HWHM of the resonance peak as a function of its own resonance frequency, with a slope equal to the magnetic damping.

The advantage of the perpendicular geometry is that both curves are linear which is really convenient

to fit. Thanks to those two lines, important intrinsic magnetic parameters are extracted and presented in the table 3.6. For those compounds, since the magnetocrystalline anisotropy is very small, it is possible to consider $M_{\text{eff}} \simeq M_S$. Magnetization values obtained are in good agreement with the XMCD results in the previous chapter, except for Co_2MnSn which we found with one supplementary μ_B with this technique. This could be due to a bad estimation of the number of holes for the determination of the magnetic moments from XMCD measurements. In any case, the magnetization of Co_2MnSn is not far from the Slater-Pauling value of 5 μ_B/f.u. Additionally, they all have a Landé g factor corresponding to the theoretical value of 2 (for a non interacting electron case), expected for $3d$ transition metals and alloys.

	M_{eff} (μ_B/f.u)	g ($\pm$0.02)	α	Δf_0 (MHz)
Co_2MnSi	5.08	2.01	$4.6 \pm 0.1 \times 10^{-4}$	14.3
Co_2MnGe	4.63	1.99	$5.1 \pm 0.2 \times 10^{-4}$	23.9
Co_2MnSn	5.51	2.00	$9.1 \pm 0.15 \times 10^{-4}$	15.9

Table 3.6: Intrinsic magnetic parameters of Co_2MnZ^{IV} compounds at room temperature.

The most important result is the very small magnetic damping obtained for each Co_2MnZ^{IV} compound, in the 10^{-4} range. It is almost one order of magnitude lower than transition metals and alloys already considered as low damping materials [24, 149] that are not HMM. Moreover, the inhomogeneous linewidth is also very small, confirming the magnetic phase homogeneity and small number of defects in the samples. A magnetic damping of $\alpha = 7 \times 10^{-4}$ was reported in this work [10] on Co_2MnSi grown with the MBE at the Cassiopée beamline. A better control of the stoichiometry is achieved on layers grown with the MBE on the IJL TUBE and explains that the damping value goes down to $\alpha = 4.6 \times 10^{-4}$ on the same compound. In addition, this ultra low magnetic damping behavior is now extended to three Heusler compounds.

Co_2MnZ^{III}

The figure 3.29 shows the χ_{yy} curves obtained for Co_2MnAl (red curves) and Co_2MnGa (green curves) compounds. The resonance peak, using $H_0 = 1.675$ T for Co_2MnAl is very well defined and narrow like it was for Co_2MnZ^{IV} alloys with a high fitting quality (black curves). The situation if very different for Co_2MnGa where the peak has shoulders, even for high magnetic field values (here 2.1 T) that make the fitting process hard to converge. It was the case for every sample of Co_2MnGa that was measured during this study.

The presence of several peaks (at least two) in figure 3.29 for Co_2MnGa means that more than one magnetic phase[15] is probed by the RF field. Still, due to the vicinity of those peaks in frequency but also in linewidth, equations 3.34 can be plotted by taking into account an "average" peak as demonstrated in figure 3.29. Nonetheless, it increases the uncertainty on the effective magnetization and magnetic damping obtained by the linear fits. Hopefully the two main peaks, very close to each other, seem to move together in frequency and in linewidth, meaning that the effective magnetization and magnetic damping

[15] With a different effective magnetization, linewidth *etc.*

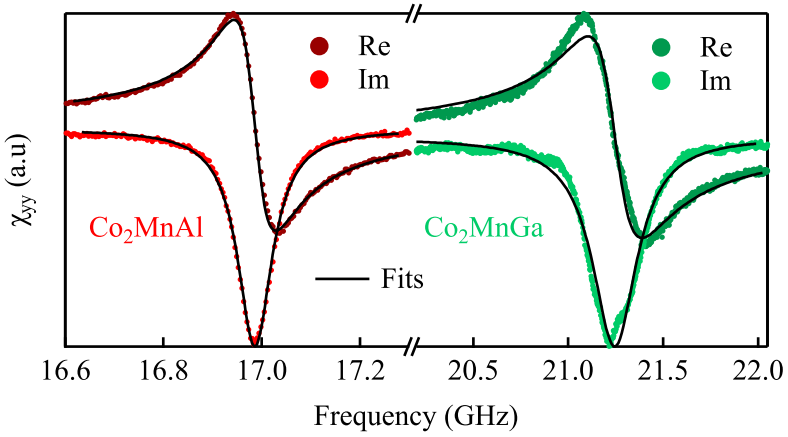

Figure 3.29: Examples of χ_{yy} measurements for Co_2MnAl (red curves) and Co_2MnGa (green curves) at room temperature. Measurements are taken at different values of static magnetic field: respectively 1.675 T and 2.1 T. Black lines are fits using the Mathematica program.

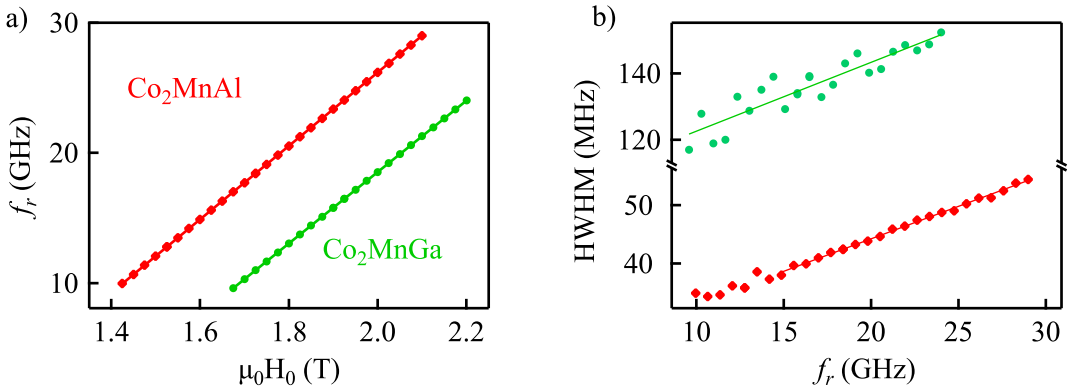

Figure 3.30: FMR measurements for Co_2MnAl (red curves) and Co_2MnGa (green curves) at room temperature.

values should be meaningful.

The corresponding $f_r(H_0)$ and HWHM(f_r) curves are plotted in figure 3.30. The variation of resonance frequencies with field is well linear for both Co_2MnZ^{III} alloys (figure 3.30-a)). The effective magnetization of Co_2MnGa is large, well visible with the right shift of the curve compared to Co_2MnAl. In figure 3.30-b), the linewidth variation is astonishingly linear for Co_2MnAl, leading to a magnetic damping value of $\alpha = 1.10 \pm 0.01 \times 10^{-3}$, slightly higher than Co_2MnSn. For Co_2MnGa though, the damping is larger $\alpha = 2.0 \pm 0.2 \times 10^{-3}$ as suspected by its large offset in linewidth visible in figure 3.30-b). Magnetic parameters of interest are listed in table 3.7.

Magnetic moments are a little higher but close to those obtained by XMCD. For Co_2MnGa, the moment is once again larger than the expected Slater-Pauling value by more than 1 μ_B. The difference of almost 0.5 μ_B between FMR and XMCD is due to the supplementary contribution of the anisotropy field H_k included in M_{eff} which can not be neglected for this compound, as suggested in figure 2.34. Landé g factors are also close to 2 with a little deviation for Co_2MnGa, which could be due to a stronger spin orbit coupling in this compound, explaining its higher magneto-crystalline anisotropy. Magnetic

	M_{eff} (μ_B/f.u)	g ($\pm$0.02)	α	Δf_0 (MHz)
Co_2MnAl	4.32	2.02	$1.1 \pm 0.01 \times 10^{-3}$	22
Co_2MnGa	5.41	1.96	$2.0 \pm 0.2 \times 10^{-3}$	102

Table 3.7: Intrinsic magnetic parameters of Co_2MnZ^{III} compounds at room temperature.

damping values are higher than Co_2MnZ^{IV} compounds but are still in the "low damping zone". Finally, inhomogeneous linewidths are very different between the two compounds. The value for Co_2MnAl is in the same range than Co_2MnZ^{IV} compounds, with a very narrow peak meaning that a strong homogeneity occurs in the layer. In the other hand, the Co_2MnGa inhomogeneous linewidth is one order of magnitude higher than all other alloys. Different phases are taking place in Co_2MnGa layers, to such an extent that other peaks are visible.

Co_2MnZ^V

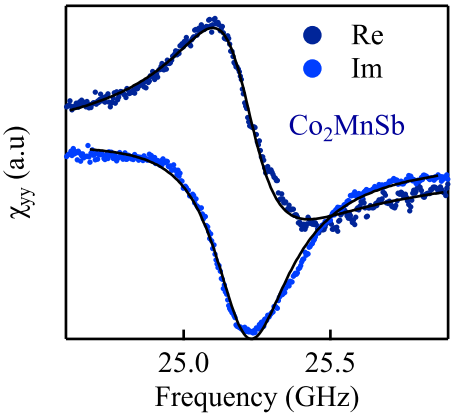

Figure 3.31: Examples of χ_{yy} measurements for Co_2MnSb at room temperature, taken at 2.025 T.

Finally, the χ_{yy} parameter of Co_2MnSb compound is plotted in figure 3.31. The resonance peak has also a distorted shape, not completely Lorentzian. There should be several magnetic phases supported by previous observation on XRD and TEM in chapter 2. However, the peak is well fitted and FMR curves are represented in figure 3.32. Once again, the variation of the resonance with the magnetic field is well linear and so is the evolution of the linewidth. The slope of the linewidth gives a damping value of $\alpha = 9.7 \pm 0.4 \times 10^{-4}$. This is quite a surprising value regarding the form of the peak and the large inhomogeneous linewidth. Indeed, Co_2MnSb has the larger inhomogeneous linewidth with 133 MHz. The intrinsic magnetic parameters are reported in table 3.8. The magnetization value is not on the Slater-Pauling curve but according to reference [8], Heusler with 30 valence electrons can never reach 6 μ_B/f.u.

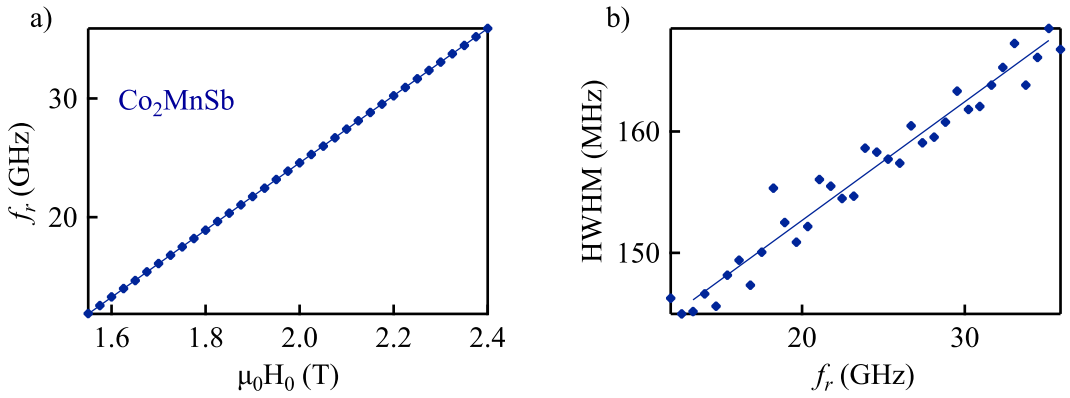

Figure 3.32: FMR measurements for Co_2MnSb at room temperature.

	M_{eff} (μ_B/f.u)	g	α	Δf_0 (MHz)
Co_2MnSb	5.05	2.02	$9.7 \pm 0.4 \times 10^{-4}$	133

Table 3.8: Intrinsic magnetic parameters of Co_2MnZ^V compound at room temperature.

3.2.4 Quaternary $Co_2MnZ^{IV}_xZ^{III}_{1-x}$ alloys

In this subsection, magnetic damping of quaternary alloys previously measured by photo-emission are presented.

$Co_2MnSi_xAl_{1-x}$

The χ_{yy} parameters measured on the $Co_2MnSi_xAl_{1-x}$ series are shown in figure 3.33. One can see that resonance peaks are not as well defined as in ternary Co_2MnAl and Co_2MnSi compounds. It looks like there are several peaks convoluted in one, resulting in distorted shapes even though shoulders or secondary peaks are not always visible (except for $x = 0.75$ where two peaks are clearly distinguishable). Despite the shoulders and distorted shape of the resonance peaks, very small linewidths are observed for

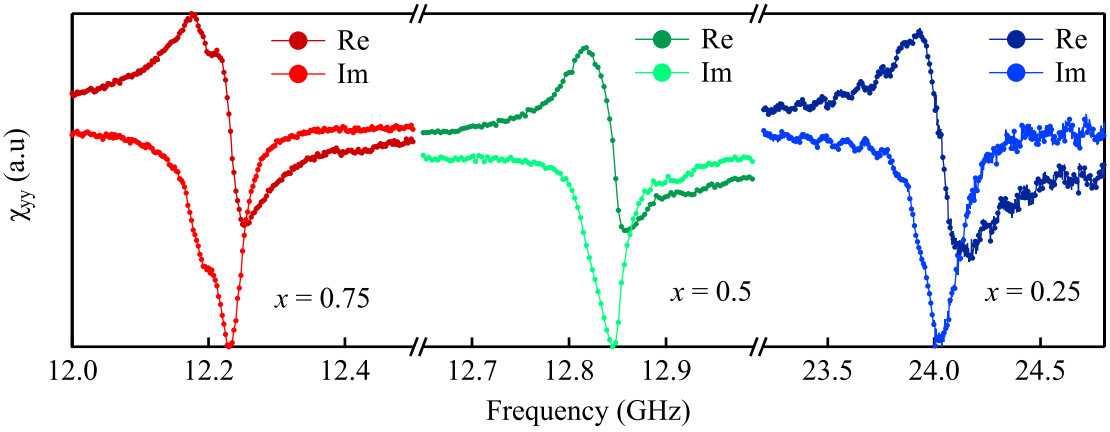

Figure 3.33: Examples of χ_{yy} parameters for different substitution rate in the $Co_2MnSi_xAl_{1-x}$ series at room temperature, respectively at 1.675 T, 1.675 T and 2.05 T.

the whole substitution range x (except at $x = 0.25$). It goes in the sense that, even if several magnetic phases are probed by the RF field, they are well homogeneous with few defects. When $0 < x < 1$, we have shown in the previous chapter that there was coexistence of B2 and $L2_1$ domains. Those two phases do not have the exact same magnetic parameters and it could explain the presence of several peaks [150]. Unfortunately, like in the case of Co_2MnGa, it is not possible to treat independently every peaks due to their convolution. However, the "average" peak can be fitted and it leads to a good estimation of the magnetic parameters.

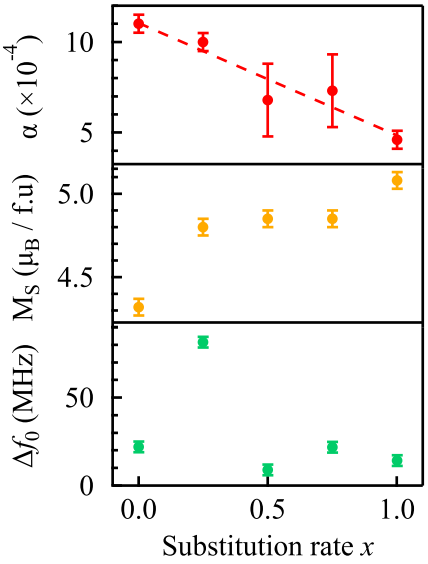

Figure 3.34: Magnetic damping, magnetization and inhomogeneous linewidth of the $Co_2MnSi_xAl_{1-x}$ series at room temperature.

The FMR parameters of the $Co_2MnSi_xAl_{1-x}$ series are plotted in figure 3.34. First of all, the number of points is very low which makes the strict interpretation of the curves shape difficult. The decrease of the damping is linear with x, going from 1.1×10^{-3} in Co_2MnAl to 4.6×10^{-4} in Co_2MnSi. In other words, the Gilbert damping coefficient is tunable with the substitution rate x. The effective magnetization[16] increases with x almost linearly as expected by the Slater-Pauling criterion. Finally, as already suspected by the narrow linewidth in figure 3.33, the inhomogeneous linewidth Δf_0 is very small for the entire range of x, except for $x = 0.25$ which is puzzling. Nonetheless, it confirms a good homogeneity and quality of the different magnetic phases in the films for all the other compounds.

$Co_2MnGe_xGa_{1-x}$

A very similar behavior is observed for the $Co_2MnGe_xGa_{1-x}$ series, as demonstrated in figure 3.35. χ_{yy} parameters show a convolution of peaks except that this time, linewidths are larger, as if the substitution of Ge by Ga atoms had added a larger inhomogeneity in the samples.

Magnetic parameters extracted from the FMR analysis are plotted in figure 3.36. As in the previous series, the magnetic damping decreases with x but this time it has a non-monotonic shape. The larger error bar at $x = 0.5$ on α is due to a higher dispersion of the HWHM on this sample. Thus, it increases the

[16]Magnetization values were calculated by taking the lattice constants obtained by XRD in the previous chapter.

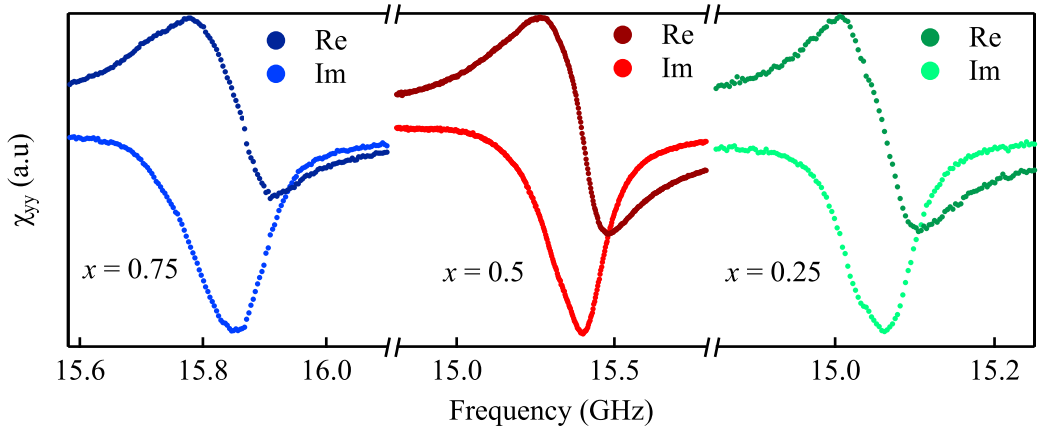

Figure 3.35: Examples of χ_{yy} parameters for different substitution rate in the $Co_2MnGe_xGa_{1-x}$ series at room temperature, each taken at 1.6 T.

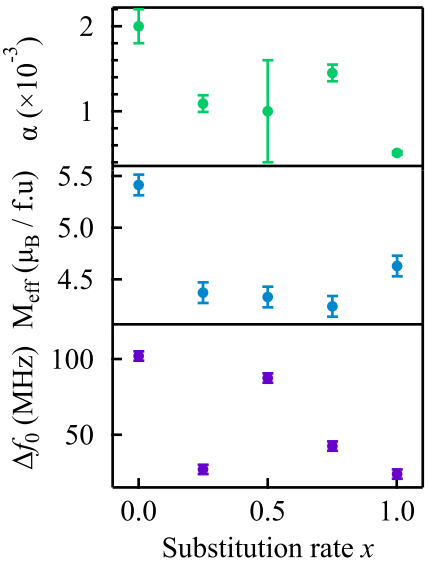

Figure 3.36: Magnetic damping, magnetization and inhomogeneous linewidth of the $Co_2MnGe_xGa_{1-x}$ series at room temperature.

uncertainty on α. Furthermore, the peculiar shape of the effective magnetization curve, first decreasing then increasing with x, can be explained by using the following argument: it has been shown previously by XMCD and FMR that Co_2MnGe follows the Slater-Pauling curve but that Co_2MnGa had at least one supplementary μ_B/f.u to follow it. Thus, in theory, the curve should increase from 4 at $x = 0$ to 5 at $x = 1$ (like in $Co_2MnSi_xAl_{1-x}$). It explains that at small Ga concentration ($x = 0.75$), the curve is decreasing. But by increasing Ga content (decreasing x), the special behavior of Co_2MnGa takes over and the curve goes up. In addition to that, the anisotropy constant H_k is stronger at high Ga content, which explains the additional 0.5 μ_B obtained in effective magnetization of Co_2MnGa compared to the moment obtained by XMCD. Eventually, inhomogeneous linewidths are higher in this series, confirming that Co_2MnGa must have more inhomogeneities and relaxation processes in the precession.

To conclude on these quaternary series of alloys $Co_2MnZ^{IV}_xZ^{III}_{1-x}$, an important result is that when $x \neq 0$, more than one resonance peak is present. It is easily understandable for the first series $Co_2MnSi_xAl_{1-x}$ since there is a competition of chemical ordering as shown by STEM-HAADF in chapter 2. Hence at least two magnetic phases are probed by the RF field in FMR experiments. In the work of Abdallah *et al.* [72], they identify the different resonance peaks belonging to B2 or $L2_1$ magnetic phases on Co_2MnSi. It cannot be done in the present study because of the vicinity of the peaks that are most of the time completely convoluted. Nonetheless, even though two magnetic phases are present in the quaternary layers, resonance peaks are very narrow with small linewidths and dampings still in the 10^{-4} range.

The second series $Co_2MnGe_xGa_{1-x}$ does not suffer a chemical transition like the previous one. It is thus puzzling to understand the presence of several peaks. It seems that even for small concentration of Ga atoms, the linewidth and magnetic damping are strongly affected. It is an additional evidence that Co_2MnGa has a peculiar magnetic and electronic behavior. This point will be discussed in the last section of this chapter.

3.2.5 Polycrystals

The polycrystals measured by SR-PES were also measured with FMR. These results will be very important to correlate the magnetic damping with the spin polarization at the end of this chapter.

χ_{yy} parameters for the three polycrystals Co_2MnSi, Co_2MnGe and Co_2MnGa taken at 1.8 T are shown in figure 3.37. Co_2MnSi and Co_2MnGe present a very well defined resonance peak, easily fitted, like in the epitaxial case. Their linewidths are small, suggesting a strong magnetic homogeneity even in a polycrystalline form. In the same way, Co_2MnGa presents a similar behavior than in the epitaxial case, with a distorted peak and a large linewidth.

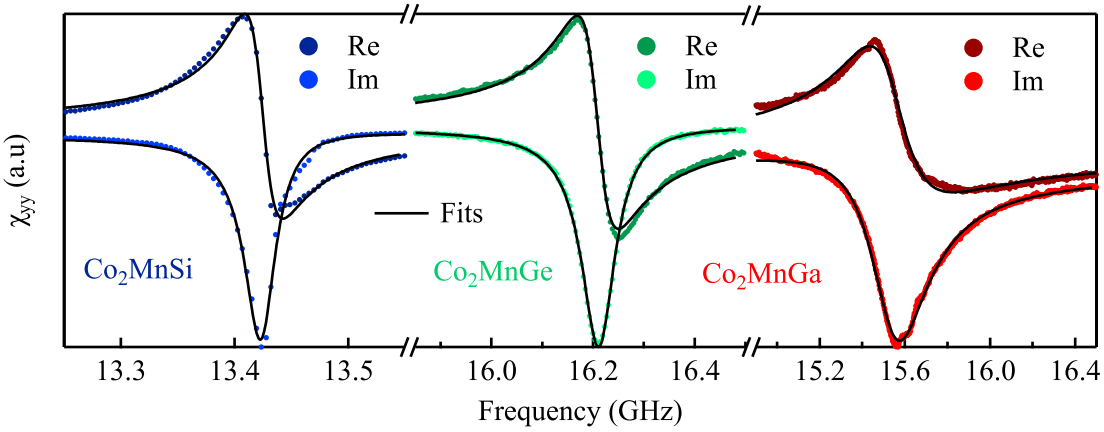

Figure 3.37: Examples of χ_{yy} parameters for Co_2MnSi (blue curves), Co_2MnGe (green curves) and Co_2MnGa (red curves) polycrystals at room temperature, each taken at 1.8 T.

FMR curves are plotted in figure 3.38 and the magnetic parameters extracted from the linear fits are shown in table 3.9. Note that the moment in μ_B/f.u are calculated using the lattice constants obtained by XRD on those polycrystalline samples ($a \simeq 5.72$ Å for Co_2MnGa and Co_2MnGe and $a \simeq 5.63$ Å for Co_2MnSi). The effective magnetization measured on polycrystalline samples is now exactly equal to the magnetization, $M_{\text{eff}} = M_S$, because there is no more magnetocrystalline anisotropy (*i. e.* samples

become isotropic). Values of magnetic moment obtained for Co_2MnSi and Co_2MnGe are almost the same than in the epitaxial case, confirming a very small anisotropy field H_k in these compounds. For Co_2MnGa though, there is a difference of almost 0.5 μ_B/f.u[17] with the single crystal. This difference is attributed to H_k as it was already suggested with the out of plane and in plane hysteresis loops in chapter 2.

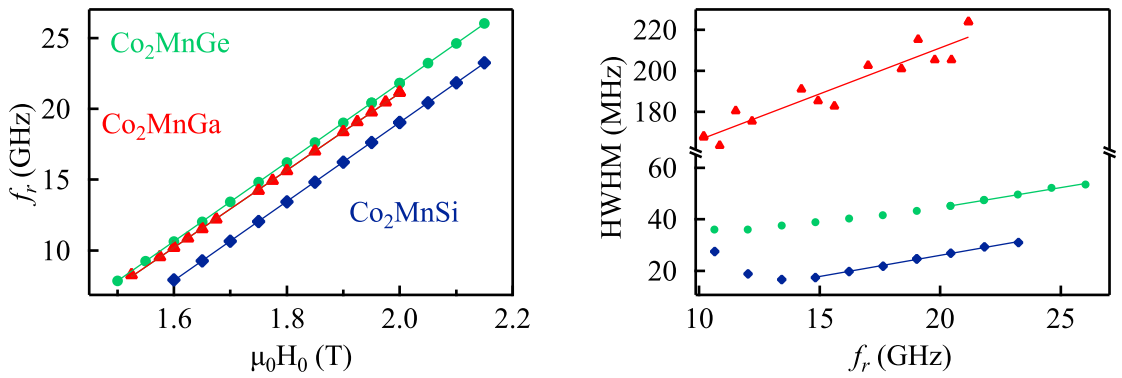

Figure 3.38: FMR measurements for Co_2MnSi (blue curves), Co_2MnGe (green curves) and Co_2MnGa (red curves) polycrystals at room temperature.

The Landé g ratio is close to 2 for Co_2MnSi and Co_2MnGe polycrystals but a little smaller for Co_2MnGa, like in single crystals. For weak ferromagnets, the Landé g ratio can be written $\frac{g-2}{2} = \frac{\mu_L}{\mu_S}$. It means that $g < 2$ in Co_2MnGa could be explained by a small orbital momentum antiferromagnetically coupled to the spin moment through spin-orbit coupling.

An important result is the small effective dampings, respectively 1.65 and 1.5×10^{-3} for Co_2MnSi and Co_2MnGe which are smaller than other polycrystalline alloys [151]. Co_2MnGa polycrystal on the other hand, has the largest damping 4.5×10^{-3}. It was already the largest one in the epitaxial case. Finally, inhomogeneous linewidths keep the same behavior than in single crystals: always smaller for Co_2MnSi and Co_2MnGe than for Co_2MnGa.

	M_{eff} (μ_B/f.u)	g ($\pm$0.02)	α	Δf_0 (MHz)
Co_2MnSi	5.03	1.99	$1.65 \pm 0.1 \times 10^{-3}$	6.9
Co_2MnGe	4.89	2.00	$1.5 \pm 0.1 \times 10^{-3}$	13.1
Co_2MnGa	4.94	1.95	$4.5 \pm 1 \times 10^{-3}$	121

Table 3.9: Intrinsic magnetic parameters of Co_2MnSi, Co_2MnGe and Co_2MnGa polycrystals at room temperature.

3.3 Magnetic damping versus electronic structure

Scattering of magnons by conduction electrons is one of the main relaxation process involved in the magnetic damping [152, 153]. Both spin flip and non spin flip mechanisms come out from this scattering

[17]Moment obtained here in excellent agreement with the one obtained by XMCD

in which an itinerant electron annihilates a magnon with energy and momentum conservation. In a HMM, the scattering involving spin flip is not possible because no DOS is available at E_F for the minority spin channel. Like in insulating ferromagnets, the magnetic damping should thus be strongly decreased.

In this section, we aim to analyze what are the important parameters, in term of electronic properties measured earlier, that leads to a significant reduction of the magnetic damping. Additionally, the case of Co_2MnGa will be discussed, where another important relaxation process seems to occur: the spin orbit coupling [154].

In figure 3.39 are shown magnetic dampings (in 10^{-3} scale) of Co_2MnZ Heusler compounds as well as a table with gap features obtained by SR-PES and calculations. Π is the distance in binding energy between the Fermi energy and the nearest DOS, either the top of the minority valence band or the bottom of the minority conduction band. Therefore, $\Pi > 0$ means that E_F is located in the minority gap whereas $\Pi < 0$ means that it is located below (above) the minority valence (conduction) band. Nevertheless, it is not possible to know where is located E_F in the spin gap using SR-PES. In order to do a comparison with calculations, $\Pi^{\text{SR-PES}}$ values reported in the table of figure 3.39 are taken by considering that the minority valence band is the nearest DOS to E_F.

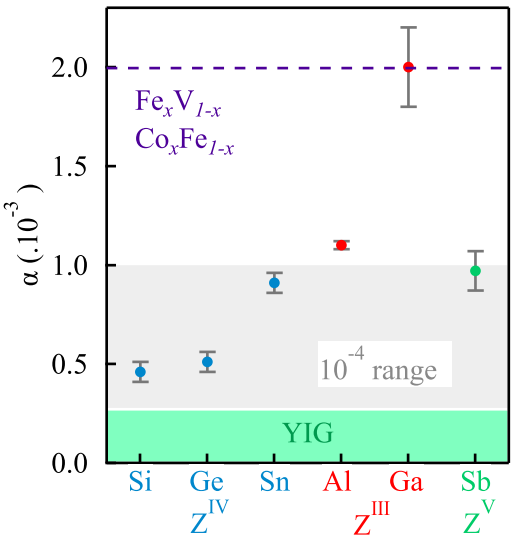

	$\Pi^{\text{SR-PES}}$	Π^{Theory}
Co_2MnSi	0.35	0.06 [7]
		0.33 [67]
		0.29 [28]
Co_2MnGe	0.2	0.09 [7]
		0.03 [67]
		0.05 [28]
Co_2MnSn	~ 0	-0.06 [7]
		-0.18 [28]
Co_2MnAl	< 0	-0.1 [7]
		< 0 [58]
		-0.17 [28]
Co_2MnGa	≥ 0	-0.36 [28]
		< 0 [58]
Co_2MnSb	-	-0.06 [7]
		0.09 [66]

Figure 3.39: Left: effective magnetic damping values of Co_2MnZ Heusler alloys. References of low damping metallic compounds Fe_xV_{1-x} [13] and Co_xFe_{1-x} [24] are indicated along with the magnetic damping range of YIG [23]. Right: distance in binding energy between E_F and the nearest DOS obtained in the present work $\Pi^{\text{SR-PES}}$ and according to different calculations Π^{Theory}.

Besides being in good agreement with theoretical calculations, Π seems well related to the magnetic damping. Let us start with Co_2MnZ^{IV} compounds. As shown in sketch 3.22, by increasing the number of electron of Z^{IV}, E_F gets closer from the top of the minority valence band. Co_2MnSi and Co_2MnGe Fermi energies are however far from any minority DOS. By looking at magnetic dampings, smallest values around 5×10^{-4} are obtained for those two compounds whereas a little larger value is observed for Co_2MnSn with 9×10^{-4}.

The situation is more puzzling for Co_2MnZ^{III} alloys. Calculations predict a similar behavior between Co_2MnAl and Co_2MnGa, with a Fermi energy falling at the top of the minority valence band. It is observed this way for Co_2MnAl but not for Co_2MnGa where a full SP is measured at E_F. Paradoxically, Co_2MnGa has the largest damping value of the series. Arguments used for Co_2MnZ^{IV} are still available here. In a band structure point of view, Co_2MnAl is similar to Co_2MnSn and so is its magnetic damping value. For Co_2MnGa however, several experiments have shown that a stronger spin-orbit coupling was occurring. Indeed, some noticeable magneto-crystalline anisotropy has been observed by magnetometry, XMCD and perpendicular VNA-FMR, as well as a Landé g factor slightly different from 2. With scattering by conduction electrons, spin orbit coupling is one of the main process responsible for the precession relaxation in a magnetic material (see chapter 1) and thus for the increase of α.

SR-PES was not fruitful for Co_2MnSb. Our PES results are not consistent with a HMM behavior (no spin gap detected and low SP). A very low magnetic damping is however observed and thus is consistent with a HMM behavior. The low SP can be explained by considering Sb segregation at the surface that does not affect the bulk SP. We conclude that Co_2MnSb is likely HMM in bulk, but its magnetic damping is higher than for Co_2MnSi and Co_2MnGe because of the proximity of E_F to the minority spin conduction band (like in Co_2MnSn where E_F is close to the minority spin valence band). These observations finally point out that our SR-PES analysis is useful for (001) Co_2MnSi, Co_2MnGe, Co_2MnSn, Co_2MnAl and Co_2MnGa but not for (001) Co_2MnSb.

Insight can also be found looking at the results obtained on quaternary compounds, particularly in $Co_2MnSi_xAl_{1-x}$ where no spin orbit coupling is involved. On the one hand, it has been shown by SR-PES that the Fermi energy is located well inside the gap for Co_2MnSi but moves continuously toward the minority spin valence band by removing one electron (see figure 3.15 with s polarization of light). In addition, the spin polarization at E_F decreases continuously by decreasing x. On the other hand, FMR measurements have shown that Gilbert damping coefficients follow an opposite linear trend with the substitution rate x (see figure 3.34). This series is thus another experimental demonstration of the impact of the electronic structure near E_F on the magnetization dynamics (at least in this type of materials).

Eventually, polycrystalline Co_2MnSi and Co_2MnGe present very low magnetic damping as well (table 3.9). Figures 3.18 and 3.19 show that the two compounds are almost HMM in s polarization of light. This time, some minority DOS of bulk bands could be suppressed by the s polarization since no further investigation was made compared to the single crystal (001) Co_2MnSi[18] [10]. Furthermore, since defects are also a channel of relaxation of the uniform precession, grain boundaries could explain the higher damping values obtained in polycrystals compared to single crystals. Nonetheless, $\alpha = 1.5$ and 1.65×10^{-3} are very small effective values for polycrystals [151] and are very promising for applications.

In summary, it is not possible to quantitatively compare the magnetic damping and photo-emission results in order to check theoretical models on the origin of the magnetic damping in metals [152, 153]. Those models rely too much on unmeasurable parameters but the present chapter aims to prove that Co_2MnZ Heusler compounds are indeed ultra low magnetic damping materials and that this property is linked to their underlying electronic structures, as predicted by those models. The reduction of the magnetic damping through the removal of spin flip processes due to scattering by conduction electrons

[18] Where the minority DOS that was killing the SP was clearly identified as the surface state $S_\downarrow$

is confirmed. In particular, the position of the Fermi energy in the gap and the width of the gap seems to be two important parameters. In addition to that, the peculiar case of Co_2MnGa (full SP but "large" damping and higher magnetic anisotropy) is attributed to its spin orbit coupling which is larger than in other Co_2MnZ compounds. This very important result has motivated our work to get Heusler compound with out-of-plane magnetic anisotropy, described in the next chapter.

Chapter 4

Perpendicular magnetic anisotropy in Heusler superlattices

As presented in the introduction chapter, getting thin films with Perpendicular Magnetic Anisotropy (PMA) is an important challenge in spintronics. For instance, it strongly decreases the critical current for magnetization reversal in STT- or SOT-based low consumption devices. Moreover, when an heterostructure exhibits PMA, all the in-plane directions are hard axis. The device is thus highly symmetrical which is convenient for stability. In this chapter, we present how to get PMA in Heusler superlattices with one main motivation: achieve PMA without losing the HMM property. In a first step, we present two ways to obtain PMA with a short state of the art on Heusler SuperLattices (SL). Then, those two ways are experimentally explored and described: Heusler superlattices Co_2MnAl/Fe_2MnAl that rely on surface anisotropy and Mn_3Ga/Co_2YZ that rely on bulk magneto-crystalline anisotropy.

4.1 Two ways to obtain PMA in Heusler superlattices

Magnetic anisotropy in thin films can be described by equation 4.1. It is an effective equation that takes into account the three main energy contributions: (i) the magneto-crystalline anisotropy K_V in J.m^{-3}, which is a bulk anisotropy (*e. g.* cubic anisotropy in Co_2MnZ Heuslers presented in chapter 2); (ii) the surface/interface anisotropy K_S in J.m^{-2} that is a phenomenological term to summarize anisotropies induced by surfaces and interfaces and (iii) the last contribution, $\frac{1}{2}\mu_0 M_S^2$ is the demagnetizing energy that always makes the out-of-plane a hard axis in the thin film geometry. V, S and τ are respectively the film's volume, surface and thickness. The resulting anisotropy of the film is due to the competition between those three terms, leading to what is called the effective anisotropy energy noted $K_{\text{eff}} \cdot V$.

$$\begin{aligned} K_{\text{eff}} \cdot V &= K_V \cdot V + K_S \cdot S - \frac{1}{2}\mu_0 M_S^2 \cdot V \\ K_{\text{eff}} &= K_V + \frac{K_S}{\tau} - \frac{1}{2}\mu_0 M_S^2 \end{aligned} \tag{4.1}$$

Perpendicular anisotropy in thin films requires overcoming the demagnetizing energy term. Thereby, PMA is obtained if $K_{\text{eff}} > 0$, in-plane anisotropy if $K_{\text{eff}} < 0$ and finally, no anisotropy if $K_{\text{eff}} = 0$. Before describing the experiments, a literature review is made in order to identify how to get PMA and what has been done already.

4.1.1 Interfacial magnetic anisotropy

SL engineering is largely used to get PMA. Two systems of interest in spintronics are Co/Ni or Co/Pt multilayers [155–157]. In these systems, PMA is obtained thanks to the interfacial anisotropy K_S between the two sublayers. Even though they are promising materials for spintronics [45], materials with better properties are desirable (spin gap, low α). In 2016, Azadani *et al.* published a study in which they perform calculations on numerous Heusler SL layered in the [001], [110] and [111] directions [158]. In particular, they showed that Heusler SL can exhibit a spin gap, sometimes larger than the one of the constituents and get enough magnetic anisotropy to overcome the demagnetizing field and thus get PMA.

4.1.2 Bulk magnetic anisotropy

Another way to obtain PMA is to choose materials with a K_V large enough in the perpendicular direction to the film plane. This time, SL are used in a different way: one sublayer is used to obtain PMA and the other one has the desirable properties like a spin gap and low magnetic damping.

Mn_2YZ Heusler-like tetragonal compounds have attracted much interest for their magnetocrystalline anisotropy properties [159]. In particular, Mn_3Ga ("Mn_2MnGa" Heusler type structure) seems to be a promising compound. First, Krén *et al.* have studied the hexagonal $D0_{19}$ phase in $Mn_{2.85}Ga_{1.15}$ compound by using neutron diffraction [160]. After annealing, they discovered another phase: the highly tetragonalized $D0_{22}$ ($I\frac{4}{m}mm$) structure[1] sketched in figure 4.1a. They measured a ferrimagnetic order between the two inequivalent sites of Mn: $Mn_I = -2.8\ \mu_B$ and $Mn_{II} = 1.6\ \mu_B$, resulting in a total moment $M_t = 0.4\ \mu_B$/f.u. In 2007, Balke *et al.* published a paper in which they have calculated that the ground state was indeed ferrimagnetic, with a total moment $M_t = 1.7\ \mu_B$/f.u. (almost 4 times higher than the experimental value of Krén *et al.*) and 0.88 spin polarization at the Fermi energy [108]. Additionally, they experimentally stabilized the $D0_{22}$ tetragonal Mn_3Ga structure and showed that it was a hard magnetic material with thermal stability up to 730 K. Also, they measured a magnetic moment between 1.1 and 0 μ_B/f.u. for $Mn_{3-x}Ga_x$ with $x \in [0, 0.15]$, thus a reduced value compared to the calculations and more consistent with the work of Krén *et al*. Finally, $D0_{22}$ $Mn_{3-x}Ga$ compounds are reported to have a strong magneto-crystalline anisotropy along their c axis ($1 < K_{eff} < 3$ MJ.m^{-3} [161, 162]). Thereby, tetragonal Mn_3Ga appears as a promising material for spin transfer applications.

Another structural phase of Mn_3Ga is the $D0_3$ fcc phase sketched in figure 4.1b for which Wurmehl *et al.* [163] have predicted a completely compensated ferrimagnetic behavior[2] with a 0.18 eV spin gap in the minority spin DOS. However, no peculiar property regarding the magneto-crystalline anisotropy have been reported on this structural phase.

In 2015, Ma *et al.* [164] have successfully grown $Mn_{62}Ga_{38}/Co_{50}Fe_{23.7}Al_{26.3}$ SL with PMA and high $K_{eff} = 0.6$ MJ.m^{-3}. They obtained a $L1_0$ ($P\frac{4}{m}mm$) phase for $Mn_{62}Ga_{38}$ which is also a tetragonalized version of a fcc, very similar to the $D0_{22}$. According to this work, the two sublayers constituting the SL are antiferromagnetically coupled between each other. They showed that this system offers the possibility to tune the magnetization amplitude and coercive fields depending on the thicknesses of the sublayers.

[1] same than $D0_3$ Heusler structure but with $\frac{c}{a} = 1.824$

[2] They consider a fundamental difference between antiferromagnets and completely compensated ferrimagnets: "In normal antiferromagnets, the compensating magnetic moments originate from the same kind of atom. A distinct symmetry element (combined with time inversion operation) relates the magnetic moments on the different sites with oppositely oriented moments. Such a symmetry is absent for the materials discussed in this work" [163].

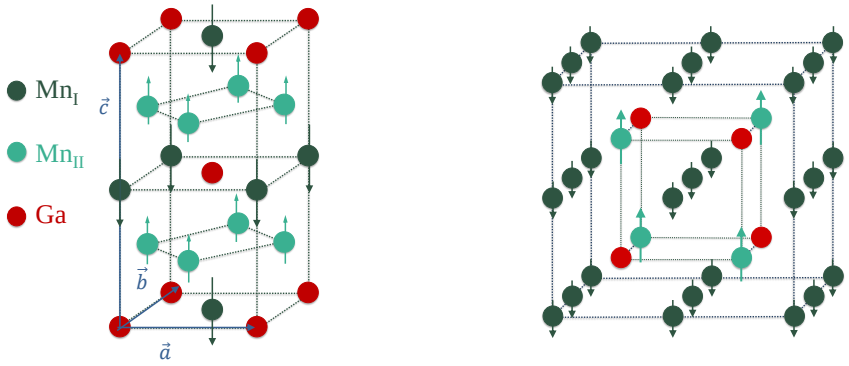

(a) D0$_{22}$ ($I\frac{4}{m}mm$)
Ferrimagnet

(b) D0$_3$ ($Fm\bar{3}m$)
Compensated ferrimagnet

Figure 4.1: Mn_3Ga tetragonal and fcc structures.

Those works have strongly motivated the use of Mn_3Ga as a sublayer in Heusler SL to obtain PMA in the present study.

4.2 Heusler superlattice Co_2MnAl/Fe_2MnAl

A joint effort between the Institut Jean Lamour, the Cassiopée beamline and the University of California Santa Barbara, has lead to the publication of a study by T. L. Brown-Heft *et al.* [78]. This experimental work relied on the theoretical calculations of Azadani *et al.* [158] on Heusler SL presented in the previous section. Here, one tries to induce PMA by using the surface anisotropy between sublayers, following equation 4.1. According to [158], $[(Co_2MnAl)_n/(Fe_2MnAl)_n]_N$ SL layered in the [001] direction is a promising system, with n the number of unit cell of the constituents and N the number of "super cell". In theory, this system should exhibit PMA when $n = 0.5$ along with a 0.3 eV spin gap with E_F falling 0.015 eV above the minority spin valence band.

High quality $[(Co_2MnAl)_n/(Fe_2MnAl)_n]_N$ epitaxial SL were grown with $n = 0.5$, 1.5 and $N = 34$, 12, respectively. The main results of the experimental study are the following:

(i) PMA is achieved under very specific conditions. Indeed, the bulk and surface anisotropies are too weak to counterbalance the demagnetizing field. Such a behavior on K_V is not surprising regarding the two previous chapters but it is a new important result about K_S. Therefore, the only way to obtain PMA in these superlattices is to reduce the demagnetizing energy and thus the magnetization amplitude. As shown by the figure 4.2-left, it is done by increasing the Al content. Additionally, superlattices undergo an out of plane spin reorientation only at T = 5 K and not at room temperature.

(ii) The surface spin polarization (measured on Cassiopée beamline set-up) has been studied only for stoichiometric superlattices with in plane anisotropy. However, it shows very interesting results: $[(Co_2MnAl)_n/(Fe_2MnAl)_n]_q$ superlattices keep the electronic structure of the termination layer[3], with an enhancement of the spin polarization up to 0.95 for Co_2MnAl-terminated superlattices, as demonstrated in figure 4.2-right.

[3] Spin polarization of Fe_2MnAl is 0.25 and Co_2MnAl is 0.65 [78]

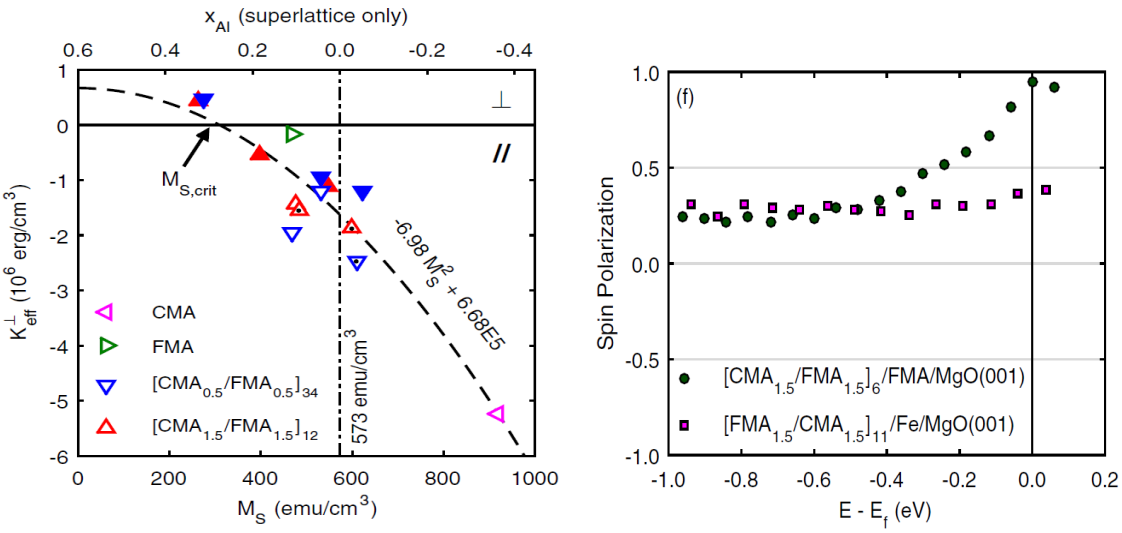

Figure 4.2: Left: effective anisotropy energy $K_{\text{eff}}^{\perp}$ versus the magnetization M_S and the excess of Al content at T = 5 K. Filled markers concern films grown on top of (001)GaAs substrates, unfilled ones for (001)MgO and markers with a black dot in the center are for (001)Cr/MgO buffer layer. Right: Spin polarization measured by SR-PES on the Cassiopée beamline for different termination of the superlattice [78].

In summary, PMA and HMM properties have been obtained on Co_2MnAl/Fe_2MnAl SL but for different samples, with different growth conditions, stoichiometry and only at low temperature. Thereby, those superlattices may not be the best systems to consider in order to get PMA and the HMM property at the same time. Nonetheless, two important points were figured out: the surface/interface anisotropy K_S appears to be small and the spin-polarization is conserved or enhanced in the termination layer. Those results have motivated the use of the bulk anisotropy K_V as the key parameter to obtain PMA in Heusler superlattices described later in this chapter.

4.3 Mn_3Ga compound

Attempts were made to grow Mn_3Ga layers directly on (001)MgO substrates. An epitaxial layer was obtained but large 3D islands was observed both during growth by RHEED and *ex situ* by TEM. Consequently, two different metallic buffer layers, V and Pd, were tested in order to stabilize the $D0_{22}$ tetragonal structure in a continuous flat film.

For the forthcoming experiments on Mn_3Ga, it is important to note that the unit cell of the $D0_{22}$ structure in figure 4.1a is the tetragonalized version of the $D0_3$ in figure 4.1b. Nonetheless, the basis vectors **a** and **b** are turned by 45° between the two unit cells. It means that the $[100]_{D0_{22}}$ direction is equivalent to the $[110]_{D0_3}$ direction in terms of surface structure factors in RHEED or zone axis in TEM.

4.3.1 Mn_3Ga on (001)V buffer layer

We have seen in chapter 2 that (001)V is a nice buffer for Heusler compounds since they adopt a Frank - van Der Merwe growth mode on it. Moreover, V buffer layers are interesting because interdiffusion with top layers grown on them often occur above 500°C. The annealing of the Heusler film on

top of V is thus possible, an important point to get chemical ordering. We then first chose this buffer. RHEED patterns in the [110] and [100] azimuth of the 20 nm thick V buffer are shown in figure 4.3a. Typical surface reconstruction along the [110] azimuths is observed on the V buffer (half-streaks), due to O surface reconstruction [165].

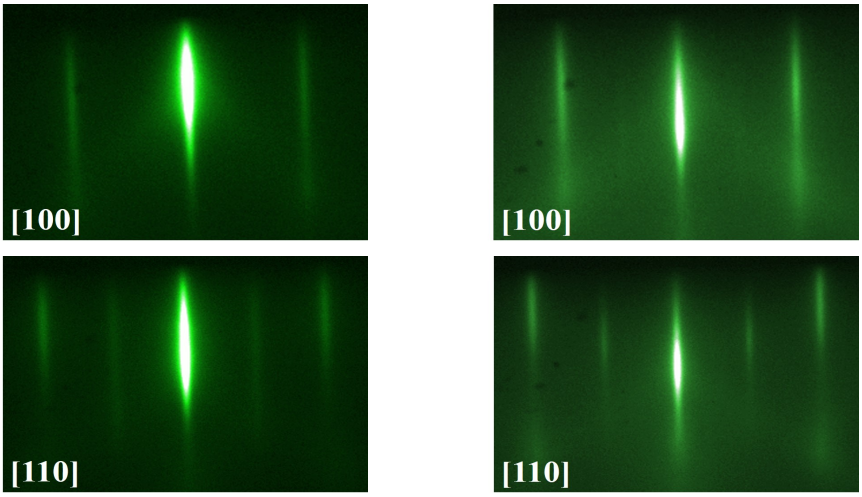

(a) V (b) Mn_3Ga

Figure 4.3: RHEED patterns along [110] and [100] azimuths of the V buffer layer and Mn_3Ga on top.

The growth of Mn_3Ga on top of V was made at T $\sim$ 470 K and RHEED patterns are shown in figure 4.3b. Since the structural phase is not known at present, it is impossible to evaluate the deposited thickness. Nonetheless, fluxes were set to $\phi_{Mn} = 3\phi_{Ga} = 1 \times 10^{14}$ at.cm^{-2}.s^{-1} and the deposition was 11 minutes long. Annealing to 820 K is performed afterward to improve the surface quality. Thin and smooth streaks for Mn_3Ga indicate a good surface quality with large crystallographic terraces. Both the $D0_{22}$ or $D0_3$ structures should exhibit the same [110] RHEED pattern (same as the one observed on Co_2MnZ Heuslers). This pattern is indeed observed in figure 4.3b, with half-streaks along the [110] azimuth. Despite the occurrence of half streaks along [110] and a square (or rectangular) surface lattice, we cannot distinguish the tetragonal or cubic structure using RHEED in the case of a growth along [001]. Nevertheless, a single crystalline Mn_3Ga layer is stabilized on top of a (001)V buffer layer.

A further structural analysis was performed using XRD. In a first step, the inter-reticular distance of the planes parallel to the surface was analyzed with a symmetrical configuration. The obtained spectrum is shown in figure 4.4. The peak at $q = 4.22$ Å^{-1} could be identified as the (004) of Mn_3Ga in the fcc $D0_3$ structure. Indeed, this value of q indicates a lattice constant $a_{Mn_3Ga} = 5.95$ Å, very close to the 5.82 Å calculated by Wurmehl *et al.* [163] (and also close to Co_2MnZ Heuslers). This difference with the calculation is consistent with the Mn_3Ga layer being in tensile strain, induced by the V buffer layer ($2a_V = 6.06$ Å). Additionally, there is a small bump at $q = 2.11$ Å^{-1} that is associated to the (002) peak of Mn_3Ga.

A $\theta-2\theta$ scan in a non-symmetrical configuration is presented in the insert of figure 4.4 (green curve). The (110) reflection that belongs to the V buffer layer is observed with a peak associated to the (220) reflection of Mn_3Ga. The position in 2θ leads to the same lattice constant than the (00l) scan in the $D0_3$ phase. It is possible to conclude that the epitaxial relationship between the two layers is V [100](001) //

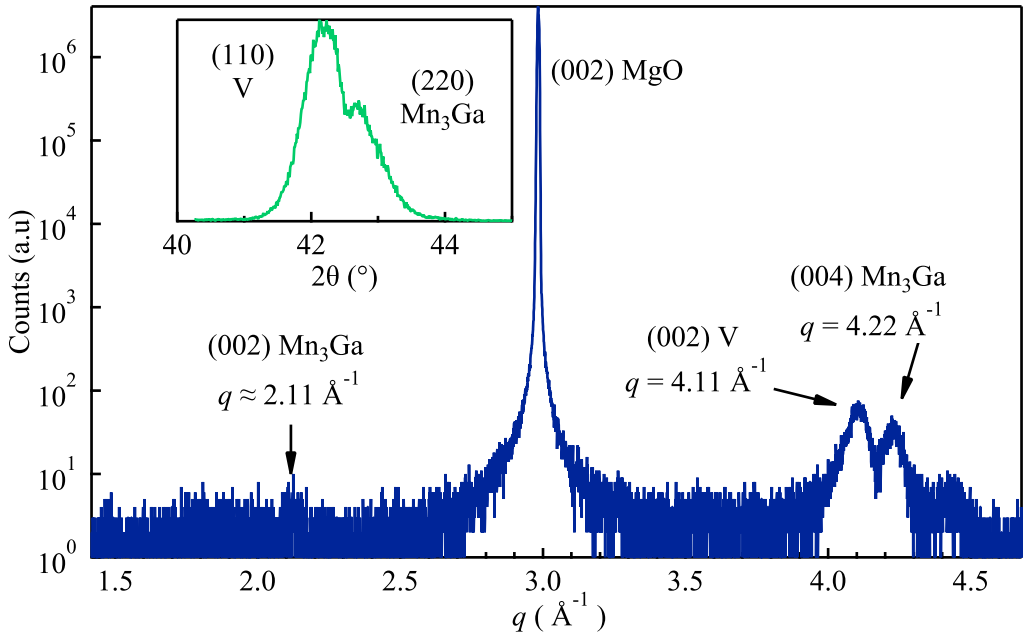

Figure 4.4: XRD spectra of Mn_3Ga/V in the symmetrical configuration (blue curve). The green curve in the insert is a scan in a non-symmetrical configuration with the following sample orientation: $\omega = \frac{2\theta}{2}$ and $\phi = \chi = 45°$.

Mn_3Ga [100](001), like with Co_2MnZ Heusler compounds (not surprising since $D0_3$ is a Heusler type structure). Moreover, as the structure is now identified, the deposited thickness can be calculated and is equal to 11.5 nm.

The magnetic properties of Mn_3Ga in the $D0_3$ phase were investigated by PPMS-VSM magnetometry. No magnetic moment was detected which is also consistent with the work of Wurmehl *et al.* in which they predicted a completely compensated ferrimagnetic behavior [163]. Even though the $D0_3$ structure is very interesting due to the spin gap predicted in the minority spin DOS, PES experiment performed on the Cassiopée beamline were unsuccessful. No spin polarization was detected on this compound. Either because this compound is non magnetic or because the magnetic field needed to reverse the magnetic moment (necessary to perform SR-PES) is too high to be achieved on the Cassiopée set-up.

At any rate, the $D0_3$ structure was not the structure desired at the beginning. In order to elaborate SL with a significant K_V, the best phase is the tetragonal $D0_{22}$ (*i. e.* strongly tetragonalized $D0_3$). In the work of Balke *et al.* [108], they recommended the use of a (001)Pd buffer layer to stabilize the $D0_{22}$ structure with the c-axis perpendicular to the film plane. This is the scope of the next section.

4.3.2 Mn_3Ga on (001)Pd buffer layer

Like for V, metallic Pd buffer layers were grown on MgO substrates at room temperature. This way, the density of small islands is significantly increased at the MgO surface and coalescence occur for very low thicknesses. It is then annealed at 820 K to smooth the surface and to obtain a flat 20 nm thick film. As shown in figure 4.5a, the Pd layer is single crystalline with an excellent surface quality. The two patterns along the [100] and [110] azimuths are compatible with the expected fcc (001)Pd structure. The

lattice constant of bulk fcc Pd is reported to be $a_{Pd} = 3.89$ Å. This lattice constant is suitable to grow epitaxially the $D0_{22}$ Mn_3Ga layer with the c axis perpendicular to the plane since $a_{Mn_3Ga} = 3.9$ Å (and $c_{Mn_3Ga} = 7.08$ Å) according to other experimental works [160, 163].

The growth of Mn_3Ga on top of the Pd buffer was made at T $\sim$ 520 K in order to stimulate chemical ordering. The fluxes were $\phi_{Mn} = 3\phi_{Ga} = 1 \times 10^{14}$ at.cm^{-2}.s^{-1} as well. The deposition was 20 minutes long and no annealing was performed afterward. The resulting RHEED patterns are presented in figure 4.5b. The [100] and [110] patterns support an excellent surface quality for an "as-deposited" layer. The two patterns do not allow us to know the structure of the Mn_3Ga layer but it is compatible with the $D0_{22}$ phase (square/rectangular surface lattice and half streaks along [110] azimuth).

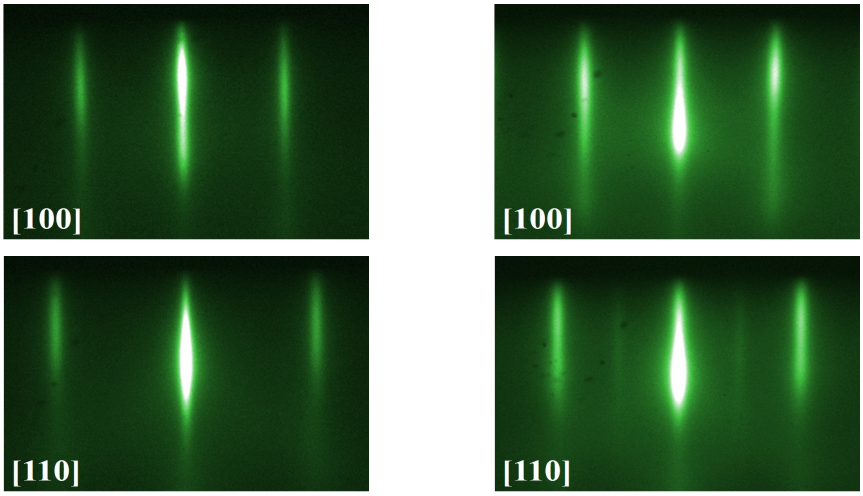

(a) Pd (b) Mn_3Ga

Figure 4.5: RHEED patterns along [110] and [100] azimuths of the Pd buffer layer and Mn_3Ga on top.

A further investigation of the structure was done thanks to XRD. The spectrum obtained in a symmetrical configuration is shown in figure 4.6. First, the Pd layer is indeed fcc with a growth direction along (001). In addition, the (002) and (004) reflections point out a lattice constant $a_{Pd} = 3.88$ Å, very close to the bulk value.

From the reflections associated to Mn_3Ga, it is obvious that the structure strongly differs from the $D0_3$ previously observed when grown on top of V. The body centered $I\frac{4}{m}mm$ space group ($D0_{22}$ structure) has the following reflection condition: $h + k + l = 2n$. It allows us to index the main reflections as the (002), (004) and (008). Like in Co_2MnZ Heusler compounds, the $h + k + l = 4n + 2$ peak intensity is given by the difference of scattering amplitudes between Mn and Ga. The fact that the (002) reflection is so small (and (006) not visible) indicates that the Mn_3Ga layer is poorly ordered. Nonetheless, the out-of-plane lattice parameter is found to be $c_{Mn_3Ga} = 7.12$ Å. This value is extremely close to the experimental value $c_{exp} = 7.09$ and calculated value $a_{calc} = 7.16$ Å reported for bulk samples by Wurmehl *et al.* [163]. Therefore, it is possible to conclude that Mn_3Ga in the $D0_{22}$ structure is here stabilized on top of a (001)Pd buffer layer, with the c axis perpendicular to the film plane. Moreover, the epitaxial relationship between the $D0_{22}$ structure from figure 4.1a and the Pd is simply Mn_3Ga [100](001) // Pd [100](001).

No magnetic moment was detected by PPMS-VSM on a 20 nm thick $D0_{22}$ Mn_3Ga layer. In the work of Balke *et al.*, they calculated a ferrimagnetic ground state as well as an experimental magnetic moment

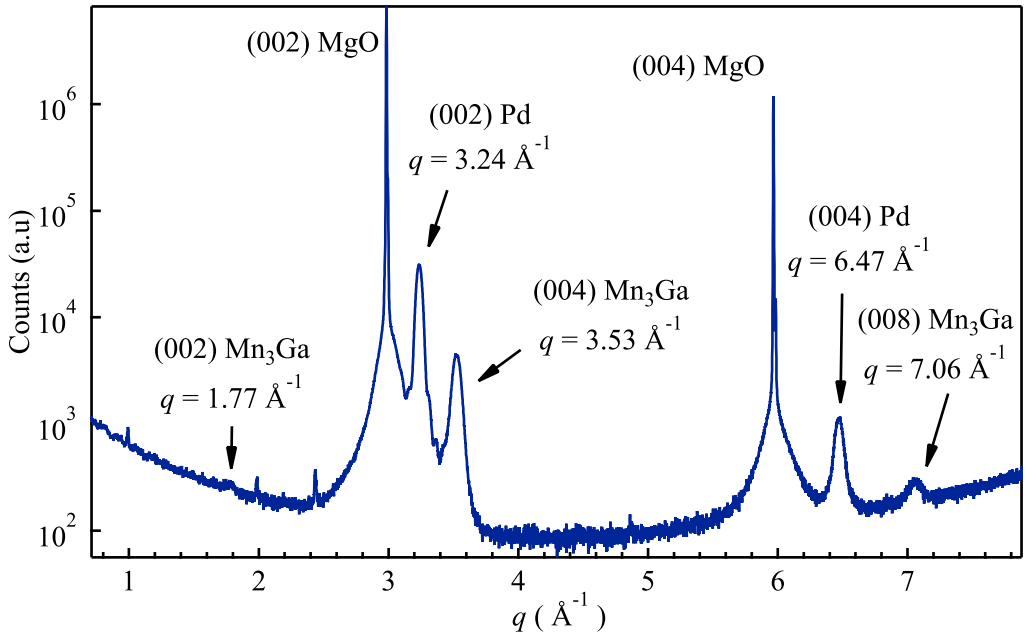

Figure 4.6: XRD spectra of Mn_3Ga/Pd in the symmetrical configuration.

varying from 0 to 1 μ_B/f.u from $Mn_{2.85}Ga$ to Mn_3Ga composition. Even though the stoichiometry is well controlled in the present work (see chapter 2), Mn_3Ga is reported to be strongly ferrimagnetic, not far from the compensation. It may explain the absence of a detectable moment by magnetometry. In the following, Mn_3Ga/Co_2YZ SL are always elaborated on top of a (001) Pd buffer layer and started with Mn_3Ga as the first sublayer.

4.4 Mn_3Ga/Co_2YZ Heusler superlattices

We have seen in the two previous chapters that Co_2MnSi was one of the best candidate for applications in the Co_2MnZ series (excellent crystal quality, large spin gap and ultralow damping, even in polycrystal). Mn_3Ga/Co_2MnSi Heusler SL are hence first analyzed by using XRD and TEM analysis. However, in the work of Ma *et al.* [164], they observed an antiferromagnetic coupling between the two sublayers in $Mn_{62}Ga_{38}/Co_{50}Fe_{23.7}Al_{26.3}$ SL that exhibit PMA. Thereby, in order to check the magnetic coupling between the sublayers in our SL by using XMCD, we had to swap Mn in Co_2MnSi by another element to study only the Mn from the Mn_3Ga layer. We thus chose to replace Co_2MnSi by Co_2FeGe, a Heusler alloy studied in a previous Ph.D thesis at the IJL [91]. This way, it is possible to measure each magnetic moment of each sites (except the two inequivalent Mn sites in Mn_3Ga). Therefore, XMCD results on Mn_3Ga/Co_2FeGe SL are also presented later in this section.

4.4.1 Mn_3Ga/Co_2MnSi

Elaboration and RHEED analysis

$[(Mn_3Ga)_n/(Co_2MnSi)_m]_N$ are thus grown on top of a Pd buffer layer. n and m are respectively the number of unit cell (u.c) of each sublayer. SL always start with Mn_3Ga and the number of super cell is

fixed to $N = 30$. To respect the stoichiometry of each compound, fluxes are set to $\frac{1}{2}\phi_{Co} = \phi_{Mn} = \phi_{Si} = 3\phi_{Ga} = 10^{14}$ at.cm^{-2}.s^{-1}. With these fluxes, one u.c (*i. e.* 4 atomic planes) of $D0_{22}$ Mn_3Ga grows in 39 seconds and one u.c of Co_2MnSi in 12.5 seconds.

The growth temperature is fixed at T = 520 K which seems to be a good compromise between crystalline quality and chemical order in the layer without inter-diffusion of chemical species. [100] and [110] RHEED patterns of the Co_2MnSi termination layer (the 30th Co_2MnSi layer of the SL) are shown in figure 4.7. Even though the surface is rougher than Co_2MnZ layers presented in chapter 2, the figure 4.7 indicates a nice surface quality with smooth streaks. The occurrence of half-streaks along the [110] azimuth (figure 4.7b) indicates a $L2_1$-compatible structure.

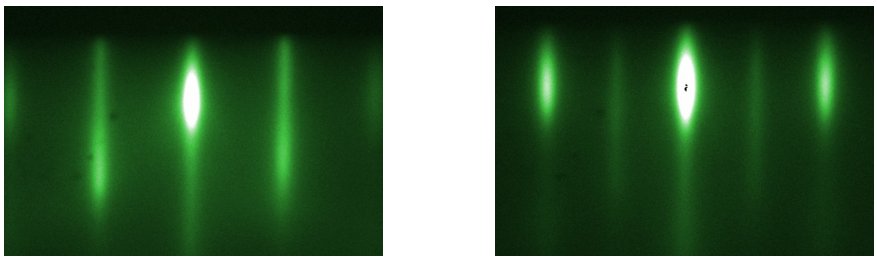

(a) [100] (b) [110]

Figure 4.7: RHEED patterns along [100] and [110] azimuths of the last Co_2MnSi layer in a $[(Mn_3Ga)_3/(Co_2MnSi)_4]_{30}$.

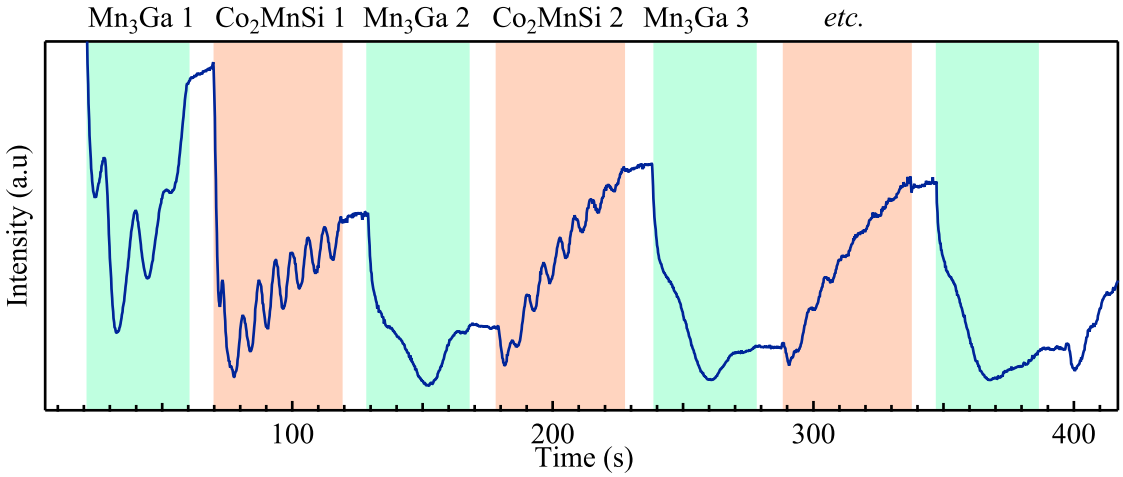

Figure 4.8: RHEED intensity oscillations recorded during the beginning of the growth of $(Mn_3Ga)_1/(Co_2MnSi)_4$ SL.

During the growth, RHEED intensity oscillations are recorded to check the growth rates. The intensity of the central streak of $(Mn_3Ga)_1/(Co_2MnSi)_4$ SL is presented in figure 4.8. The first Mn_3Ga layer seems to oscillate in a layer by layer growth mode with almost 4 visible oscillations, which is consistent with a 1 u.c thickness. Next Mn_3Ga sublayers barely oscillate but the patterns suggest a bi-layer by bi-layer growth with double period oscillations. On the other hand, oscillations are well visible for Co_2MnSi layers with a 6.3 second period. This is exactly the expected value with the present fluxes, by taking into

account a bi-layer by bi-layer growth mode. One oscillation is 2 atomic planes (see chapter 2) hence 1 u.c. is made in 12.6 seconds. Oscillations fade for subsequent Co_2MnSi sublayers. This might be due to the adsorbed atoms at the surface, that directly diffuse to step edges and therefore never change the density of step (no oscillations regime). Such a stepflow growth regime was already observed in the case of Co_2MnZ compounds growing on top of a (001)V buffer layer in chapter 2.

XRD analysis

The formalism of XRD on SL is described in many thesis and books [166]. It is not explained in detail in the present work. Nonetheless, the basic principle of XRD on SL is sketched in figure 4.9. Two sublayers A and B scatter X-rays according to their structure, with their scattering amplitudes represented by $F_A(q)$ and $F_B(q)$ in figure 4.9 (like in XRD performed on single crystals). The additional feature with SL is the convolution of the scattered intensity by a comb that is due to the super cell periodicity Λ in the out of plane direction, with $\Lambda = n_A d_A + n_B d_B$ where $n_{A,B}$ are the number of planes in the sublayers A and B and $d_{A,B}$ the distances between planes in layer A and B. The total diffracted intensity results in many reflections located around the scattering vectors q of A and B reciprocal lattices with an additional $\frac{2\pi}{\Lambda}$ periodicity (blue curve at the bottom of figure 4.9). Therefore, XRD is a powerful tool to check the Λ periodicity and thus the thickness of the super cell (and the quality of interfaces).

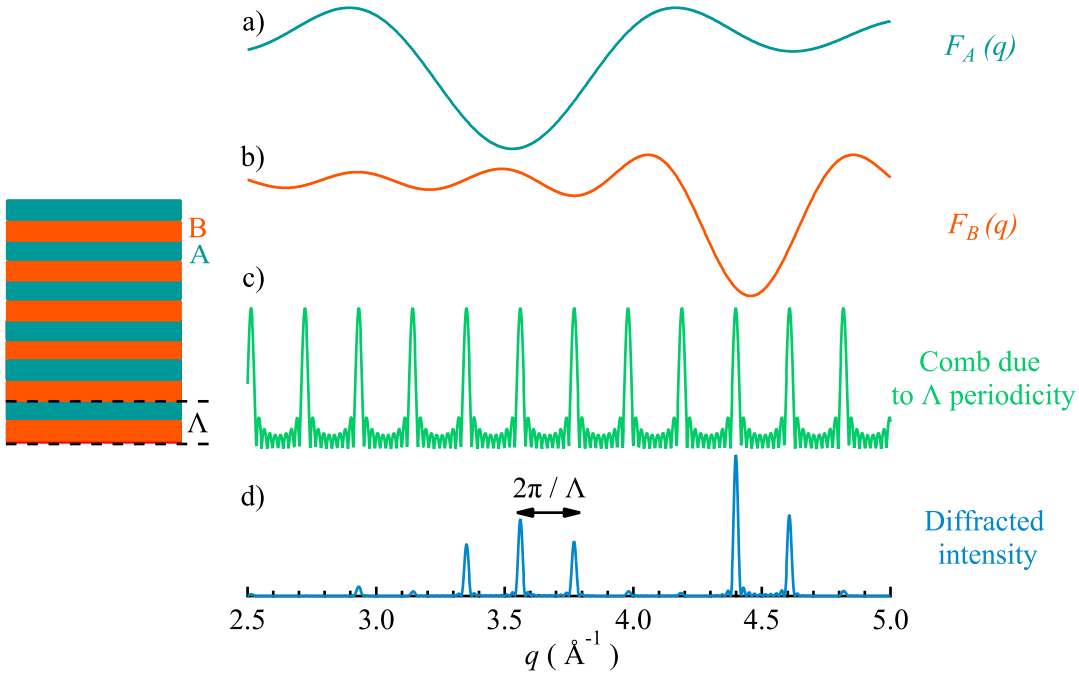

Figure 4.9: Sketch of a XRD spectrum performed on a SL. a) and b) are the scattering amplitudes of the two sublayers A and B, c) is the comb due to the super cell periodicity Λ and d) the resulting intensity diffracted by a SL.

An XRD spectrum performed on $[(Mn_3Ga)_2/(Co_2MnSi)_4]_{30}$ SL is presented in figure 4.10. As presented in figure 4.9, many peaks are observed. They are indeed spaced by a constant q value (the comb). Peaks indexed by blue bars are coming from (004) Mn_3Ga sublayers. The green ones from (004) Co_2MnSi sublayers and the orange ones from both (002) sublayers. The green curve in the insert represents the q

position of each peak as a function of an arbitrary indexation. Data points are well linear which indicates regular and flat interfaces in the SL and thus an excellent control of the thickness of each super cell. The slope of the curve is naturally $\frac{2\pi}{\Lambda}$ (see figure 4.9d). With 2 u.c of Mn_3Ga and 4 u.c of Co_2MnSi, the super cell should be $\Lambda = 2 \times 7.12 + 4 \times 5.65 = 36.8$ Å. In the insert of figure 4.10, data points are fitted and the resulting slope gives $\Lambda = 37$ Å, very consistent with the expected one. In addition, the fact that the measured Λ value matches well the expected one indicates that both layers keep their lattice constant and hence their respective structure all along the growth.

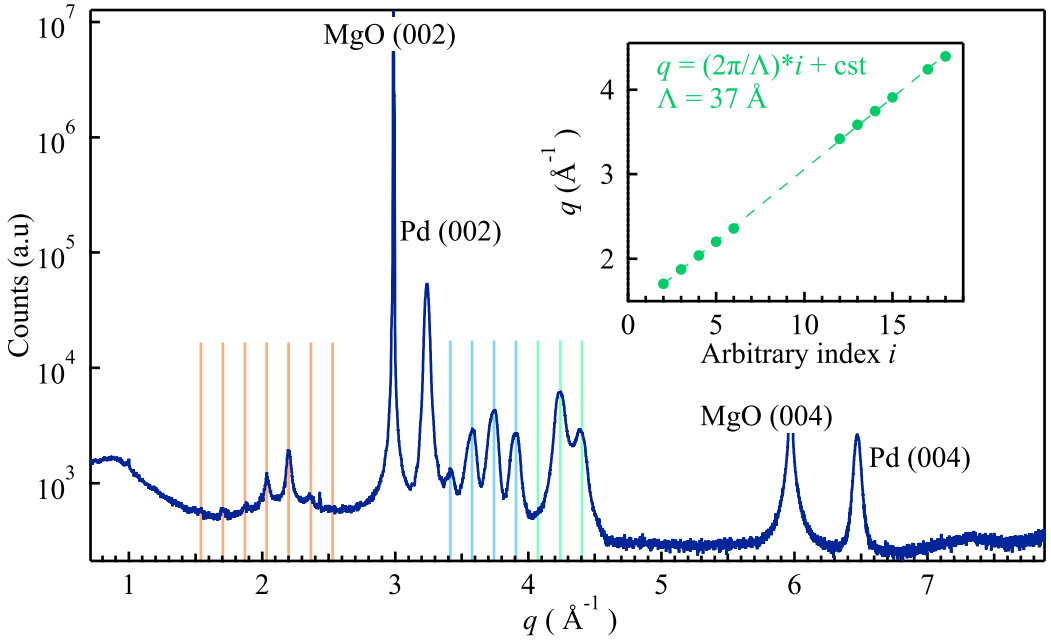

Figure 4.10: XRD spectrum of $[(Mn_3Ga)_2/(Co_2MnSi)_4]_{30}$ SL. Many peaks are observed and separated by a constant q due to the comb sketched in figure 4.9. The position of each peak in q is reported in the insert (green curve) that allows us to precisely determine the super cell thickness Λ.

The experimental Λ value obtained by XRD on every SL are presented in table 4.1. For each composition,

n	m	Λ_{XRD} (Å)	Λ_{calc} (Å)
1	1	13.1	12.8
	2	18.8	18.4
	3	27.2	24
	4	30.4	29.7
2	2	25.9	25.5
	4	37.0	36.8
	6	51.9	48.1
3	2	33.3	32.7
	4	44.6	44.0

Table 4.1: XRD analysis on each SL $(Mn_3Ga)_n/(Co_2MnSi)_m$ where n and m stand for the number of u.c of each sublayers.

the concordance with the expected value is really good and shows an excellent control of thicknesses during the growth process. However, XRD on SL is very tricky in non-symmetrical configurations. It means that a further investigation on the chemical ordering of each sublayer by looking at (311) peaks for instance is too complex. Thereby, SL were also investigated by TEM where a direct imaging of atomic columns is much simpler to resolve the chemical order.

TEM analysis

Cross sections of $(Mn_3Ga)/(Co_2MnSi)$ SL were prepared by focused ion beam like in Co_2MnZ bulk samples of chapter 2, along the $[100]_{Mn_3Ga}$ zone axis (still considering the mesh from figure 4.1a). Thus, atomic columns of Mn and Ga atoms should be observed with the same alternation than in Co_2MnSi layer. The only differences are the contrast and the out of plane spacing between planes. Every image presented in the following were obtained in a $(Mn_3Ga)_3/(Co_2MnSi)_4$ SL, with a significant thickness of each sublayer to analyze contrasts with the eye. A large view of the cross section is shown in figure 4.11-left in STEM-HAADF mode. Both the Pd buffer layer and the SL layer are very flat and homogeneous in thickness, as suggested by RHEED and XRD analysis. Sharp and smooth interfaces between sublayers are shown in figure 4.11-right, with a regular thickness of the super cell (as suggested by XRD).

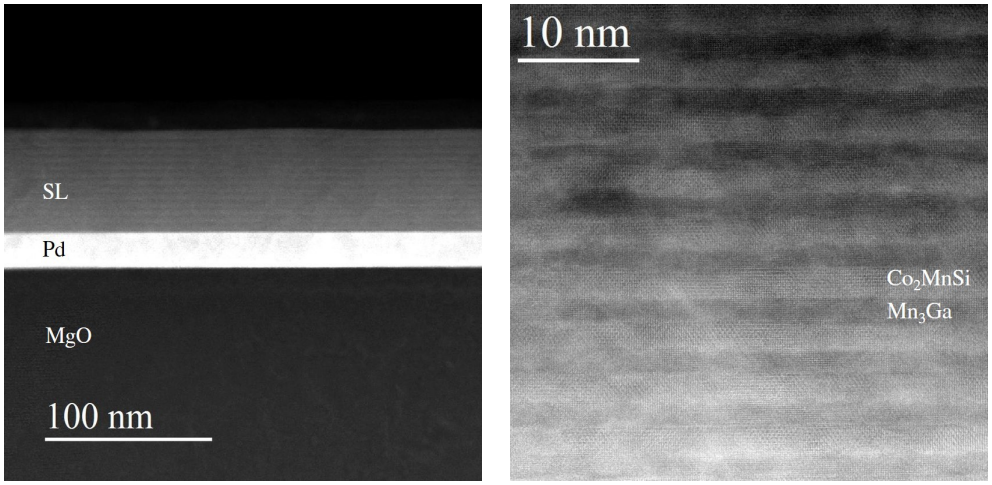

Figure 4.11: STEM-HAADF raw images along the [110] zone axis of Co_2MnSi ([100] zone axis of Mn_3Ga with the unit cell depicted in the figure 4.1).

Although a contrast between sublayers is already observed in figure 4.11, an accurate chemical analysis is done by EDX. The result is presented in figure 4.12 where a mapping at the Co K edge is shown in red, Mn K edge in blue, Si K edge in orange and Ga L edge in violet. All those chemical maps are consistent with the chemical nature of the sublayers. Even a contrast between the Mn atoms from Mn_3Ga and Mn atoms from Co_2MnSi is visible, consistent with their respective stoichiometric ratio.

STEM-HAADF images with a high magnification are presented in figure 4.13-left (raw image) and 4.13-right (inverse FFT of the red area). $L2_1$ chemical order is visible in Co_2MnSi sublayers since the contrast is the same than in figure 2.22 in chapter 2. On the other hand, Mn_3Ga chemical ordering is more difficult to see. Nonetheless, an intensity line profile of the blue rectangle is presented at the bottom of the figure 4.13. This profile is indicating chemical ordering between Mn and Ga atomic columns, confirming the $D0_{22}$ structure. However, chemical ordering near interfaces is hardly quantifiable. That makes the

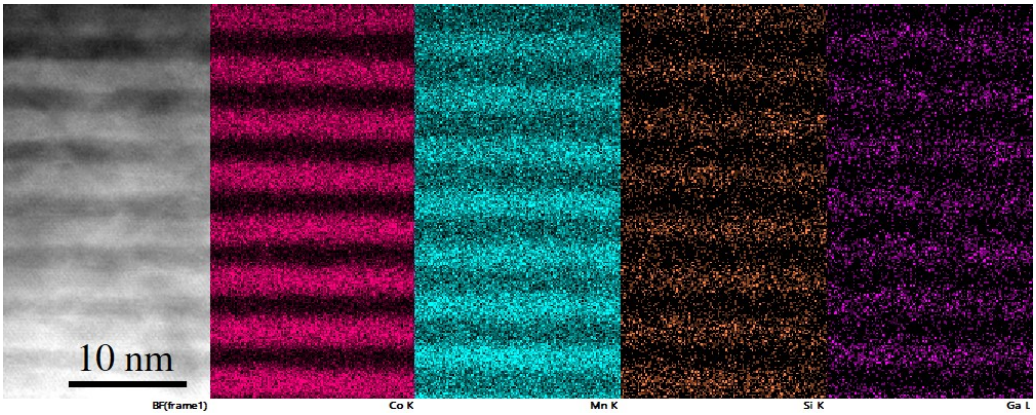

Figure 4.12: EDX mapping of $(Mn_3Ga)_3/(Co_2MnSi)_4$ SL at K edges of Co (red), Mn (blue), Si (orange) and at L edge of Ga (violet).

chemical analysis of SL with very thin sublayers too complex. Finally, one should see in the figure 4.13 that the out of plane inter reticular distance is larger for Mn_3Ga than for Co_2MnSi, thus confirming an out of plane lattice constant around 7 Å for Mn_3Ga and around 5.6 for Co_2MnSi.

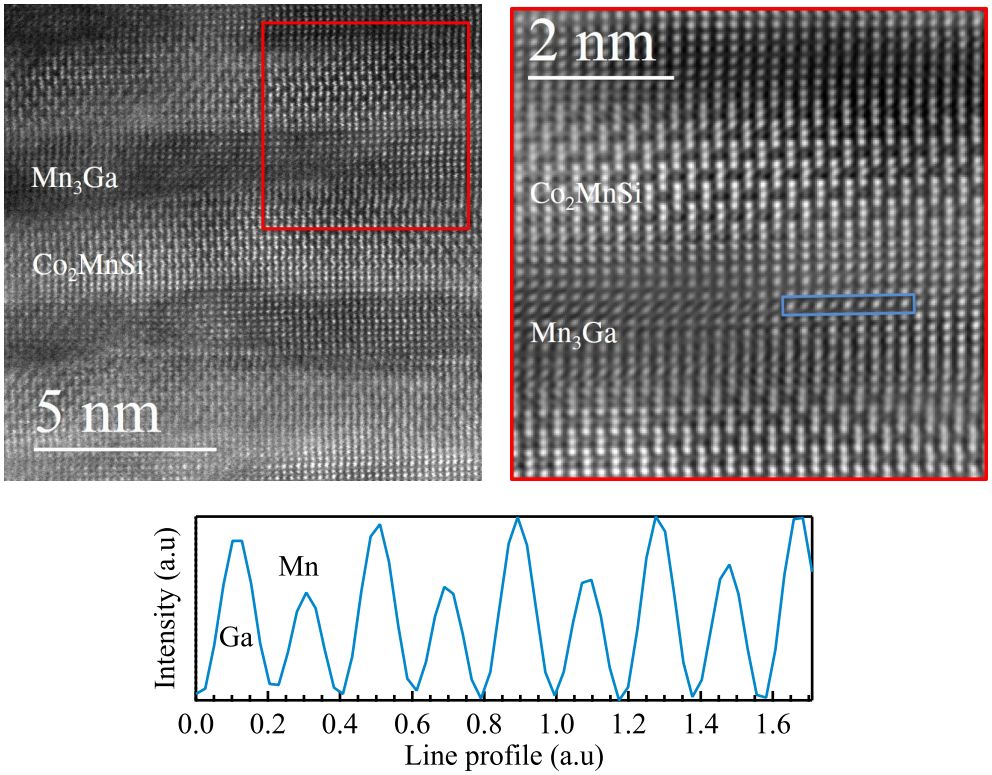

Figure 4.13: Left: STEM-HAADF raw image of $(Mn_3Ga)_3/(Co_2MnSi)_4$. Right: inverse FFT of the red area. The intensity line profile of the blue rectangle is presented at the bottom.

The present TEM analysis shows the high epitaxial quality of these SL (as well as the Pd buffer layer). We have seen that the respective structures of each sublayer is conserved. Nonetheless, there must not be chemical order everywhere in each sublayers, especially near interfaces hence in SL with very thin sublayers ($(Mn_3Ga)_1/(Co_2MnSi)_1$ for instance). It is important to keep that in mind for the magnetic

analysis in the following.

Magnetic properties

Magnetic properties of a series of $[(Mn_3Ga)_n/(Co_2MnSi)_m]_{30}$ Heusler SL were investigated by PPMS-VSM in order to have a look at the magnetic anisotropy, between the In Plane (IP) and Out Of Plane (OOP) directions. Results are shown in figure 4.14 for different $(n - m)$ sublayers thicknesses.

Before analyzing the data, an important point has to be clarified. Due to the slope coming from the diamagnetic signal of MgO substrate and Pd buffer layer, it was very hard to know if the samples were saturated or not (especially in the IP direction). Since no quantitative analysis on anisotropies are possible with such hysteresis loops, we made the assumption that each sample was saturated around 4.5 T in order to be able to compare between the two directions. Therefore, the slopes of the loops in figure 4.14 are certainly wrong, particularly for 4.14-a and b.

First, a very promising result is that all SL are perpendicularly magnetized with a clear hysteretic behavior in the OOP direction. Additionally, the two sublayers of the SL act coherently together, meaning that they are magnetically coupled (no supplementary steps or kinks in the hysteresis loops). The effective anisotropy K_{eff} that put the magnetization in the OOP direction (equation 4.1) is a competition between two characteristics of the SL. Indeed, the Co_2MnSi sublayer is strongly ferromagnetic[4] with a small cubic anisotropy. It means that by increasing its thickness m in the SL, the demagnetizing energy contribution increases and tends to put the magnetization IP (like in 20 nm Co_2MnZ compounds of chapter 2). On the other hand, Mn_3Ga compound is strongly anisotropic with an easy axis along c, here along the OOP direction. The balance of those two contributions easily explains that the anisotropy is decreasing by increasing m over n, as presented in figure 4.14.

The origin of the increasing coercive fields for small n and m thicknesses can be qualitatively explained by considering magnetization reversal in the macrospin approximation (*i. e.* single domain or Stoner-Wohlfarth model). In the OOP direction, the coercive field H_c is approximated by $H_c \sim H_k - M_S = \frac{2K_{\text{eff}}^{\perp}}{\mu_0 M_S} - M_S$ (with $H_k > M_S$ since the sample exhibit PMA). When M_S decreases, H_c increases.

The fact that all the hysteresis loops are not square with small remanences is puzzling. It is certainly linked to the magnetic configuration of Mn_3Ga in thin layer and/or in the vicinity of Co_2MnSi. Even though no magnetic moment was detected for a 20 nm thick Mn_3Ga layer (suggesting a completely compensated ferrimagnetic behavior), one hypothesis is that Mn_3Ga in very thin layer is a ferrimagnet, as reported in literature for bulk samples [108, 160]. But, the TEM analysis has shown that chemical order was not clear near interfaces in the present SL. Moreover, we have seen in chapter 1 that disorder in the unit cell could strongly affects the magnetic property. The disorder may be responsible for several local magnetic configurations favoring the creation of magnetic domains, explaining small moment values at remanence.

Further investigations are necessary to understand the magnetic configuration of those SL. For this reason, we performed XMCD on a similar SL: $(Mn_3Ga)_n/(Co_2FeGe)_m$ using DEIMOS beamline at SOLEIL synchrotron source.

[4] 5 μ_B/f.u, see chapter 2

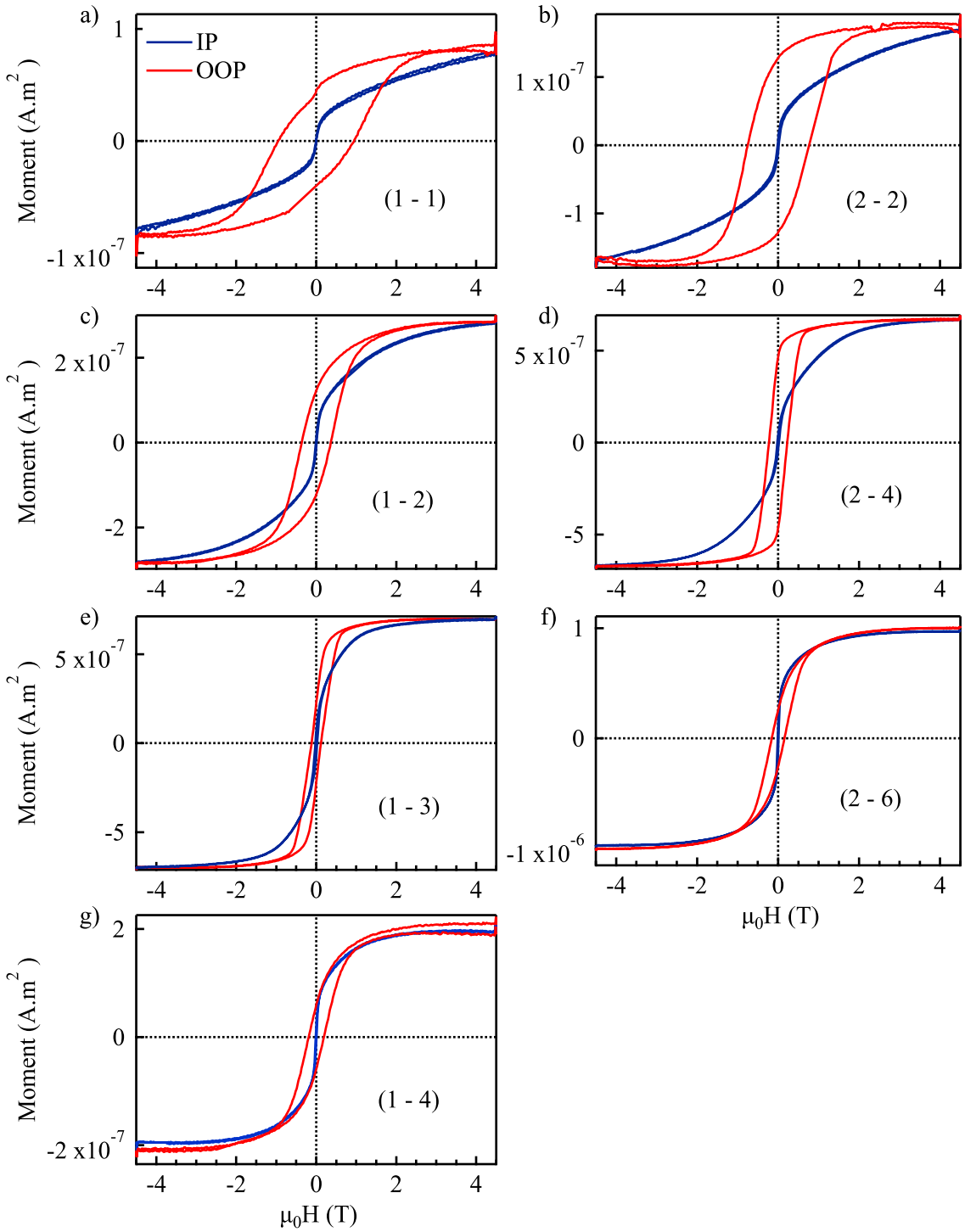

Figure 4.14: PPMS-VSM measurements in the IP (blue curves) and OOP (red curves) for $(Mn_3Ga)_n/(Co_2MnSi)_m$ Heusler SL. Sublayers thicknesses, in u.c, are (*n*-*m*): a) (1-1), c) (1-2), e) (1-3), g) (1-4) on the left column and b) (2-2), d) (2-4), f) (2-6) and the right column.

4.4.2 Mn_3Ga/Co_2FeGe

As explained at the beginning of this section dedicated to SL, it was necessary to swap Mn by Fe atoms in the fcc Heusler layer in order to differentiate each moment by XMCD. Co_2FeGe Heusler compound has been widely studied as well [92, 167]. It has a similar behavior than Co_2MnGe, with a lattice constant

$a = 5.75$ Å and a magnetic moment on the Slater Pauling curve: $M_t = 2 \times \mathrm{Co}(3d^7 4s^2) + \mathrm{Fe}(3d^6 4s^2) + \mathrm{Ge}(4s^2 4p^2) - 24 = 6\ \mu_B$ /f.u.

Elaboration and structural analysis

The elaboration conditions were exactly the same than Mn_3Ga/Co_2MnSi SL, on a Pd buffer layer on MgO substrates. They were capped with Ag instead of Au, because there are no absorption edges in the energy range of interest with Ag. Fluxes were fixed to $\phi_{Co} = 2\phi_{Fe} = 2\phi_{Ge} = 1 \times 10^{14}$ and $\phi_{Mn} = 3\phi_{Ga} = 1.5 \times 10^{14}$ at.cm^{-2}.s^{-1}. With those fluxes, one atomic plane of Mn_3Ga is made in 6.6 seconds and one of Co_2FeGe in 6.3 seconds.

RHEED patterns obtained on the termination layer of $[(Mn_3Ga)_2/(Co_2FeGe)_2]_{10}$ SL are presented in figure 4.15a and 4.15b. The streaks are very thin and homogeneous in intensity, supporting a nice surface quality. The pattern along [110] azimuth is compatible with the $L2_1$ ordering. Furthermore, RHEED intensity oscillations are presented in figure 4.15c. The first Mn_3Ga layer on Pd adopt a layer by layer growth mode as previously observed with Co_2MnSi SL, with an oscillation period of 6.5 seconds/plane. Starting from the second Mn_3Ga layer, a bi-layer by bi-layer mode is well visible with a period two times larger. Co_2FeGe also grows in a bi-layer by bi-layer mode with 12.2 seconds/2planes rate. This supports chemical ordering in both layers.

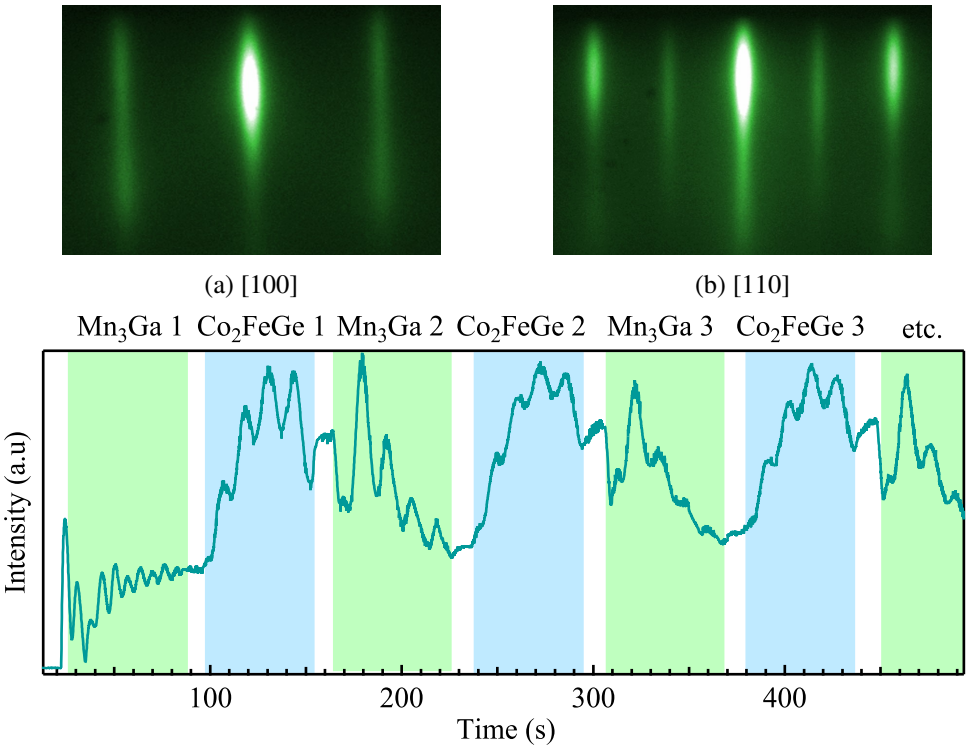

(c) Intensity oscillations

Figure 4.15: RHEED patterns along a) [100] and b) [110] azimuths of the termination layer Co_2FeGe of $[(Mn_3Ga)_2/(Co_2FeGe)_2]_{10}$ SL. c) is the intensity of the central streak recorded at the beginning of the SL growth.

In order to prove that $(Mn_3Ga)_n/(Co_2FeGe)_m$ can be compared to $(Mn_3Ga)_n/(Co_2MnSi)_m$ SL, a TEM analysis was performed to check the structure. Raw STEM-HAADF images on $(Mn_3Ga)_2/(Co_2FeGe)_2$

are presented in figure 4.16. On the left, we can see that the Pd buffer layer and the SL layer are flat and homogeneous in thickness. The Ag capping layer is not continuous and droplets are observed. The last sublayer of the SL has certainly been oxidized since a slightly different contrast from others Co_2FeGe sublayers is observed. It is important to keep that in mind for the forthcoming XMCD analysis. A contrast between sublayers of the SL is already visible. A highly magnified image is shown on the right of figure 4.16. The inter reticular distance in the Mn_3Ga layer indicates indeed the $D0_{22}$ structure , with $c \sim 7$ Å. Additionally, chemical order is visible with the eye in some region of both layers, but not everywhere. Intensity line profiles of the green rectangle (Fe-Ge alternation) and the red one (Mn-Ga alternation) are shown at the bottom of figure 4.16 and indicate chemical ordering in both layers. Therefore, like in $(Mn_3Ga)_n/(Co_2MnSi)_m$ SL, the respective structure of each compound is conserved and a partial ordering is taking place.

As we have checked that $(Mn_3Ga)_n/(Co_2FeGe)_m$ SL adopt the right structure, their magnetic properties can be compared to $(Mn_3Ga)_n/(Co_2MnSi)_m$ SL (even if the Co_2YZ layers differ of one μ_B/f.u.).

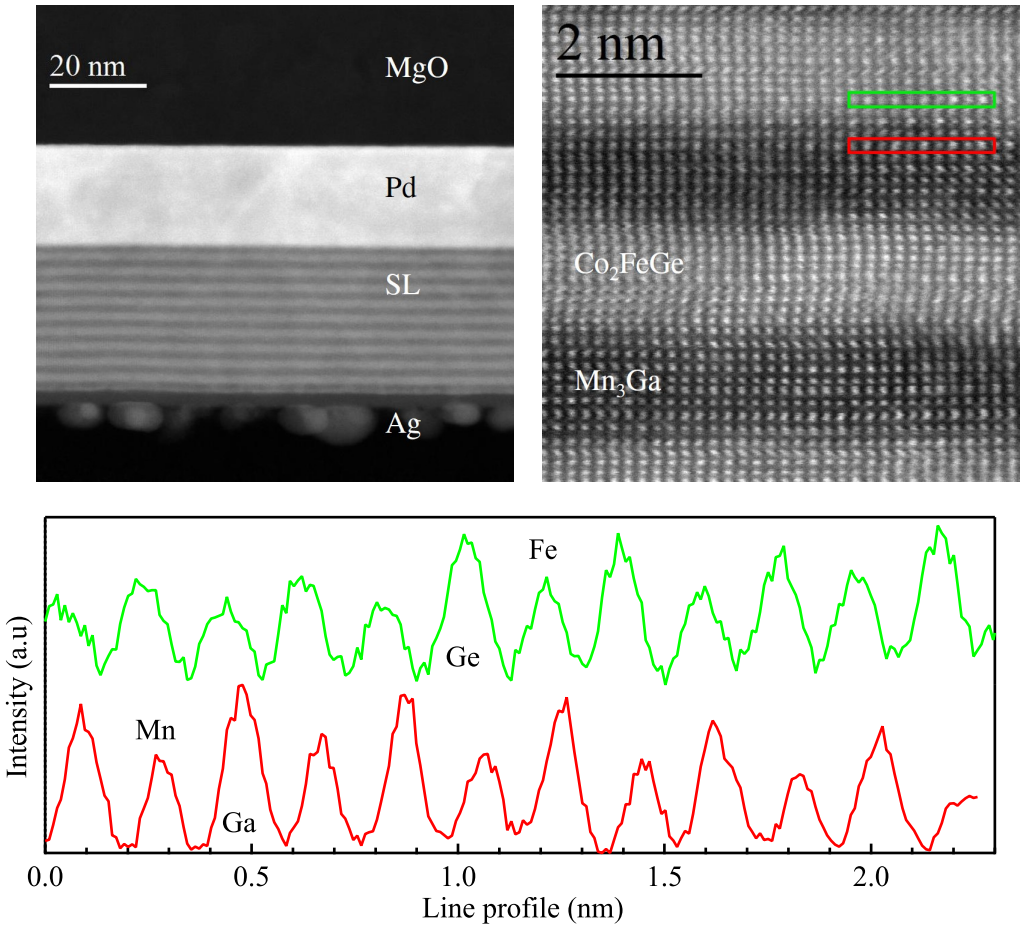

Figure 4.16: STEM-HAADF raw images along the [110] zone axis of Co_2FeGe ([100] zone axis of Mn_3Ga with the unit cell depicted in the figure 4.1) on $[(Mn_3Ga)_2/(Co_2FeGe)_2]_{10}$ SL. Intensity line profiles of the green and red rectangle are presented at the bottom, indicating chemical order in both layers.

XMCD analysis

$(Mn_3Ga)_n/(Co_2FeGe)_m$ SL were analyzed by XMCD at the DEIMOS beamline described in chapter 2. Absorption spectra at Mn, Fe and Co $L_{2,3}$ edges were investigated on $(Mn_3Ga)_n/(Co_2FeGe)_m$ for different $(n-m)$ thicknesses: $(1-1)$, $(1-2)$, $(1.5-1.5)$ and $(2-2)$. $(Mn_3Ga)_1/(Co_2FeGe)_2$ XAS and XMCD signals are presented in figure 4.17. Those spectra were obtained under a 2 T magnetic field at 4 K.

The Mn_3Ga sublayer has indeed a magnetic moment (unlike 20 nm thick Mn_3Ga). Additionally, the direction of the XMCD signals of Co, Fe and Mn indicates a ferromagnetic coupling between every chemical element. However, it is not possible to obtain the relative orientation of the magnetic moments between the two types of Mn atoms[5], within the Mn_3Ga layer (we measure the "average Mn moment"). In the three XAS spectra, a multiplet structure is observed traducing a complex chemical environment, as it was already observed for bulk Co_2MnZ compounds in chapter 2. Indeed, for this $(1-2)$ SL, the super cell thickness is $\Lambda \sim 18.6$ Å and contains 5 chemical elements. This makes a lot of different hybridization type by taking into account each element and crystallographic site.

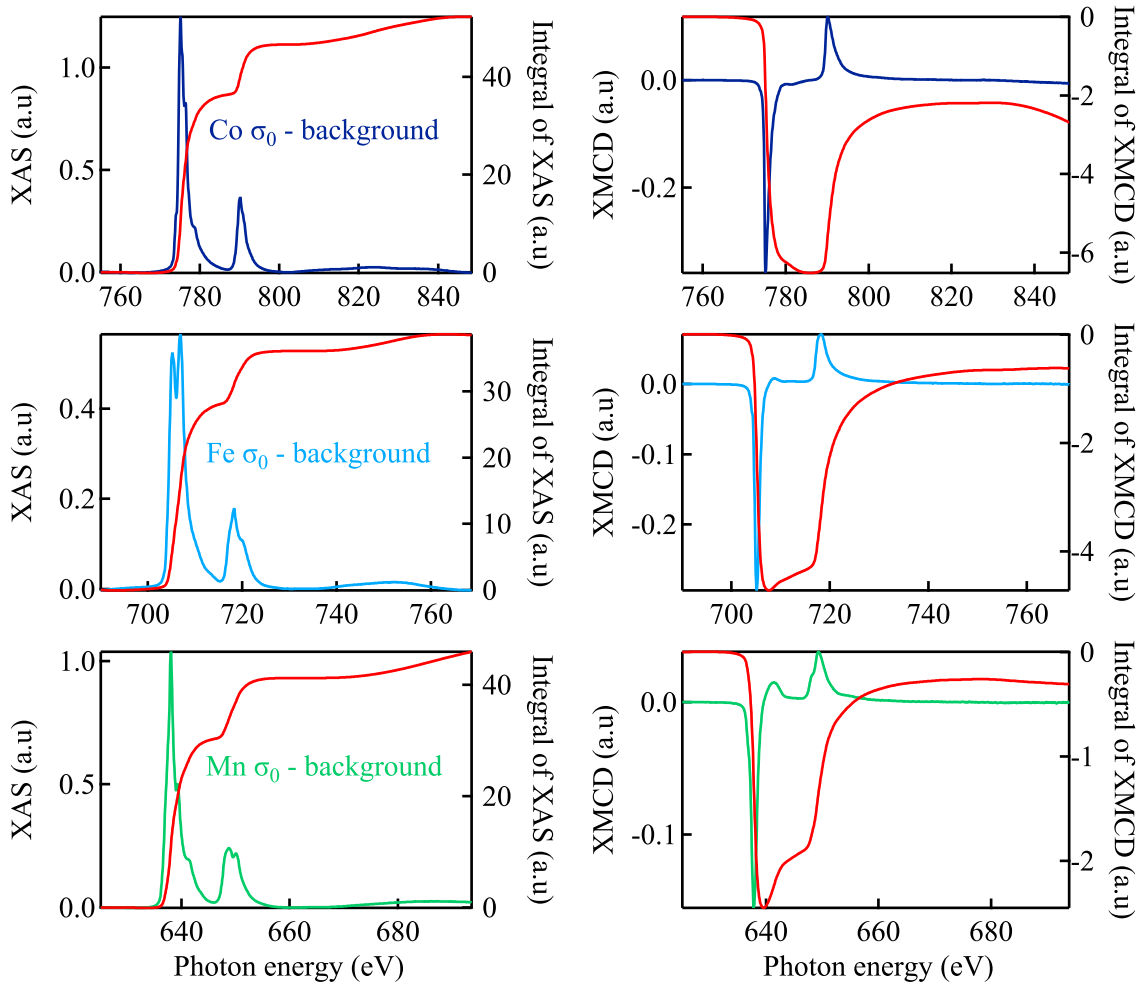

Figure 4.17: $(Mn_3Ga)_1/(Co_2FeGe)_2$ total XAS and XMCD signals at $L_{2,3}$ edges of Co (dark blue), Fe (light blue) and Mn (green) in the OOP direction and under a 2 T magnetic field and at 4 K.

[5]From neutron diffraction [160], $Mn_I = -2.8\ \mu_B$ and $Mn_{II} = 1.6\ \mu_B$

Magnetic moments obtained by XMCD on $(Mn_3Ga)_n/(Co_2FeGe)_m$ SL are summarized in table 4.2. There are not enough $(n-m)$ compositions to draw conclusions on the trend followed by the moment of each sublayer. Nonetheless, we can make the following observations. The moment of the Co_2FeGe layer is strongly reduced compared to the expected 6 μ_B/f.u. Moreover, it seems to increase when increasing m (surely toward its bulk value for $m \to \infty$). On the other hand, the Mn_3Ga moment is larger than the ~ 1 μ_B/f.u reported for bulk or thicker films [108, 159] (with much care taken to estimate the Mn moment extraction process). Besides, it seems that the moment decreases when n increases. One hypothesis is that Mn_3Ga is ferrimagnetic and that it gets closer to the full compensation by increasing the thickness, thus explaining why we do not detect a moment on a 20 nm thick Mn_3Ga layer. In this case, the larger moment of Mn_3Ga at small n could be explained by two arguments: either there is a strong coupling with Co_2FeGe that induces a ferromagnetic behavior on Mn_3Ga interfaces or, it is due to the chemical disorder in Mn_3Ga at small thicknesses that increases its moment [162]. However, this strong hypothesis needs more experiments to be confirmed.

n	m	M_{Mn_3Ga} (μ_B/f.u.)	M_{Co_2FeGe} (μ_B/f.u.)
1	1	2.13	2.16
	2	3.81	3.08
1.5	1.5	2.33	2.12
2	2	1.14	2.59

Table 4.2: Total magnetic moments obtained by XMCD on each SL $(Mn_3Ga)_n/(Co_2FeGe)_m$ where n and m stand for the number of u.c of each sublayer.

In order to verify that SL are perpendicularly magnetized and that each atom are well magnetically coupled to each other, OOP hysteresis loops were performed at L_2 edges of Co, Mn and Fe (maximum of XMCD signal). An example on $(Mn_3Ga)_1/(Co_2FeGe)_2$ SL is shown in figure 4.18. According to these

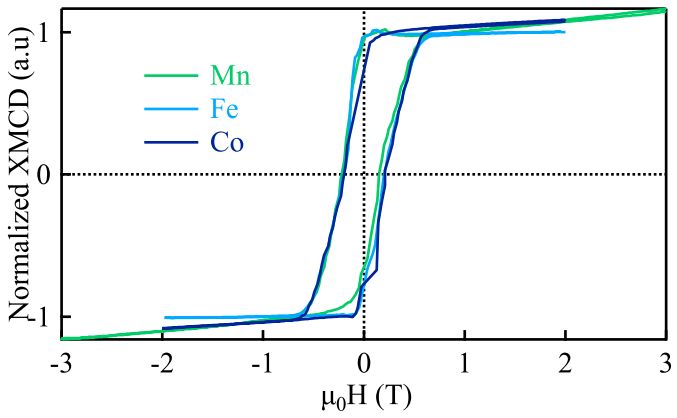

Figure 4.18: $(Mn_3Ga)_1/(Co_2FeGe)_2$ hysteresis loops at L_2 edges of Co (dark blue), Fe (light blue) and Mn (green) in the OOP direction at 4 K.

hysteresis loops, the OOP direction is indeed an easy axis[6]. Since the cross section of interaction and the

[6]The experimental set-up does not allow us to perform loops in the IP direction but it was still possible to check that IP was a hard axis, by doing a loop with the sample rotated by 70°

amount of each chemical element within a SL is not the same, all hysteresis loops are normalized to be compared to each other. All elements have the same behavior with same coercive fields which means that they are indeed strongly ferromagnetically coupled.

Every $(Mn_3Ga)_n/(Co_2FeGe)_m$ SL from table 4.2 exhibit PMA with a ferromagnetic coupling between sublayers. Such a result is very promising because it means that PMA is obtained here for SL with Co_2MnSi and Co_2FeGe, therefore probably for other similar Co_2YZ compounds. However, the fact that the Ag capping layer has not grown continuously on the SL may have oxidized the termination layer. Since XMCD is a surface technique, the magnetic moment values in table 4.2 may not be accurate.

4.5 Discussion and perspectives

We have seen in this section that it is possible to induce PMA in Heuslers SL with two different ways. Co_2MnAl/Fe_2MnAl SL are possible candidates using interfacial anisotropy to overcome the demagnetizing energy from equation 4.1. It turns out that K_S is not as large as expected and the only way to obtain PMA is to reduce the demagnetizing contribution (thus the magnetization amplitude) by excess Al content. However, a first milestone was reached with the observation of PMA at low temperature as well as the experimental proof that the electronic structure of the termination layer was conserved.

We then chose to focus on solution using bulk anisotropy K_V in tetragonalized Heusler Mn_3Ga to obtain PMA. Very promising preliminary results were obtained in the present work on Mn_3Ga/Co_2YZ SL that exhibit a strong PMA for various thicknesses of the sublayers. The magnetization remanence and coercive fields seems to be tunable in those systems but the full understanding requires a missing piece of the puzzle: the magnetic state of Mn_3Ga. The fact that no moment was detected on a 20 nm Mn_3Ga layer is puzzling since it is experimentally and theoretically reported to be ferrimagnetic with $\sim$1 μ_B/f.u. in bulk samples [108, 168] and thin epitaxial films [162]. However, we know now thanks to XMCD that Mn_3Ga is magnetic when incorporated in our SL, but with a larger moment than in the literature. Indeed, several studies all point out that the magnetic moment in Mn_xGa_{1-x} compounds is very sensitive to the x composition as well as the chemical disorder rate [160–162]. In particular, Mizukami *et al.* [162] showed that the $L1_0$ disorder, which mixes Mn_I and Ga[7] as shown in the figure 4.1a, destroys the moment of Mn_I which is anti-parallel to Mn_{II}. Since the moment of Mn_{II} is conserved under $L1_0$ disorder, the total moment increases toward a complete ferromagnetic behavior. In our SL, the fraction of disorder is difficult to estimate and may be thickness-dependent. It could explain the difference of behavior between ultra-thin Mn_3Ga that is magnetic and the 20 nm layer where no moment was detected.

In addition, contrary to the work of Ma *et al.* [164], we observed a ferromagnetic coupling between the two sublayers in the SL. Nevertheless, they worked with slightly higher thicknesses of Mn_3Ga, which could explain such a difference of coupling and supports the assumption that the magnetic state of Mn_3Ga depends on its thickness.

Many further experiments and perspectives are envisaged with those SL. First of all, the key point is to understand how Mn_3Ga magnetically behaves. We have seen from XMCD measurements that Mn_3Ga was magnetic for 1 and 2 u.c when incorporated in SL. It would be interesting to do the same experiment with 3 and more u.c in order to check how the moment varies and if the coupling between the sublayers is

[7]The $L1_0$ disorder is the tetragonalized equivalent to the B2 disorder in Co_2MnZ fcc Heusler alloys.

still parallel. Additionally, a completely compensated ferrimagnetic behavior could be detected by using neutron diffraction on our 20 nm thick Mn_3Ga layer. Once the magnetic ordering of Mn_3Ga is known, it will be possible to understand the tuning of the magnetic moment, the magnetization remanence and coercive fields of Mn_3Ga/Co_2YZ SL by varying the thickness of each sublayer or maybe the growth conditions. Then, further characterization like SR-PES and VNA-FMR will be possible to prove that these SL are interesting systems for spin transfer applications.

Chapter 5

Ultrafast demagnetization and Gilbert damping

On a very short timescale, excitation of a ferromagnetic material by an intense laser pulse of few tens of femtoseconds has been shown to result in a quenching of the magnetization, within hundreds of femtoseconds [169], in many different materials [170]. In some specific materials, it may also result in a complete reversal of the magnetization [171]. Over the years, different models have been proposed to explain this phenomenon, among which local spin-flip processes induced by electron scattering with particles or quasi-particles. In these models, the macroscopic Gilbert damping parameter α and the ultrafast characteristic demagnetization time τ_M are related if the same mechanism contributes to the transfer of angular momentum at both timescales. The first attempt to connect those two quantities was carried out by Koopmans *et al.* [172] using a quantum mechanical model calculations based on spin-flip scattering of electrons by impurities and phonons (similar to the model of Kamberský discussed in chapter 1). In this model, the demagnetization time τ_M reads:

$$\tau_M = c_0 \frac{\hbar}{k_B T_C \alpha}, \tag{5.1}$$

Where c_0 is a constant, k_B the Boltzmann constant and T_C the Curie temperature. In addition, several experimental studies pointed out that the demagnetization time τ_M in higly spin polarized materials increases with the spin polarization P as $\tau_M \propto \frac{1}{1-P}$ due to the removal of ordinary spin-flip scattering processes [170, 173]. However, the spin polarization of the different materials in those studies was never directly measured, but deduced from spin transport measurement and/or *ab initio* calculations. For instance, Co_2MnSi spin polarization in reference [173] is considered to be 60 % whereas it is well known now that it is fully polarized. Moreover, a 88 % spin polarization is claimed for Co_2FeAl, although we measured 35 % by SR-PES in this compound (see appendix B). In reference [170], the spin polarization is deduced from Meservey-Tedrow measurements in which the extraction of the polarization depends on many parameters. It must be noted that these results deserve to be confirmed. Here, we got a chance to test the models by exploring ultrafast dynamics on a unique type of materials, $Co_2MnSi_xAl_{1-x}$, for several reasons. First we were able to measure the true spin polarization by SR-PES. Second, Gilbert damping coefficients were determined independently by FMR and were shown to be linked to the spin polarization[1]. Third, a pump-probe laser set-up available in the group allowed us to explore the ultrafast

[1]Through the reduction of spin-flip scattering processes, see chapter 3.

dynamics in these compounds. Finally, all those properties are tunable by playing with the substitution rate x.

5.1 Review of $Co_2MnSi_xAl_{1-x}$ compounds

This series of compounds was discussed in chapters 2 and 3. The fact that the series undergoes a continuous chemical order transition from Co_2MnSi to Co_2MnAl will be put aside for the rest of the chapter. Nonetheless, important reminders regarding the electronic properties and Gilbert coefficients are made in this section. SR-PES measurements performed on $Co_2MnSi_xAl_{1-x}$ compounds are reminded in figure 5.1 with a p and s photon electric polarization. The Fermi energy moves toward the minority spin valence band by removing progressively one electron, *i. e.* by decreasing the substitution rate x. As reported in chapter 3, the use of p photon polarization (left column in figure 5.1) excites surface states transitions that suppresses the spin polarization at E_F in $Co_2MnSi_xAl_{1-x}$ when $x > 0.5$. Decreasing x shifts E_F downward in the DOS and the surface states move to the empty states for $x > 0.5$. Nonetheless, these surface states transitions are not excited anymore by using s photon polarization (middle column in figure 5.1), allowing us to measure the bulk spin polarization at E_F which is reported in figure 5.2.

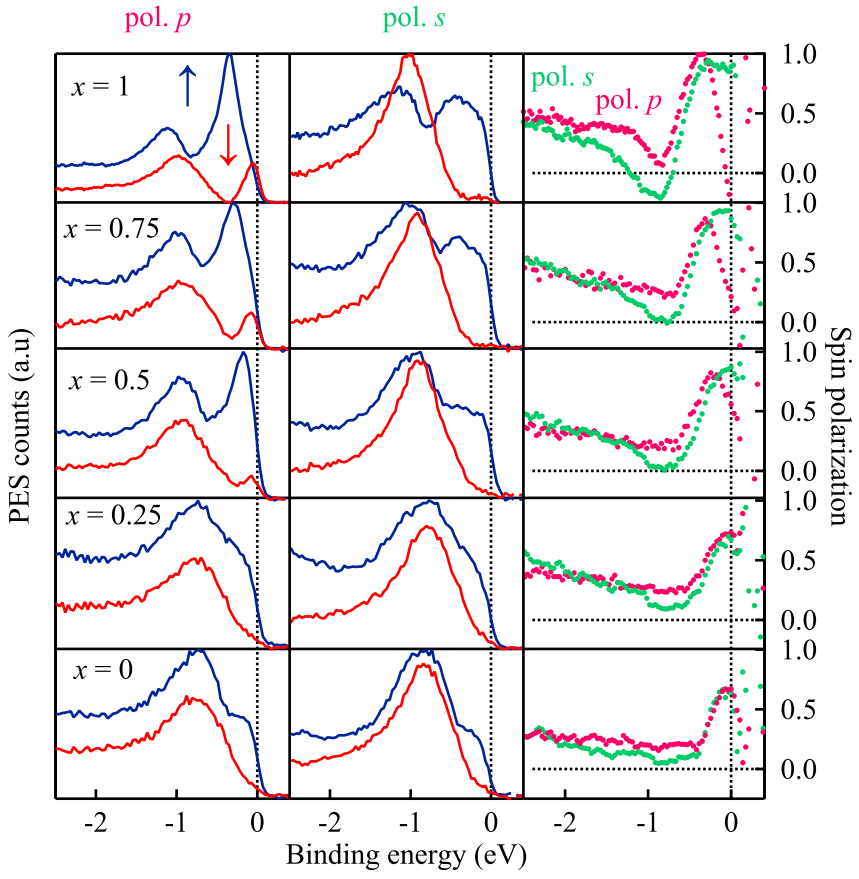

Figure 5.1: SR-PES experiment with $\hbar\omega = 37$ eV photon energy on $Co_2MnSi_xAl_{1-x}$ compounds. The left column is for p polarized photon, the middle column for s polarized photon and the right column is the corresponding spin polarizations.

The spin polarization as well as the Gilbert coefficient are plotted in figure 5.2 as a function of the

substitution rate x. Both quantities vary linearly with x, with an opposite trend. Thereby, it demonstrates that in $Co_2MnSi_xAl_{1-x}$ compounds, the Gilbert coefficient is directly linked to the underlying electronic structure (*i. e.* spin polarization at E_F). In addition, these materials provide a series of materials with a tunable spin polarization and Gilbert damping, hence being promising candidates to study the relation between the Gilbert coefficient, the spin polarization at E_F and the ultrafast demagnetization time.

$Co_2MnAl_xSi_{1-x}$	Spin pol.	M_S (μ_B/f.u)	α ($\times 10^{-3}$)	Δf_0 (MHz)	g-factor
$x = 1$	96 %	5.08	0.46	14.3	2.01
$x = 0.75$	90 %	4.85	0.73	21.7	1.99
$x = 0.5$	85 %	4.85	0.68	9	2.01
$x = 0.25$	75 %	4.80	1.0	81.5	2.00
$x = 0$	65 %	4.32	1.1	22	2.01

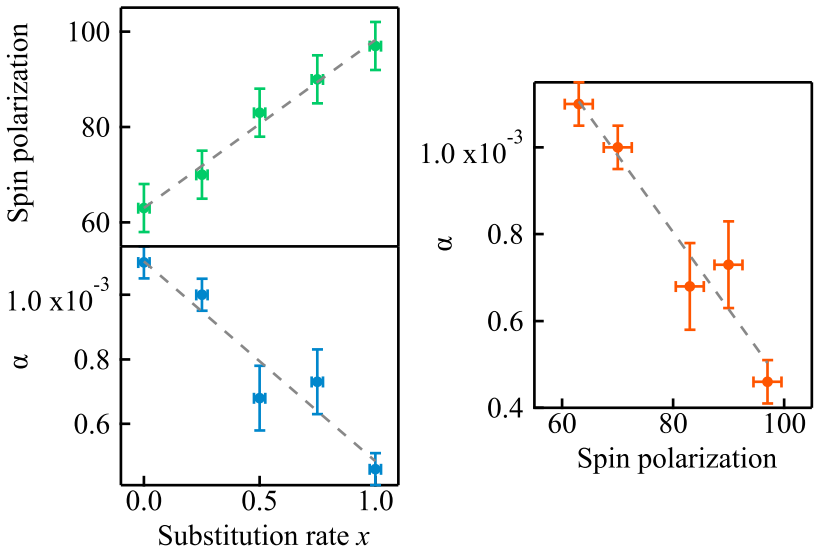

Figure 5.2: SR-PES experiment with $\hbar\omega = 37$ eV photon energy on $Co_2MnSi_xAl_{1-x}$ compounds. The left column is for p polarized photon, the middle column for s polarized photon and the right column is the corresponding spin polarizations.

5.2 Ultrafast demagnetization experiments

Ultrafast demagnetization experiments were carried out using Time-Resolved Magneto-Optical Kerr Effect (TR-MOKE) in a pump probe geometry. The experimental set-up is briefly described in reference [174] and the main elements are sketched in figure 5.3 (courtesy of M. Deb - IJL). A Ti-sapphire laser was used to generate a linearly polarized 35 fs pulse of 800 nm (1.55 eV). The pulse is then split in two separate beams: the pump that goes straight to the sample at time t_0 and the probe that get through the delay line and acquires a delay $t - t_0$ with respect to the pump (in the following, we set $t_0 = 0$). Additionally, to avoid interference effects, artifacts and measurements of the pump signal instead of the probe, the probe beam gets through a Beta Barium Borate (BBO) crystal for second harmonic generation

that doubles the radiation frequency. The probe signal arrives at the sample with an incident angle smaller than 6°. After being reflected by the ferromagnetic layer, the canting of the probe electric polarization due to the magneto-optical Kerr effect is analyzed. The projection of the magnetization (saturated in the out of plane direction with a field B = 1 T) is then measured at different time after the pump excitation.

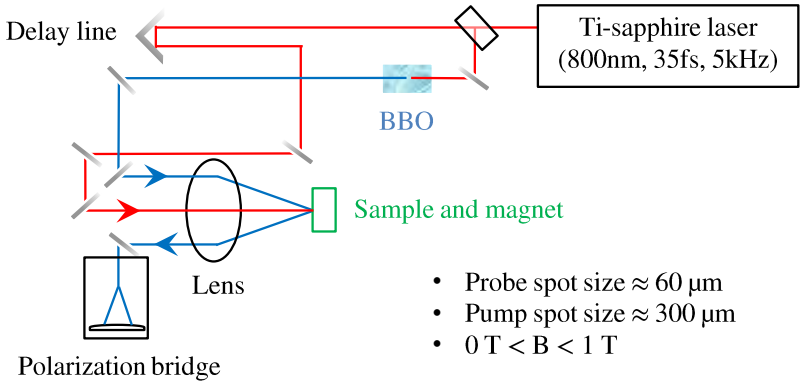

Figure 5.3: Sketch of the TR-MOKE set-up (courtesy of M. Deb - IJL).

Results of demagnetization measurements on $Co_2MnSi_xAl_{1-x}$ are presented in figure 5.4-left, with a maximum of magnetization quenching around 10 % for each layer. The temporal changes of the Kerr angle $\Delta\theta_k(t)$ are normalized by the saturation value θ_k just before the pump laser excitation.

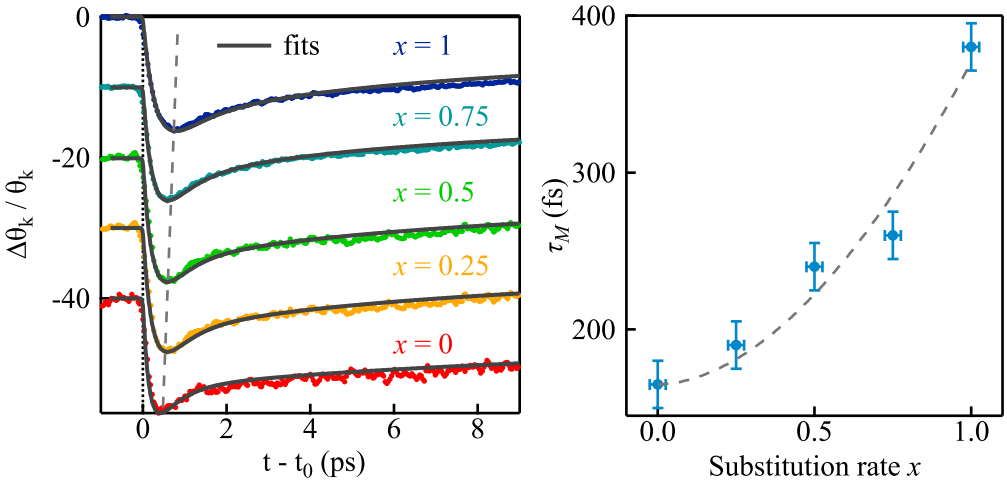

Figure 5.4: Demagnetization experiments on $Co_2MnSi_xAl_{1-x}$ compounds saturated with a static field $B = 1$ T. Left: normalized Kerr angle deviation at different delay times fitted using the 3-temperature model at each x composition. Right: characteristic demagnetization time τ_M plotted as a function of the substitution rate x (dashed line is only a guide to the eyes).

The time evolution of magnetization on a sub-picosecond timescale can be fitted according to equation 5.2 in terms of the 3-temperature model [169, 175]. This model was first introduced phenomenologically by Beaurepaire *et al.* [169] and was then described more accurately by Koopmans *et al.* [176] which gives the energy distribution among electrons, phonons and spins (considered as three distinct baths) after laser

excitation.

$$-\frac{\Delta M_z}{M_z} = \left[\left(\frac{A_1}{\sqrt{\left(\frac{t}{\tau_0}+1\right)}} - \frac{(A_2\tau_E - A_1\tau_M)e^{-\frac{t}{\tau_M}}}{\tau_E - \tau_M} - \frac{\tau_E(A_1 - A_2)e^{-\frac{t}{\tau_E}}}{\tau_E - \tau_M}\right)\Theta(t)\right] \otimes \Gamma(t) \qquad (5.2)$$

Where $\otimes\Gamma(t)$ is the convolution with the Gaussian laser pulse profile, $\Theta(t)$ is a step distribution and $A_{1,2}$ are treated here as fitting parameters (physically, A_1 is related to the value of $\frac{\Delta M_z}{M_s}$ after the long-term recovery and A_2 is proportional to the elevation of the electrons bath temperature). The time parameter τ_M is the ultrafast demagnetization time and τ_0 is a phenomenological parameter. In the low fluence regime, which corresponds to our measurements, τ_E represents the electron-phonon relaxation time. The value of $\tau_E = 520 \pm 20$ fs was used to fit all the demagnetization curves. The ultrafast demagnetization time τ_M is observed to increase from 165 ± 15 fs in Co_2MnAl to 380 ± 15 fs in Co_2MnSi (figure 5.4-right). The dashed line is a guide for the eyes. The dependence of τ_M with the composition rate x in $Co_2MnSi_xAl_{1-x}$ is plotted in figure 5.4-right and presents a very smooth increasing trend. In the following, the relation between τ_M, the Gilbert damping α and the spin polarization P is discussed.

5.3 Discussion

The evolution of the demagnetization time with both spin polarization P and Gilbert damping α is presented in figure 5.5-left and 5.5-right. On the one hand, a clear linear variation between $\frac{1}{\tau_M}$ and $1-P$ is observed in this series, as proposed in Mann *et al.* work [170]. As the magnetic damping α is proportional to P here, this means that $\frac{1}{\tau_M}$ is proportional to α too. This is partly in agreement with Koopmans model [172] who proposed this dependence. However, they also obtained a dependence with the Curie temperature of the films (see equation 5.1). As the Curie temperature in Heusler compounds changes with the number of valence electron and because the $Co_2MnSi_xAl_{1-x}$ behave as solid solutions (see chapter 2), we thus consider a linear T_C decrease with x, going from 985 K to 697 K as experimentally measured for $x = 1$ and $x = 0$ [59], respectively. To test this possible dependence with the Curie temperature, we plot in figure 5.5-right first the product $\tau_M \cdot \alpha$ and second the product $\tau_M \cdot \alpha \cdot \frac{T_C(x)}{T_C(x=1)}$. We clearly observed that the demagnetization time is not linked to the variation in Curie temperature in this series.

Our results offer a nice opportunity to disentangle the two different effects proposed to be responsible for the increase of the demagnetization time, *i. e.* the spin polarization on the one hand and thermal effects on the other hand. According to Koopmans model [172], when the ambient temperature is very close to the Curie temperature of a film, the demagnetization would be very slow. This is the so called "slowdown effect". In other words, if the ambient temperature is room temperature, a larger T_C would lead to a faster demagnetization. In our samples however, T_C goes up from Co_2MnAl to Co_2MnSi, whereas the demagnetization process is slower, so the inverse variation is observed in our series. Therefore, the T_C are too high here to see any slowdown effect and the change of τ_M only comes from the intrinsic properties of the films, *i. e.* Gilbert damping and spin polarization. This also clarifies some points in the work of Müller *et al.* [173]. In their study, they first reported a very fast demagnetization process in $Co_2MnSi(110)$ and second a slow one in CrO_2 and $LaSrMnO_3$ films with T_C values close to room temperature (390 K and 360 K, respectively). So on the bases of Koopmans model one cannot know if the very slow demagnetization process in these compounds is due to a low T_C or a large spin polarization. In our samples we disentangle these two effects and the longest demagnetization time is found for Co_2MnSi

(τ_M = 380 fs), a true half-metal magnet with a 0.8 eV spin gap and a large T_C.

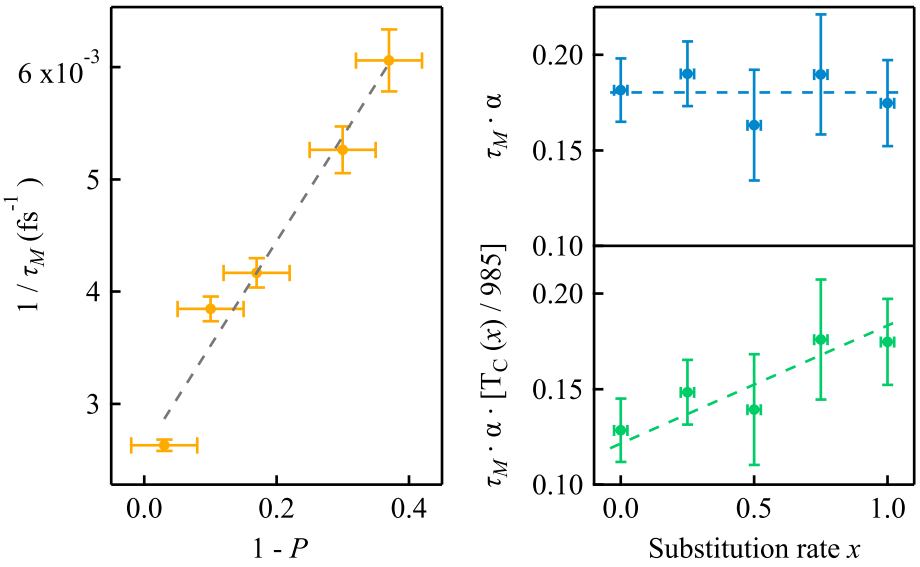

Figure 5.5: Left: inverse of the ultrafast demagnetization time τ_M in $Co_2MnSi_xAl_{1-x}$ compounds as a function of $1 - P$. Right: product $\tau_M \cdot \alpha$ and $\tau_M \cdot \alpha \cdot \frac{T_C(x)}{T_C(x=1)}$ to visualize the thermal effects contribution in the demagnetization process.

The present study thus demonstrate experimentally that the high spin polarization in these Heusler compounds responsible for the reduction of spin-flip scattering processes leads to an increase of the demagnetization time as predicted for HMM materials. It is worth noticing that much larger demagnetization times in the picosecond timescale would be expected for large band gap and full spin-polarization. In the case of small band gap of the order of 0.1 eV, Mann *et al.* [170] showed that thermal effects from the heated electron system lead to a reduction of spin-flip scattering and therefore a reduction of τ_M. They calculated a reduction of the spin-flip suppression factor from 10^4 for a gap of 1 eV to 40 for a gap of 0.3 eV. However, the band gap of our Co_2MnSi was calculated to be around 0.8 eV with a Fermi energy in the middle of the gap [8, 12]. This was corroborated by direct measurement using spin SR-PES [10]. Therefore, according to their model, we should expect a much longer demagnetization time for Co_2MnSi. But an important experimental condition should be considered: the 1.5 eV photon energy of the laser much larger than the spin gap. Electrons occupying the top of the minority spin valence band are thus excited, allowing spin flips during the demagnetization process. The effect of the spin gap is however visible since much more majority spin electrons are excited compared to minority ones. Even if this photon absorption process is considered to occur at a much faster time than the demagnetization process this point should be addressed experimentally.

To conclude, the $Co_2MnSi_xAl_{1-x}$ series provides a continuous change in electronic and dynamic properties, without adding any uncontrolled ingredients. This Heusler series of compounds exhibits a tunable spin polarization measured by SR-PES and offer a robust experimental evidence of the impact of spin-flip scattering processes in the ultrafast demagnetization characteristic time. This clearly supports the assumption used in the models proposed in the literature.

Summary and perspectives

Through this thesis, some Heusler compounds grown by MBE were investigated in details. After showing that such compounds in thin films were ideal candidates for spintronics and magnonics, some special efforts were made to demonstrate the full spin polarization and ultralow damping in these compounds.

In a first part, different high quality epitaxial films of Co_2MnZ (Z=Al, Si, Si_xAl_{1-x}, Ga, Ge, Ge_xGa_{1-x}, Sn, Sb) were grown epitaxially, confirming the high stability of this family of compounds. The structural and chemical order was clarified in these 20 nm thick films and their static magnetic properties were found to be close to the theoretical ones. This entire set of characterization was necessary to confirm that they were ideal systems, the closest as possible from perfect crystals used in calculations that predict outstanding properties in those compounds. Afterward, we have investigated the spin-resolved electronic structure of such layers and we were particularly interested in their spin polarization. We have demonstrated experimentally that all Co_2MnZ thin films exhibit a gap[2] in their minority spin density of states, with a changing gap width and Fermi energy location, depending on the Z element, in agreement with *ab initio* calculations. In particular, we have shown that Co_2MnZ with Z=Si, Ga, Ge and Sn were HMM, *i. e.* with a Fermi energy located in the spin gap. The tunable Fermi energy position in the spin gap was an excellent opportunity to confirm the reduction of the Gilbert damping coefficient in such materials, where relaxation mechanisms involving spin-flip are forbidden. We have demonstrated that Co_2MnZ compounds were all ultralow damping materials, in particular for Z=Si and Ge where values down to $\alpha = 4.1 \times 10^{-4}$ were measured. The interplay between the measured electronic properties and magnetization dynamics was consistent with the reduction of the Gilbert coefficient associated to the HMM behavior.

In a second part, we have investigated the properties of tetragonal Heusler type Mn_3Ga compound that exhibit a strong magneto-crystalline bulk anisotropy. This anisotropy property has been used to obtain perpendicular magnetic anisotropy in Heusler superlattices Mn_3Ga/Co_2YZ Heusler compounds. This is a very important step in order to combine ultralow damping coefficients, spin gaps and perpendicularly magnetized layers which represents a challenging step forward toward efficient devices. Promising preliminary results were obtained such as high quality superlattices and perpendicular anisotropy for various thicknesses of the sublayers, for two different Co_2YZ Heusler sublayers.

Finally, $Co_2MnSi_xAl_{1-x}$ quaternary compounds were used to study the microscopic mechanisms that play a role in the quenching of the magnetization at the subpicosecond timescale. Particularly, we have demonstrated that spin-flip mechanisms were responsible for the loss of angular momentum at two different timescales: the Gilbert damping (nanosecond) and the ultrafast demagnetization time (hundreds of femtoseconds), thereby confirming some theoretical models.

[2]Except for Z=Sb.

Consequently, we have demonstrated that Co_2MnZ Heusler layers are promising compounds for spintronics and offer many possibilities for future works. Indeed, the only way to prove that they are efficient materials for applications is to grow heterostructures and devices. To do that, it is first necessary to study if those compounds maintain their properties in very thin layers of few nanometers necessary in devices (for instance, switching currents by STT or SOT are proportional to the thickness). Then, Co_2MnZ based MTJs or spin valves stacks must be grown to verify the expected large magneto-resistance ratios. Furthermore, the low switching currents associated to the ultralow damping coefficients measured must be tested, either in STT-based systems or with SOT by growing Co_2MnZ / NM bilayers (NM stands for a non-magnetic layer with a large spin Hall angle, like Pt or Ta). Finally, Co_2MnZ Heusler layers should be integrated as magnonic crystals[3] to prove their efficiency in devices such as magnon transistors, logic gates *etc*.

Heusler superlattices have shown to exhibit PMA for many thicknesses of each sublayer. Nonetheless, the magnetic properties are not fully understood. It is of the utmost importance to discover how Mn_3Ga magnetically behaves when incorporated in a superlattice. Several experiments are possible to resolve its magnetic configuration such as neutrons scattering, XMCD or wedges with a constant thickness of Mn_3Ga and a varying thickness of Co_2MnSi on top of it[4]. Additionally, substituting Mn_3Ga by Mn_3Ge appears to be interesting as well. This compound is theoretically predicted to be similar to Mn_3Ga but with a better chemical ordering, a comparable K_V and a spin gap along the ΓZ direction of the Brillouin zone (momentum **k** along c in the tetragonal $D0_{22}$ structure) [177, 178].

In addition, these compounds are model systems to test the understanding of ultrafast dynamics, especially, by tuning the excitation photon energy. Indeed, the ultrafast demagnetization experiments done here were performed with a photon energy $\hbar\omega = 1.55$ eV, larger than the spin gap width in all Co_2MnZ layers. It means that when electrons are excited by the laser pulse, they are sent into empty states where there is no gap and thus, some spin-flip processes may occur like in standard metals. It may explain that the measured τ_M are at least one order of magnitude smaller than expected by theory on HMM. Ultrafast demagnetization experiments with the laser photon energy tuned below the half band gap width of Co_2MnSi (≤ 0.4 eV) will be performed on the same quaternary series in the near future.

More generally, we have noticed that many Heusler compounds were stable in thin films. Through the present work and other unpublished works from the laboratory, other series of Heusler compounds like Mn_2CoGe and Pd_2MnZ (Z=In, Sn, Sb) were successfully elaborated. Besides giving a infinite lattice constant tunability for MBE growth, Heusler compounds offer many noteworthy properties that may be of great interest in spintronics: half metallic antiferromagnetism [179], magnetostriction [180], topological states [181] and so on.

[3]Like photonic crystals, a magnonic crystal is a metamaterial in which a band gap in the spin wave dispersion curve is artificially created by patterning and allows to select the desired spin wave frequency.

[4]Thereby, the total macroscopic moment should be linear with the increasing Co_2MnSi thickness, and the intercept with the y axis should correspond to the Mn_3Ga moment.

References

[1]M. N. Baibich, J. M. Broto, A. Fert, F. N. Van Dau, F. Petroff, P. Eitenne, G. Creuzet, A. Friederich, and J. Chazelas, "Giant magnetoresistance of (001)Fe/(001)Cr magnetic superlattices", Physical Review Letters **61**, 2472–2475 (1988).

[2]J. C. Slonczewski, "Current-driven excitation of magnetic multilayers", Journal of Magnetism and Magnetic Material **159**, L1–L7 (1996).

[3]L. Berger, "Emission of spin waves by a magnetic multilayer traversed by a current", Physical Review B **54**, 9353–9358 (1996).

[4]J. A. Katine, F. J. Albert, R. A. Buhrman, E. B. Myers, and D. C. Ralph, "Current-Driven Magnetization Reversal and Spin-Wave Excitations in Co/Cu/Co Pillars", Physical Review Letters **84**, 3149 (2000).

[5]S. Mangin, D. Ravelosona, J. A. Katine, and E. E. Fullerton, "Current-induced magnetization reversal in nanopillars with perpendicular anisotropy", Nature Materials **5**, 210–215 (2006).

[6]F. Heusler, "Über die Synthese ferromagnetischer Manganlegierungen", Verhandlungen der Deutschen physikalischen Gesellschaft **5**, 219 (1903).

[7]S. Ishida, S. Fujii, S. Kashiwagi, and S. Asano, "Search for Half-Metallic Compounds in Co_2MnZ (Z=IIIb, IVb, Vb Element)", Journal of the Physical Society of Japan **64**, 2152–2157 (1995).

[8]I. Galanakis, P. H. Dederichs, and N. Papanikolaou, "Slater-Pauling behavior and origin of the half-metallicity of the full-Heusler alloys", Physical Review B **66**, 174429 (2002).

[9]R. A. de Groot, F. M. Mueller, P. G. van Engen, and K. H. J. Buschow, "New Class of Materials: Half-Metallic Ferromagnets", Physical Review Letters **50**, 2024 (1983).

[10]S. Andrieu, A. Neggache, T. Hauet, T. Devolder, A. Hallal, M. Chshiev, A. M. Bataille, P. Le Fèvre, and F. Bertran, "Direct evidence for minority spin gap in the Co_2MnSi Heusler compound", Physical Review B **93**, 094417 (2016).

[11]V. Kamberský, "On ferromagnetic resonance damping in metals", Czechoslovak Journal of Physics **26**, 1366–1383 (1976).

[12]B. Pradines, R. Arras, I. Abdallah, N. Biziere, and L. Calmels, "First-principles calculation of the effects of partial alloy disorder on the static and dynamic magnetic properties of Co_2MnSi", Physical Review B **95**, 094425 (2017).

[13]T. Devolder, T. Tahmasebi, S. Eimer, T. Hauet, and S. Andrieu, "Compositional dependence of the magnetic properties of epitaxial FeV/MgO thin films", Applied Physics Letters **103**, 242410 (2013).

[14]W. H. Butler, X.-G. Zhang, T. C. Schulthess, and J. M. MacLaren, "Spin-dependent tunneling conductance of Fe|MgO|Fe sandwiches", Physical Review B **63**, 054416 (2001).

[15]I. M. Miron, K. Garello, G. Gaudin, P. J. Zermatten, M. V. Costache, S. Auffret, S. Bandiera, B. Rodmacq, A. Schuhl, and P. Gambardella, "Perpendicular switching of a single ferromagnetic layer induced by in-plane current injection", Nature **476**, 189–193 (2011).

[16]C.-H. Lambert, S. Mangin, B. S. D. C. S. Varaprasad, Y. K. Takahashi, M. Hehn, M. Cinchetti, G. Malinowski, K. Hono, Y. Fainman, M. Aeschlimann, and E. E. Fullerton, "All-optical control of ferromagnetic thin films and nanostructures", Science **345**, 1337–1340 (2014).

[17]F. Hellman, A. Hoffmann, Y. Tserkovnyak, G. S. D. Beach, E. E. Fullerton, C. Leighton, A. H. MacDonald, D. C. Ralph, D. A. Arena, H. A. Dürr, P. Fischer, J. Grollier, J. P. Heremans, T. Jungwirth, A. V. Kimel, B. Koopmans, I. N. Krivorotov, S. J. May, A. K. Petford-Long, J. M. Rondinelli, N. Samarth, I. K. Schuller, A. N. Slavin, M. D. Stiles, O. Tchernyshyov, A. Thiaville, and B. L. Zink, "Interface-induced phenomena in magnetism", Reviews of Modern Physics **89**, 025006 (2017).

[18]I. L. Prejbeanu, S. Bandiera, J. Alvarez-Hérault, R. C. Sousa, B. Dieny, and J. P. Nozières, "Thermally assisted MRAMs: Ultimate scalability and logic functionalities", Journal of Physics D: Applied Physics **46**, 074002 (2013).

[19]A. V. Chumak, V. I. Vasyuchka, A. A. Serga, and B. Hillebrands, "Magnon spintronics", Nature Physics **11**, 453–461 (2015).

[20]C. Kittel, "On the theory of ferromagnetic resonance absorption", Physical Review **73**, 155–161 (1948).

[21]J. Z. Sun, "Spin-current interaction with a monodomain magnetic body: A model study", Physical Review B **62**, 570–578 (2000).

[22]D. C. Ralph and M. D. Stiles, "Spin transfer torques", Journal of Magnetism and Magnetic Materials **320**, 1190–1216 (2008).

[23]C. Hauser, T. Richter, N. Homonnay, C. Eisenschmidt, M. Qaid, H. Deniz, D. Hesse, M. Sawicki, S. G. Ebbinghaus, and G. Schmidt, "Yttrium Iron Garnet Thin Films with Very Low Damping Obtained by Recrystallization of Amorphous Material", Scientific Reports **6**, 20827 (2016).

[24]M. A. W. Schoen, D. Thonig, M. L. Schneider, T. J. Silva, H. T. Nembach, O. Eriksson, O. Karis, and J. M. Shaw, "Ultra-low magnetic damping of a metallic ferromagnet", Nature Physics **12**, 839–842 (2016).

[25]C. Liu, C. K. A. Mewes, M. Chshiev, T. Mewes, and W. H. Butler, "Origin of low Gilbert damping in half metals", Applied Physics Letters **95**, 022509 (2009).

[26]A. Sakuma, "First-principles study of the Gilbert damping constants of Heusler alloys based on the torque correlation model", Journal of Physics D: Applied Physics **48**, 164011 (2015).

[27]V. Kamberský, "On the Landau–Lifshitz relaxation in ferromagnetic metals", Canadian Journal of Physics **48**, 2906–2911 (1970).

[28]H. C. Kandpal, G. H. Fecher, and C. Felser, "Calculated electronic and magnetic properties of the half-metallic, transition metal based Heusler compounds", Journal of Physics D: Applied Physics **40**, 1507–1523 (2007).

[29]M. Jourdan, J. Minár, J. Braun, A. Kronenberg, S. Chadov, B. Balke, A. Gloskovskii, M. Kolbe, H. J. Elmers, G. Schönhense, H. Ebert, C. Felser, and M. Kläui, "Direct observation of half-metallicity in the Heusler compound Co_2MnSi", Nature Communications **5**, 3974 (2014).

[30]S. Trudel, O. Gaier, J. Hamrle, and B. Hillebrands, "Magnetic anisotropy, exchange and damping in cobalt-based full-Heusler compounds : an experimental review", Journal of Physics D: Applied Physics **43**, 193001 (2010).

[31]M. Oogane, T. Kubota, H. Naganuma, and Y. Ando, "Magnetic damping constant in Co-based full heusler alloy epitaxial films", Journal of Physics D: Applied Physics **48**, 164012 (2015).

[32]M. Oogane, A. P. McFadden, K. Fukuda, M. Tsunoda, Y. Ando, and C. J. Palmstrøm, "Low magnetic damping and large negative anisotropic magnetoresistance in half-metallic $Co_{2-x}Mn_{1+x}Si$ Heusler alloy films grown by molecular beam epitaxy", Applied Physics Letters **112**, 262407 (2018).

[33]J. M. Shaw, E. K. Delczeg-Czirjak, E. R. J. Edwards, Y. Kvashnin, D. Thonig, M. A. W. Schoen, M. Pufall, M. L. Schneider, T. J. Silva, O. Karis, K. P. Rice, O. Eriksson, and H. T. Nembach, "Magnetic damping in sputter-deposited Co_2MnGe Heusler compounds with A2,B2, and $L2_1$ orders: Experiment and theory", Physical Review B **97**, 094420 (2018).

[34]M. Julliere, "Tunneling between ferromagnetic films", Physics Letters **54A**, 225–226 (1975).

[35]J. C. Slonczewski, "Conductance and exchange coupling of two ferromagnets separated by a tunneling barrier", Physical Review B **39**, 6995–7002 (1989).

[36]J. C. Rojas-Sánchez and A. Fert, "Compared Efficiencies of Conversions between Charge and Spin Current by Spin-Orbit Interactions in Two- and Three-Dimensional Systems", Physical Review Applied **11**, 054049 (2019).

[37]L. Liu, O. J. Lee, T. J. Gudmundsen, D. C. Ralph, and R. A. Buhrman, "Current-Induced Switching of Perpendicularly Magnetized Magnetic Layers Using Spin Torque from the Spin Hall Effect", Physical Review Letters **109**, 096602 (2012).

[38]K.-S. Lee, S.-W. Lee, B.-C. Min, and K.-J. Lee, "Threshold current for switching of a perpendicular magnetic layer induced by spin Hall effect", Applied Physics Letters **102**, 112410 (2013).

[39]Y. Kim, X. Fong, K.-W. Kwon, M.-C. Chen, and K. Roy, "Multilevel Spin-Orbit Torque MRAMs", IEEE Transactions on Electron Devices **62**, 561–568 (2014).

[40]S. I. Klselev, J. C. Sankey, I. N. Krivorotov, N. C. Emley, R. J. Schoelkopf, R. A. Buhrman, and D. C. Ralph, "Microwave oscillations of a nanomagnet driven by a spin-polarized current", Nature **425**, 380–383 (2003).

[41]J. Torrejon, M. Riou, F. A. Araujo, S. Tsunegi, G. Khalsa, D. Querlioz, P. Bortolotti, V. Cros, K. Yakushiji, A. Fukushima, H. Kubota, S. Yuasa, M. D. Stiles, and J. Grollier, "Neuromorphic computing with nanoscale spintronic oscillators", Nature **547**, 428–431 (2017).

[42]A. V. Chumak, A. A. Serga, and B. Hillebrands, "Magnon transistor for all-magnon data processing", Nature Communications **5**, 4700 (2014).

[43]V. E. Demidov, S. O. Demokritov, K. Rott, P. Krzysteczko, and G. Reiss, "Linear and nonlinear spin-wave dynamics in macro- and microscopic magnetic confined structures", Journal of Physics D: Applied Physics **41**, 164012(10pp) (2008).

[44]F. Bonell, T. Hauet, S. Andrieu, F. Bertran, P. Le Fèvre, L. Calmels, A. Tejeda, F. Montaigne, B. Warot-Fonrose, B. Belhadji, A. Nicolaou, and A. Taleb-Ibrahimi, "Spin-polarized electron tunneling in bcc FeCo/MgO/FeCo(001) magnetic tunnel junctions", Physical Review Letters **108**, 176602 (2012).

[45]S. Andrieu, T. Hauet, M. Gottwald, A. Rajanikanth, L. Calmels, A. M. Bataille, F. Montaigne, S. Mangin, E. Otero, P. Ohresser, P. Le Fevre, F. Bertran, A. Resta, A. Vlad, A. Coati, and Y. Garreau, "Co/Ni multilayers for spintronics: high spin-polarization and tunable magnetic anisotropy", Physical Review Materials **2**, 064410 (2018).

[46]T. Fischer, M. Kewenig, D. A. Bozhko, A. A. Serga, I. I. Syvorotka, F. Ciubotaru, C. Adelmann, B. Hillebrands, and A. V. Chumak, "Experimental prototype of a spin-wave majority gate", Applied Physics Letters **110**, 152401 (2017).

[47]T. Jungwirth, X. Marti, P. Wadley, and J. Wunderlich, "Antiferromagnetic spintronics", Nature Nanotechnology **11**, 231–241 (2016).

[48]G. Joshi, T. Dahal, S. Chen, H. Wang, J. Shiomi, G. Chen, and Z. Ren, "Enhancement of thermoelectric figure-of-merit at low temperatures by titanium substitution for hafnium in n-type half-Heuslers Hf0.75-xTixZr0.25NiSn0.99Sb0.01", Nano Energy **2**, 82–87 (2013).

[49]Y. Oner, O. Kamer, E. Alveroglu, M. Acet, and T. Krenke, "Superconductivity in the Heusler alloy Pd_2YbPb", Journal of Alloys and Compounds **429**, 64–71 (2007).

[50]C. Shekhar, S. Ouardi, A. K. Nayak, G. H. Fecher, W. Schnelle, and C. Felser, "Ultrahigh mobility and nonsaturating magnetoresistance in Heusler topological insulators", Physical Review B **86**, 155314 (2012).

[51]Z. Fisk, P. C. Canfield, W. P. Beyermann, J. D. Thompson, M. F. Hundley, H. R. Ott, E. Felder, M. B. Maple, M. A. Lopez De La Torre, P. Visani, and C. L. Seaman, "Massive electron state in YbBiPt", Physical Review Letters **67**, 3310–3313 (1991).

[52]I. Galanakis, "Theory of Heusler and Full-Heusler Compounds", in *Heusler alloys*, Vol. 222, Springer (2016), pp. 3–36.

[53]J. Kübler, "First principle theory of metallic magnetism", Physica **127B**, 257–263 (1984).

[54]C. Bilzer, "Microwave susceptibility of thin ferromagnetic films: metrology and insight into magnetization dynamics", PhD thesis (Université Paris Sud - Paris XI, 2007).

[55]R. J. Elliott, "Theory of the effect of spin-Orbit coupling on magnetic resonance in some semiconductors", Physical Review **96**, 266–279 (1954).

[56]B. Heinrich, R. Urban, and G. Woltersdorf, "Magnetic relaxation in metallic films: Single and multilayer structures", Journal of Applied Physics **91**, 7523–7525 (2002).

[57]R. Arias and D. L. Mills, "Extrinsic contributions to the ferromagnetic resonance response of ultrathin films", Physical Review B - Condensed Matter and Materials Physics **60**, 7395–7409 (1999).

[58]K. Özdoğan, E. Şaşioğlu, B. Aktaş, and I. Galanakis, "Doping and disorder in the Co_2MnAl and Co_2MnGa half-metallic Heusler alloys", Physical Review B - Condensed Matter and Materials Physics **74**, 172412 (2006).

[59]J. Kübler, G. H. Fecher, and C. Felser, "Understanding the trend in the Curie temperatures of Co_2-based Heusler compounds: Ab initio calculations", Physical Review B - Condensed Matter and Materials Physics **76**, 024414 (2007).

[60]P. J. Webster, "Magnetic and chemical order in Heusler alloys containing cobalt and manganese", Journal of Physics and Chemistry of Solids **32**, 1221 (1971).

[61]H. Liu, "Giant tunneling magnetoresistance in epitaxial Co_2MnSi/MgO/Co_2MnSi magnetic tunnel junctions by half-metallicity of Co_2MnSi and coherent tunneling", Applied Physics Letters **101**, 132418 (2012).

[62]T. Ishikawa, H. Liu, T. Taira, K. Matsuda, T. Uemura, and M. Yamamoto, "Influence of film composition in Co_2MnSi electrodes on tunnel magnetoresistance characteristics of Co_2MnSi/MgO/Co_2MnSi magnetic tunnel junctions", Applied Physics Letters **95**, 232512 (2009).

[63]B. M. Ludbrook, B. J. Ruck, and S. Granville, "Perpendicular magnetic anisotropy in Co_2MnGa and its anomaleous Hall effect", Applied Physics Letters **110**, 062408 (2017).

[64]H. Chudo, K. Ando, K. Saito, S. Okayasu, R. Haruki, Y. Sakuraba, H. Yasuoka, K. Takanashi, and E. Saitoh, "Spin pumping efficiency from half metallic Co_2MnSi", Journal of Applied Physics **109**, 073915 (2011).

[65]T. Stückler, C. Liu, H. Yu, F. Heimbach, J. Chen, J. Hu, S. Tu, M. S. Alam, J. Zhang, Y. Zhang, I. L. Farrell, C. Emeny, S. Granville, Z. M. Liao, D. Yu, and W. Zhao, "Spin wave propagation detected over 100μm in half-metallic Heusler alloy Co_2MnSi", Journal of Magnetism and Magnetic Materials **450**, 13–17 (2018).

[66]H. M. Huang, S. J. Luo, and K. L. Yao, "First-principles investigation of the electronic structure and magnetism of Heusler alloys CoMnSb and Co_2MnSb", Physica B: Condensed Matter **406**, 1368–1373 (2011).

[67]S. Picozzi, A. Continenza, and A. J. Freeman, "Co_2MnX (X = Si, Ge, Sn) Heusler compounds: An ab initio study of their structural, electronic, and magnetic properties at zero and elevated pressure", Physical Review B **66**, 094421 (2002).

[68]Y. Sakuraba, J. Nakata, M. Oogane, Y. Ando, H. Kato, A. Sakuma, T. Miyazaki, and H. Kubota, "Magnetic tunnel junctions using B2-ordered Co_2MnAl Heusler alloy epitaxial electrode", Applied Physics Letters **88**, 022503 (2006).

[69]M. Oogane, T. Wakitani, S. Yakata, R. Yilgin, Y. Ando, A. Sakuma, and T. Miyazaki, "Magnetic damping in ferromagnetic thin films", Japanese Journal of Applied Physics **45**, 3889–3891 (2006).

[70]M. Hahn, G. Schönhense, E. A. Jorge, and M. Jourdan, "Significant spin polarization of Co_2MnGa Heusler thin films on MgO(100) measured by ultraviolet photoemission spectroscopy", Applied Physics Letters **98**, 232503 (2011).

[71]M. Kolbe, S. Chadov, E. Arbelo Jorge, G. Schönhense, C. Felser, H. J. Elmers, M. Kläui, and M. Jourdan, "Test of band structure calculations for Heusler compounds by spin-resolved photoemission spectroscopy", Physical Review B **86**, 024422 (2012).

[72]I. Abdallah, B. Pradines, N. Ratel-Ramond, G. BenAssayag, R. Arras, L. Calmels, J. F. Bobo, E. Snoeck, and N. Biziere, "Evolution of magnetic properties and damping coefficient of Co_2MnSi Heusler alloy with Mn/Si and Co/Mn atomic disorder", Journal of Physics D: Applied Physics **50**, 359501 (2017).

[73]S. V. Faleev, Y. Ferrante, J. Jeong, M. G. Samant, B. Jones, and S. S. Parkin, "Unified explanation of chemical ordering, the Slater-Pauling rule, and half-metallicity in full Heusler compounds", Physical Review B **95**, 045140 (2017).

[74]R. E. Honig, *Vapor pressure data for the solid and liquid elements* (RCA Laboratories, David Sarnoff Research Center (1969), 1969).

[75]S. Andrieu and P. Müller, *Les surfaces solides : concepts et méthodes* (EDP Sciences, 2005).

[76]M. Volmer and A. Z. Weber, "Nucleus Formation in Supersaturated Systems", Zeitschrift für Physikalische Chemie **119**, 277–301 (1926).

[77]F. C. Frank and J. H. Van Der Merwe, "One-dimensional dislocations. I. Static theory", Proceedings of the Royal Society A: Mathematical, Physical and Engineering Sciences **198**, 205–216 (1949).

[78]T. L. Brown-Heft, J. A. Logan, A. P. McFadden, C. Guillemard, P. Le Fèvre, F. Bertran, S. Andrieu, and C. J. Palmstrøm, "Epitaxial Heusler superlattice Co_2MnAl/Fe_2MnAl with perpendicular magnetic anisotropy and termination-dependent half-metallicity", Physical Review Materials **2**, 034402 (2018).

[79]J. K. Kawasaki, A. Sharan, L. I. M. Johansson, M. Hjort, R. Timm, B. Thiagarajan, B. D. Schultz, A. Mikkelsen, A. Janotti, and C. J. Palmstrøm, "A simple electron counting model for half-Heusler surfaces", Science Advances **4**, eaar2018 (2018).

[80]P. Turban, S. Andrieu, B. Kierren, E. Snoeck, C. Teodorescu, and A. Traverse, "Growth and characterization of single crystalline NiMnSb thin films and epitaxial NiMnSb/MgO/NiMnSb(001) trilayers", Physical Review B **65**, 134417 (2002).

[81]J. J. Harris, B. A. Joyce, and P. J. Dobson, "Oscillations in the surface structure of Sn-doped GaAs during growth by MBE", Surface Science **103**, L90–L96 (1981).

[82]H. Yang, M. Wassermeier, E. Tournié, L. Däweritz, and K. Ploog, "Double period RHEED oscillations during MBE growth of GaAs and AlAs on the GaAs (110) surface", Surface Science **331-333**, 479–484 (1995).

[83]J. Sudijono, M. D. Johnson, C. W. Snyder, M. B. Elowitz, and B. G. Orr, "Surface evolution during molecular-beam epitaxy deposition of GaAs", Physical Review Letters **69**, 2811–2814 (1992).

[84]G. E. Bacon and J. S. Plant, "Chemical ordering in Heusler alloys with the general formula A_2BC or ABC", Journal of Physics F: Metal Physics **1**, 524–532 (1971).

[85]S. Wurmehl and M. Wójcik, "Structural Order in Heusler Compounds", in *Heusler alloys*, Vol. 222 (2016), pp. 87–109.

[86]J. Protas, *Diffraction des rayonnements*, Dunod (1999).

[87]W. Cochran, "The correction of measured structure factors for thermal diffuse scattering", Acta Crystallographica Section A **A25**, 95–101 (1969).

[88]G. J. McIntyre, "Single-crystal diffractometry with monochromatic X-Rays and Neutrons", in *Neutron and synchrotron radiation for condensed matter studies. volume i : theory, instruments and methods*, Les éditio (1993), pp. 179–206.

[89]M. Khalid, A. Setzer, M. Ziese, P. Esquinazi, D. Spemann, A. Pöppl, and E. Goering, "Ubiquity of ferromagnetic signals in common diamagnetic oxide crystals", Physical Review B - Condensed Matter and Materials Physics **81**, 214414 (2010).

[90]M. J. Pechan, C. Yu, D. Carr, and C. J. Palmstrøm, "Remarkable strain-induced magnetic anisotropy in epitaxial Co_2MnGa (001) films", Journal of Magnetism and Magnetic Materials **286**, 340–345 (2005).

[91] A. Neggache, "Propriétés électroniques des alliages d'Heusler $Co_{1.5}Fe_{1.5}Ge$ et Co_2MnSi", PhD thesis (Université de Lorraine, 2014).

[92] A. Neggache, T. Hauet, F. Bertran, P. Le Fèvre, S. Petit-Watelot, T. Devolder, P. Ohresser, P. Boulet, C. Mewes, S. Maat, J. R. Childress, and S. Andrieu, "Testing epitaxial $Co_{1.5}Fe_{1.5}Ge(001)$ electrodes in MgO-based magnetic tunnel junctions", Applied Physics Letters **104**, 252412 (2014).

[93] C. T. Chen, F. Sette, Y. Ma, and S. Modesti, "Soft-x-ray magnetic circular dichroism at the $L_{2,3}$ edges of nickel", Physical Review B **42**, 7262–7265 (1990).

[94] B. T. Thole, P. Carra, F. Sette, and G. Van Der Laan, "X-ray circular dichroism as a probe of orbital magnetization", Physical Review Letters **68**, 1943–1946 (1992).

[95] S. W. Lovesey and S. P. Collins, *X-ray Scattering and Absoprtion by Magnetic Materials* (Clarendon Press, 1996).

[96] P. Ohresser, E. Otero, F. Choueikani, K. Chen, S. Stanescu, F. Deschamps, T. Moreno, F. Polack, B. Lagarde, J. P. Daguerre, F. Marteau, F. Scheurer, L. Joly, J. P. Kappler, B. Muller, O. Bunau, and P. Sainctavit, "DEIMOS: A beamline dedicated to dichroism measurements in the 350-2500 eV energy range", Review of Scientific Instruments **85**, 013106 (2014).

[97] L. Joly, E. Otero, F. Choueikani, F. Marteau, L. Chapuis, and P. Ohresser, "Fact continuous energy scan with dynamic coupling of the monochromator and undulator at the DEIMOS beamline", Journal of Synchrotron Radiation **21**, 502–506 (2014).

[98] J. Grabis, A. Bergmann, A. Nefedov, K. Westerholt, and H. Zabel, "Element-specific x-ray circular magnetic dichroism of Co_2MnGe Heusler thin films", Physical Review B - Condensed Matter and Materials Physics **72**, 024437 (2005).

[99] D. Asakura, T. Koide, S. Yamamoto, K. Tsuchiya, T. Shioya, K. Amemiya, V. R. Singh, T. Kataoka, Y. Yamazaki, Y. Sakamoto, A. Fujimori, T. Taira, and M. Yamamoto, "Magnetic states of Mn and Co atoms at Co_2MnGe/MgO interfaces seen via soft x-ray magnetic circular dichroism", Physical Review B - Condensed Matter and Materials Physics **82**, 184419 (2010).

[100] D. Weller, J. Stöhr, R. Nakajima, A. Carl, M. G. Samant, C. Chappert, R. Mégy, P. Beauvillain, P. Veillet, and G. A. Held, "Microscopic Origin of Magnetic Anisotropy in Au/Co/Au Probed with X-Ray Magnetic Circular Dichroism", Physical Review Letters **75**, 3752–3755 (1995).

[101] H. Dürr, G. van der Laan, D. Spanke, and F. Hillebrecht, "Electron-correlation-induced magnetic order of ultrathin Mn films", Physical Review B - Condensed Matter and Materials Physics **56**, 8156–8162 (1997).

[102] V. R. Singh, "X-ray magnetic circular dichroism study of oxide-based magnetic materials and half-metallic alloys", PhD thesis (University of Tokyo, 2011).

[103] K. Miyamoto, "Element-resolved magnetic moments of Heusler-type ferromagnetic ternary alloy Co_2MnGe", Journal of Physics: Condensed Matter **16**, S5797–S5800 (2004).

[104] Y. J. Chen, D. Basiaga, J. R. O'Brien, and D. Heiman, "Anomalous magnetic properties and Hall effect in ferromagnetic Co_2MnAl epilayers", Applied Physics Letters **84**, 4301–4303 (2004).

[105] C. D. Damsgaard, M. C. Hickey, S. N. Holmes, R. Feidenhans'l, S. O. Mariager, C. S. Jacobsen, and J. B. Hansen, "Interfacial, electrical, and spin-injection properties of epitaxial Co_2MnGa grown on GaAs(100)", Journal of Applied Physics **105**, 124502 (2009).

[106]T. Ambrose, J. J. Krebs, and G. A. Prinz, "Epitaxial growth and magnetic properties of single-crystal Co_2MnGe Heusler alloy films on GaAs (001)", Applied Physics Letters **76**, 3280–3282 (2000).

[107]M. R. Paudel, C. S. Wolfe, H. Patton, I. Dubenko, N. Ali, J. A. Christodoulides, and S. Stadler, "Magnetic and Transport Properties of $Co_2MnSn_xSb_{1-x}$ Heusler Alloys", Journal of Applied Physics **105**, 013716 (2009).

[108]B. Balke, G. H. Fecher, J. Winterlik, and C. Felser, "Mn_3Ga, a compensated ferrimagnet with high Curie temperature and low magnetic moment for spin torque transfer applications", Applied Physics Letters **90**, 152504 (2007).

[109]A. Rajanikanth, D. Kande, Y. K. Takahashi, and K. Hono, "High spin polarization in a two phase quaternary Heusler alloy $Co_2MnAl_{1-x}Sn_x$", Journal of Applied Physics **101**, 09J508 (2007).

[110]J. P. Wüstenberg, R. Fetzer, M. Aeschlimann, M. Cinchetti, J. Minár, J. Braun, H. Ebert, T. Ishikawa, T. Uemura, and M. Yamamoto, "Surface spin polarization of the nonstoichiometric Heusler alloy Co_2MnSi", Physical Review B - Condensed Matter and Materials Physics **85**, 064407 (2012).

[111]L. Bainsla and K. G. Suresh, "Equiatomic quaternary Heusler alloys: A material perspective for spintronic applications", Applied Physics Reviews **3**, 031101 (2016).

[112]A. F. Andreev, "The Thermal Conductivity Of The Intermediate State In Superconductors", Journal of Experimental and Theoretical Physics (U.S.S.R) **19**, 1228 (1964).

[113]K. E. H. M. Hanssen and P. E. Mijnarends, "Positron-annihilation study of the half-metallic ferromagnet NiMnSb: Theory", Physical Review B **34**, 5009–5016 (1986).

[114]K. E. H. M. Hanssen, P. E. Mijnarends, L. P. L. M. Rabou, and K. H. J. Buschow, "Positron-annihilation study of the half-metallic ferromagnet NiMnSb: Experiment", Physical Review B **42**, 1533–1540 (1990).

[115]C. N. Berglund and W. E. Spicer, "Photoemission Studies of Copper and Silver: Theory", Physical Review **136**, A1030 (1964).

[116]S. Hüfner, *Photoelectron Spectroscopy* (Springer-Verlag Berlin Heidelberg, 1970).

[117]W. Schattke and M. A. Van Hove, *Solid-State Photoemission and Related Methods*, edited by W. Schattke and M. A. Van Hove (WILEY-VCH GmbH, 2003).

[118]F. Bonell, "Analyse du transport dans les jonctions tunnel magnétiques épitaxiées à barrière de MgO(001) par manipulation des interfaces, de la barrière et des électrodes", PhD thesis (Université Henri Poincaré, 2009).

[119]T. Scheunemann, S. V. Halilov, J. Henk, and R. Feder, "Spin reversal and circular dichroism in valence-band photoemission from 3d-ferromagnets", Solid State Communications **91**, 487–490 (1994).

[120]I. Tamm, "Über eine mögliche Art der Elektronenbindung an Kristalloberflächen.", Zeitschrift für Physik **76**, 849–850 (1932).

[121]W. Shockley, "On the surface states associated with a periodic potential", Physical Review **56**, 317–323 (1939).

[122]J. A. Stroscio, D. T. Pierce, A. Davies, R. J. Celotta, and M. Weinert, "Tunneling spectroscopy of bcc (001) surface states", Physical Review Letters **75**, 2960–2963 (1995).

[123]F. Reinert, G. Nicolay, S. Schmidt, D. Ehm, and S. Hüfner, "Direct measurements of the L-gap surface states on the (111) face of noble metals by photoelectron spectroscopy", Physical Review B - Condensed Matter and Materials Physics **63**, 115415 (2001).

[124]J. Kirschner and R. Feder, "Spin Polarization in Double Diffraction of Low-Energy Electrons from W(001): Experiment and Theory", Physical Review Letters **42**, 1008–1011 (1979).

[125]T. Okuda, K. Miyamoto, A. Kimura, H. Namatame, and M. Taniguchi, "A double VLEED spin detector for high-resolution three dimensional spin vectorial analysis of anisotropic Rashba spin splitting", Journal of Electron Spectroscopy and Related Phenomena **201**, 23–29 (2015).

[126]D. M. Campbell, C. Hermann, G. Lampel, and R. Owen, "A compact cylindrical Mott electron polarimeter operating with accelerating voltage in the range 20-100 kV", Journal of Physics E: Scientific Instruments **18**, 664–672 (1985).

[127]F. B. Dunning, L. G. Gray, J. M. Ratliff, F. C. Tang, X. Zhang, and G. K. Walters, "Simple and compact low-energy Mott polarization analyzer", Review of Scientific Instruments **58**, 1706–1708 (1987).

[128]N. F. Mott, "The Scattering of Fast Electrons by Atomic Nuclei", Proceedings of the Royal Society A: Mathematical, Physical and Engineering Sciences **124**, 425–442 (1929).

[129]N. F. Mott, "The Polarisation of Electrons by Double Scattering", Proceedings of the Royal Society A: Mathematical, Physical and Engineering Sciences **135**, 429–458 (1932).

[130]J. Kessler, *Polarized Electrons*, edited by H. W. G. Ecker, P. Lambropoulos (Springer-Verlag, 1976).

[131]N. Sherman, "Coulomb Scattering of Relativistic electrons by point Nuclei", Physical Review **103**, 1601–1607 (1956).

[132]C. M. Cacho, S. V. Vlaic, M. Malvestuto, B. Ressel, E. A. Seddon, and F. Parmigiani, "Absolute spin calibration of an electron spin polarimeter by spin-resolved photoemission from the Au(111) surface states", Review of Scientific Instruments **80**, 043904 (2009).

[133]J. H. Scofield, *Theoretical Photoionization Cross Sections*, edited by J. H. Scofield (Lawrence Livermore Laboratory - University of California, 1973).

[134]J. Hermanson, "Final-state symmetry and polarization effects in angle-resolved photoemission spectroscopy", Solid State Communications **22**, 9–11 (1977).

[135]W. Eberhardt and F. J. Himpsel, "Dipole selection rules for optical transitions in the fcc and bcc lattices", Physical Review B **21**, 5572–5576 (1980).

[136]A. Tejeda and D. Maleterre, *Photoémission dans les solides : Concepts et applications*, EDP scienc (2015).

[137]S. Andrieu and P. Fréchard, "What information can be obtained by RHEED applied on polycrystalline films?", Surface Science **360**, 289–296 (1996).

[138]A. Akriche, H. Bouafia, S. Hiadsi, B. Abidri, B. Sahli, M. Elchikh, M. A. Timaoui, and B. Djebour, "First-principles study of mechanical, exchange interactions and the robustness in Co2MnSi full Heusler compounds", Journal of Magnetism and Magnetic Materials **422**, 13–19 (2017).

[139]S. Petit-Watelot, "Influence du couple de transfert de spin sur les fluctuations magnétiques thermiquement activées dans les jonctions tunnel magnétiques", PhD thesis (Université Grenoble I - Joseph Fourier, 2008).

[140]L. D. Landau and E. Lifshitz, "On the theory of the dispersion of magnetic permeability in ferromagnetic bodies", Physikalische Zeitschrift der Sowjetunion **8**, 153 (1935).

[141]T. L. Gilbert, "Lagrangian formulation of the gyromagnetic equation of the magnetization field", Physical Review Letters **100** (1955).

[142]E. Du Tremolet De Lacheisserie, *Magnétisme tome I : fondements*, Edp Scien. (1999).

[143]D. M. Pozar, *Microwave Engineering*, edited by H. Printing, 4th (John Wiley and Sons, Inc., 2011).

[144]R. D. McMichael, M. D. Stiles, P. J. Chen, and W. F. Egelhoff, "Ferromagnetic resonance linewidth in thin films coupled to NiO", Journal of Applied Physics **83**, 7037–7039 (1998).

[145]K. Lenz, H. Wende, W. Kuch, K. Baberschke, K. Nagy, and A. Jánossy, "Two-magnon scattering and viscous Gilbert damping in ultrathin ferromagnets", Physical Review B - Condensed Matter and Materials Physics **73**, 144424 (2006).

[146]K. Zakeri, J. Lindner, I. Barsukov, R. Meckenstock, M. Farle, U. Von Hörsten, H. Wende, W. Keune, J. Rocker, S. S. Kalarickal, K. Lenz, W. Kuch, K. Baberschke, and Z. Frait, "Spin dynamics in ferromagnets: Gilbert damping and two-magnon scattering", Physical Review B - Condensed Matter and Materials Physics **76**, 104416 (2007).

[147]M. A. Schoen, J. M. Shaw, H. T. Nembach, M. Weiler, and T. J. Silva, "Radiative damping in waveguide-based ferromagnetic resonance measured via analysis of perpendicular standing spin waves in sputtered permalloy films", Physical Review B - Condensed Matter and Materials Physics **92**, 184417 (2015).

[148]P. Laczkowski, J. C. Rojas-Sánchez, W. Savero-Torres, H. Jaffrès, N. Reyren, C. Deranlot, L. Notin, C. Beigné, A. Marty, J. P. Attané, L. Vila, J. M. George, and A. Fert, "Experimental evidences of a large extrinsic spin Hall effect in AuW alloy", Applied Physics Letters **104**, 142403 (2014).

[149]C. Scheck, L. Cheng, I. Barsukov, Z. Frait, and W. E. Bailey, "Low relaxation rate in epitaxial vanadium-doped ultrathin iron films", Physical Review Letters **98**, 117601 (2007).

[150]I. Abdallah, "Spin dynamics and structural modifications of Co_2MnSi Heusler alloy by Helium ions irradiation", PhD thesis (Université Toulouse 3 Paul Sabatier, 2016).

[151]H. S. Körner, M. A. Schoen, T. Mayer, M. M. Decker, J. Stigloher, T. Weindler, T. N. Meier, M. Kronseder, and C. H. Back, "Magnetic damping in poly-crystalline $Co_{25}Fe_{75}$: Ferromagnetic resonance vs. spin wave propagation experiments", Applied Physics Letters **111**, 132406 (2017).

[152]B. Heinrich, D. Fraitová, and V. Kamberský, "The Influence of s-d Exchange on Relaxation of Magnons in Metals", Physica Status Solidi (B) **23**, 501–507 (1967).

[153]L. Berger, "A simple theory of spin-wave relaxation in ferromagnetic metals", Journal of Physics and Chemistry of Solids **38**, 1321–1326 (1977).

[154]V. Kamberský, "Spin-orbital Gilbert damping in common magnetic metals", Physical Review B **76**, 134416 (2007).

[155]M. Gottwald, S. Andrieu, F. Gimbert, E. Shipton, L. Calmels, C. Magen, E. Snoeck, M. Liberati, T. Hauet, E. Arenholz, S. Mangin, and E. E. Fullerton, "Co/Ni(111) superlattices studied by microscopy, x-ray absorption, and ab initio calculations", Physical Review B **86**, 014425 (2012).

[156]R. Sbiaa, J. M. Shaw, H. T. Nembach, M. Al Bahri, M. Ranjbar, J. Åkerman, and S. N. Piramanayagam, "Ferromagnetic resonance measurements of (Co/Ni/Co/Pt) multilayers with perpendicular magnetic anisotropy", Journal of Physics D: Applied Physics **49**, 425002 (2016).

[157]W. B. Zeper, F. J. A. M. Greidanus, P. F. Carcia, and C. R. Fincher, "Perpendicular magnetic anisotropy and magneto-optical Kerr effect of vapor-deposited Co/Pt-layered structures", Journal of Applied Physics **65**, 4971–4975 (1989).

[158]J. G. Azadani, K. Munira, J. Romero, J. Ma, C. Sivakumar, A. W. Ghosh, and W. H. Butler, "Anisotropy in layered half-metallic Heusler alloy superlattices", Journal of Applied Physics **119**, 043904 (2016).

[159]L. Wollmann, S. Chadov, J. Kübler, and C. Felser, "Magnetism in tetragonal manganese-rich Heusler compounds", Physical Review B - Condensed Matter and Materials Physics **92**, 064417 (2015).

[160]E. Krén and G. Kádár, "Neutron diffraction study of Mn_3Ga", Solid State Communications **8**, 1653–1655 (1970).

[161]F. Wu, S. Mizukami, D. Watanabe, H. Naganuma, M. Oogane, Y. Ando, and T. Miyazaki, "Epitaxial $Mn_{2.5}Ga$ thin films with giant perpendicular magnetic anisotropy for spintronic devices", Applied Physics Letters **94**, 122503 (2009).

[162]S. Mizukami, T. Kubota, F. Wu, X. Zhang, T. Miyazaki, H. Naganuma, M. Oogane, A. Sakuma, and Y. Ando, "Composition dependence of magnetic properties in perpendicularly magnetized epitaxial thin films of Mn-Ga alloys", Physical Review B - Condensed Matter and Materials Physics **85**, 014416 (2012).

[163]S. Wurmehl, H. C. Kandpal, G. H. Fecher, and C. Felser, "Valence electron rules for prediction of half-metallic compensated- ferrimagnetic behaviour of Heusler compounds with complete spin polarization", Journal of Physics: Condensed Matter **18**, 6171–6181 (2006).

[164]Q. L. Ma, X. M. Zhang, T. Miyazaki, and S. Mizukami, "Artificially engineered Heusler ferrimagnetic superlattice exhibiting perpendicular magnetic anisotropy", Scientific Reports **5**, 7863 (2015).

[165]F. Dulot, P. Turban, B. Kierren, J. Eugène, M. Alnot, and S. Andrieu, "(001) V surface structures analyzed by RHEED and STM", Surface Science **473**, 172–182 (2001).

[166]M. Nemoz, "Etude nano-structurale de superréseaux d'oxydes ferroélectriques", PhD thesis (Université Joseph Fourier - Grenoble I, 2004).

[167]N. V. Uvarov, Y. V. Kudryavtsev, A. F. Kravets, A. Y. Vovk, R. P. Borges, M. Godinho, and V. Korenivski, "Electronic structure, optical and magnetic properties of Co_2FeGe Heusler alloy films", Journal of Applied Physics **112**, 063909 (2012).

[168]J. Winterlik, B. Balke, G. H. Fecher, C. Felser, M. C. M. Alves, F. Bernardi, and J. Morais, "Structural, electronic, and magnetic properties of tetragonal $Mn_{3-x}Ga$: Experiments and first-principles calculations", Physical Review B **77**, 054406 (2008).

[169]E. Beaurepaire, J.-C. Merle, A. Daunois, and J.-Y. Bigot, "Ultrafast Spin Dynamics in Ferromagnetic Nickel", Physical Review Letters **76**, 4250 (1996).

[170]A. Mann, J. Walowski, M. Münzenberg, S. Maat, M. J. Carey, J. R. Childress, C. Mewes, D. Ebke, V. Drewello, G. Reiss, and A. Thomas, "Insights into ultrafast demagnetization in pseudogap half-metals", Physical Review X **2**, 041008 (2012).

[171]M. S. El Hadri, M. Hehn, G. Malinowski, and S. Mangin, "Materials and devices for all-optical helicity-dependent switching", Journal of Physics D: Applied Physics **50**, 133002 (2017).

[172]B. Koopmans, J. J. M. Ruigrok, F. Dalla Longa, and W. J. M. De Jonge, "Unifying ultrafast magnetization dynamics", Physical Review Letters **95**, 267207 (2005).

[173]G. M. Müller, J. Walowski, M. Djordjevic, G. X. Miao, A. Gupta, A. V. Ramos, K. Gehrke, V. Moshnyaga, K. Samwer, J. Schmalhorst, A. Thomas, A. Hütten, G. Reiss, J. S. Moodera, and M. Münzenberg, "Spin polarization in half-metals probed by femtosecond spin excitation", Nature Materials **8**, 56–61 (2009).

[174]M. Deb, E. Popova, M. Hehn, N. Keller, S. Mangin, and G. Malinowski, "Picosecond acoustic-excitation-driven ultrafast magnetization dynamics in dielectric Bi-substituted yttrium iron garnet", Physical Review B **98**, 174407 (2018).

[175]G. Malinowski, F. Dalla Longa, J. H. H. Rietjens, P. V. Paluskar, R. Huijink, H. J. M. Swagten, and B. Koopmans, "Control of speed and efficiency of ultrafast demagnetization by direct transfer of spin angular momentum", Nature Physics **4**, 855–858 (2008).

[176]B. Koopmans, G. Malinowski, F. Dalla Longa, D. Steiauf, M. Fähnle, T. Roth, M. Cinchetti, and M. Aeschlimann, "Explaining the paradoxical diversity of ultrafast laser-induced demagnetization", Nature Materials **9**, 259–265 (2010).

[177]S. Mizukami, A. Sakuma, A. Sugihara, T. Kubota, Y. Kondo, H. Tsuchiura, and T. Miyazaki, "Tetragonal $D0_{22}Mn_{3+x}Ge$ Epitaxial Films Grown on MgO(100) with a Large Perpendicular Magnetic Anisotropy", Applied Physics Express **6**, 123002 (2013).

[178]A. Sugihara, K. Z. Suzuki, T. Miyazaki, and S. Mizukami, "Magnetic properties of ultrathin tetragonal Heusler $D0_{22}$-Mn_3Ge perpendicular-magnetized films", Journal of Applied Physics **117**, 17B511 (2015).

[179]J. Li, H. Chen, Y. Li, Y. Xiao, and Z. Li, "A theoretical design of half-metallic compounds by a long range of doping Mn for Heusler-type Cr_3Al", Journal of Applied Physics **105**, 083717 (2009).

[180]A. E. Clark, M. Wun-Fogle, J. B. Restorff, and T. A. Lograsso, "Magnetostrictive Properties of Galfenol Alloys Under Compressive Stress", Materials Transactions **43**, 881–886 (2002).

[181]K. Manna, Y. Sun, L. Muechler, J. Kübler, and C. Felser, "Heusler, Weyl and Berry", Nature Reviews Materials **3**, 244 (2018).

Appendix A

Polycrystal structures

The three polycrystals Co_2MnSi, Co_2MnGa and Co_2MnGe were elaborated directly on a glass substrate at T = 600 K, roughly. The fluxes of each element were calibrated using quartz microbalances and the deposited thickness was around 40 nm. They were then annealed at approximatively 1000 K. RHEED patterns of the three layers are presented in figure A.1 and show rings of diffraction like in the case of powders. This is due to the high roughness of the surface that acts like a 3D polycrystal for the electron beam. The rings are presenting small region of extinction that could be due to a small texture axis

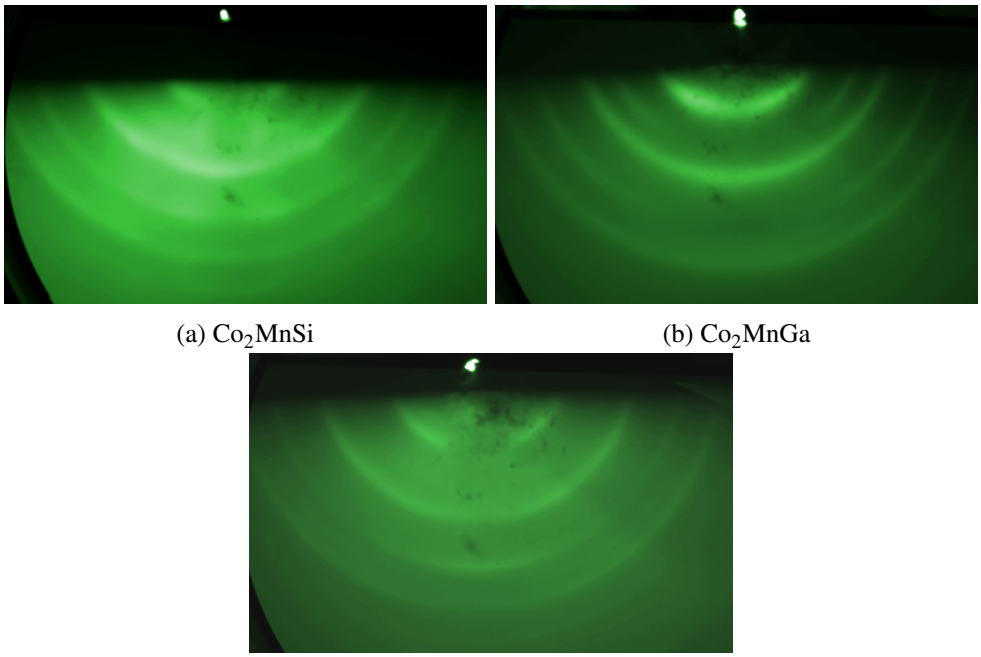

(a) Co_2MnSi (b) Co_2MnGa

(c) Co_2MnGe

Figure A.1: RHEED patterns on Co_2MnSi, Co_2MnGa and Co_2MnGe polycrystals.

[137]. To investigate on this texture possibility and on the chemical ordering occurring in polycrystals, Co_2MnSi was investigated by TEM. To do that, the surface of the sample was scratched with a tweezers and the powder was fixed on the sample holder. Results are shown in figure A.2. The diffraction pattern in figure A.2a does not show any preferential texture axis. In figure A.2b, the lateral grain size appears to be around 20-30 nm. Very small dark grains of less than 10 nm come from the Au capping layer. We finally managed to find a [110] oriented grain to check the chemical ordering in this polycrystalline layer.

Figures A.2c and A.2d are showing B2 and $L2_1$ domains.

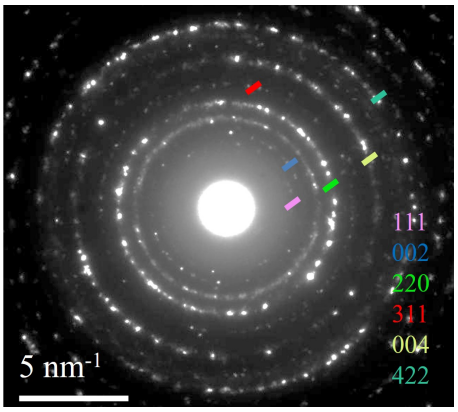

(a) Diffraction pattern

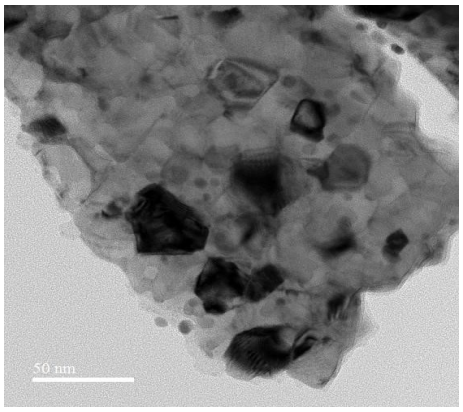

(b) Grains

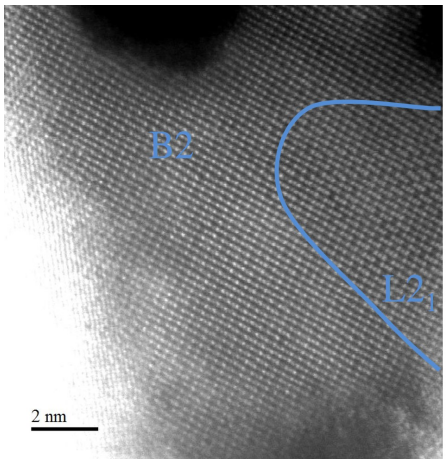

(c) HAADF micrograph on a [110] oriented grain

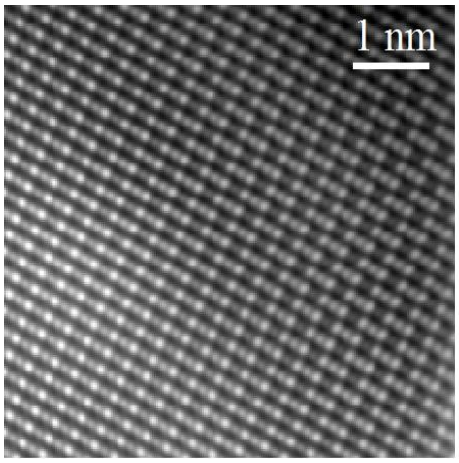

(d) IFFT

Figure A.2: TEM and HAADF micrographs on Co_2MnSi polycrystal.

Appendix B

Spin-resolved photoemission spectroscopy on Co_2FeAl

Co_2FeAl was elaborated by MBE in the same conditions than Co_2MnZ compounds. RHEED and XRD patterns indicated a B2 disorder like in Co_2MnAl, as reported by the literature. The spin polarization was measured at the CASSIOPEE beamline and results are shown in figure B.1. The maximum of spin polarization of 35 % is obtained at 37 eV in *p* polarization of photons.

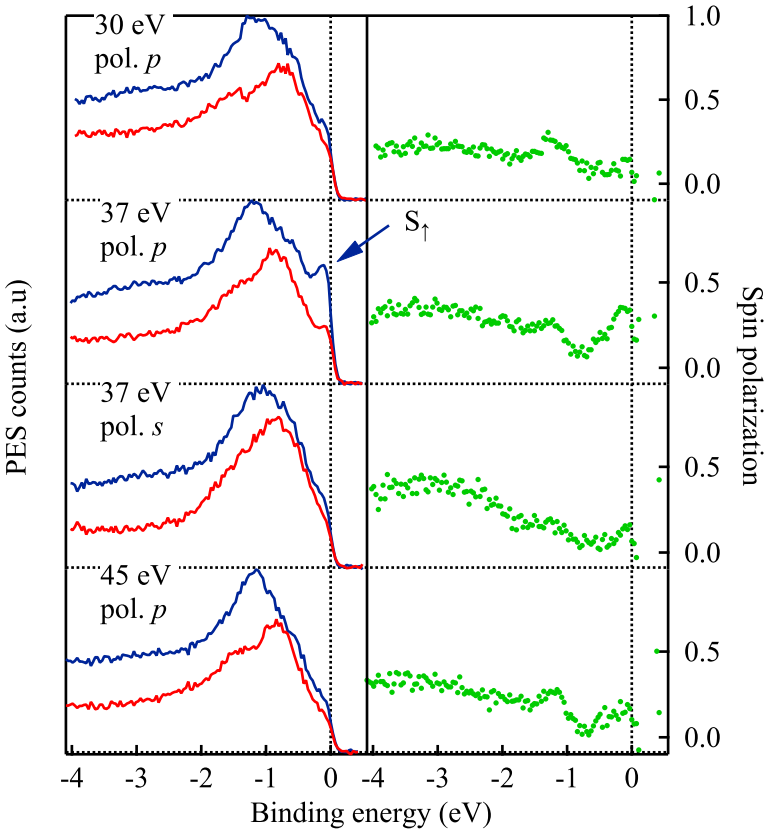

Figure B.1: SR-PES spectra obtained on Co_2FeAl Heusler compound.

Remerciements

Je souhaite remercier profondément les nombreuses personnes qui ont contribué à ce travail.

D'abord pour la bourse de thèse : Paul Morin et le synchrotron SOLEIL, la région Grand Est, le LLB, L'institut Jean Lamour et l'université de Lorraine.
L'équipe 101 "permanente" : Stéphane, Olivier, Karine, Sébastien, François, Jon, Julius, Carlos, Daniel, Michel et Stéphane qui m'ont tous apporté, à un moment, un soutien précieux ou une expertise quelconque.
La ligne de lumière Cassiopée : Julien, Françoise, Daniel, Patrick et François pour leur disponibilité, l'ambiance chaleureuse et la haute performance de cette ligne de lumière.
L'équipe 101 "volatile" : Gauthier, Maryam, Kosseila, Ibrahim, Quentin, Elmer, Alexandre, Claudia, Thibaud, Yassine, Mohammed, Victor, Wei, Boris, Vincent et Jean-Loïs pour l'ambiance, l'entraide et la bonne humeur de chacun.
Daniel pour les nombreuses discussions. Alexandre, Hervé et Bertrand pour avoir suivi avec attention l'évolution de mon travail.
Le CC Daum : Danielle, Ludovic, Alexandre et Olivier (Vinci) pour cet outil formidable et opérationnel qu'est le TUBE. Le CC 3M : Jaafar et Sylvie pour leur savoir-faire et leur travail acharné. Le CC X-Gamma : Sylvie et Pascal. Le CC Magnétisme : Crosby, Thomas, Tom et Stéphane. Le CC Minalor : François, Gwladys, Laurent et Carlos.

Je veux remercier par-dessus tous les personnes suivantes.

Patrick pour avoir été disponible tout le temps pendant les périodes synchrotron, pour le ravitaillement (indispensable), pour les histoires, pour les Houches et tout le reste. Sébastien pour m'avoir épaulé, enseigné et fait confiance tout au long de ma thèse. Carlos pour son bel accent et sa motivation sans faille. Elmer pour avoir partagé le bureau et toutes sortes d'anecdotes avec moi. Ludovic pour son efficacité constante.

Jean-Loïs, Vincent et Yannis. Arnaud et Jimmy.

Et puis finalement, François et Stéphane qui m'ont tout appris, avec patience et gentillesse, et que je considère maintenant comme des amis proches.

Abstract: Improvements in thin film elaboration methods and a deeper understanding of condensed matter physics have led to new exciting phenomena in spin electronics (spintronics). In particular, magnetization reversal by spin-orbit and spin-transfer torque as well as the development of spin waves based devices have placed the Gilbert magnetic damping coefficient as a key parameter for future data storage and information processing technologies. The prediction of ultralow magnetic damping in Co_2MnZ Heusler half-metal magnets is explored in this study and the damping response is shown to be linked to the underlying electronic structure. By substitution of the Z element in high quality Co_2MnZ (Z=Al, Si, Ga, Ge, Sn and Sb) epitaxial thin films, electronic properties such as the minority-spin band gap, Fermi energy position in the band gap, and spin polarization can be tuned and the consequences for magnetization dynamics analyzed. Experimental results allow us to directly explore the interplay of spin polarization, spin gap and Fermi energy position, with the magnetic damping obtained in these films (together with predictions from ab initio calculations). The ultralow magnetic damping coefficients measured in the range from 4.1×10^{-4} to 9×10^{-4} for Co_2MnSi, Co_2MnGe, Co_2MnSn and Co_2MnSb are the lowest values obtained on conductive layers and offer a clear experimental demonstration of theoretical predictions on half metal magnetic Heusler compounds. Then, the relation between the Gilbert damping and the ultrafast demagnetization time in quaternary $Co_2MnSi_xAl_{1-x}$ compounds with a tunable spin polarization is analyzed. This way, it is possible to confront theoretical models unifying those two quantities that live in different timescales. Finally, structural and magnetic properties of Mn_3Ga/Co_2YZ Heusler superlattices are investigated in order to combine ultralow Gilbert damping coefficient, minority spin band gap and perpendicularly magnetized heterostructures, another requirement for low energy consumption devices. Through the present work, we aim to evidence that Heusler compounds provide an excellent playground to study fundamental magnetism and offer a pathway for future materials design. **Keywords: spintronics, Heusler, half metal magnets, Gilbert damping, perpendicular anisotropy, ultrafast dynamics.**

Résumé : L'amélioration des techniques de dépôts et l'évolution de la compréhension de la physique de la matière condensée a conduit à la découverte de phénomènes nouveaux en électronique de spin (spintronique). En particulier, le retournement de l'aimantation par couple de transfert de spin et couple spin-orbite, ainsi que le développement de dispositifs basés sur la propagation d'ondes de spin ont fait de l'amortissement magnétique de Gilbert un paramètre central pour les futures technologies de stockage et de traitement de l'information. Dans cette étude, la prédiction de valeurs très faibles d'amortissement dans les alliages d'Heusler demi métaux magnétiques Co_2MnZ est expérimentalement observée et directement corrélée à la structure électronique sous-jacente. En effet, en substituant l'élément Z dans des couches minces monocristallines de haute qualité de Co_2MnZ (Z= Al, Si, Ga, Ge, Sn, Sb) faites par épitaxie par jet moléculaire, les propriétés électroniques telles que le gap de spin minoritaire, la position du niveau de Fermi et la polarisation en spin peuvent être accordées et leurs conséquences sur la dynamique de l'aimantation sont analysées. Les résultats expérimentaux nous permettent de comprendre la relation existante entre la structure électronique mesurée et la valeur d'amortissement magnétique, ainsi que de les comparer aux calculs ab initio. Les valeurs d'amortissement entre 4.1×10^{-4} et 9×10^{-4} pour Co_2MnSi, Co_2MnGe, Co_2MnSn et Co_2MnSb sont les plus petites valeurs jamais reportées pour des couches conductrices et constituent une preuve expérimentale qui confirme les prédictions théoriques sur ces alliages d'Heusler demi métaux magnétiques. Ensuite, la relation entre l'amortissement magnétique de Gilbert et le temps de désaimantation ultra-rapide induit par pulse laser dans la série d'alliages quaternaires $Co_2MnSi_xAl_{1-x}$ à polarisation en spin variable est étudiée. Cette partie vise à vérifier des modèles théoriques qui essaient d'unifier ces deux quantités vivant sur des échelles de temps différentes. Finalement, les propriétés structurales et magnétiques de super réseaux Mn_3Ga/Co_2YZ sont étudiées dans le but de combiner un amortissement de Gilbert très faible, un gap de spin minoritaire ainsi que l'aimantation perpendiculaire aux plans des couches, une caractéristique indispensable pour des dispositifs à faible consommation d'énergie. En résumé, ce travail contribue à démontrer la souplesse et la richesse des propriétés des alliages d'Heusler pour l'étude du magnétisme fondamental ainsi que pour la conception des matériaux et dispositifs de demain. **Mots clés : spintronique, alliages d'Heusler, demi métaux magnétiques, amortissement de Gilbert, anisotropie perpendiculaire, dynamique ultrarapide.**